Crustal structure of the spreading plate boundary in Iceland and the north Atlantic from gravity data

Field, Paul R.

Crustal Structure of the Spreading Plate Boundary in Iceland and the North Atlantic from Gravity Data

A thesis presented for the degree of

Doctor of Philosophy

by

Paul R. Field

University of Durham
Department of Geological Sciences

April 1994

DECLARATION

I declare that the work contained in this thesis has not been submitted elsewhere for any other degree or qualification, and is my own work, unless otherwise referenced.

Paul R. Field

University of Durham

April 1994

Abstract

Gravity datasets from two geothermal areas in Iceland, an Iceland-wide gravity dataset, and marine gravity data from the Reykjanes Ridge at 58°N, which can be seen as the submarine extension of the Icelandic accretionary system, have been studied in this thesis.

Results of previous local earthquake seismic tomography studies of the shallow crustal structure of two spreading segments in Iceland have been used, in conjunction with gravity observations, to assess the fidelity of the tomographic method and further refine the description of the crustal structure for these areas. This was accomplished by predicting the component of the observed gravity field which may be produced by the tomographically imaged bodies and in the process attempting to explain any residual anomalies. Results showed additional shallow structure inferred from gravity observation and suggested that local earthquake seismic tomography can 'overlook' some geological structure.

The Icelandic gravity field was separated into long and short wavelength components which were attributed to mantle plume and crustal effects, respectively. Physical parameters were attributed to the sources of these anomalies where possible. Results showed that a simple cylinder model (radius ~100 km) of anomalous mantle density (~ -35 kg m^{-3}) could explain the large scale gravity field over Iceland. Shallow density variations in the top 1 km of the crust appeared to be mainly responsible for smaller scale gravity anomalies. A simple Bouguer slab model suggests that the crust may be ~7 km thicker beneath Iceland compared to neighbouring oceanic areas, consistent with an underplating mechanism for crustal accretion in Iceland.

Gravity data were acquired on a cruise over the Reykjanes Ridge in the North Atlantic. The marine gravity data were reduced systematically to a residual anomaly and showed that there was the possibility of crustal thinning associated with a bathymetric offset which was interpreted as a second order discontinuity. The form of the residual gravity was similar to other discontinuities of this order on the Mid-Atlantic Ridge, although not of the same amplitude.

Contents

Abstract
Contents
List of Figures
List of Tables

Chapter 1 1
Structure of the Iceland Plateau 1
1.1 Introduction 1
1.2 Formation of the Iceland Plateau 3
1.3 Tectonics and the Position of the Present Plate Boundary in Iceland 3
1.4 Shifting of the Plate Boundary in Iceland 8
1.5 Accretion at the Plate Boundary 10
1.6 Crustal Structure 10
1.7 The Crust-Mantle Boundary 16
1.8 Sub-Crustal Structure 16
1.9 Iceland and the Reykjanes Ridge 18
1.10 Summary 20

Chapter 2 21
Structure of the Hengill-Grensdalur and Krafla Spreading Centres 21
2.1 Introduction 21
2.2 Combining Gravity and Seismic Data 21
2.2.1 Joint Inversion 21
2.2.2 Forward Modelling 23
2.2.3 Joint Inversion or Forward Model? 24
2.2.4 Methodology 24
2.3 The Hengill-Grensdalur spreading segment 24
2.3.1 Introduction 24
2.3.2 The Hengill-Grensdalur Tomographic Study 27
2.3.2.1 The Tomographic Inversion Method 27
2.3.2.2 Tomographic Results from the Hengill-Grensdalur Area 28
2.3.3 Forward Modelling using the Tomographic Result 30
2.3.3.1 Seismic Velocity and Density 30
2.3.3.2 Obtaining the Predicted Gravity Anomaly from the Tomographic Velocity Structure 31

2.3.4 The Hengill-Grensdalur Gravity Dataset 34
2.3.4.1 Acquisition 34
2.3.4.2 Bouguer Reduction Density 36
2.3.4.3 Removal of the Regional 40
2.3.5 Field Continuation 45
2.3.5.1 Introduction 45
2.3.5.2 The Continuation Method 45
2.3.5.3 The Equivalent Source Method 47
2.3.5.4 Testing the Equivalent Source Method 48
2.3.6 Comparison of the Predicted and Real De-trended Bouguer Anomaly Fields 51
2.3.7 Assessment of Errors 52
2.3.8 Interpretation of the Hengill-Grensdalur Results 54
2.4 The Krafla Spreading Segment 59
2.4.1 Introduction 59
2.4.2 The Krafla Tomography Study 63
2.4.2.1 The Tomographic Inversion 63
2.4.2.2 Tomographic Results from the Krafla Area 63
2.4.3 Forward Modelling of the Tomographic Solution 65
2.4.4 The Krafla Gravity Dataset 65
2.4.4.1 Acquisition 65
2.4.4.2 Bouguer Reduction Density 67
2.4.4.3 Removal of the Regional 67
2.4.4.2 Continuation of the Gravity Field 67
2.4.5 Comparison of the Predicted and Real Bouguer Anomaly Fields 70
2.4.6 Assessment of Errors 71
2.4.7 Gravity Inversion 71
2.4.7.1 Density Distribution Within a Horizontal Slab 71
2.4.7.2 The Inversion Parameters 72
2.4.7.3 Result of the Inversion 77
2.4.8 Interpretation of the Krafla Results 77
2.5 Discussion 79
2.6 Summary 82

Chapter 3 83
Analysis of the Icelandic Gravity Field 83
3.1 Introduction 83

3.1.1 Components of the Icelandic Gravity Field 83
3.1.2 A Mantle Plume 84
3.1.3 The Lithospheric Thermal Effect 87
3.1.4 Previous Gravity Work 88
3.2 Methodology 89
3.3 The Gravity Dataset 89
3.3.1 Description of the Data 89
3.3.2 Assessment of Data Errors 90
3.4 Reduction of the Gravity Data 90
3.4.1 The Free Air Anomaly over Iceland 90
3.4.2 Bouguer Correction 94
3.4.3 Continuation of the Bouguer Anomalies 95
3.4.4 Separation of the Long and Short Wavelength Components of the Continued Bouguer Field 98
3.5 Results: The Gravity Anomalies 103
3.5.1 Free Air Anomaly 103
3.5.2 The Continued Bouguer Fields 103
3.5.3 Long Wavelength Anomaly 104
3.5.4 Short Wavelength Anomaly 107
3.6 Interpretation 110
3.6.1 The Long Wavelength Component 110
3.6.1.1 Introduction 110
3.6.1.2 Crustal Thickness Variations 110
3.6.1.3 Sub-Crustal Density Structure 112
3.6.1.4 Cylinder Model 116
3.6.1.5 A Comparison of Regional Tomography and Gravity Observations over Iceland 120
3.6.2 The Short Wavelength Component 125
3.6.2.1 Introduction 125
3.6.2.2 Gravity Signature of Iceland's Spreading Plate Boundaries 134
3.6.2.3 The Short Wavelength Gravity Anomalies 137
3.7 Mantle Flow 142
3.8 Discussion 146
3.9 Summary 149

Chapter 4 150

The Reykjanes Ridge at 58°N 150
4.1 The Oceanic Spreading Boundary 150
4.1.1 Introduction 150
4.1.2 The Oceanic Crust 152
4.1.3 Ridge Axis Models 159
4.1.4 Previous Work 162
4.1.4.1 Geophysical Investigations of the Reykjanes Ridge 162
4.1.4.2 Three-Dimensional Marine Gravity Work 163
4.1.5 Summary 164
4.2 Methodology 164
4.2.1 Outline of the Reduction Method 164
4.2.2 Theory 165
4.2.2.1 Introduction 165
4.2.2.2 The 'Forward' Computation 165
4.2.2.3 The Inverse Problem 166
4.2.2.4 Lithospheric Thermal Models 167
4.2.3 Implementation 169
4.2.3.1 Implementing the 'Forward' Computation 169
4.2.3.2 Implementing the Lithospheric Model 169
4.2.3.3 Implementing the Inversion 171
4.3 Data 171
4.3.1 Acquisition 171
4.3.2 Shipboard Data Reduction 174
4.3.3 Errors in Sea Gravimetry 176
4.4 Modelling the Oceanic Crust 178
4.4.1 Introduction 178
4.4.2 One Layer Crust versus Multilayered Crust 178
4.4.3 Crustal Densities 179
4.4.4 The Thickness of the Crust 182
4.4.5 Density of the Upper Mantle 185
4.4.6 The Model 185
4.5 Results 185
4.5.1 Bathymetry 185
4.5.2 TOBI Observations 186
4.5.3 Tectonics at 58°N 186
4.5.4 Gravity 189

4.5.4.1 Free Air Anomaly 189
4.5.4.2 The Mantle Bouguer Anomaly 189
4.5.4.3 Residual Anomaly 192
4.5.4.4 Inversion 192
4.6 Discussion 195
4.6.1 Causes of the Residual Gravity Anomaly 195
4.6.2 Crustal Thickness Variations 195
4.6.3 Variations in Crustal Density 195
4.6.4 Mantle Density Variations 196
4.6.5 Isostasy on the Reykjanes Ridge 198
4.6.6 Comparison of Other Work with Reykjanes Ridge Residual Gravity Field 198
4.7 The Reykjanes Ridge and the Icelandic Mantle Plume 201
4.8 Summary 201

Chapter 5 203
Summary 203
5.1 Icelandic Plateau 203
5.1.1 The Mantle 203
5.1.2 Crustal Accretion 203
5.1.3 Shallow Crustal Heterogeneity 204
5.1.3.1 Axial Structure 204
5.1.3.2 Regional Structure 204
5.1.4 Reykjanes Ridge 205
5.2 The Fidelity of Seismic Tomography 205

References 208
Appendix 218

List of Figures

Chapter 1

Figure 1.1 Location map of Iceland and the Reykjanes Ridge..... 2
Figure 1.2 Simplified geological and tectonic map of Iceland..... 4
Figure 1.3a Location map of place names used in this thesis..... 6
Figure 1.3b Topographic map of Iceland..... 6
Figure 1.4 Epicentres and focal mechanisms of earthquakes in the Iceland area.... 7
Figure 1.5 Development of the present pattern of the volcanic zones in Iceland.... 9
Figure 1.6 (Top) Section through the lithosphere according to the accretion model of Pálmason (1980). (Bottom left) Kinematics of crustal accretion. (Bottom right) Petrological structure of the lithosphere, as derived from the kinematic model..... 11
Figure 1.7 (Top) Geothermal areas and the geological structure of Iceland. (Bottom) The temperature gradient in SW-Iceland..... 13
Figure 1.8 (Top) Regional resistivity of Iceland at 500 m depth. (Bottom) Regional P-wave velocity of Iceland at 500 m depth..... 14
Figure 1.9 Isostatic anomaly of Iceland..... 15
Figure 1.10 Calculated depth to the basalt solidus below Iceland..... 17
Figure 1.11 3-D structure of the Icelandic magma system..... 19

Chapter 2

Figure 2.1 Map showing the geographic locations of the Hengill-Grensdalur and Krafla areas in Iceland..... 22
Figure 2.2 The Hengill-Grensdalur seismometer network, showing the locations of seismometers, earthquakes, and schematic tectonics..... 25
Figure 2.3 3-D image of the seismic velocity field obtained by local earthquake tomography..... 29
Figure 2.4 Compressional wave velocity versus wet bulk density for rock samples from the Reydarfjördur borehole, eastern Iceland..... 32
Figure 2.5 A parallelepiped in space, of density contrast $\Delta\rho$, bounded by two opposite corners..... 33
Figure 2.6 Gravity station coverage for the Hengill-Grensdalur area..... 35
Figure 2.7 Map of the Hengill-Grensdalur area showing the locations where rock samples were collected for density determinations..... 38
Figure 2.8 (a) Bouguer anomaly map of the Hengill-Grensdalur area..... 41
Figure 2.8 (b) De-trended Bouguer anomaly map of the Hengill-Grensdalur area..... 42

Figure 2.8 (c) The regional gravity trend for the Hengill-Grensdalur area..... 43
Figure 2.9 Gravity and predicted gravity maps of the area studied tomographically.....44
Figure 2.10 Explanation of why Bouguer anomaly values do not lie in a common plane.....45
Figure 2.11 Testing of the program EQSM.....49
Figure 2.12 Continued gravity and predicted gravity maps in the area studied tomographically.....50
Figure 2.13 The high temperature geothermal zone in the Hengill-Grensdalur area.....55
Figure 2.14 Combined gravity cross-section across the residual low gravity zone. 57
Figure 2.15 Candidate interpretations of the residual low gravity zone in the geothermal area..... 58
Figure 2.16 Area covered by the Krafla local earthquake tomography experiment. 61
Figure 2.17 3-D image of the final tomographic velocity model for the Krafla region..... 64
Figure 2.18 Gravity station coverage for the Krafla area..... 66
Figure 2.19 Gravity and predicted gravity fields for the Krafla region..... 68
Figure 2.20 Upward continued gravity and predicted gravity fields..... 69
Figure 2.21 Testing the inversion program INVRHO..... 74
Figure 2.22 Plots of the natural logarithm of the power spectrum versus wave number for three synthetically generated gravity maps..... 75
Figure 2.23 Plots of the natural logarithm of the power spectrum versus wave number for the upward continued gravity field..... 76
Figure 2.24 The result of a gravity inversion..... 78
Figure 2.25 Seismic rays travelling through a heterogeneous medium..... 81

Chapter 3

Figure 3.1 The first two stages of a hypothetical plume's evolution..... 84
Figure 3.2 Sleep's (1990) plume model..... 85
Figure 3.3 Structure of a thermal plume impinging on the base of the lithosphere..... 86
Figure 3.4 Schematic diagrams representing the possible thermal and density structure of a plume below a rifting and non-rifting lithosphere..... 87
Figure 3.5 Perturbation of the basalt solidus from the normal parabola shaped curve to the near horizontal due to the proximity of an extensive thermal anomaly..... 88
Figure 3.6 The position of gravity stations used in this chapter..... 91

Figure 3.7 An error map constructed to show the effect of an incorrect choice of Bouguer density 92
Figure 3.8 The Free Air Anomaly map of Iceland 93
Figure 3.9 Map depicting the density zoning used for assigning different Bouguer reduction densities to the Icelandic gravity stations 96
Figure 3.10 RMS signal of a subset of the Iceland dataset which has been continued versus depth to the equivalent source layer used for the continuation. 97
Figure 3.11 CBA1. Contour map of the continued Bouguer gravity anomalies for single density reduction 99
Figure 3.12 CBA2. Contour map of the continued Bouguer gravity anomalies for dual density reduction 100
Figure 3.13 Radial power spectrum for CBA1 and post-filtered power spectra for CBA1 101
Figure 3.14 Plot of the natural logarithm of the power versus wave number for CBA1 102
Figure 3.15 The long wavelength component of the Icelandic gravity field, derived from CBA1 105
Figure 3.16 The long wavelength component of the Icelandic gravity field, derived from CBA2 106
Figure 3.17 The short wavelength component of the Icelandic gravity field, derived from CBA1 108
Figure 3.18 The short wavelength component of the Icelandic gravity field, derived from CBA2 109
Figure 3.19 Contour map of the crust-mantle relief beneath Iceland 111
Figure 3.20 Testing the effect of different parameters on a constant thickness slab that has laterally varying density 113
Figure 3.21 Density distribution within a 200 km thick slab at a depth of 25 km, derived from CBA1 114
Figure 3.22 Density distribution within a 200 km thick slab at a depth of 25 km, derived from CBA2 115
Figure 3.23 The cylinder model 117
Figure 3.24 Anomalous density required by an infinitely long cylinder to produce a given radial change in gravity 118
Figure 3.25 Gravity forward model of a cylinder model 119
Figure 3.26 Icelandic seismograph network and results of tomography by Tryggvason et al. (1983) 121
Figure 3.27 Bouguer anomaly values for Iceland versus ΣB. (velocity perturbation %) 124

Figure 3.28 (a) Density distribution within a 1 km thick slab derived from the short wavelength component of CBA1 126
Figure 3.28 (b) Density distribution within a 1 km thick slab derived from the short wavelength component of CBA2 127
Figure 3.29 (a) Density distribution within a 5 km thick slab derived from the short wavelength component of CBA1 128
Figure 3.29 (b) Density distribution within a 5 km thick slab derived from the short wavelength component of CBA2 129
Figure 3.30 (a) Density distribution within a 10 km thick slab derived from the short wavelength component of CBA1 130
Figure 3.30 (b) Density distribution within a 10 km thick slab derived from the short wavelength component of CBA2 131
Figure 3.31 (a) Density distribution within a 25 km thick slab derived from the short wavelength component of CBA1 132
Figure 3.31 (b) Density distribution within a 25 km thick slab derived from the short wavelength component of CBA2 133
Figure 3.32 Trace of ridge geometry used for calculating lithospheric cooling effect 135
Figure 3.33 Gravitational effect of cooling lithospheric plates 136
Figure 3.34 Simplified geological map of an area that straddles the WVZ and density variations within a 1 km thick slab across it 138
Figure 3.35 Map of the depth to the top of the lower crust 141
Figure 3.36 Spatial location of the mantle plume beneath Iceland 144
Figure 3.37 Flow within a pipe 145
Figure 3.38 Plot of shallow P-wave velocity versus density variation in the top 1 km of crust across the WVZ 147

Chapter 4

Figure 4.1 Ship tracks for the EW9008 cruise in the North Atlantic 151
Figure 4.2 A model representing the life cycle of Rayleigh-Taylor instability initiated diapirs 153
Figure 4.3 Plot of four ridge-normal bathymetric profiles from the Mid-Atlantic Ridge 154
Figure 4.4 Seasat gravity for the North Atlantic area 155
Figure 4.5 (a) Lithologies encountered in DSDP hole 504b 156
Figure 4.5 (b) Schematic cross-section through an ophiolite 157
Figure 4.6 An example of necking of the lithosphere 160

Figure 4.7 (a) Tapponier and Francheteau's (1978) ridge axis model..... 161
Figure 4.7 (b and c) Chen and Morgan's (1990a) mechanism for creating a median valley/axial rise at slow/fast spreading ridges..... 161
Figure 4.8 Geometry used in Parker's (1972) method to calculate the potential field caused by a non-uniform and uneven layer of material..... 165
Figure 4.9 Example of short wavelength instability..... 167
Figure 4.10 Ship tracks for EW9008 cruise in area C..... 170
Figure 4.11 Ridge-normal gravity signatures from two lithospheric cooling models..... 172
Figure 4.12 RMS gravity versus RMS crust-mantle relief for different filters..... 173
Figure 4.13 Bathymetry plot for area C..... 175
Figure 4.14 A sketch defining the term cross-over error..... 177
Figure 4.15 Composition of modelled crusts used to test the gravitational effect of a one-layer crust versus multi-layered crust..... 179
Figure 4.16 Contour plots showing the effect of using multiple density stratifications for the crust when using the Parker method..... 180
Figure 4.17 P-wave seismic velocity and density after Ludwig, Nafe and Drake (1970)..... 181
Figure 4.18 A scatter plot of Free Air Anomaly versus depth for area C..... 183
Figure 4.19 Plot showing the difference in the forward modelled gravity field due to crusts of thickness 6 and 8 km..... 184
Figure 4.20 TOBI mosaic for the median valley region of area C..... 187
Figure 4.21 Map of bathymetric gradients in excess of 0.4..... 188
Figure 4.22 Free Air Anomaly for area C..... 190
Figure 4.23 Mantle Bouguer Anomaly for area C..... 191
Figure 4.24 Residual Anomaly for area C..... 193
Figure 4.25 Crust-mantle relief for area C..... 194
Figure 4.26 The mantle diapir model..... 197
Figure 4.27 Contour maps of gravity anomalies from other parts of the Mid-Atlantic Ridge..... 200

List of Tables

Table 2.1 Porosities, wet densities and standard deviations of rock samples from the Hengill-Grensdalur area 39

Table 2.2 Tabulation of the results from testing source depth determination 73

Table 2.3 Table of anomalous body thicknesses that would be invisible to the tomographic method 81

Table 3.1 Summary of Bouguer reduction densities 93

Chapter 1

Structure of the Iceland Plateau

1.1 Introduction

Iceland and its relationship with the Mid-Atlantic Ridge, have been studied for over two decades from the perspective of plate tectonics. Diverse geological, geochemical and geophysical evidence suggest that Iceland formed as the consequence of the superposition of the Mid-Atlantic Ridge and a mantle plume, producing a sub-aerial platform containing the trace of the North American-Eurasian plate boundary. The character and structure of this plate boundary in Iceland can provide insights into the nature of its submarine extension; the Reykjanes Ridge.

This thesis investigates the crustal structure of Iceland and the North Atlantic using gravity data, at both local and regional scales. The aims of this dissertation are to: (i) interpret the gravity fields of two volcanic systems lying on the spreading boundary in southwest and northeast Iceland, in conjunction with local earthquake seismic tomography results; (ii) test the fidelity of the tomographic results used in (i); (iii) analyse and interpret the country-wide Icelandic gravity field as a plume and crustal component, thereby giving some estimates of the physical structure of these features based upon simple model assumptions; and (iv) reduce and interpret marine gravity data from the Reykjanes Ridge, relating the results to the Icelandic plume hypothesis.

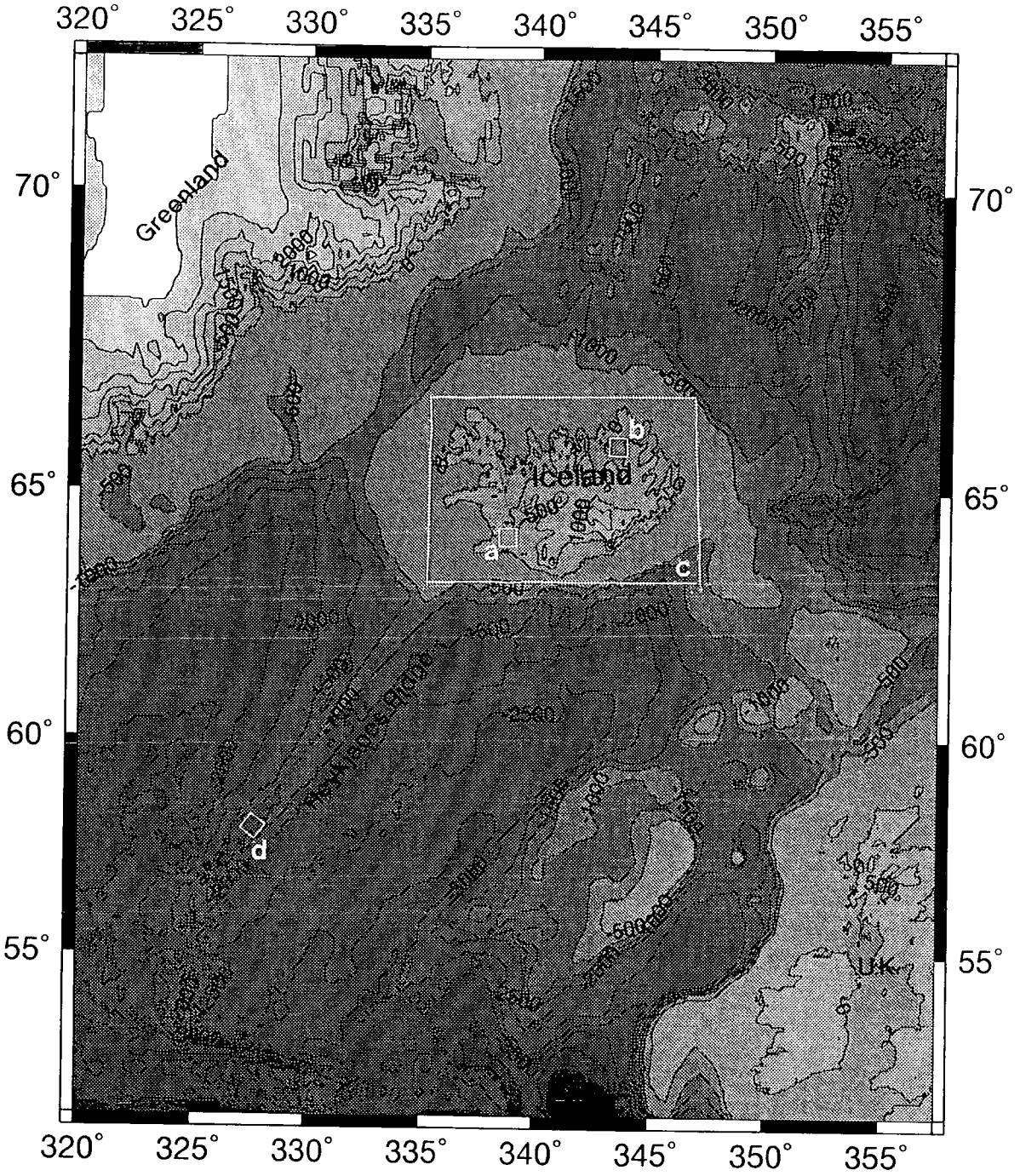

Figure 1.1. Location map for Iceland and the Reykjanes Ridge, including surrounding bathymetry. Contours are in metres. White boxes represent the approximate positions and extents of the gravity datasets used in this thesis. a) Hengill-Grensdalur area. b) Krafla area. c) Whole of Iceland. d) Reykjanes Ridge at 58°N.

1.2 Formation of the Iceland Plateau

Iceland straddles the Mid-Atlantic Ridge and is the recent product of plume-related basaltic volcanism (Sæmundsson, 1979). When the North Atlantic began to open, possibly as a result of a significant mantle event such as a convective overturn (~60 Ma) (Bott, 1973), the plume fed the Mid-Atlantic Ridge with material from a position beneath Greenland, forming the Iceland-Faeroe Ridge as spreading proceeded. Subsequent emergence of the plume from beneath Greenland caused the ridge to jump westwards, leading to the formation of the Greenland-Iceland Ridge (Vink, 1984). It is thought that an increase in eruptive intensity at around 25 Ma, due to repositioning of the ridge crest above the plume, may have been responsible for the origin of the Iceland plateau (Vink, 1984; Sæmundsson, 1986). The Iceland plateau is ~ 400 km by ~ 800 km in north-south and east-west extent, as defined by the 500 m isobath. On Iceland itself, a few peaks approach 2000 m above sea level, but most of the country is less than 900 m above sea level (figure 1.1).

1.3 Tectonics and the Position of the Present Plate Boundary in Iceland

The active zones of volcanism on Iceland, defined by the extent of the Upper Pleistocene (0.7 Ma - 9 Ka) and post-glacial (9 Ka - present) rocks, are referred to as the *neovolcanic zones* (figure 1.2). The neovolcanic zones display a variety of volcanic forms. Areas that experience very high magmatic production are termed *central volcanoes* (e.g. Askja, Krafla) and are usually fed from an extensive mid-crustal magma chamber. Most central volcanoes are associated with a *fissure swarm* which, together with the central volcano, constitutes a *volcanic system*. Central volcanoes are usually characterised by a caldera (indicating the presence of a magma chamber), and evolved magma (Sæmundsson, 1979). Volcanism also occurs as *fissure eruptions*, that can range from a few to tens of kilometres in length, and monogenetic *shield volcanoes* that are thought to have magmas originating from a deep source (Walker, 1992). During the Plio-Pleistocene (3.1 Ma - 0.7 Ma) and Upper Pleistocene, the eruptive environment was sometimes glacial giving rise to hyaloclastite table mountains and ridges formed above central vents and fissures, respectively.

The neovolcanic zones are divided into *axial* and *flank zones* on a petrochemical and tectonic basis (Sæmundsson, 1978) (figure 1.2). The axial zones are thought to mark the plate boundary where accretion is taking place, and cross the country from the south-west where they connect with the Reykjanes Ridge, to the north-east, where they connect via the Tjörnes Fracture Zone (TFZ) to the Kolbeinsey Ridge. There are thought

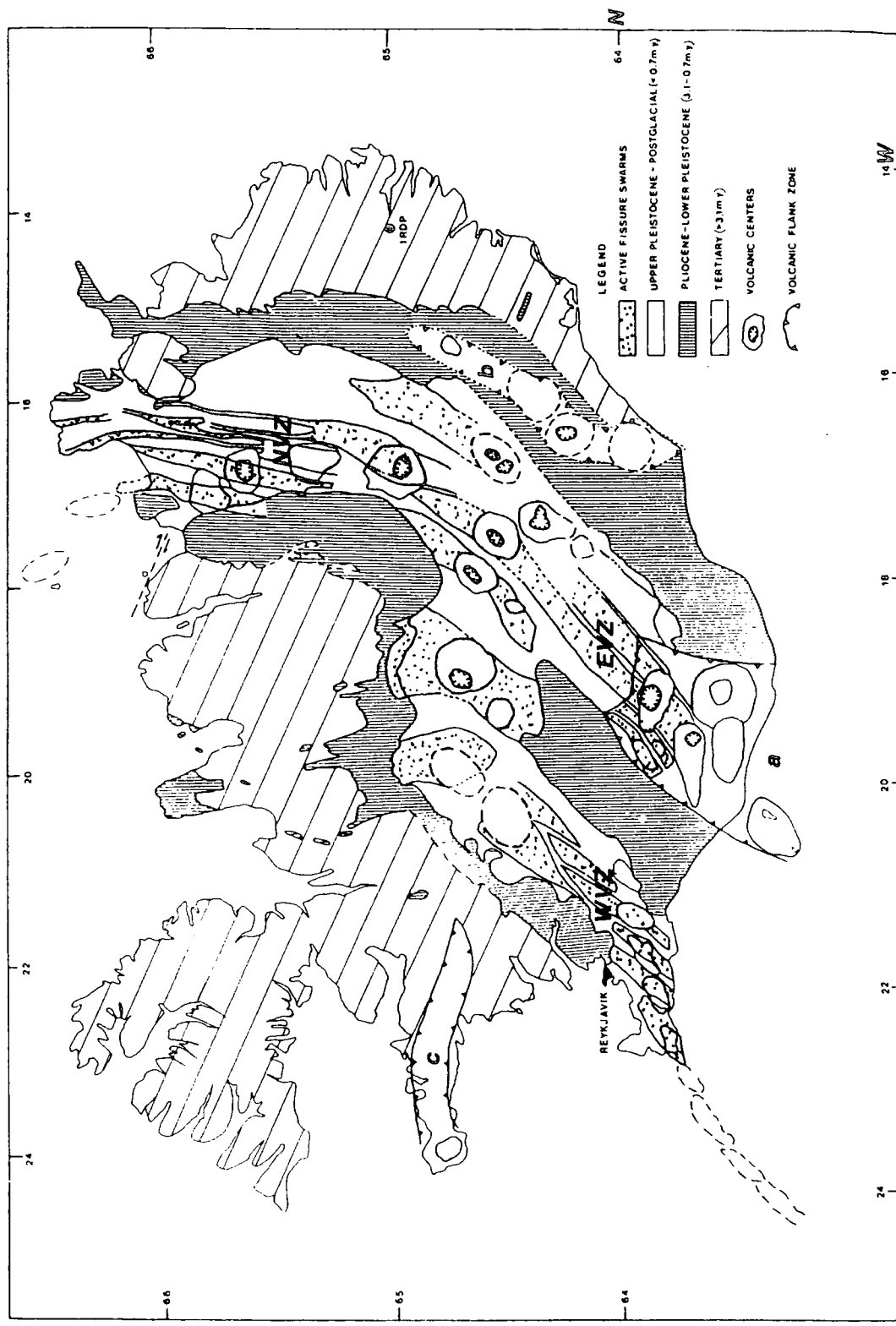

Figure 1.2. Simplified geological and tectonic map of Iceland. Adapted from Helgason (1984).

to be three main actively spreading neovolcanic zones in Iceland. The Reykjanes Ridge continues on land becoming the Western Volcanic Zone (WVZ), stretching from the Reykjanes Peninsula to Langjökull (for locations of place names, refer to figure 1.3) and displaying an en-echelon arrangement of volcanic systems. The Eastern Volcanic Zone (EVZ) strikes sub-parallel to the WVZ from Vestmannaeyjar to Vatnajökull. The Northern Volcanic Zone (NVZ) strikes essentially northward from Vatnajökull to the Tjörnes Peninsula. The South Iceland Seismic Zone (SISZ) and the TFZ are the regions in Iceland where earthquakes in excess of magnitude 7 have occurred (Einarsson and Björnsson, 1979). In the SISZ, which links the WVZ and the EVZ, earthquakes have been located in the 6-14 km depth range. In conjunction with the ridge system geometry, a strike slip fault plane solution is taken as evidence that the SISZ is a transform fault (figure 1.4). The TFZ is a broad zone of seismicity connecting the NVZ to the Kolbeinsey Ridge which also exhibits strike slip fault plane solutions and, similarly, is interpreted as a transform fault (Einarsson, 1991) (figure 1.4).

In the axial zones the en-echelon volcanic systems are dominated by extensional tectonic features - linear fissure or dyke swarms which are usually, but not always, associated with a central volcano. These volcanic systems are commonly 50-100 km in length and 10-30 km in width (Sæmundsson, 1979). Transitional and alkalic eruptions occur in Iceland's flank zones, located at Torfajökull-Vestmannaeyjar, Oræfajökull-Snaefell and the Snaefellsnes Peninsula (figure 1.2). These zones are dominated by large stratovolcanoes and have poorly developed extensional features (Sæmundsson, 1979).

Nearly all of the seismicity in Iceland is associated with the tectonic plate boundary, in particular central volcanoes and geothermal zones (Einarsson, 1991) (figure 1.4). Within the Reykjanes Peninsula, the seismic zone is narrow and enters Iceland at Reykjanes. Events are distributed throughout a depth range of 1-5 km apparently caused by deformation of a brittle crust above a deep aseismic zone of deformation. The Reykjanes Peninsula seismic zone branches at the Hengill triple junction (Ridge-Ridge-Transform): northwards as the WVZ and eastwards as the SISZ. The Hengill triple junction is an area of persistent seismicity. Foulger (1988a and b) gives hypocentral depths for the Hengill triple junction in the 1-7 km depth range. A major source of seismicity in the area is provided by circulating groundwater causing cooling and contraction of the crust leading to extensional failure of the rock (heat cracking). It has been suggested that the WVZ is being gradually replaced by the EVZ, but recent seismicity shows that the WVZ is still seismically more active than the EVZ. The NVZ displays quite low seismicity even though a major rifting episode has been in progress since 1975 at the Krafla central volcano. Seismicity is associated with magma body inflation, deflation and rifting caused

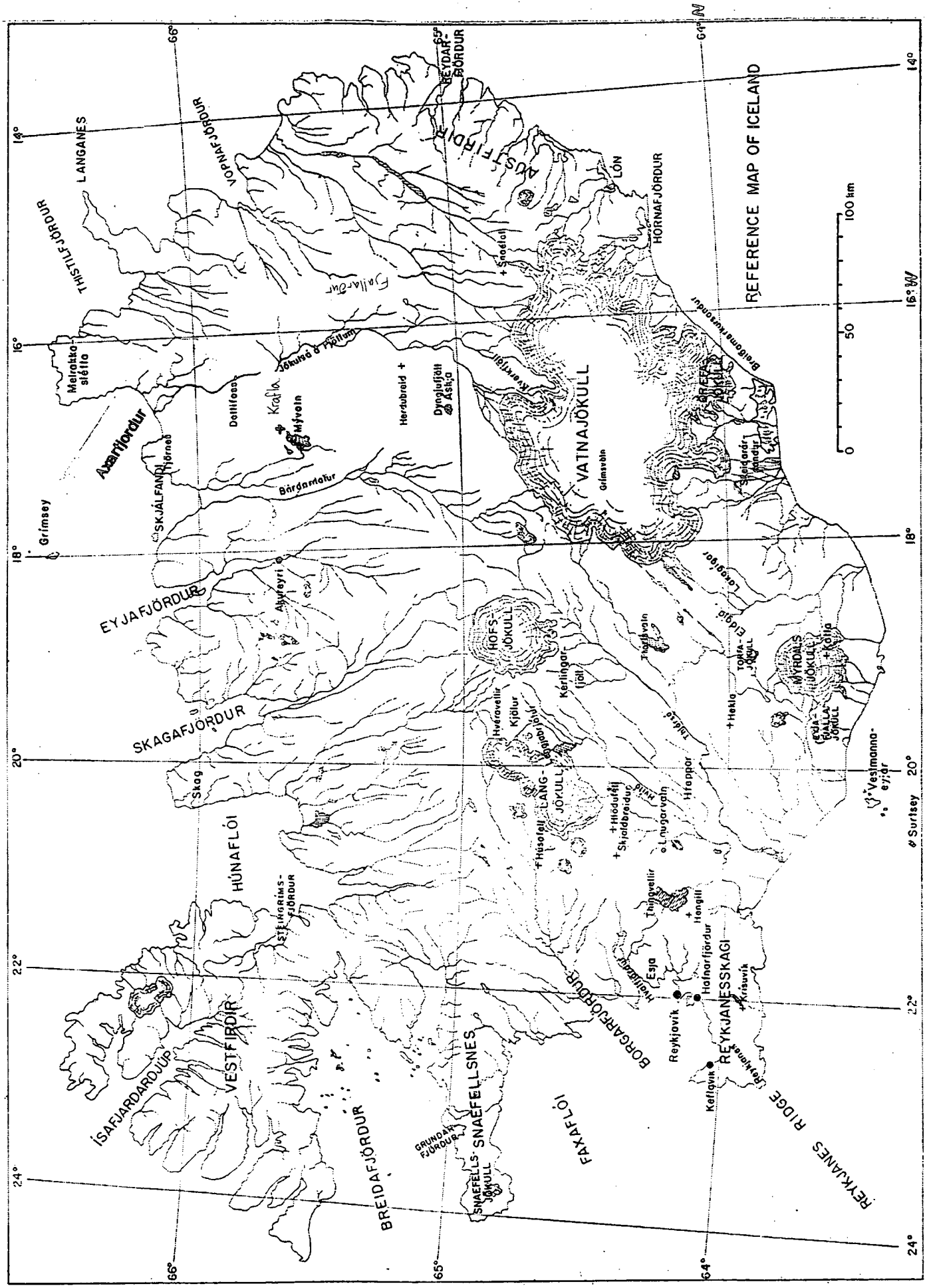

Figure 1.3. Location map for place names used in this thesis. From Björnsson (1967).

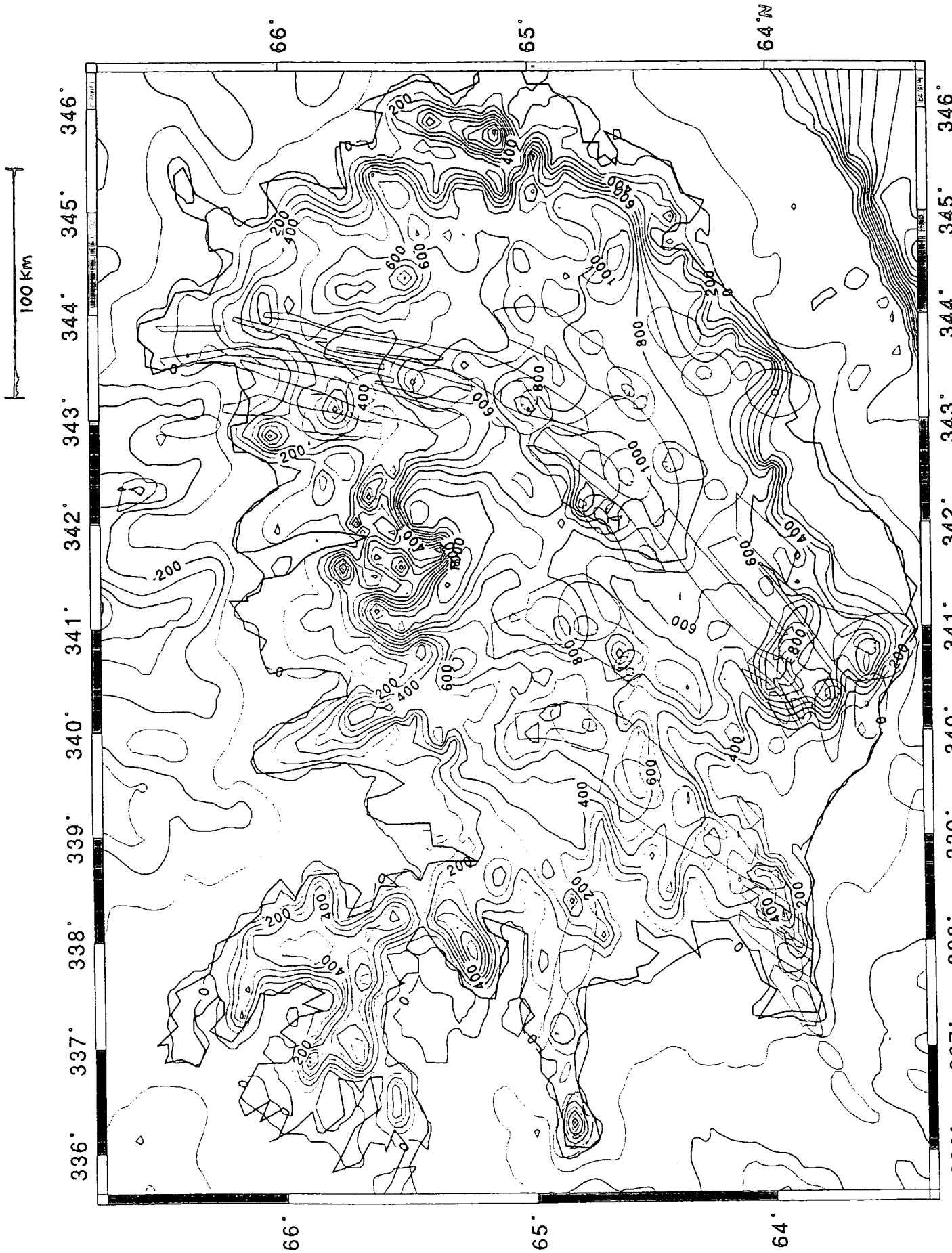

Figure 1.3b. Topographic map of Iceland. Contours are in metres. The tectonic units are marked for reference.

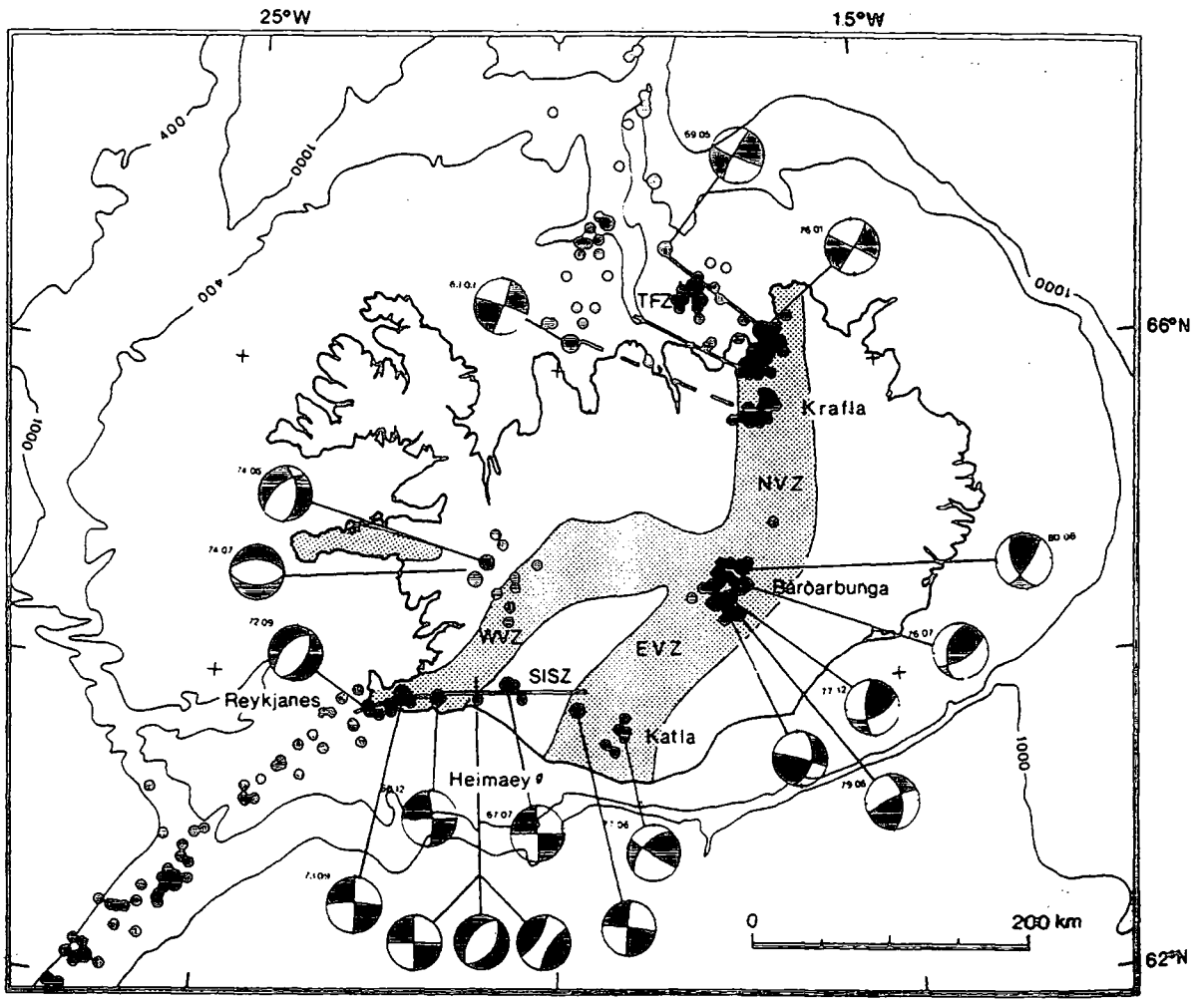

Figure 1.4. Epicentres and focal mechanisms of earthquakes in the Iceland area. Epicentres are taken from the earthquake lists (PDE) of the U.S. Geological Survey for the period 1963-1987; only epicentres determined using ten or more stations are included. Larger dots are events of magnitude (m_b) >=5. Focal mechanisms are shown schematically on lower hemisphere stereographic projections of the focal sphere; compressional quadrants are black. The volcanic zones (WVZ, EVZ, and NVZ) are stippled, and seismic belts in the South Iceland Seismic Zone (SISZ) and the Tjörnes Fracture Zone (TFZ) are shown with a heavy line (from Einarsson, 1991).

by dyke intrusion. Hypocentre locations are in the 1-8 km depth range, above and below crustal magma chambers. In central and south east Iceland, activity is again associated with central volcanoes (below the ice caps of Vatnajökull, Mýrdalsjökull) and also with geothermal activity, i.e. heat cracking. Sub-glacial seismicity is thought to be due to inflation and deflation events, plus temporal load changes as glacial ice melts during the summer. Einarsson (1991) proposes that in the EVZ, NVZ and central Iceland, seismicity between central volcanoes may be causally linked.

1.4 Shifting of the Plate Boundary in Iceland

K-Ar age dating of Icelandic surface rocks indicate an increase in age with distance from the axial neovolcanic zone. The oldest rock dated as 16 Ma, comes from the extreme north west and east of the island (Pálmason and Sæmundsson, 1974). Reconstruction of the tectonic evolution in Iceland is not easily determined because of the irregular nature of the magnetic anomalies over Iceland, and only anomaly 5 (10 Ma) can be traced from offshore over the NW peninsula (Jonsson et al., 1991).

The neovolcanic zones are flanked by Plio-Pleistocene aged rocks, and at greater distance Tertiary (> 3.1 Ma) flood basalts which exhibit dips that increase from near zero in the highest exposed levels to 5-10° at sea level. Dipping of the lava beds is thought to be caused by the lava pile growing as lenticular units, each associated with a volcanic system (Sæmundsson, 1978). Thus, dipping of the lavas will be towards the accretionary axis. Knowledge of dips within the Tertiary rocks can be used to infer the positions of extinct accretionary axes.

In Iceland there appears to be two scales of ridge migration. Large scale ridge jumps occur over distances of ~150 km and on a time scale of ~6 Ma. Small scale ridge jumps occur over distances of ~50 km on a time scale of 2 Ma (Helgason, 1985). At about 4-6 Ma, the configuration of the zone of accretion is thought to have been different from that of the present. Previously, the zone is thought to have extended from Reykjanes Peninsula to the Skagi Peninsula (Helgason, 1985) (figure 1.5). It is also possible that spreading may have occurred along the Snaefellsnes Peninsula, prior to spreading along the Reykjanes Peninsula, as Jonsson et al. (1991) suggest after identifying potential anomaly 5 magnetic lineations north and south of the peninsula. At ~ 4 Ma, accretion began along an accretionary axis in the northeast of Iceland and the geometry of this axis relative to the Kolbeinsey Ridge may have possibly initiated the TFZ (Sæmundsson, 1974). This large scale eastward shifting of the plate boundary is thought to be in response to the position of the hotspot relative to the accretionary axis as it migrates

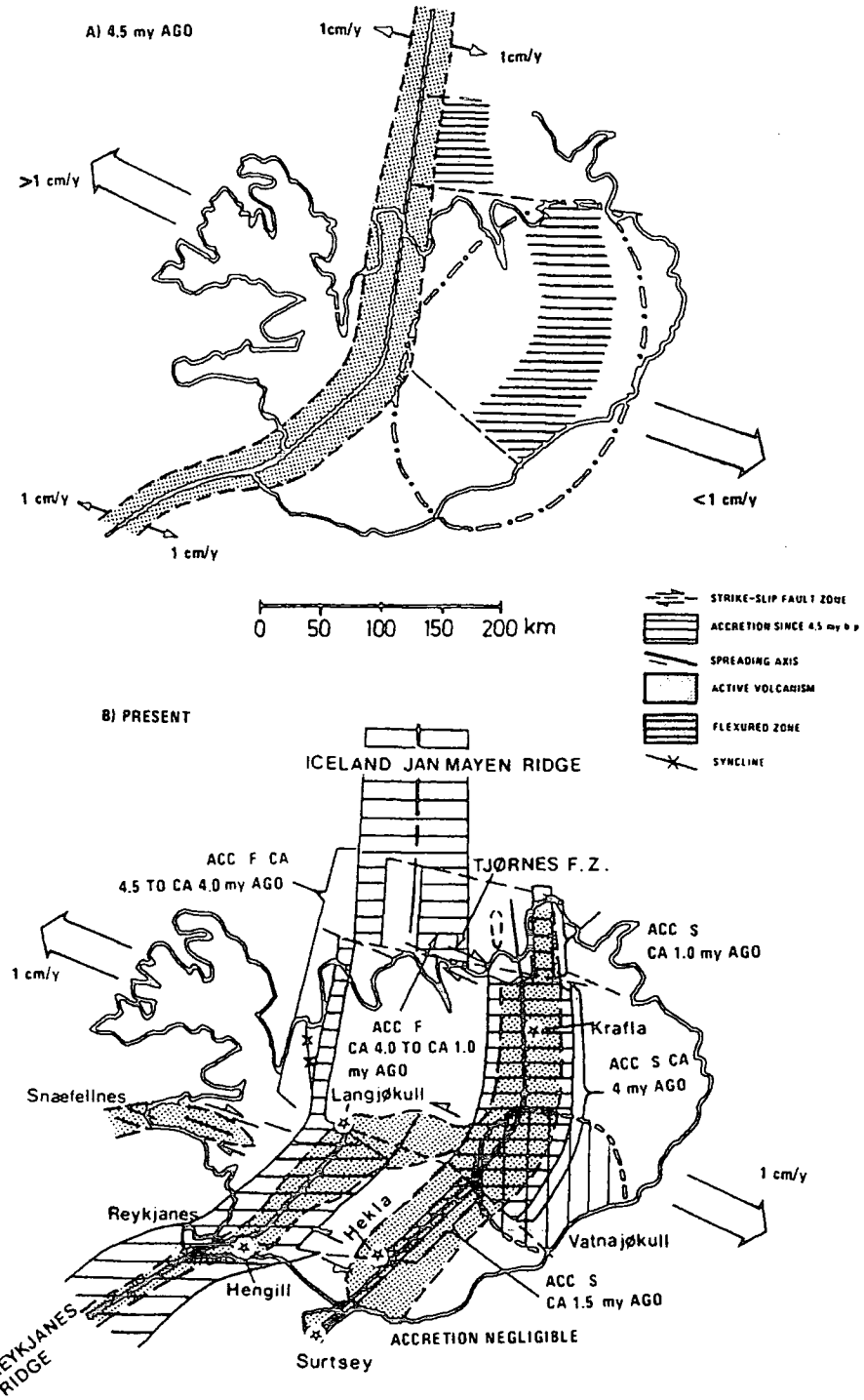

Figure 1.5. Development of the present pattern of the volcanic zones in Iceland. (a) Reconstruction of the rift zones in Iceland before the eastward shift to the present position. The axial rifting zone continues north from the Reykjanes Ridge and joins the Kolbeinsey Ridge more or less directly. To the east, new rifting zones have begun to develop as troughs where thick sediment is being deposited. Offset positions of these troughs within and to the south of the TFZ are responsible for the discontinuity of the flexured zone at Vopnafjördur. (b) After the shift was completed, the positions of the earlier rifting zones are indicated by synclinal structures in the Tertiary plateau-basalt sequence. Accretion back to 4.5 m.y. should be regarded only as an approximation. Spreading rates after Talwani et al. (1971), (from Sæmundsson, 1974).

eastwards relative to the Iceland plateau (Sæmundsson, 1974). The smaller scale 'ridge-jumps' are superimposed on such large scale migrations of the spreading axes, and these have occurred at least three times between 12-8 Ma within the eastern Tertiary zone (Helgason, 1984 and 1985). Another small scale shift occurred at about 1 Ma. Activity moved from the Fjallgarður Ridge in northeast Iceland, a hyaloclastite ridge stretching 150 km north from Kverkfjöll, westwards to the present location of the axis in the NVZ (Helgason, 1985).

1.5 Accretion at the Plate Boundary

Crustal accretion proceeds by extrusion of lava at the surface in conjunction with dyke intrusions, both occurring concurrently with plate separation (Pálmason, 1980). Both dyke injection and lava extrusion are modelled as Gaussian functions about the axis. The model predicts that lavas subside as they are buried under new flows and transported away from the axis. Figure 1.6 (top) depicts modelled trajectories of lavas through the crust, isotherms, and the predicted surface geothermal gradient. The width of the Gaussian bells, strain rate, lava production rate, and spreading velocity can be measured or inferred from measurements made of properties within the Tertiary crust. In conjunction with Pálmason's (1980) model, Steinthorsson et al. (1985) include metamorphic facies boundaries from Oskarsson et al. (1982) to generate a crustal structure consistent with observations. This hybrid model predicts layering of alteration facies within an upper crust that is formed by extrusives and a lower crust formed by intrusives underlain by a significant amount of 'underplated crust' (figure 1.6 bottom).

1.6 Crustal Structure

Sub-surface crustal structure has been mainly inferred from seismic work (Båth, 1960; Pálmason, 1971; Flóvenz, 1980; Zverev et al., 1980a,b; Gebrande et al., 1980; Angenheister et al., 1980; Flóvenz and Gunnarsson, 1991). Seismically the crust has been divided into two zones: the upper crust which is described either by a layered velocity model increasing from about 2-3 km s^{-1} at the surface to about 6.5 km s^{-1} at 2-6 km depth (Pálmason, 1971), depending upon the amount of surface erosion, or, perhaps better, by continuously increasing velocity with depth (Flóvenz, 1980); and the lower crust, which is thought to be equivalent to oceanic layer 3 (Angenheister et al., 1980), has an approximately constant velocity of 6.5 km s^{-1} and extends for a further ~5 km depth. Drilling into Tertiary upper crust in eastern Iceland (Christensen and Wilkins, 1982) has revealed that P-wave velocity can vary within lava flows, being

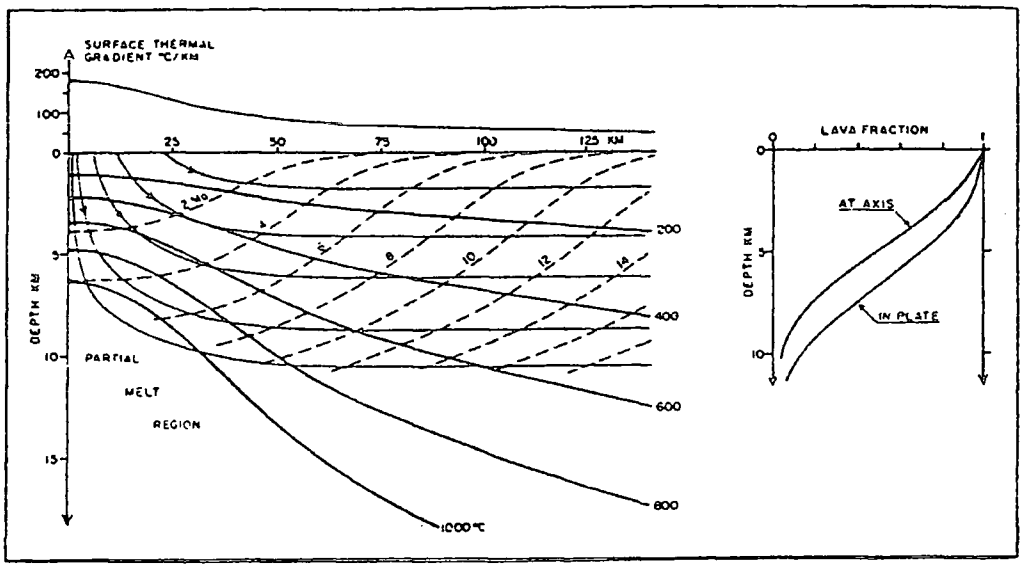

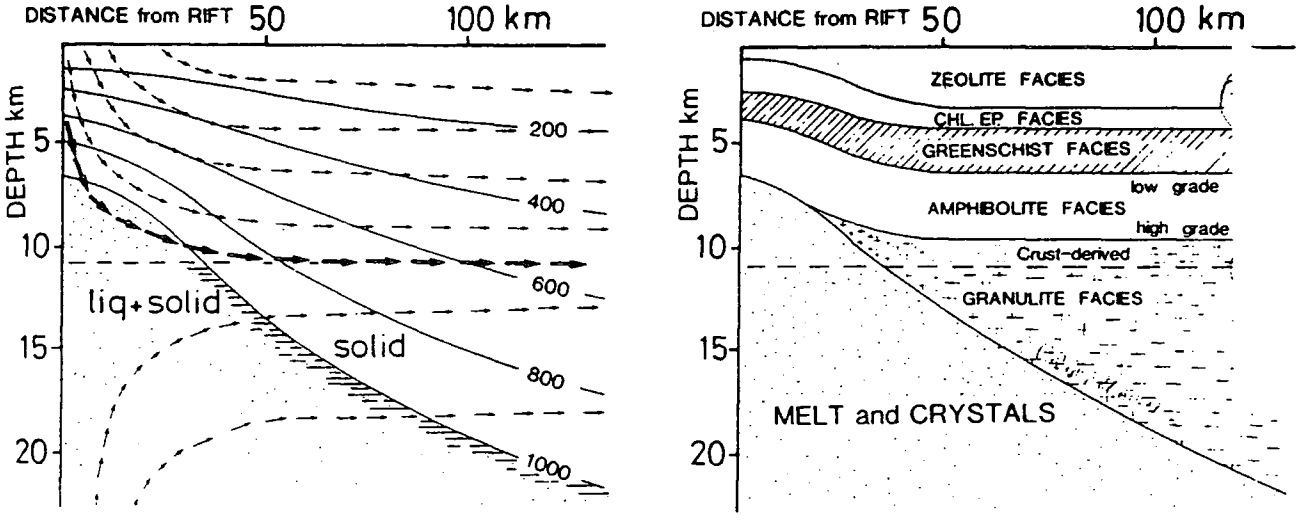

Figure 1.6. (top) Section through the lithosphere according to the accretion model of Pálmason (1980). Trajectories (arrows) and isochrons (dashed) of lava elements are shown together with isotherms and surface gradient. The lava fraction at the axis and in the distant lithosphere is shown on the right. Model parameters used are: spreading velocity 10 mm a^{-1}; lava production rate 1.33 x 10^{-4} km^2 a^{-1}. See Pálmason (1980) for more detailed parameters. (bottom left) Kinematics of crustal accretion. Isotherms and material trajectories (trains of arrows) for the upper 10 km, according to Pálmason (1980). Boundary of partial melt beneath the underplated crust (horizontal pattern) from Beblo and Björnsson (1980). Material trajectories for the upper mantle are hypothetical. (bottom right) Petrological structure of the lithosphere as derived from the kinematic model (bottom left). The facies boundaries of progressive metamorphism in the crust (Oskarsson et al., 1982) are formed in the rift zones at depths defined by material trajectories reaching the appropriate maximum temperatures. Note that the top of the granulite facies material is crust-derived, the remainder mantle-derived (from Steinthorsson et al., 1985).

greatest at the dense centre of a flow, but overall generally increasing with depth as secondary minerals occupy the free pore space and cracks in the rocks with increased depth. Drilling elsewhere in the country has revealed that zeolite facies lie on top of greenschist facies, indicating that alteration of the rock increases with depth throughout the upper crust (Pálmason et al., 1979). Drill holes have not penetrated the lower crust but it is thought that 25% epidote content within the basalt is sufficient to produce the lower crustal P-wave velocities (Christensen and Wilkins, 1982). Investigations into small scale upper crustal structure have been made through tomographic inversions of local earthquake data. These experiments were conducted in the Hengill-Grensdalur volcanic system (Foulger and Toomey, 1989) and the Krafla hydrothermal system (Arnott, 1990; Foulger and Arnott, 1993). Both studies yielded significant structural inhomogeneity within the shallow crust, including high velocity bodies, interpreted as high density intrusions, and low velocity bodies, interpreted as regions of hydrothermal alteration, or possibly containing some component of partial melt.

High temperature geothermal fields are distributed evenly along the neovolcanic zones and heat flow outside of the zones falls off with distance (Flóvenz and Sæmundsson, 1993; Pálmason and Sæmundsson, 1974; Pálmason et al., 1979) (figure 1.7). An aero-magnetic survey of Iceland showed that magnetic lineations across the island are quite irregular in comparison to oceanic magnetic lineations. Lineations with the highest amplitude are over and around the active zones, probably due in part to the relatively unfaulted nature of the newly magnetised layer (Jonsson et al., 1991). Sparse, shallow resistivity soundings outside of the complex neovolcanic zone, and shallow P-wave velocity observations (500 m below the surface), both show a general increase with distance from the neovolcanic zones due to infilling of pore spaces through a process of secondary mineralisation (Flóvenz et al., 1985) (figure 1.8). A joint inversion of P-wave travel time and polarisation direction across the WVZ was conducted by Hu et al. (1993), and detected a northeast striking low velocity zone within the crust to a depth of at least 15 km, consistent with the tectonic grain of the WVZ. Isostatic gravity anomalies also show some indication of increasing with distance from the axial neovolcanic zones (Einarsson, 1954) (figure 1.9). These observations are consistent with a crustal spreading hypothesis of injection of new 'hot' material at the plate boundary which cools and becomes progressively buried and faulted as it is transported away.

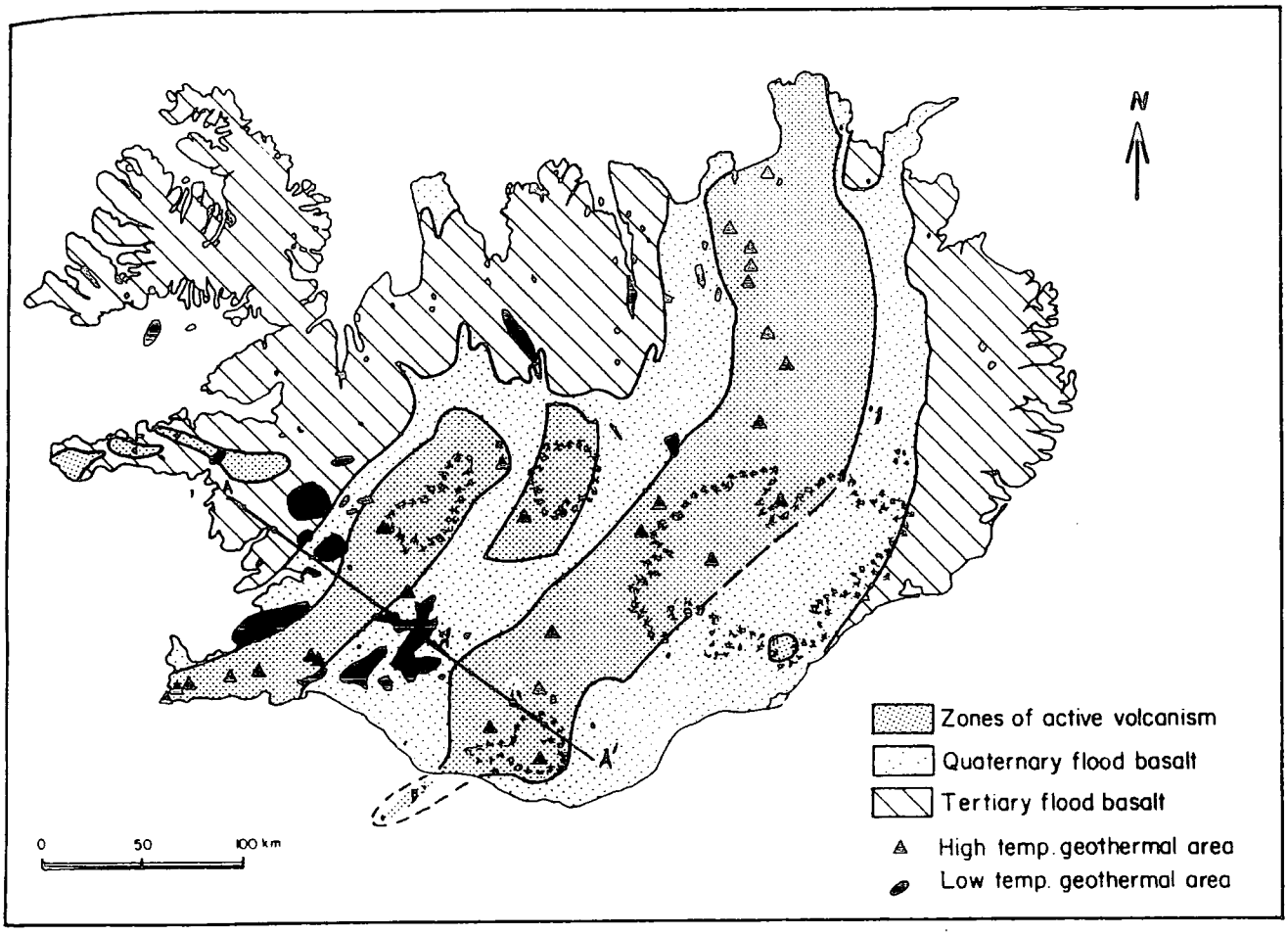

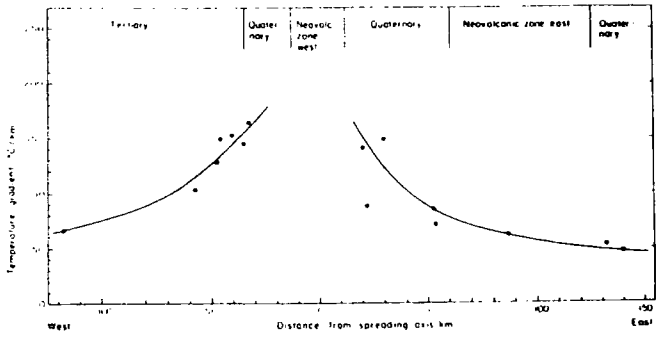

Figure 1.7. (top) Geothermal areas and the geological structure of Iceland (from Flóvenz et al., 1985). (bottom) The temperature gradient in SW-Iceland as measured along the profile of the figure above. The data originate from Pálmason (1973) and Pálmason et al. (1979) (from Hersir et al., 1984).

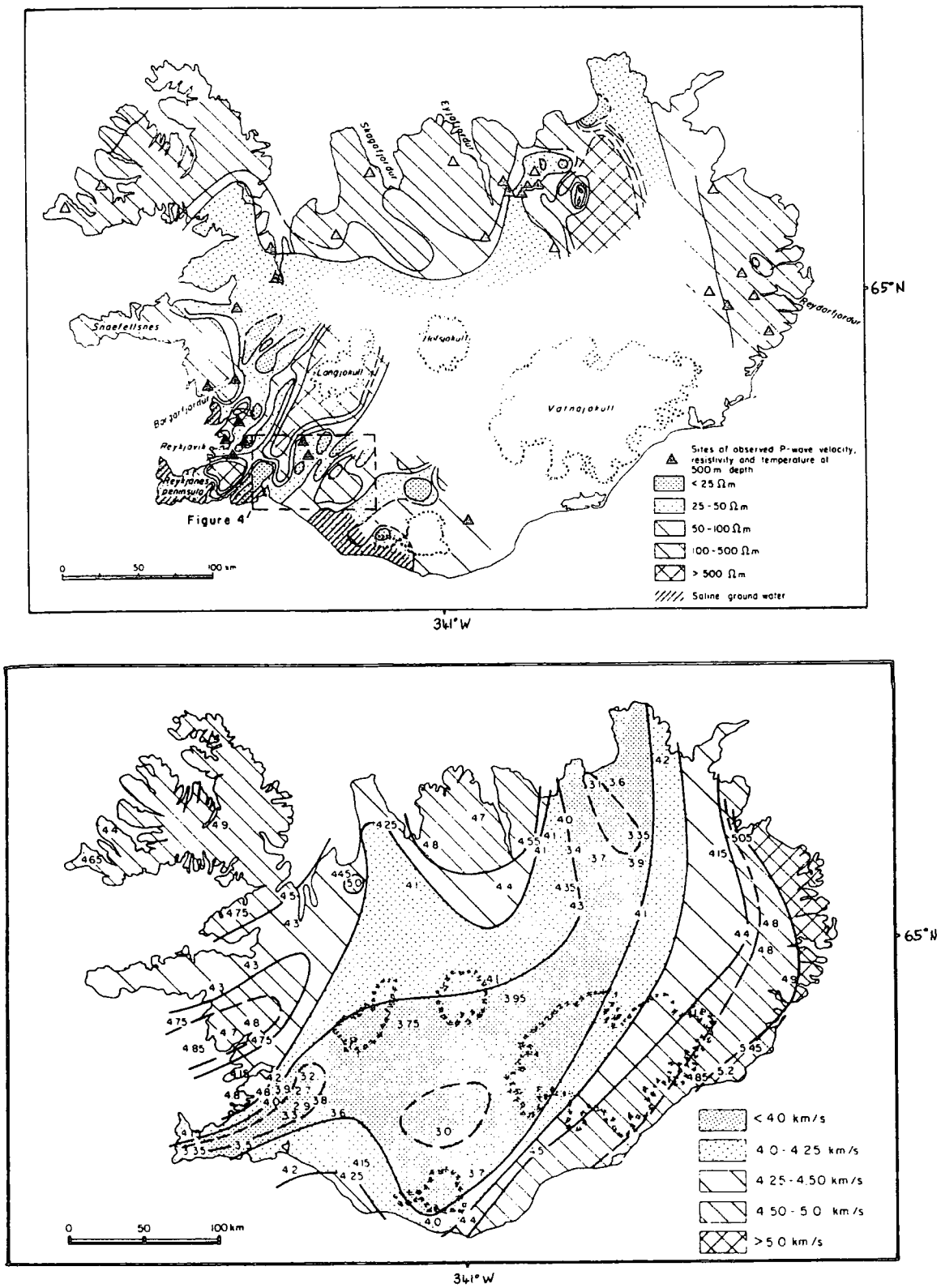

Figure 1.8. (top) Regional resistivity of Iceland at 500 m depth (from Flóvenz et al., 1985). (bottom) Regional P-wave velocity of Iceland at 500 m depth. Numbers represent velocities in km s^{-1} from which the contours were constructed (from Flóvenz et al., 1985).

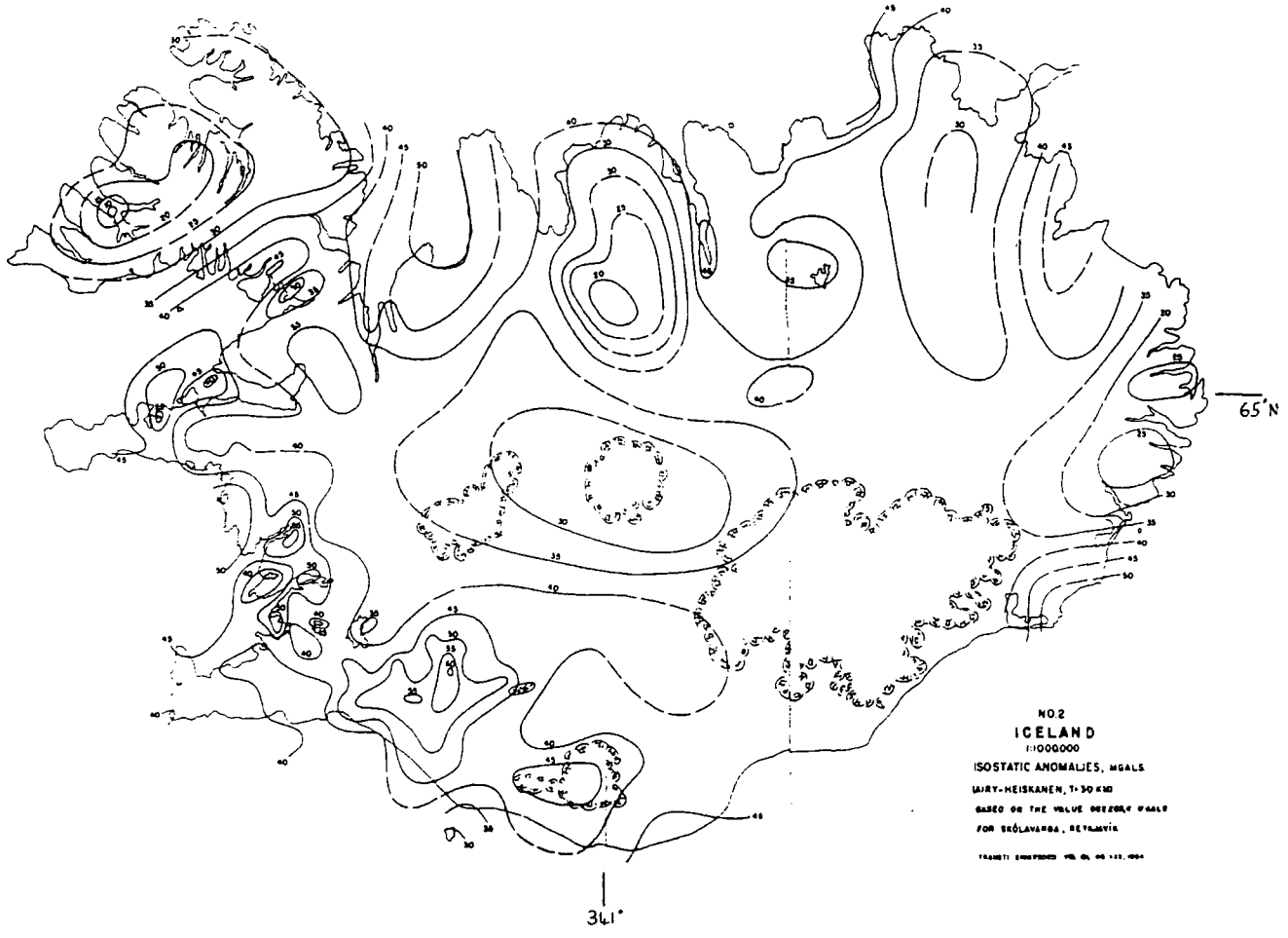

Figure 1.9. Isostatic anomaly of Iceland in mGal. The isostatic anomaly is the difference between the Bouguer anomaly over Iceland and the anomaly produced by an Airy-type compensation of the topography. The crustal block is set at a thickness of 30 km when the top of the crust is at sealevel. A 600 kg m^{-3} density contrast is assumed for the compensating root that deepens as it approaches the centre of the island (From Einarsson, 1954).

1.7 The Crust-Mantle Boundary

Magnetotelluric experiments infer that a highly conductive layer, interpreted as partial melt, is located within 8-10 km of the surface below the axial neovolcanic zones and deepens to 20-30 km below the flanks of the WVZ, EVZ, and NVZ (Beblo et al., 1983; Hersir,1984; Eysteinsson and Hermance, 1985). Seismic evidence for the crust-mantle transition in Iceland is poor, but depth estimates to the top of the mantle range from 10-16 km beneath the volcanic zones (Flóvenz and Gunnarsson, 1991). Bjarnason et al. (1993) observe wide-angle phases in south west Iceland which are interpreted as reflectors at 20-24 km depth below the flanks of the WVZ. Measurements conducted in drillholes of geothermal gradients have been extrapolated to obtain the depth to the basalt solidus, approximated by an isotherm, and have yielded values of ~10 km just outside the axial neovolcanic zone increasing to in excess of 20 km at 50 km from the axis (Flóvenz and Sæmundsson, 1993) (figure 1.10). Thickening of the crust away from the axes is supported by surface wave studies, which infer that the Iceland plateau is 20 km thick on average, and Bott and Gunnarsson (1980), who suggest that the Moho near Iceland is at a depth of 28 km on the basis of seismic data.

1.8 Sub-Crustal Structure

A topographic swell dominates the North Atlantic, uplifting much of Greenland and the seafloor north of 45°N, reaching a maximum elevation of 2 km on Iceland. A temperature anomaly of 100°C could give rise to a sufficient mantle density contrast to a depth of 200 km to isostatically support the swell (Bott, 1988). Such a temperature anomaly would make the Icelandic region responsible for 2% of the global heat loss from oceanic regions. This amount of heat cannot be generated in the upper mantle or conducted from deeper parts of the mantle. Instead, the transport of energy by a convective plume is more plausible (Bott, 1988).

The Icelandic crust features geochemical anomalies compared with normal oceanic crust. These differences are attributed to a chemically distinct mantle source from which the crust is derived, possibly a deep mantle plume (Schilling, 1973).

A 'bowl-shaped' Bouguer anomaly is centred on Iceland coinciding with the topographic anomaly of Iceland. A minimum of -30 mGal is found near the centre, increasing to ~+40 - +50 mGal at the coast (Einarsson, 1954). The gravity bowl has also been recognised in gravity work by Thorarinsson et al. (1989), Thorbergsson et al. (1990), Schleusener et al. (1976). A low density mantle extending a hundred kilometres

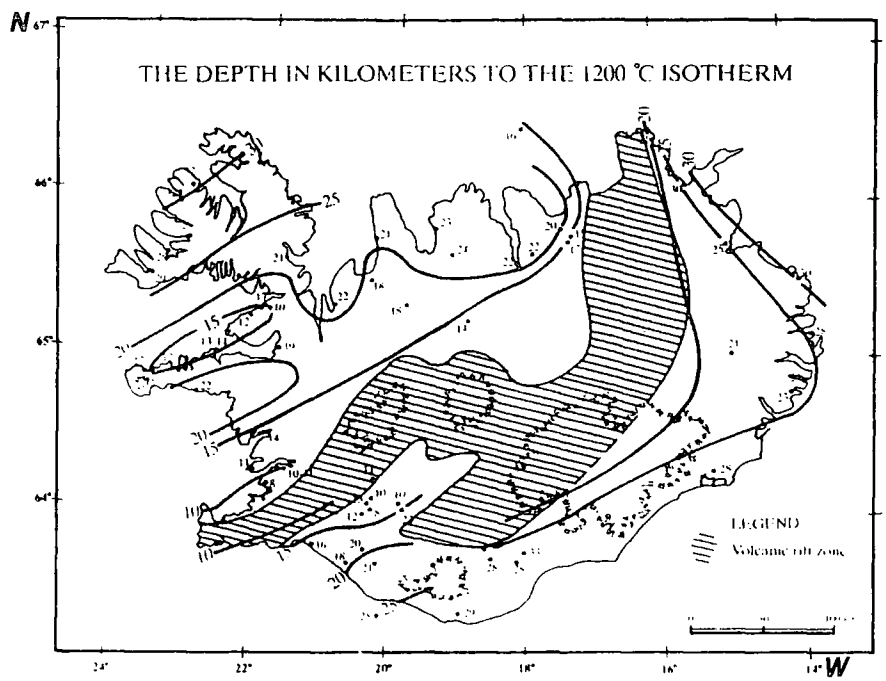

Figure 1.10. Calculated depth to the basalt solidus (taken as the 1200°C isotherm) below Iceland. The calculations are based on heat flow measurements and the assumption that thermal conductivity increases with depth in the upper crust due to reduction in porosity. Possible changes in thermal conductivity due to temperature and pressure effects are ignored as well as effects of chemical alteration in the crust. The heat generation due to radioactivity is estimated to be 0.5 $\mu W\ m^{-2}$ (from Flóvenz and Sæmundsson, 1993).

or so is seen as the mechanism for generating such a Bouguer gravity anomaly. Lowered density is thought to be due to thermal expansion effects, solid-solid phase changes and the presence of partial melt (Hermance, 1981a; Bott, 1965, 1988). Further mass compensation relative to older adjacent areas may be accomplished by underplating of the crust by up to 20 km (Hermance, 1981a and b).

Consistent with a low density mantle, possibly containing partial melt, are P-wave teleseismic travel time delays. Tryggvason (1964) and Long and Mitchell (1970) calculated a depth to the base of the anomalous mantle to be in excess of 200 km. An analysis of the P-S ratio by Gebrande et al. (1980) was used to infer a maximum partial melt content of ~20% beneath Iceland. Tryggvason et al. (1983) inverted teleseismic P-wave travel time residuals to investigate the mantle structure beneath Iceland. The depth of the mantle anomaly is thought to exceed 300 km. Horizontal flow of material is thought to be taking place in keeping with the plume hypothesis. Flow at a depth of ~ 150 km migrates north and southwest below the EVZ towards the Reykjanes Ridge, as Vogt (1974) suggests, from below the Vatnajökull ice cap. At greater depth, the anomaly is seen to be confined to a more centralised plume, having an estimated radius of ~ 50 km (Tryggvason et al., 1983) (figure 1.11).

A viscosity anomaly is also present below Iceland. Post-glacial rebound shows that the mantle viscosity must be less than 10^{19} Pa s (Sigmundsson, 1991). Lake level measurements near the Vatnajökull ice cap provide another estimate of viscosity for the mantle below Iceland in the range of 10^{18} - $5x10^{19}$ Pa s (Sigmundsson and Einarsson, 1992). Foulger et al. (1992) studied geodetic measurements of post dyking stress relaxation, and obtained values in the range 0.3-$2x10^{19}$ Pa s, in close agreement with values obtained from post-glacial rebound. These values are two orders of magnitude below those obtained for beneath Fennoscandia (e.g. McConnel, 1965), and Japan (Aki, 1981), but of the same order ($7x10^{18}$ Pa s) as for the South Atlantic (Morgan and Smith, 1992). An increase in temperature will decrease viscosity, so these results support the postulate that a thermal anomaly is contained in the mantle below Iceland.

1.9 Iceland and the Reykjanes Ridge

The Reykjanes Ridge strikes southwest for ~ 1000 km from the Reykjanes Peninsula on Iceland (64°N) to the Bight Fracture Zone at 57°N. The ridge is oriented at 036° and has a half-spreading rate of 10 mm a^{-1} along a 096° direction (Talwani et al., 1971; DeMets et al., 1990). Morphologically, the ridge can be divided into a northern and

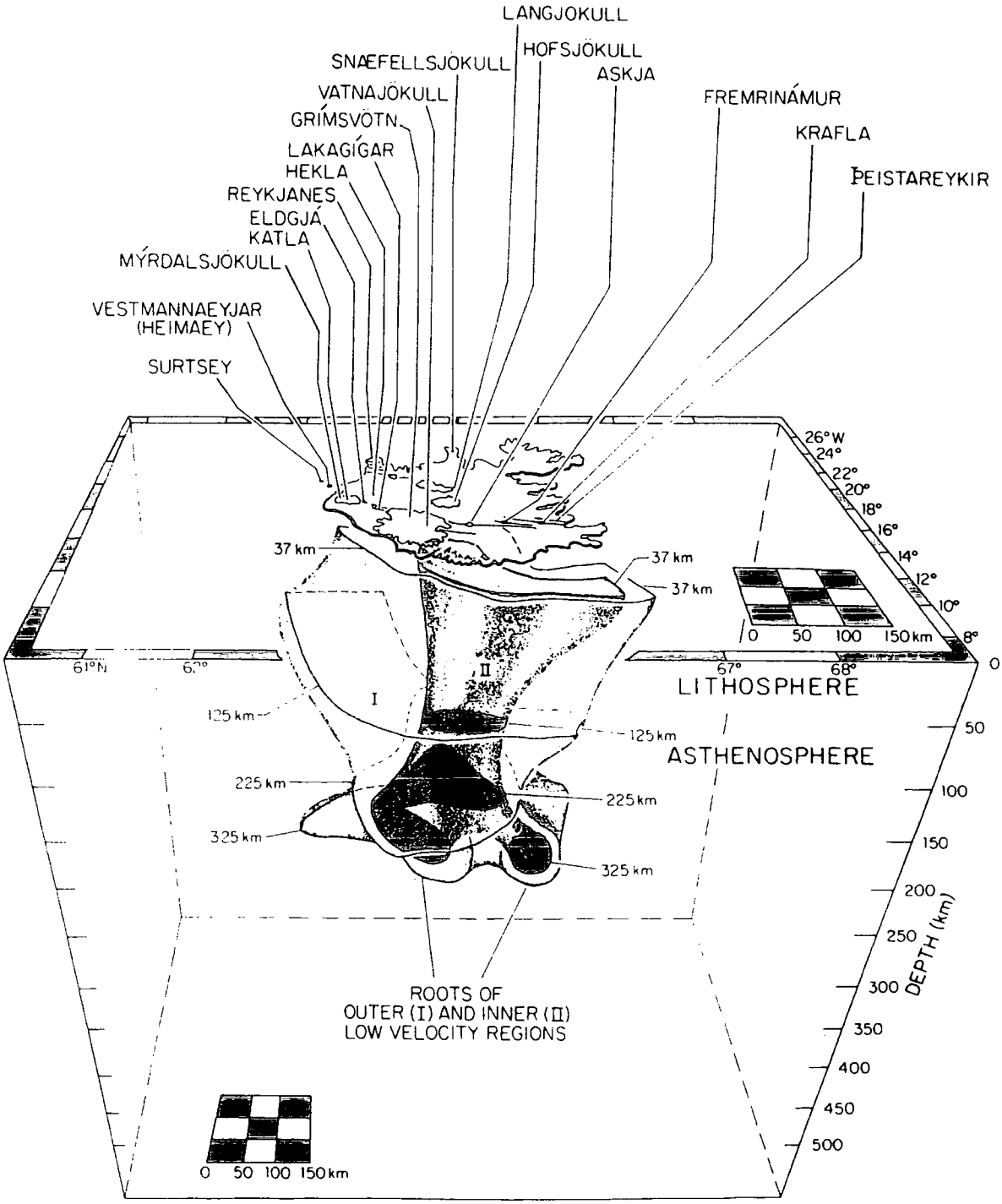

Figure 1.11. The three-dimensional structure of the Icelandic magma system. The view is westward-directed, towards the North American plate. The composite structure is made up of a set of nested low-velocity volumes. In the outer volume (I), compressional wave velocities are as much as 2% slower than average. In the inner core (II) the velocities are in excess of 2% slower than the average velocity on a given level (from Ryan, 1990).

southern section (Parson et al., 1993). The northern segment displays an axial ridge high which is similar in appearance to that of the fast spreading East Pacific Rise. South of ~59°N, a median valley has formed at the plate boundary. The occurrence of two dissimilar ridge axis morphologies, sharing the same ridge orientation and spreading rate, suggests that the Iceland mantle plume has some effect upon the structure and evolution of the Reykjanes Ridge. This effect is presumably reduced with increased distance from Iceland. Vogt (1974) proposed that a pipe-like flow of plume material (possibly in pulses) is occurring beneath the Reykjanes Ridge, mixing with upwelling mantle that is associated with the ridge system. Thus, when this laterally injected plume material is expended, the slow spreading ridge system displays a more 'normal' median valley morphology.

1.10 Summary

Beneath Iceland, seismic, geodetic, geochemical, and gravity observations infer the existence of a low density thermal anomaly associated with an upwelling mantle plume, which is responsible for Iceland's sub-aerial nature. Partial melt from the plume accumulates at the base of the Icelandic crust at a depth of 20-30 km. Below the active volcanic zones, partial melt rises to within 10 km of the surface, and shallower still if it resides in a crustal magma chamber. Magma is intruded or extruded during rifting episodes through dyke injection at central volcanoes and along fissure swarms. Repeated volcanism within a volcanic system causes down-sagging of the lava pile, subsidence and metamorphism, as the lavas are transported away from the accretionary axis, forming the top 10 km of crust. The shallow crust undergoes hydrothermal alteration, erosion and tectonism resulting in structural heterogeneity. Partial melt which is not intruded or erupted will cool and freeze onto adjacent, cold crust as mantle derived 'underplated' crust. As the plume migrates eastwards relative to the Iceland plateau, so the spreading plate boundary repositions itself above the plume, creating a varied and complex geology. To the southwest, the Reykjanes Ridge presumably receives some fraction of the upwelling plume material which produces the near-Iceland ridge axis high. With increased distance from Iceland, the effect of the plume is reduced and the ridge axis becomes characterised by a median valley.

Chapter 2

Structure of the Hengill-Grensdalur and Krafla Spreading Centres

2.1 Introduction

Using local earthquake seismic tomography, the shallow crustal structure of two spreading segments in Iceland, Hengill-Grensdalur and Krafla (figure 2.1), have been investigated. This chapter combines gravity observations with these tomographic results to assess the fidelity of the tomographic method and further refine the description of the crustal structure for these areas. This is accomplished by predicting the component of the observed gravity field which may be produced by the tomographically imaged bodies and in the process attempting to explain any residual anomalies.

There is a difference in the ability of gravity and P-wave arrival time data to detect geological structure. The amplitude of the gravity field at the Earth's surface associated with a given body decreases as the inverse of the square of depth to the body and therefore the sensitivity of the gravity field to structure is greatest for shallow bodies. In contrast, the resolving power of tomography is governed by the geometry of seismic rays rather than depth. Thus, the surface gravity field is most strongly correlated with the shallow seismic velocity structure and is better than tomography at locating the horizontal positioning and extent of anomalous bodies.

2.2 Combining Gravity and Seismic Data

2.2.1 Joint Inversion

Several approaches can be taken to combine seismic and gravity data. The Bouguer anomaly field and original seismic travel-time residuals may be simultaneously inverted to calculate structure. This method was applied to teleseismic and gravity data from Yellowstone, WY and the Imperial Valley, CA (Savino et al., 1977, 1979; Evoy, 1978). In these studies, Birch's velocity-density relationship (Birch, 1961) was used to relate the two different data types. For Yellowstone, the subsurface structure was successfully modelled as varying density in a block 190 x 190 km in area and extending from the surface down to a depth of 100 km. A broad low-density, low-velocity structure with lateral variations in density of approximately 250 kg m^{-3} in the upper 30 km and 150 kg

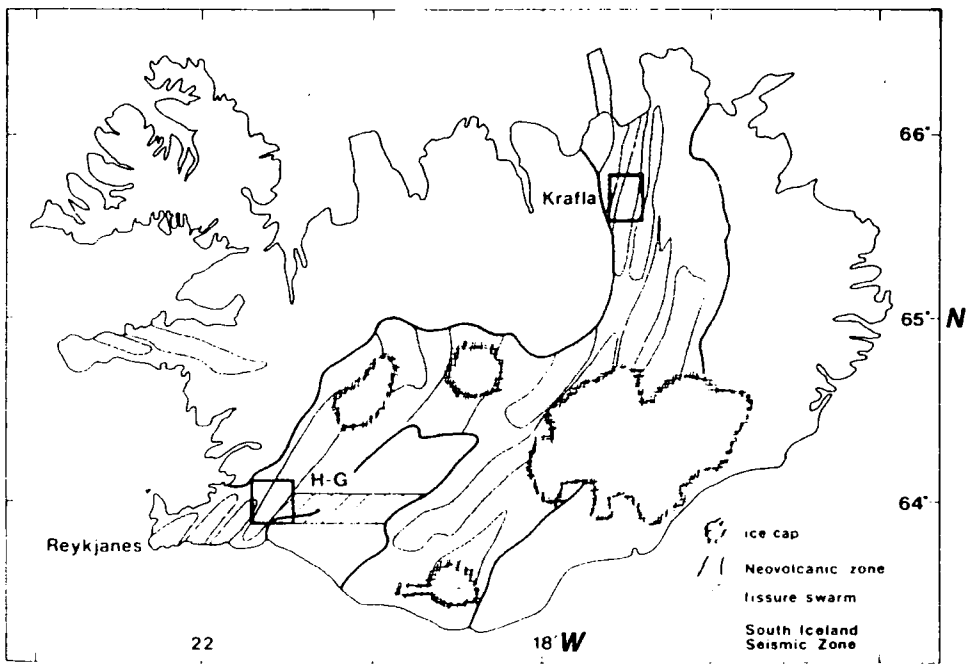

Figure 2.1. Map showing the geographic locations of the Hengill-Grensdalur (H-G) and Krafla areas in relation to Iceland and its neovolcanic zones. From Foulger and Arnott (1993).

m^{-3} in the lower 70 km fit the data well. The method failed, in the neighbourhood of the Mallard Lake resurgent dome, where the gravity and seismic data were not well correlated. This was attributed to the presence of partial melt, for which Birch's relationship does not apply (Murase and McBirney, 1973). The structure predicted by the Murase and McBirney (1973) study was different to that obtained by modelling of the gravity data alone (Eaton et al., 1975), which placed the entire source of the gravity anomaly in a surface layer 8-12 km thick with a density contrast of 450 kg m^{-3}. The Imperial Valley study revealed crustal thinning near all the known geothermal areas, in particular the Salton Sea area, and large crustal-thickness gradients at the locations of major fault systems.

Oppenheimer and Herkenhoff (1981) simultaneously inverted the Bouguer anomaly field and seismic velocity perturbations calculated using teleseismic tomography for the Geysers-Clear Lake area, California, U.S.A. The gravity and seismic data types correlate well, but the best-fit velocity-density relationship that they found differed from that of Birch (1961). They concluded that partial melt and a composition change were required beneath Mt. Hannah to satisfy both the seismic velocity and the gravity fields. For the same region Isherwood (1976) provided a different interpretation of the sub-surface structure. Isherwood (1976) estimated that a sphere at a depth of 13.5 km would best fit the gravity data. The preferred model consisted of a magma body with a radius of 6.9 km and density of contrast of -500 kg m^{-3}.

2.2.2 Forward Modelling

Ellsworth and Koyanagi (1977) compared the three-dimensional seismic velocity structure derived from teleseismic tomography for Kilauea volcano, Hawaii, to the Bouguer anomaly field. To relate velocity to density in an environment where partial melt is expected, a theoretical relationship derived by Sato (1952) for the change in compressional wave velocity caused by the presence of fluid-filled spherical inclusions in an otherwise homogeneous, elastic solid was used. The Bouguer anomaly field was predicted from the tomographic velocity structure and was found to be in agreement in form and amplitude with the true Bouguer anomaly field. This provided evidence to support the tomographic model between 0-12 km depth within the crust, the depth range for structure to which the surface gravity field used is sensitive.

2.2.3 Joint Inversion or Forward Model?

The method of joint inversion of P-wave arrival time data and gravity observations requires that the root mean square (RMS) residual of both the signals be reduced simultaneously. To accomplish this a 'coupling' equation is used which allows one variable (e.g. V_p) to be written in terms of the other (e.g. ρ). There is also a weighting factor which must be applied before the inversion is performed. This factor controls the reliance of the inversion on seismic data relative to gravity data and can give rise to a large number of potential solutions. Unfortunately, there seems to be no objective way to choose the value of this factor. Another problem is that this factor will tend to mask any imperfections the tomography has at detecting structure. Thus, forward modelling of the seismic data has the advantage in that it can test the limits of the tomographic method.

2.2.4 Methodology

In this chapter the procedure is similar to the method of Ellsworth and Koyanagi (1977). After removal of the regional, the de-trended Bouguer anomaly field and the results of local earthquake seismic tomography are considered jointly for the Hengill-Grensdalur spreading segment, southwest Iceland, and the Krafla spreading segment, northeast Iceland. The de-trended Bouguer anomaly field is predicted by converting the three-dimensional seismic velocity field to density using a velocity-density relationship for Icelandic rocks (Christensen and Wilkins, 1982). In the case of the Hengill-Grensdalur segment the predicted gravity field is subtracted from the real field and the resulting residual is interpreted. This approach avoids difficulties inherent in a simultaneous inversion of assessing the effects of uncertainties in: (i) the tomography results; (ii) the Bouguer reduction density; and (iii) choosing relative weightings for the gravity and tomography data. For the Krafla area the de-trended Bouguer anomaly is again predicted, but in addition an inversion of the gravity data is performed.

2.3 The Hengill-Grensdalur spreading segment

2.3.1 Introduction

The Hengill-Grensdalur area is located at a ridge-ridge-transform triple junction at the eastern end of the Reykjanes Peninsula zone (figure 2.1). Small-scale westward migration of the locus of spreading at this triple junction has occurred over the last ~1 Ma and the area now contains three volcanic systems (Arnason et al., 1987).

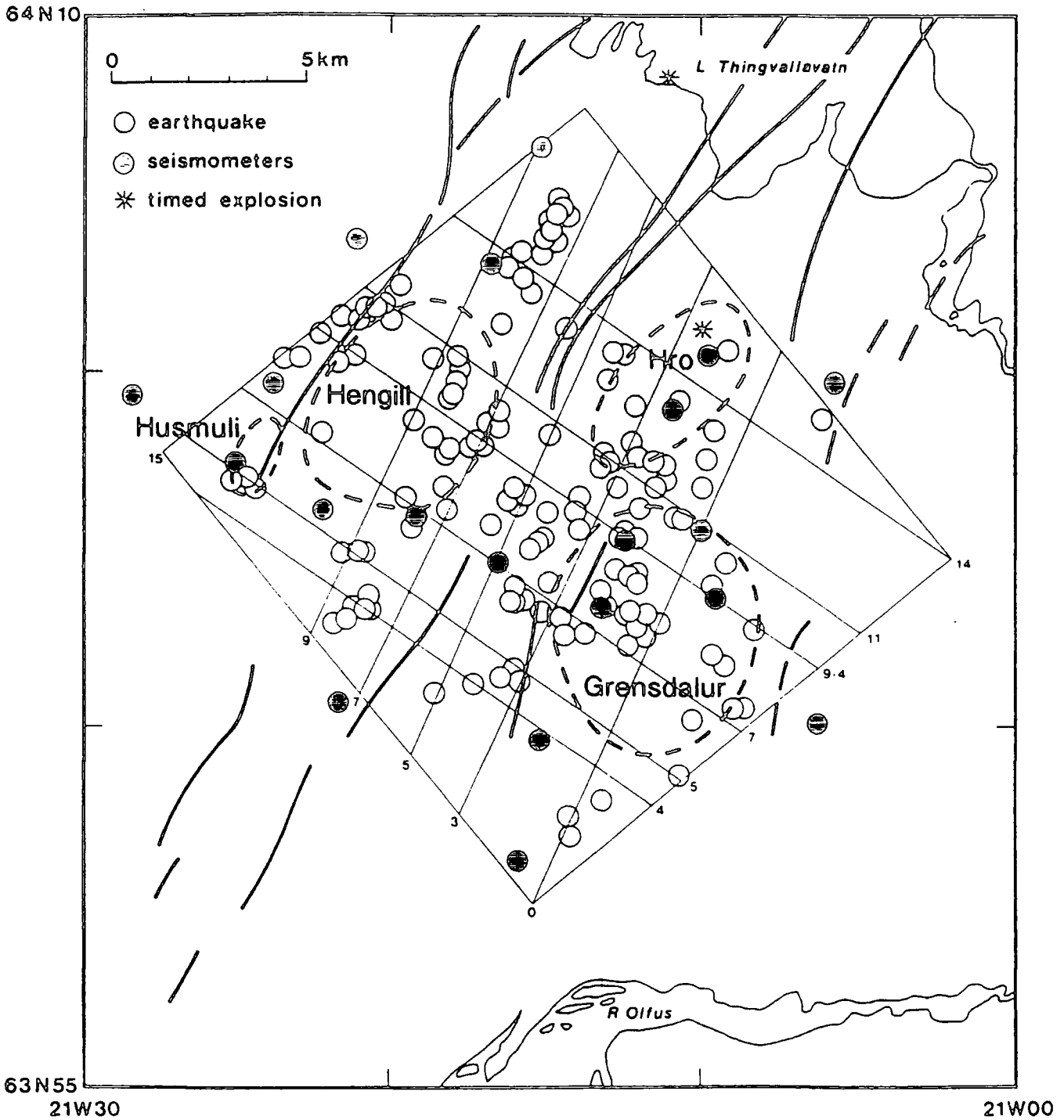

Figure 2.2. The Hengill-Grensdalur seismometer network showing the locations of seismometers (black circles), earthquakes (white circles), and schematic tectonics. Bold lines indicate the outlines of the Hengill, Hrómundartindur (Hro) and Grensdalur volcanic systems. Dashed lines indicate outlines of the Hengill and Hrómundartindur topographic highs and the extinct Grensdalur volcano. Box indicates the surface area of the volume imaged by local earthquake tomography (Toomey and Foulger, 1989; Foulger and Toomey, 1989, Foulger and Arnott, 1993).

The easternmost system, the Grensdalur system, is the oldest, contains the remnants of an extinct central volcano, and was the locus of spreading prior to 0.3 Ma, when activity migrated west and the new Hengill system began to form. The Hengill system is currently the most active system in the area and crustal spreading at this triple junction is thought to occur along the Hengill fissure swarm. The system is dominated topographically by the 800 metre high hyaloclastite Mt. Hengill. This is generally assumed to be a central volcano, but its morphology and lithology cast doubt on this (Sæmundsson, 1967; Walker, 1992). Between the Grensdalur and Hengill systems lies the Hrómundartindur system, a zone of volcanism that formed simultaneously with the Hengill system but which lacked extensional tectonics and is now almost extinct. The whole area also contains several monogenetic basalt shields (e.g. Husmuli, to the southwest of Mt. Hengill). Six post-glacial eruptions have occurred within the area. Acid and intermediate rocks around Mt. Hengill provide evidence for magma evolution in long-lived partial melt accumulations in the shallow crust. A high-temperature geothermal area encompasses all three systems, indicating that material at very high temperatures exists at depths within the range of groundwater circulation. The three volcanic systems are thought to have separate heat sources (Torfason et al., 1983; Foulger, 1988a and b). Drilling in the geothermal area within the Hengill system to the north of Mt. Hengill encountered temperatures of over 374°C at shallow depth (Steingrimsson et al., 1986) suggesting the proximity of an extremely hot heat source.

The surface geology of the area is dominated by hyaloclastites, tuffs, sub-aerial lava flows and exposed intrusions in the neighbourhood of the eroded Grensdalur volcano. Geothermal wells drilled in the Hengill system penetrate to 2265 m and reveal that intrusions form < 5% of rocks down to 400 m below sea level but that this increases to about 20% at 1500 m below sea level and may rise to over 50% in some localities at greater depths (Franzson, 1988).

Deeper structure is inferred from geophysical observations only. Resistivity measurements indicate that the geothermal reservoir broadens with depth (Hersir, 1980). Deep soundings in the Hengill system indicate an increase in resistivity with depth below about 800 m below sea level which was interpreted by Hersir et al. (1990) as an indication of alteration facies. A possible steam reservoir beneath Mt. Hengill was suggested by Stefansson et al. (1983) on the basis of drilling. This interpretation was consistent with the view of Mt. Hengill as an active central volcano. Magnetotelluric measurements indicate that the depth to partial melt is approximately 8 km beneath the spreading plate boundary, deepening to 25 km at distances of 25-40 km (Hersir et al. 1984). The maximum depths of local earthquakes varies from 3-7 km within the area and

this indicates the depth to the onset of plastic creep (Foulger, 1988a). The most detailed study of shallow structure down to about 5 km beneath the area is provided by local earthquake tomography (Toomey and Foulger, 1989; Foulger and Toomey, 1989).

2.3.2 The Hengill-Grensdalur Tomographic Study

2.3.2.1 The Tomographic Inversion Method

P-wave velocity tomography was conducted for the Hengill-Grensdalur and Krafla areas (Foulger and Arnott, 1993) using the method of Thurber (1983). In general, a target volume is selected that is filled as far as possible with seismic events and whose surface is covered as uniformly as possible with seismic stations. The wave-speed is defined by values (initially a-priori estimates) at the nodes of a three-dimensional grid. Values between the nodes are obtained by linear interpolation. The trajectories of rays passing through the volume are determined by 'approximate ray tracing' (Thurber, 1983), in which the fastest ray between a hypocentre and station is selected after calculating the travel times of several rays. In the inversion procedure, the earthquake hypocentral parameters and nodal velocities are iteratively adjusted to minimise the RMS residual of the travel times. Thurber's method is applicable to the scale of the Hengill-Grensdalur and Krafla studies and yields a continuous velocity structure which is more realistic than structures consisting of assemblages of uniform blocks.

The Hengill-Grensdalur area is structurally heterogeneous and continuously seismically active. Rapid surface heat loss causes cooling and thermal cracking in the geothermal heat sources, resulting in continuous small-magnitude earthquake activity throughout the area in the depth range 2-7 km (Foulger and Long, 1984; Foulger, 1988a and b). In 1981 a large earthquake dataset was recorded on an optimally designed 23-station seismometer network (figure 2.2) providing a good dataset for a seismic tomographic analysis (Foulger, 1988a; Toomey and Foulger, 1989; Foulger and Toomey, 1989).

A volume 14 x 15 km in area and 5 km in depth encompassing the central parts of all three volcanic systems was studied using 158 well-distributed events, two explosions and 20 stations (Toomey and Foulger, 1989). These yielded 2409 arrival times with overall timing uncertainties of approximately $\pm$ 0.03 s. Nodal spacings for the inversion were set at 2 km in the horizontal and 1 km in the vertical directions, which is fine enough to resolve the major structures in the volume. An initial RMS arrival time residual of 0.05 s decreased to 0.04 s after inversion and the velocity structure calculated for the volume was found to be insensitive to the starting conditions, indicating a reliable result. The

resolution quality of the results was assessed using the density of rays passing close to each node (Toomey and Foulger, 1989). To decide which volumes are least well constrained the introduction of a statistic is necessary. The derivative weighted sum (DWS) was the statistic used by Toomey and Foulger (1989) and by Arnott (1990) for choosing between which volumes were 'good' and which were 'bad'. The DWS is essentially a measure of how many rays pass near the solution node. Those rays passing closest were weighted highest. Hence, a node with a high DWS was considered well constrained. About half the nodes are well-resolved at the surface and at 5 km depth, and the majority are well-resolved in the depth range 1- 4 km.

2.3.2.2 Tomographic Results from the Hengill-Grensdalur Area

Considerable heterogeneity was detected, which corresponds well with the known geology and tectonic structure of the area (figure 2.3). High velocity bodies exist in the 0-2 km depth range beneath the Grensdalur central volcano and at 0-3 km depth beneath the Husmuli basalt shield. A high-velocity body at a depth 3-4 km occurs beneath the most intense part of the geothermal area within the Hrómundartindur system. These bodies are interpreted as high density gabbroic intrusives. The body underlying Husmuli has a cylindrical shape and is interpreted as the frozen magma feeder that supplied the surface eruption (Foulger and Toomey, 1989).

A single, relatively small (~ 5 km^3) low-velocity body is imaged at 2-4 km depth beneath the northern flank of Mt. Hengill. This was interpreted by Foulger and Toomey (1989) as possibly representing a volume of partial melt, an interpretation that is supported by the high temperatures (> 374^oC) encountered by nearby drilling (Steingrimsson et al., 1986). The amplitude of the velocity anomaly (~-7%) suggests a partial melt fraction of approximately 1-7% (Mavko, 1980). A few earthquakes were located within this low-velocity body, suggesting that if partial melt is present it probably occurs in pockets and not as a homogeneous body. As far as a large mid-crustal magma chamber is concerned, no major, coherent, low-velocity body is imaged directly beneath Mt. Hengill, and velocities beneath the fissure swarm in general are not significantly low compared with volumes away from the spreading axis.

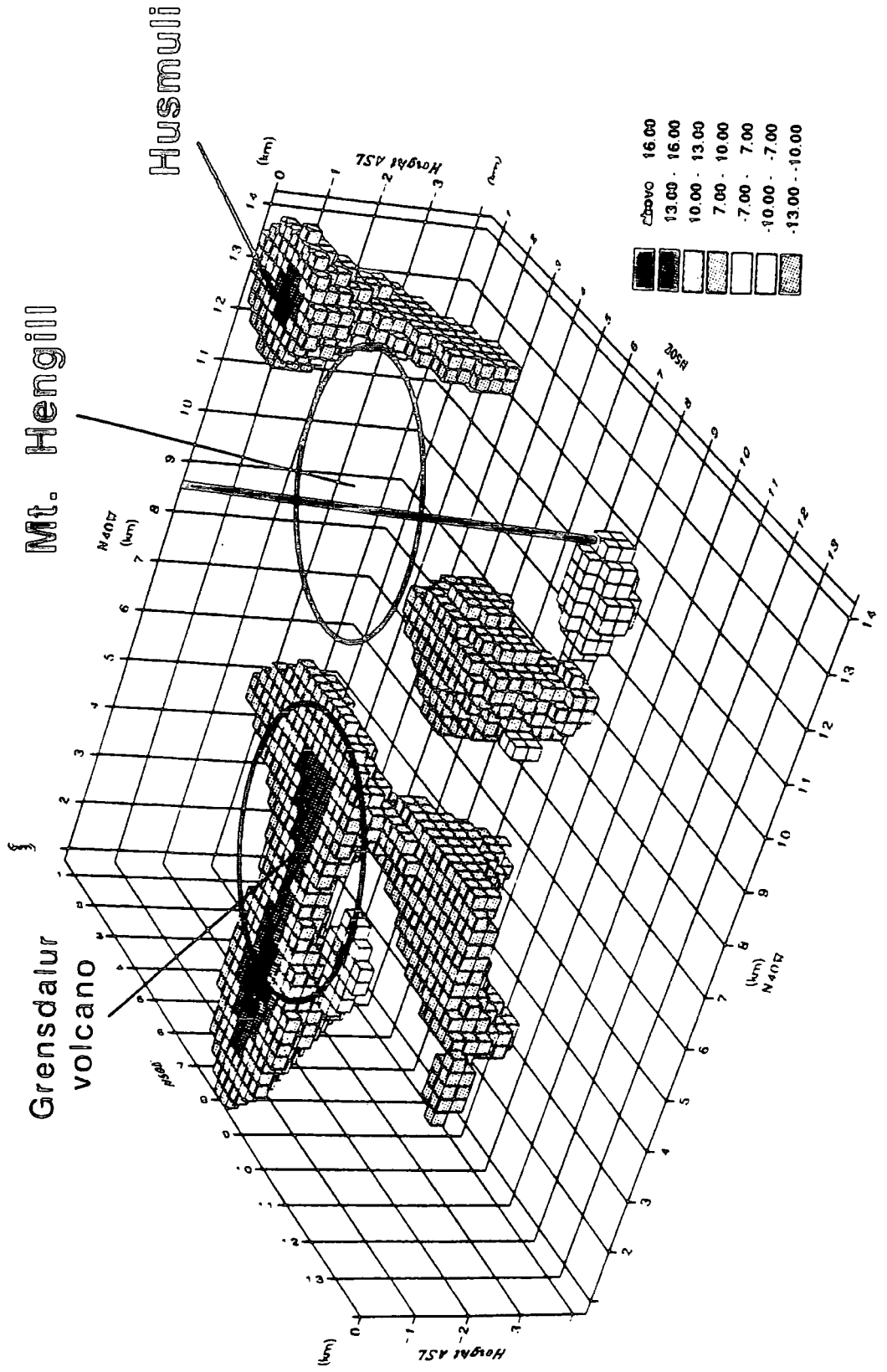

Figure 2.3. Three-dimensional image of the seismic velocity field obtained by local earthquake tomography (Toomey and Foulger, 1989; Foulger and Toomey, 1989). View is from the north. The grey scale denotes percentage difference in velocity from the one-dimensional starting structure used. The model is represented by constant velocity cubic blocks of dimension 0.25 km^3. The low-velocity bodies are lighter coloured. (From Toomey and Foulger, 1989.)

2.3.3 Forward Modelling using the Tomographic Result

2.3.3.1 Seismic Velocity and Density

The compressional velocity (V_p) can be written as:

$$V_p = \sqrt{\frac{K + \frac{4}{3}\mu}{\rho}} \qquad (2.1)$$

where K is the bulk modulus (incompressibility), μ is the shear modulus (rigidity), and ρ is the bulk density. At first sight the compressional velocity would seem to be proportional to $\rho^{-1/2}$. In fact, both K and μ are correlated with ρ, increasing more rapidly than ρ^1, giving rise to a different form of the equation (2.1) in most cases.

Birch (1961) empirically investigated the velocity-density relationship for igneous and metamorphic rocks and found that a simple equation of the form:

$$\rho = \alpha V_p + \beta \qquad (2.2)$$

could be used to describe the correlation of V_p and ρ for igneous and metamorphic rock samples (α and β are constants). Equation 2.2 is often referred to as Birch's law (e.g. Gebrande et al. 1980), and states that the bulk density of a volume of rock is directly proportional to compressional velocity of the rock in that same volume.

Gravity forward models of two dimensional seismic crustal structure of thickness ~10 km (and thicker) were computed by directly converting velocities into densities using the Ludwig, Nafe and Drake (1970) velocity-density relationship (Barton, 1986). Numerous gravity models were inconsistent with observations because of the scatter of data about the velocity-density relationship. Barton (1986) concluded that for crustal units of large thickness > 1 km, errors accumulate quickly and degrade the usefulness of the 'seismic to gravity' forward modelling technique. However, the velocity-density relationship used in these cases was drawn from widely differing rock types making the problem worse than for the case where a local relationship is available.

As part of the Iceland Drilling Research Project (Christensen and Wilkins, 1982), 90 samples obtained from a borehole of depth 1.9 km in eastern Iceland were used to obtain the velocity-density relationship, in the form of Birch's law (figure 2.4):

$$\rho = 1530 + 230V_p \qquad (2.3)$$

where V_p is the compressional wave velocity in km s^{-1} and ρ is the rock density in kg m^{-3}. A similar investigation was carried out using 77 samples of oceanic basalt from various Deep Sea Drilling Project surveys (Christensen and Salisbury, 1975). This study yielded the formula:

$$\rho = 1270 + 265V_p \qquad (2.4)$$

For this chapter equation 2.3 was used to relate seismic P-wave velocity to density since it was likely to be the most representative of Icelandic crustal rocks.

2.3.3.2 Obtaining the Predicted Gravity Anomaly from the Tomographic Velocity Structure

Application of the tomographic method to a study volume, such as Krafla or Hengill-Grensdalur, yields a three-dimensional velocity structure (of velocity contrasts within each layer) centred on the nodes of a coarse three-dimensional grid. The study volume is divided into cubes and the seismic velocities derived from the tomographic inversion are interpolated linearly to determine the average velocity for each cube. The velocity contrasts are then used to calculate a density contrast for each cube using equation 2.5 (obtained from equation 2.3):

$$\Delta\rho = 230\Delta V_p \qquad (2.5)$$

where $\Delta\rho$ is the density contrast in kg m^{-3}, and ΔV_p is the compressional wave velocity contrast in km s^{-1}.

The expression for the gravitational effect of a rectangular parallelepiped (e.g. Talwani, 1973) is used to calculate the combined effect of all the cubes at each station to give the final, predicted de-trended Bouguer anomaly field.

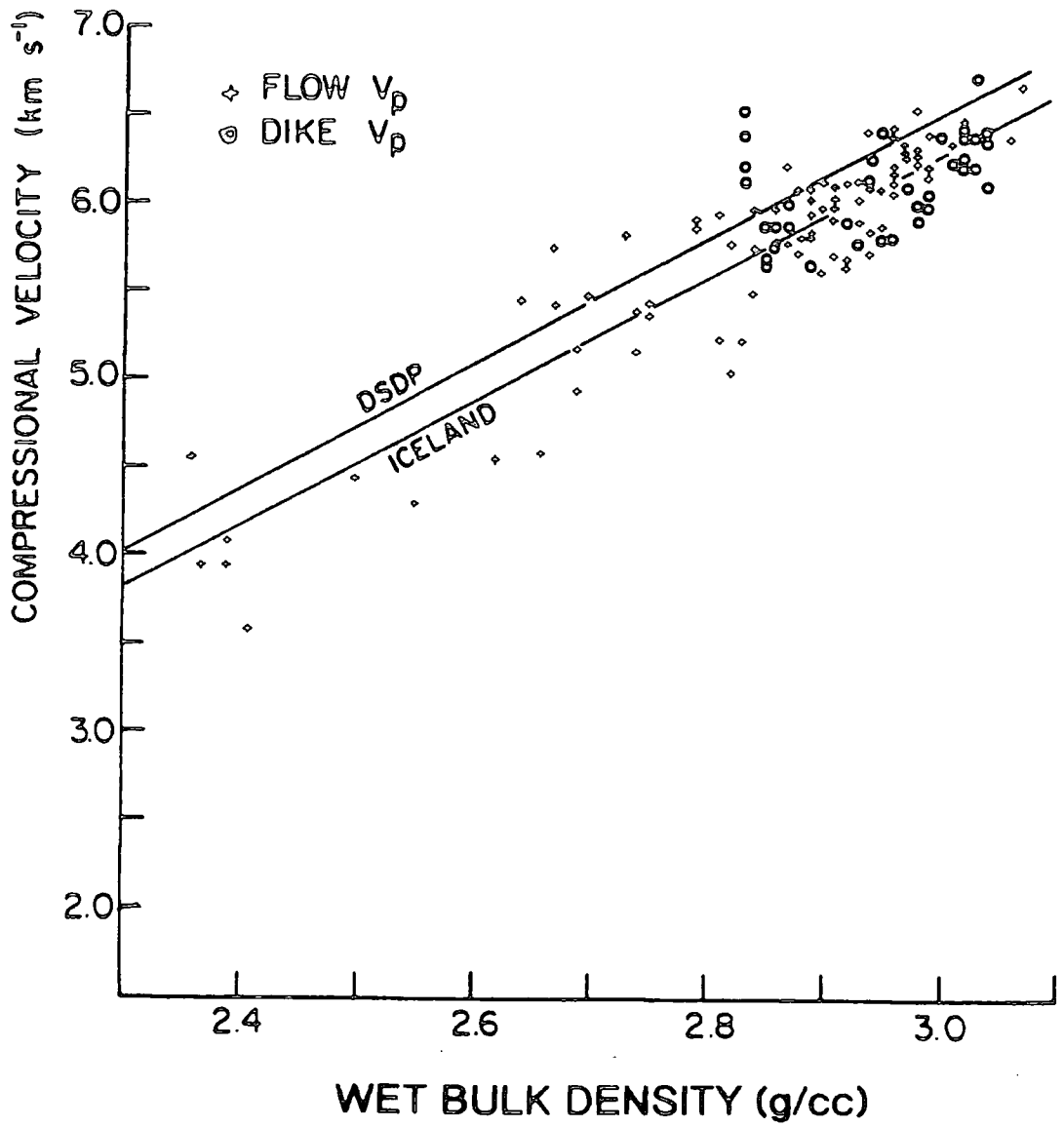

Figure 2.4. Compressional wave velocity versus wet bulk density for rock samples from the Reydarfjördur borehole, eastern Iceland. Values measured at 1.0 kbar pressure. The linear least squares solution is shown (ICELAND) along with the equation that best fits DSDP data (DSDP) (from Christensen and Wilkins, 1982).

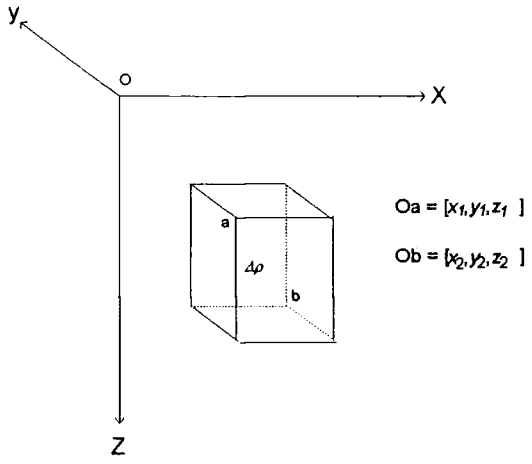

Figure 2.5. A parallelepiped in space, of density contrast Δρ, bounded by two opposite corners: a at x_1,y_1,z_1, and b at x_2,y_2,z_2, relative to the origin at O.

Talwani (1973) gives the analytical solution for the gravitational effect, $(\Delta g)_{ab}$, of a perturbing parallelepiped in space (figure 2.5) of density contrast Δρ, as:

$$
\begin{aligned}
(\Delta g)_{ab} = G\Delta\rho\Bigg\{ & -z_1 \tan^{-1}\frac{x_1 y_1}{z_1 R_{111}} + z_1 \tan^{-1}\frac{x_2 y_1}{z_1 R_{211}} + z_1 \tan^{-1}\frac{x_1 y_2}{z_1 R_{121}} - z_1 \tan^{-1}\frac{x_2 y_2}{z_1 R_{221}} \\
& + z_2 \tan^{-1}\frac{x_1 y_1}{z_2 R_{112}} - z_2 \tan^{-1}\frac{x_2 y_1}{z_2 R_{212}} - z_2 \tan^{-1}\frac{x_1 y_2}{z_2 R_{122}} + z_2 \tan^{-1}\frac{x_2 y_2}{z_2 R_{222}} \\
& + x_1 \log\left(\frac{R_{111}+y_1}{R_{112}+y_1}\frac{R_{122}+y_2}{R_{121}+y_2}\right) + x_2 \log\left(\frac{R_{212}+y_1}{R_{211}+y_1}\frac{R_{221}+y_2}{R_{222}+y_2}\right) \\
& + y_1 \log\left(\frac{R_{111}+x_1}{R_{112}+x_1}\frac{R_{212}+x_2}{R_{211}+x_2}\right) + y_2 \log\left(\frac{R_{122}+x_1}{R_{121}+x_1}\frac{R_{221}+x_2}{R_{222}+x_2}\right) \Bigg\}
\end{aligned}
\qquad (2.6)
$$

where $R_{abc} = \sqrt{x_a^2 + y_b^2 + z_c^2}$

Equation 2.6 has been encoded in a program GRAV3D written by the author (see appendix). This program was tested by calculating the gravity fields generated by collections of cubes arranged to comprise infinite line masses, half infinite slabs and point masses. The results were compared with values produced using analytical equations for these shapes. It was found that when a collection of cubes were sufficiently deep they closely approximated the theoretical bodies. At shallow depth the appearance of the computed gravitational field is not smooth and the effects of the discrete cubes is visible. This unrealistic feature can be overcome by using a much smaller cube size.

Two predicted fields were calculated: one to coincide with the surface gravity measurements and another on a horizontal plane 1 km above sea level.

2.3.4 The Hengill-Grensdalur Gravity Dataset

2.3.4.1 Acquisition

A detailed local gravity survey of the Hengill-Grensdalur area was conducted in 1982 and 1983 (Thorbergsson et al., 1984). An area of approximately 450 km^2 was surveyed with 315 gravity stations, spaced at average intervals of about 1.5 km (figure 2.6). The measurements were made using a LaCoste and Romberg gravimeter and following conventional field practice, repeating measurements at a base station at the start and end of each day.

The data were reduced in the standard way to obtain absolute gravity at each point. Corrections were made for solid earth tides (Longman, 1959), and the best estimates of instrument drift and gravity at the stations were made using the method of least squares. The measurements were tied to station 5451 at Skolavordurholt in Reykjavik, where g = 982273.69 mGal, and is tied to the International Gravity Standardisation Net 1971 (Torge, 1980). The calculated values of gravity at most stations have estimated uncertainties of less than 0.5 mGal.

Thorbergsson et al. (1984) calculated Bouguer anomalies, for a truncated Bouguer plate of radius 2615 m, using a Bouguer density of 2600 kg m^{-3}. Terrain corrections out to 2615 m from the stations were made using Hammer tables (Hammer, 1939) and estimates of the height differences from the stations were obtained both from estimates made in the field and from maps. At distances between 2615 m and 50 km, the terrain correction and the Bouguer correction for each station were combined by correcting for the effect of all the mass above sea level, or the absence of mass at sea. Heights were obtained using a database of digitised topography for Iceland and the surrounding sea. The remaining Free Air and air pressure corrections required were made in the standard way.

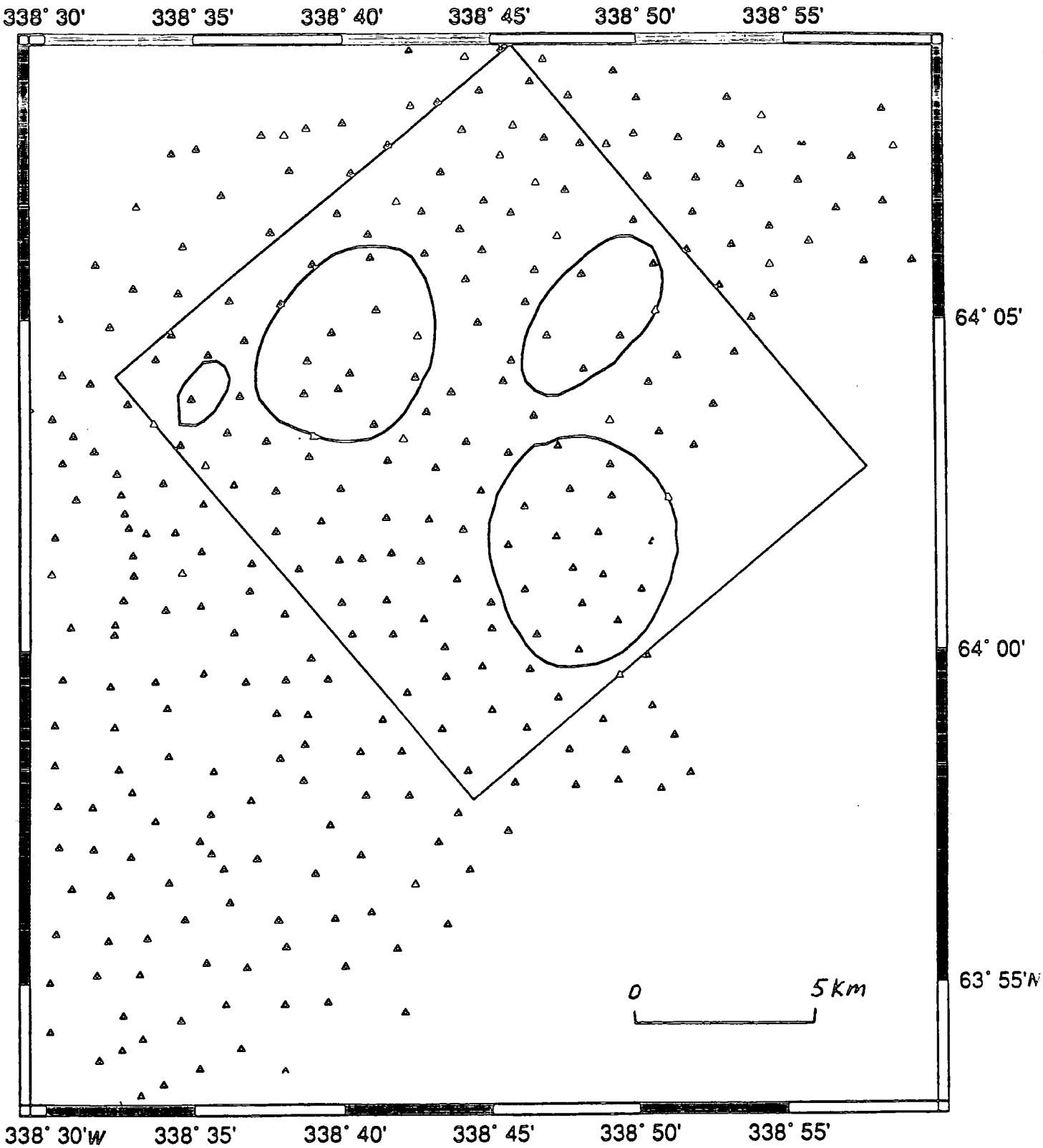

Figure 2.6. Gravity station coverage for the Hengill-Grensdalur area. Box indicates the surface area of the volume imaged by local earthquake tomography (Toomey and Foulger, 1989; Foulger and Toomey, 1989).

2.3.4.2 Bouguer Reduction Density

Critical to gravity analysis is an accurate knowledge of the densities of the rocks above sea level in the area, which is required to calculate Bouguer anomalies. Rock densities were therefore studied in this chapter using two independent procedures; laboratory measurements and Parasnis' method (Parasnis, 1962). Although the dominant rock type in Iceland is basalt, volcanic processes have generated rocks with a wide range of densities. The surface, sub-aerial layer within the neovolcanic zone is composed mostly of relatively low density lavas, hyaloclastites, tuffs and ash layers, which vary in density according to composition and compaction. Below the eruptive layer and away from the central volcanoes the crust comprises of sheeted dykes, increasing in age away from the accretionary boundary. Near central volcanoes, massive, high density intrusions occur and relatively low density partial melt accumulations may also underlie active centres.

Active geothermal processes may either increase or decrease bulk rock densities (e.g. Locke, 1988). These processes include the dissolution and removal of minerals, redeposition and the alteration of competent rock to clay minerals. The effect of geothermal activity on the underground hydrothermal system, e.g. boiling and the replacement of water with steam as the rock pore fluid, may also have an effect on densities.

The wet densities of 15 rock specimens collected in the Hengill-Grensdalur area (Walker, 1992) were determined by measuring their masses, volumes and porosities in the laboratory. The wet density is used for rocks in situ in Iceland. A RUSKA Universal Porometer was used to measure the bulk volumes (the volumes of the whole samples including pore spaces) (RUSKA Universal Porometer data sheet). Each specimen was placed inside a chamber of known volume which was then completely filled with mercury. Mercury does not penetrate the pores of a rock specimen, so knowledge of the volume of mercury necessary to fill the chamber allows the bulk volume of the sample to be determined.

Porosities were obtained using a method that relies on Boyle's Law, which states that the product of pressure and volume of an ideal gas is a constant for a constant temperature. The dry samples were placed inside a chamber of known volume, which was then contracted, raising the pressure inside the chamber. Then:

$$(V_{c1} - V_g)P_1 = (V_{c2} - V_g)P_2 \qquad (2.7)$$

where V_{c1} is the initial volume of the chamber, V_g is the grain volume of the rock, V_{c2} is the contracted volume of the chamber and P_1 and P_2 are the initial and final pressures in the chamber. It follows that:

$$V_g = \frac{V_{c2}P_2 - V_{c1}P_1}{P_2 - P_1} \tag{2.8}$$

and the porosity, ϕ is

$$\phi = \frac{V_b - V_g}{V_b}, \tag{2.9}$$

where V_b is the bulk volume. The wet density, ρ_w, is then:

$$\rho_w = \frac{m_d + \phi V_b \rho_{water}}{V_b} \tag{2.10}$$

where m_d is the dry mass of the sample and ρ_{water} is the density of water.

Large samples were split into 5 or 6 blocks 6-10 cm^3 in volume and individual density determinations were made for each. The results for these blocks were combined and a mean and standard deviation was obtained for each sample (Table 2.1).

The samples studied came from a post-glacial lava flow northeast of Mt. Hengill and hyaloclastite units within the Hrómundartindur system and the Grensdalur central volcano (figure 2.7). The wet densities of the samples vary from 2110 to 2800 kg m^{-3} and the porosities lie in the range 8-40%. The results illustrate the large variation in the density and porosity of the near-surface rocks. The average wet density of the samples is 2450 $\pm$ 100 kg m^{-3}.

Parasnis' method was applied quantitatively to estimate the near-surface bulk rock density (Parasnis, 1962). In Parasnis' method the Bouguer anomaly, g_B, which can be written as:

$$g_B = g_{obs} - g_t + \Delta g_{fa} - 2\pi G\rho z + \Delta g_T \tag{2.11}$$

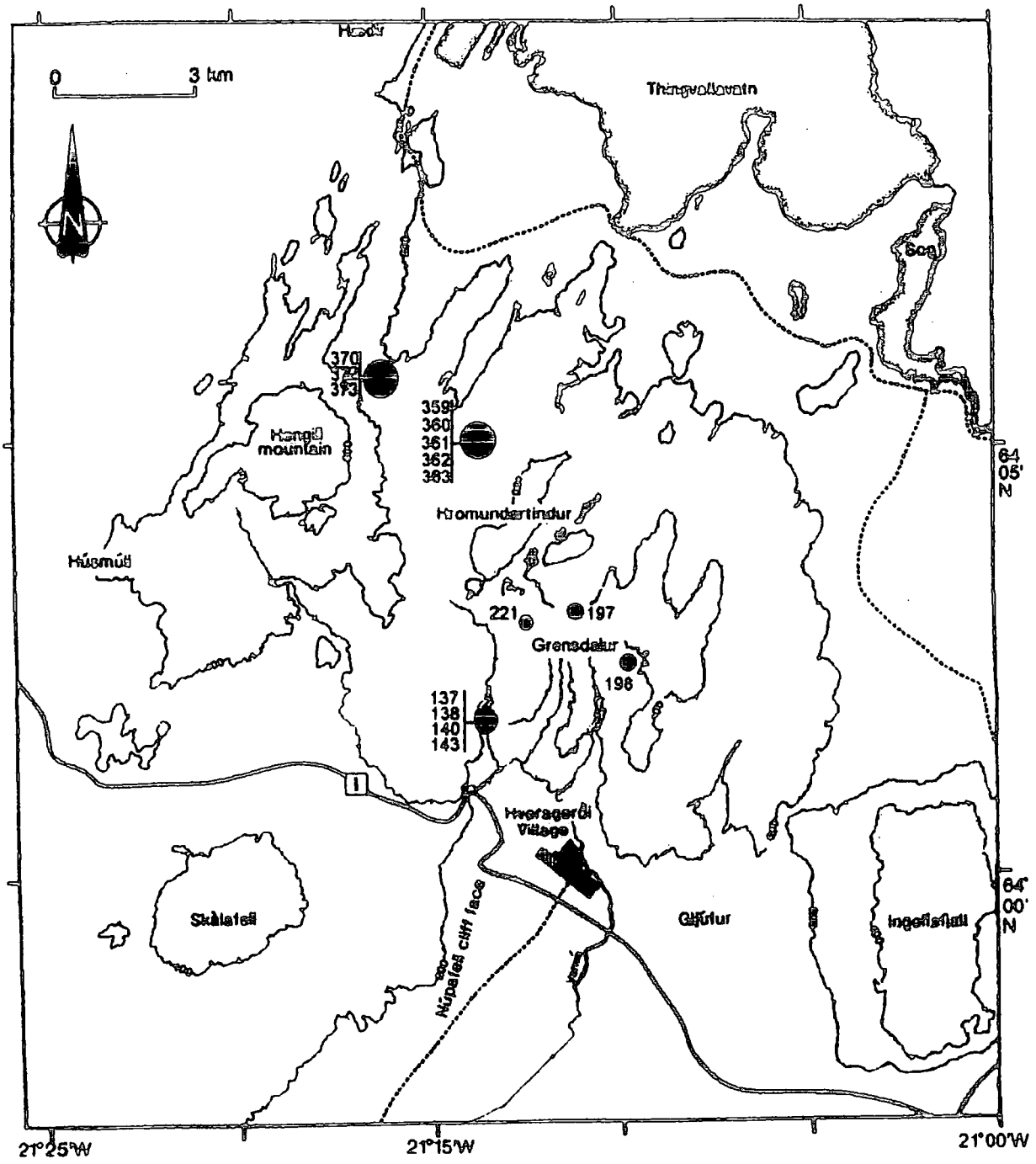

Figure 2.7. Map of the Hengill-Grensdalur area showing the locations where rock samples were collected for density determinations. Numbers indicate sample numbers used in Table 2.1.

Sample #	Porosity	st. dev. of porosity	wet density kg/cu. m	st. dev. of density
137	0.25	0.03	*2,110	*20
138	*0.08	*0.02	2,800	70
140	0.12	0.01	*3,350	*10
143	*0.40	*0.03	2,180	40
197	0.22	0.03	2,570	40
198	0.36	0.06	2,170	50
221	0.28	0.05	2,370	60
359	0.24	0.01	2,510	30
360	0.25	0.02	2,510	70
361	0.33	0.02	2,300	40
362	0.21	0.01	2,550	30
363	0.31	0.02	2,310	30
370	0.15	0.02	2,600	60
372	0.29	0.01	2,470	30
373	0.18	0.01	2,710	20
Av. for whole suite	0.25	0.02	2,465	44

* indicates not used in determination of average

Table 2.1. Porosities, wet densities and standard deviations (1σ) of rock samples from the Hengill-Grensdalur area. The average values for the whole suite are calculated from the blocks studied in the laboratory.

where g_{obs} is the observed gravity, g_t is the theoretical gravity at the observation point, Δg_{fa} is the free air correction, ρ is the Bouguer density, z is the topographic height, Δg_T is the terrain correction, can be rearranged to give:

$$\left(g_{obs} - g_t + \Delta g_{fa}\right) = \left(2\pi Gz - \frac{\Delta g_T}{\rho}\right)\rho + g_B \qquad (2.12)$$

By considering the Bouguer anomaly as a random error having a mean value of zero, the best fit straight line through a plot of $\left(g_{obs} - g_t + \Delta g_{fa}\right)$ versus $\left(2\pi Gz - \frac{\Delta g_T}{\rho}\right)$ will have a gradient of ρ. In this study, the regional gravity trend was removed first. A bulk rock density of 2400 kg m^{-3} was obtained.

On the basis of these studies it was decided to use a Bouguer density of 2450 kg m^{-3}, a value that differs by 6% from the value of 2600 kg m^{-3} used by Thorbergsson et al. (1984).

2.3.4.3 Removal of the Regional

The Bouguer anomaly field computed using a density of 2450 kg m^{-3} is shown in figure 2.8a. A northeast-southwest regional gradient of approximately 0.3-0.4 mGal km^{-1} over the area can be seen, which is part of the ~70 mGal bowl-shaped Bouguer low that covers the whole of Iceland (Thorbergsson et al., 1990). The field was de-trended to remove this regional gradient. Various polynomial surfaces were tried and a quadratic surface was found to minimise the RMS gravity residual and was therefore selected. The final, de-trended Bouguer gravity field for the area is shown in figure 2.8b. The regional exhibits an almost linear character, especially within the area of tomographic coverage (figure 2.8c). The de-trended field for the area studied in the seismic tomography analysis is shown in figure 2.9a.

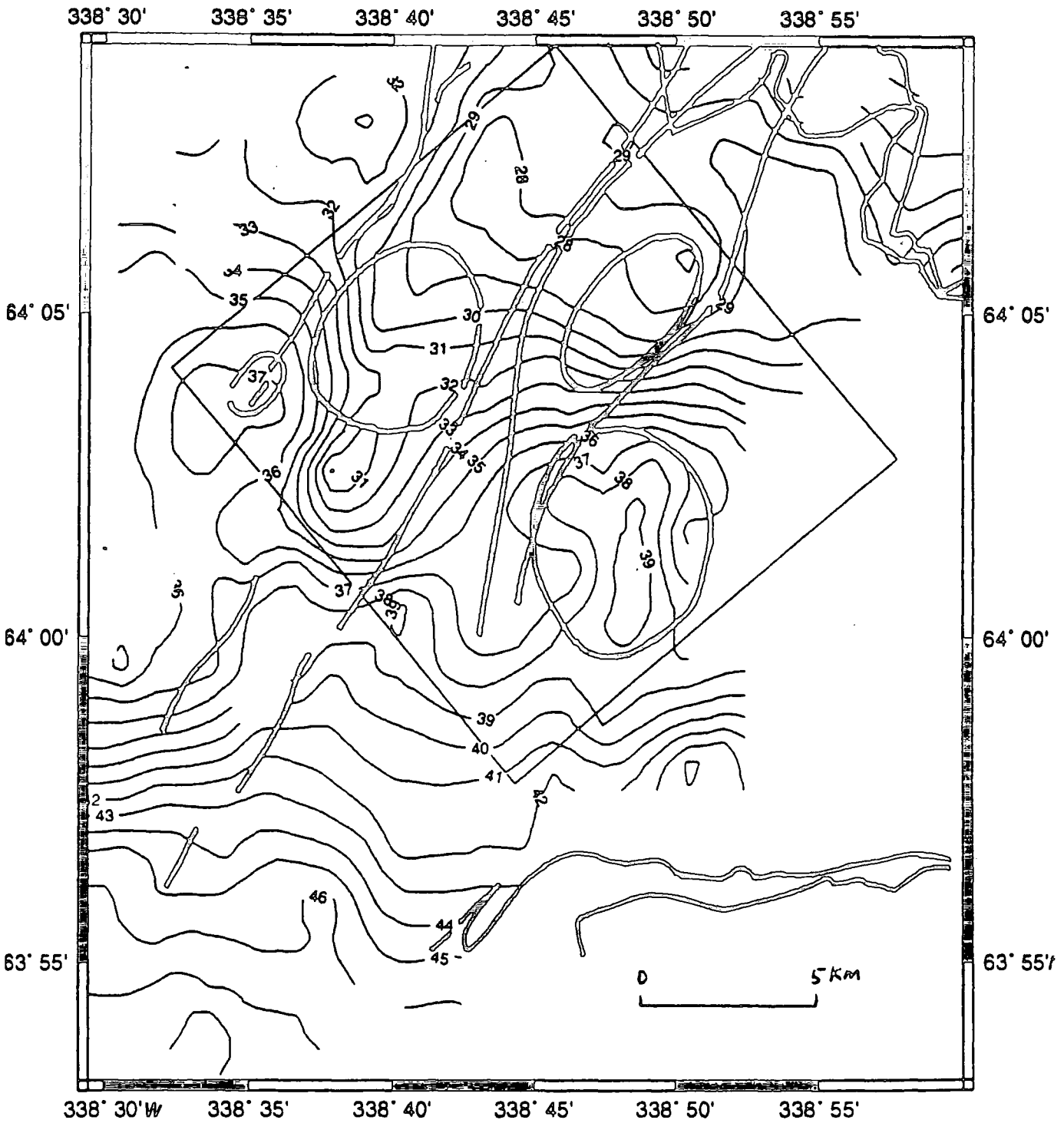

Figure 2.8. (a) Bouguer anomaly map of the Hengill-Grensdalur area, calculated using a Bouguer density of 2450 kg m^{-3}. Box indicates the area studied using local earthquake tomography (Toomey and Foulger, 1989; Foulger and Toomey, 1989). Bold lines schematically indicate the main tectonic features, Lake Thingvallavatn in the north of the area and the River Olfus in the south. Contours are labelled in mGal.

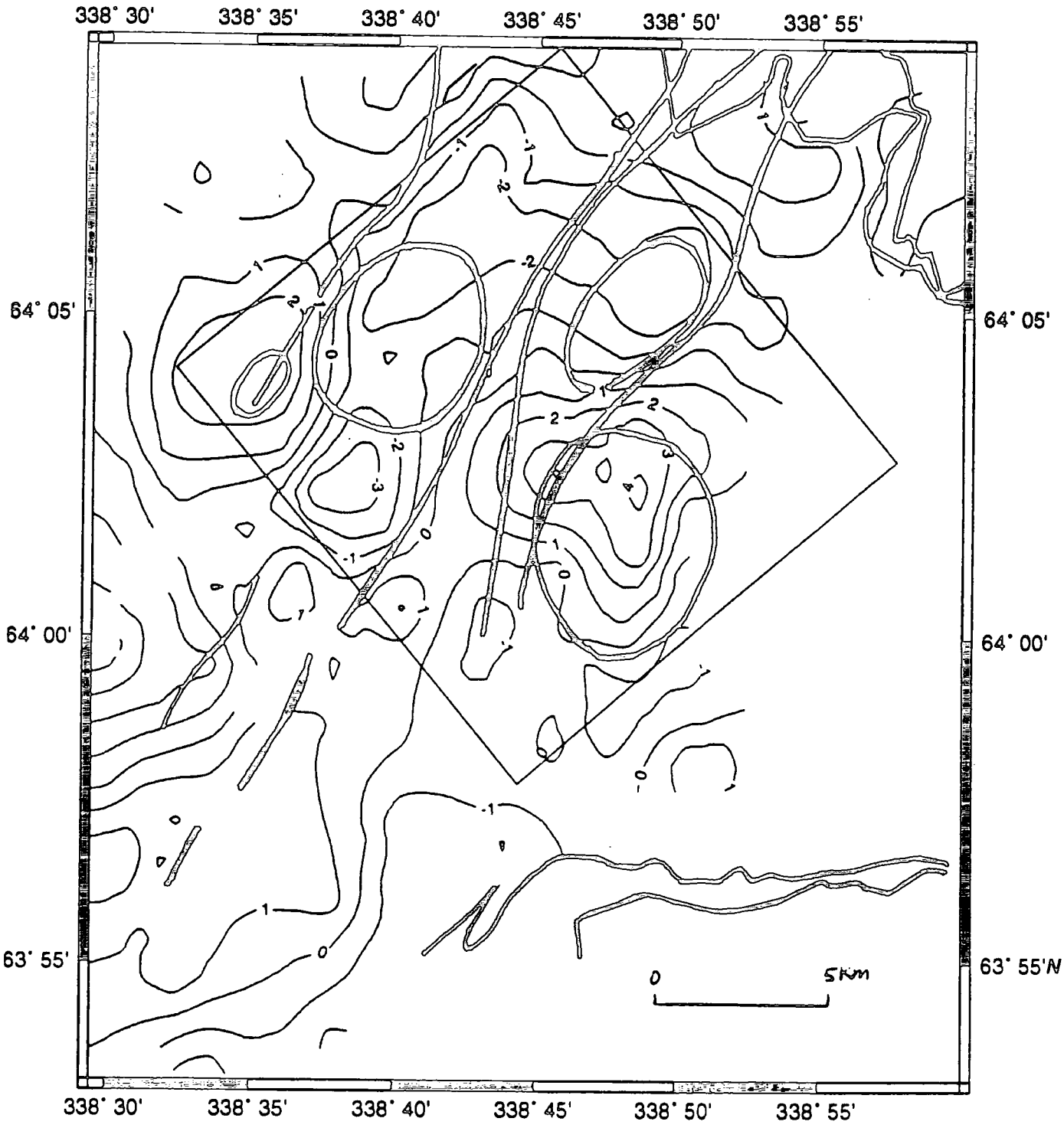

Figure 2.8 (b) Same as (a) except with the regional gravity trend removed.

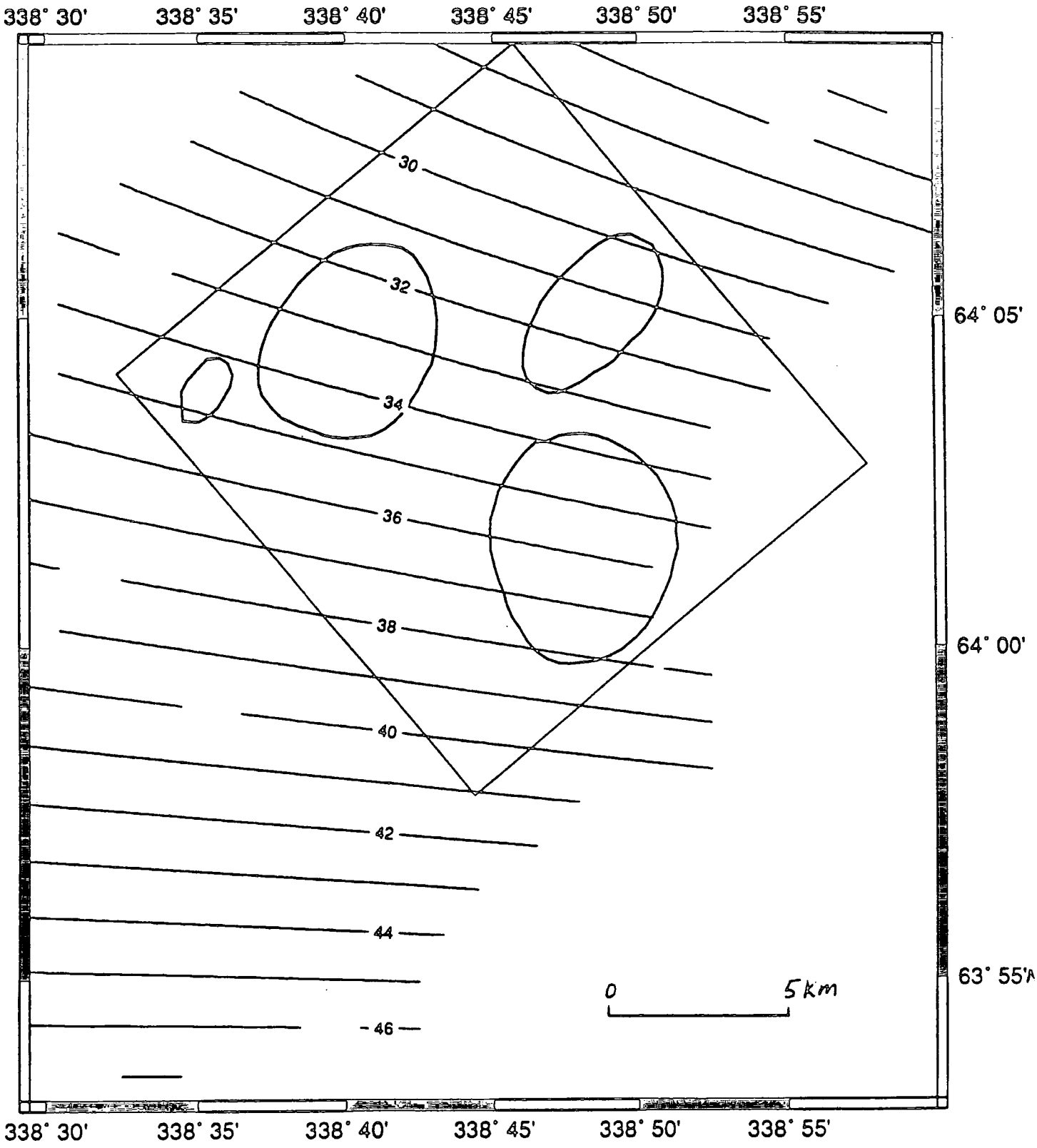

Figure 2.8 (c) The regional removed from (a) to obtain (b). The contour interval is 1 mGal.

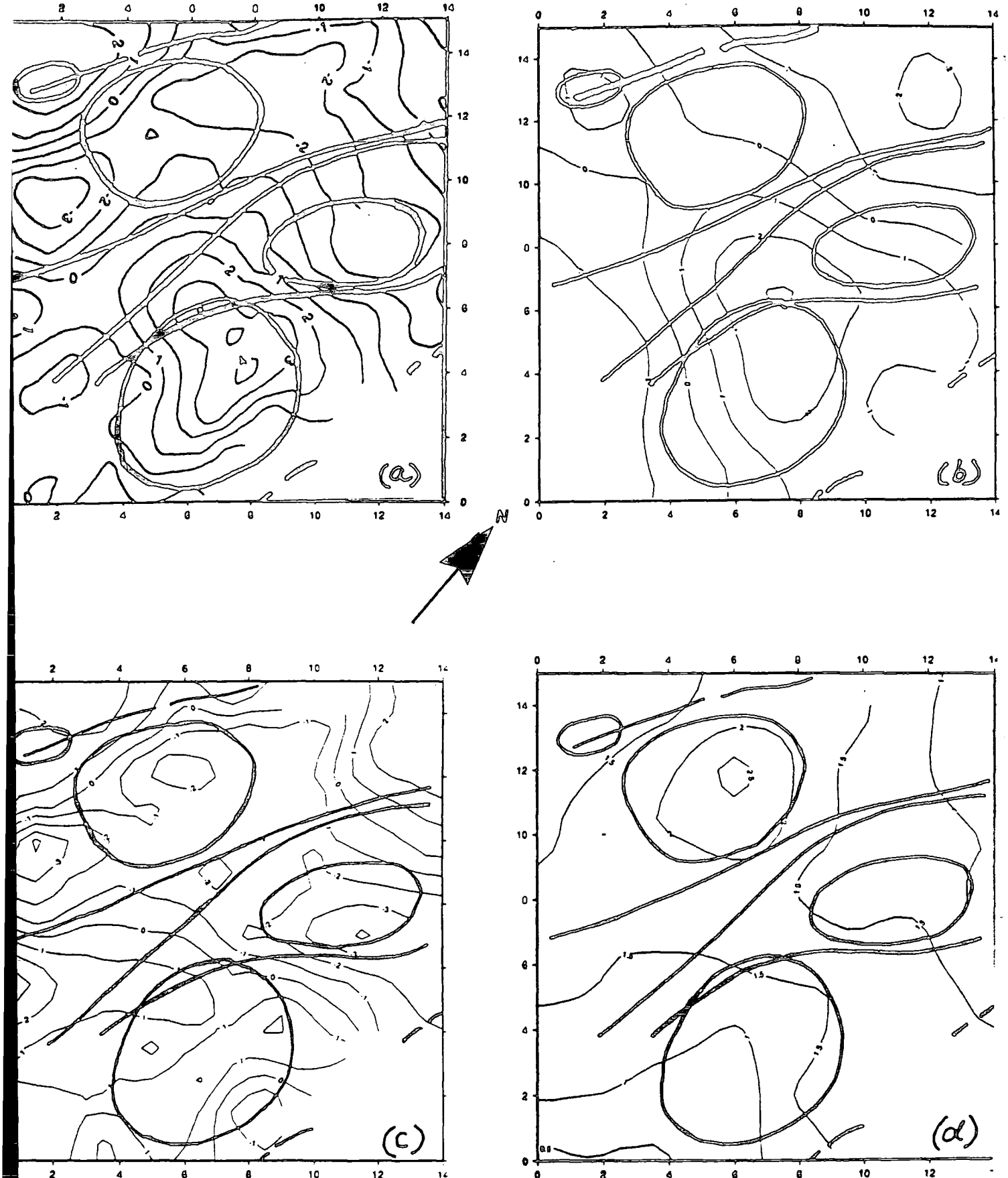

Figure 2.9. Maps of the area studied tomographically. Bold lines schematically indicate the main tectonic features. Contours are labelled in mGal. (a) The de-trended Bouguer anomaly field, (b) the predicted Bouguer anomaly field obtained using the tomographically-derived three-dimensional seismic velocity field, (c) the residual Bouguer anomaly field obtained by subtracting the predicted field (b) from the real field (a), and (d) the 1σ error field.

2.3.5 Field Continuation

2.3.5.1 Introduction

To eliminate some of the shorter wavelength anomalies present in the de-trended Bouguer anomaly, the gravity field was continued onto a horizontal plane one kilometre above sea level.

2.3.5.2 The Continuation Method

The Bouguer anomaly is most commonly used to investigate geological problems on land. However, there is a confusion which arises from the practice of describing the Bouguer anomaly as having been reduced to a common datum, which suggests that the reduced values are those that would be observed if the gravity measurements were carried out on that datum plane. This is not true. To see this, consider three gravity observations made around a hill (figure 2.10): one at the top (A), one at the base (B), and another directly below A but at the same height as B (A'). It can be seen that even when the Bouguer reduction is carried out, and the perturbing effect of the hill is removed, the gravitational effect of O at A is not equivalent to that at A'. Therefore the individual Bouguer anomaly values do not lie in a common plane, but at their respective points of measurement (Ervin, 1977).

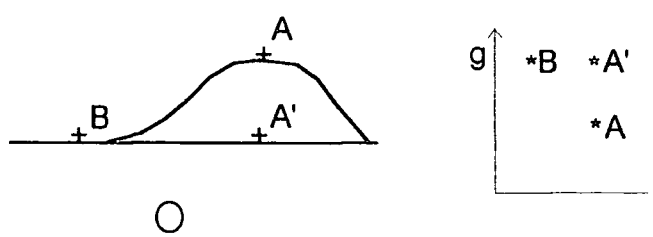

Figure 2.10. +s indicate the positions of three gravity measurements about a hill. A' is directly below A, and A'BO form an isosceles triangle with a perturbing mass O at the apex. The graph on the right schematically indicates Bouguer anomaly values at each point.

To allow ease of interpretation and application of analytical methods to the data it would be desirable to obtain the anomaly at regular grid intervals on a plane. Efforts to achieve this have been made by numerous authors who have developed methods of continuing discretely observed potential field data onto flat regular grids [see Taib (1990), Lahmeyer (1988), Ivan (1986), Hansen and Miyazaki (1984), Bhattacharyya and Chan (1977), Henderson and Cordell (1971), and Dampney (1969)].

All of these authors carried out synthetic testing of their methods to continue irregularly spaced data on an uneven terrain onto a plane, and in some cases applied it to real data. The synthetic tests were of the form:

(1) define an uneven terrain and a continuation plane;
(2) calculate the effect of a perturbing body at stations located on the uneven terrain;
(3) calculate the effect of the perturbing body on the continuation plane;
(4) use a continuation method to continue the values obtained from (2) onto the continuation plane; and
(5) subtract the results of (4) from (3) to give the misfit between the theoretical field and the continued field.

Where quoted, the amplitude of the misfit ranged between 2 and 5% of the amplitude of the continued field.

Taib's (1990) method was applied to reduce unevenly acquired aeromagnetic data to a horizontal plane over Scotland. The aeromagnetic data is expressed as a double Fourier series with the height represented by a Taylor series. By re-ordering an expression, and linking the aeromagnetic data to the height, an inversion method was developed which allowed iterative calculation of the anomaly on a plane. This method still required interpolation of the data to be made at the end of each iteration. Lahmeyer (1988) approached the problem of continuing gravity anomalies onto a horizontal plane by applying least squares collocation techniques which require substantial pre-processing and application of an intelligent iterative convergence to the final solution. Application of this method was made to data from Chile which demonstrated that the continuation method could modify parts of the gravity field by 15 mGal. Ivan (1986) relied upon the solution of surface integrals of the Dirichlet type to continue synthetic gravity data from an irregular surface onto a plane, but suffered the restriction that the best results were obtained when the continuation plane was sufficiently distant from the observation surface. The method of continuation proposed by Henderson and Cordell (1971) relied upon representing each of the gravity observations by a finite Fourier series that were modified to allow upward or downward continuation. As with most Fourier techniques, pre-processing in the form of tapering was required. Hansen and Miyazaki (1984), Bhattacharyya and Chan (1977) and Dampney (1969) all proposed slightly differing versions of the equivalent source technique. The equivalent source method has two stages. The first stage is to find an arbitrary mass distribution which will give rise to the observed gravity anomaly. The second stage is to use this mass distribution to evaluate the anomaly on a different surface.

2.3.5.3 The Equivalent Source Method

The continuation method chosen for this thesis follows the initial theory of Dampney (1969), but departs slightly from the original solution. This equivalent source method was chosen for its economic use of computer memory, ease of application and intuitive appeal.

The vertical component of the gravitational attraction, Δg_{ij}, at a point x_i, y_i, z_i by a mass m_j located at x_j, y_j, z_j is:

$$\Delta g_{ij} = a_{ij} m_j \tag{2.13}$$

where $a_{ij} = \dfrac{G(z_j - z_i)}{\left[(x_j - x_i)^2 + (y_j - y_i)^2 + (z_j - z_i)^2\right]^{3/2}}$, and G is the Universal Constant of Gravitation.

Therefore, for a collection of n masses, the total attraction, g_i, at a point x_i, y_i, z_i is:

$$g_i = a_{i1} m_1 + a_{i2} m_2 + \cdots + a_{in} m_n \tag{2.14}$$

which can be written in matrix form for all stations and perturbing masses as:

$$\mathbf{g} = \mathbb{A}\mathbf{m} \tag{2.15}$$

where $\mathbf{g}$ is a vector containing gravity observations from each station, $\mathbb{A}$ is the matrix representation of the components a_{ij}, and $\mathbf{m}$ is a vector containing the perturbing masses.

Equation 2.15 contains two unknowns, $\mathbb{A}$ and $\mathbf{m}$, illustrating the non-uniqueness of any solution obtained using gravity observations alone. However, if $\mathbb{A}$ is set to represent point masses lying in a plane below the observation surface, then it is possible to calculate the mass distribution in that plane. To solve equation 2.15 Dampney (1969) resorted to a recursive method. With the computers currently available it is possible to obtain the vector $\mathbf{m}$, the equivalent source masses, given the vector $\mathbf{g}$, the gravity observations, and matrix $\mathbb{A}$ using the method of LU decomposition (e.g. Press et al.,

1992). LU decomposition is chosen rather than direct inversion of the matrix, $\mathbb{A}$, because for solving a linear set of equations this method is three times faster than direct methods such as Gauss-Jordan elimination (Press et al., 1992). The planar mass distribution can now be used to 'continue' the Bouguer anomalies observed on an undulating terrain onto a plane.

2.3.5.4 Testing the Equivalent Source Method

The continuation method described above has been encoded in a program (EQSM; see appendix) which was tested on synthetic data to study its accuracy and robustness. The synthetic test followed the numbered method outlined in section 2.3.5.2.

Three cubes of volume 10^6 m^3 were placed at depths of 1.7, 6.5 and 5 km. Densities of $2x10^2$, $13.5x10^2$, and $7x10^2$ kg m^{-3} were assigned. The station positions used were those of an actual gravity network (Hengill-Grensdalur). The topography has a total relief of 800 m and the stations are irregularly positioned but have an average separation of about 1.5 km. The gravitational effect of the three bodies was calculated using the program GRAV3D at each of the stations which formed the observed data. The effect of the three test bodies was also calculated at 0, 1, 2, and 5 km above sea level on 32x32 node grids to be compared with the results of the continuation. During computation of the continued data the depth of the equivalent source layer was varied between 0 and 8 km. To assess the accuracy of the continuation method the theoretical results obtained on the 32x32 grids were compared with the result of continuing the gravity field, using EQSM, from uneven topography onto the 32x32 grid - the continuation plane. The RMS difference between the theoretical field and the continued field (the RMS misfit) was scaled as a percentage of the RMS of the theoretical field to give a percentage misfit. Figure 2.11a shows the percentage misfit on the continuation plane at an altitude of 1 km as a function of the depth to the equivalent source layer. This figure indicates that the continued data are stable when the depth of the equivalent source layer is between 1 and 5 km. Figure 2.11b shows the percentage misfit as a function of the altitude of the continuation plane. This figure displays a minimum in percentage misfit for an altitude of 1 km. In practice, for real data, it is not possible to find the percentage misfit as the actual distribution of mass is unknown. However, a depth for the equivalent sources which will produce accurate results can be found by plotting the RMS of the continued data as a function of the depth to the equivalent sources (figure 2.11c). Figure 2.11c displays a plateau region which correlates closely with the region in figure 2.11a where the data are stable. This test may be used when tackling real datasets.

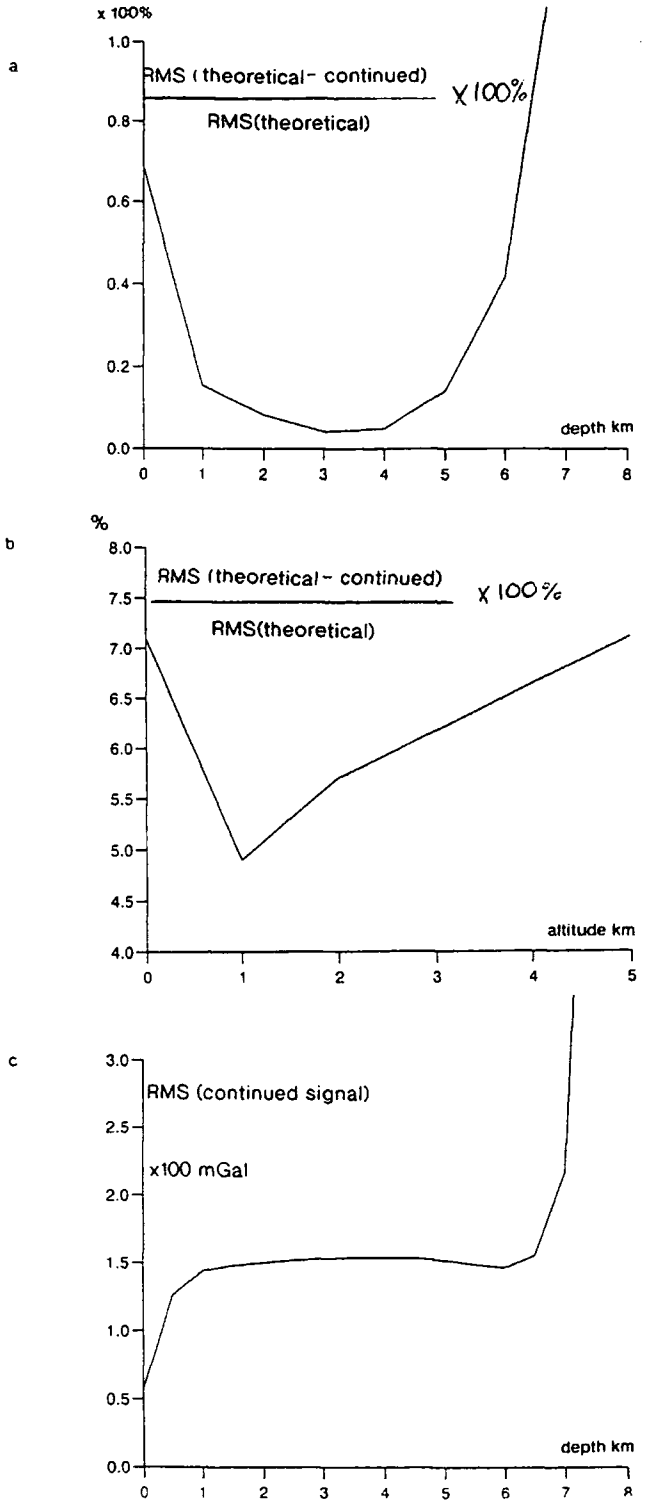

Figure 2.11. Testing of the program EQSM. a) The RMS misfit between the continued gravity field and the theoretical gravity field on a continuation plane at a fixed altitude of 1 km, scaled as the percentage of the RMS of the theoretical field versus depth to the equivalent source array. b)The RMS misfit between the continued gravity field, using an equivalent array at 3 km depth, and the theoretical gravity field scaled as a percentage of the theoretical field versus the altitude of the continuation plane. c) The RMS of the continued field on a continuation plane (1km altitude) versus depth to the equivalent source layer.

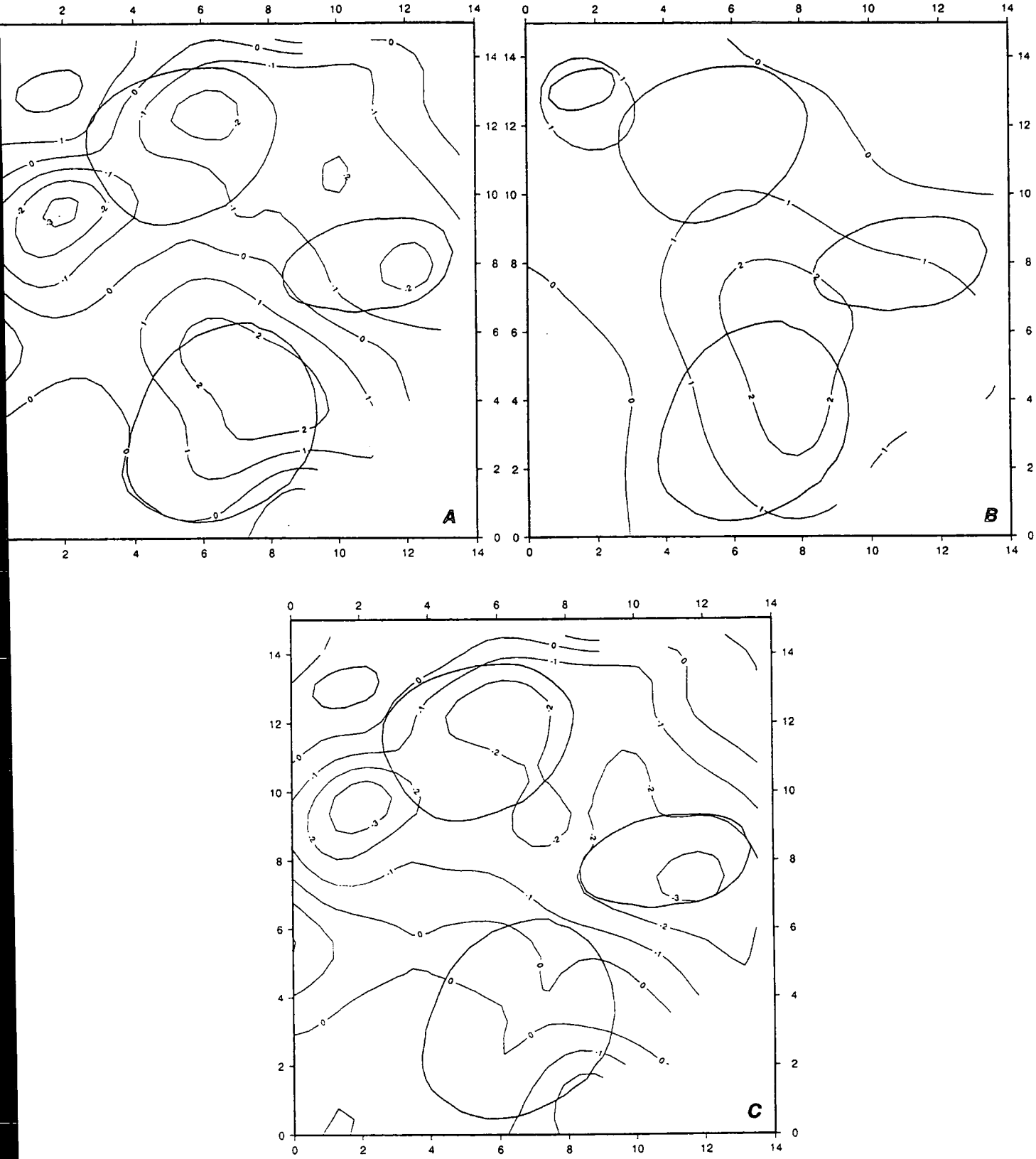

Figure 2.12. a) De-trended Bouguer anomaly continued to an altitude of 1 km using equivalent sources arrayed at 5 km depth. b) Predicted gravity field of the forward modelled three-dimensional velocity structure at 1 km altitude. c) The difference between the real and predicted gravity fields. The contour interval is 1 mGal for all plots.

Continuation is most successful when the equivalent sources are located at a depth between certain upper and lower limits. These upper and lower limits are controlled by ability of the equivalent sources to reproduce the frequency content of the original observations and empirically are found to be ~2 and 5 times the average station spacing. It is also found that continuation is best carried out onto a horizontal plane above the majority of the stations.

Figure 2.12a represents the continued de-trended Bouguer field at 1 km above sea level after using an equivalent source array at a depth of 5 km.

2.3.6 Comparison of the Predicted and Real De-trended Bouguer Anomaly Fields

The de-trended Bouguer anomaly field and the continued de-trended Bouguer anomaly field (figures 2.9a and 2.12a) correlate quite well with the known structure of the area. With reference to figure 2.9a the major features are as follows:

(a) An anomaly of approximately +2 mGal at coordinates (2, 14) correlates well with the Husmuli basalt shield;
(b) A roughly circular anomaly of ~ +4 mGal at (8, 4) is where the extinct Grensdalur volcano is exposed; and
(c) An L-shaped zone of low gravity extends from (2, 9) to (9, 14) and (12, 7). It has an amplitude of up to approximately -3 mGal, and corresponds to the Hengill and Hrómundartindur systems. Mt. Hengill is not associated with a specific gravity low, but instead is associated with a high-gravity saddle in the low-gravity zone.

The forward modelled gravity fields have received a 'dc' shift to give them a mean of zero mGal so that the predicted and actual de-trended Bouguer field can be compared directly. It can be seen that the predicted gravity field bears similarity to the real field. An anomaly of about +1 mGal is seen at (2, 13) over Husmuli and a +3 mGal is centred at about (8, 6), in the Grensdalur area (figure 2.8b). These correlate well with the positive anomalies observed in the real de-trended Bouguer anomaly map (figure 2.9a). A negative anomaly of about -2 mGal is predicted at approximately (12, 13), north of Mt. Hengill. It arises from low velocities at shallow depth and not the small body imaged at 2-4 km depth beneath the northeast flank of Mt. Hengill that is interpreted as a possible volume of partial melt (Foulger and Toomey, 1989). That body is too small and deep to generate a significant gravity anomaly at the surface. Low values in the real de-

trended Bouguer anomaly field correlate with the predicted low north of Mt. Hengill. Upward continuation of the de-trended gravity field produced a smoother map which contains anomalies of similar amplitude to those predicted at 1 km. This is a good indication that the correct velocity-density relationship has been used.

The predicted de-trended Bouguer anomaly field was subtracted from the real field and the residual field is illustrated in Figure 2.9c. The residual field contains fewer and smaller anomalies than the real field. The RMS de-trended Bouguer anomaly for the real field is 2.05 mGal compared with a normalised RMS anomaly of 1.81 mGal for the residual field. figure 2.9c indicates the pattern and amplitudes of relative residuals in the area. A significant trough in the residual Bouguer anomalies runs from about (0, 9) to (14, 7). This zone corresponds to the southern parts of the Hengill and Hrómundartindur systems. The flanking areas correspond to the Grensdalur and Husmuli areas. The largest relative residuals, which reach -4 mGal, occur south of Mt. Hengill, and beneath Mt. Hrómundartindur at (12, 7).

2.3.7 Assessment of Errors

The uncertainties were assessed in the study before proceeding to the interpretation stage in order to determine which residual anomalies were statistically significant.

Errors arose from five sources:

1. The values of gravity determined for the stations in the area;
2. The Bouguer density used;
3. The tomographic velocity model;
4. The velocity-density relationship; and
5. Bodies outside the study volume.

Errors in the values of gravity determined for the area arose from uncertainties in the station heights and meter readings. Thorbergsson et al. (1984) estimated the errors to be up to about 0.5 mGal.

A Bouguer density of 2450 kg m^{-3} was used here. The value was chosen to be consistent with the measurements of rock sample densities and application of Parasnis' method. In addition to the uncertainty in the average density determined, a large variation in the density of the material above sea level is expected within the area. For example, the near-surface rocks in the Grensdalur area contain a large percentage of

relatively high density intrusive rocks, whereas Mt. Hengill itself is a mainly relatively low-density hyaloclastite formation (Saemundsson, 1967; Walker, 1992). The tomographic results reflect this near surface heterogeneity, indicating variations of up to 20% in the seismic velocities at sea level (Toomey and Foulger, 1989). The possibility of a laterally varying surface rock density must be taken into account when interpreting the residual Bouguer anomaly field derived from a single density reduction. This is because residual anomalies of small amplitude may result from this effect and not be due to deeper structure. The investigations in this chapter yielded average density results that varied by a few percent, indicating the variation in surface rock density throughout the area and the accuracy to which it may be determined.

Errors in the tomographic seismic velocity model are difficult to assess quantitatively. Volumes that are well sampled with rays are well constrained, and this applies to most of the interior of the volume down to a depth of about 4 km (Toomey and Foulger, 1989). Peripheral volumes are in general poorly sampled, including the near-surface layer. Good sampling of this layer was restricted to volumes immediately beneath the seismic stations. The spatial resolution of the method is limited by the wavelength of the seismic waves, which was a few hundred metres.

The gradient of the seismic velocity-density relationship is the critical factor when making the conversion from velocity to density. The gradients determined by Christensen and Wilkins (1982) and Christensen and Salisbury (1975) in their studies of Icelandic and offshore rocks differ by roughly 10%, and this is assumed to be the uncertainty inherent in this part of the analysis.

Variations in density in the material outside the study volume will generate gravity anomalies inside the study area. There is no way of assessing the magnitude of these effects, if they exist. They would, however, be greatest in peripheral parts of the area.

The residual Bouguer anomaly field results from a linear combination of the gravity values, the Bouguer reduction operation and the forward modelled tomography. The errors associated with each operation combine as:

$$E_{final} = (E_{grav}^2 + E_{Boug}^2 + E_{fwdmod}^2)^{1/2} \qquad (2.16)$$

where E_{final} is the total error, E_{grav} is the error resulting from uncertainties in the observed gravity value, E_{Boug} is the error resulting from uncertainties in the Bouguer

density used and E_{fwdmod} is the error resulting from uncertainties in the forward model (assuming that all the errors are uncorrelated).

The effects of errors arising from inaccuracy in the tomographic velocity model and the velocity-density relationship were estimated by perturbing the forward model, i.e. by changing the velocity of each cell and the gradient of the velocity-density relationship by amounts thought to be realistic. The velocities in each cell were changed by 0.1 km s^{-1} and the gradient of the velocity-density relationship was changed by 10%. The perturbations were made to be additive, and the difference between the perturbed and the original forward models was taken to be an estimate of the error from these two sources. The error in the gravity values was set to be the maximum value estimated for any station in the area by Thorbergsson et al. (1984), 0.5 mGal, and the error in the Bouguer density used was assumed to be 100 kg m^{-3}, from the spread of the various estimates available. The total estimated error field is shown in figure 2.9d. It has an RMS of 1.48 mGal. When compared with figure 2.9c, this analysis suggests that the residual zone of low gravity relative to the flanking areas is significant where the residual difference is greater than about -3 mGal.

2.3.8 Interpretation of the Hengill-Grensdalur Results

Comparison of the residual anomaly field shown in figure 2.9c with the error field of figure 2.9d shows that a mismatch exists between the structure obtained from local earthquake tomography and that required to satisfy the gravity field. This mismatch forms a continuous northeast trending zone of relatively low gravity compared with neighbouring areas. It includes portions of the Hengill and Hrómundartindur volcanic systems. The residual field to the south of Mt. Hengill and in the Mt. Hrómundartindur area display the greatest relative residual anomaly that are each constrained by several stations. The zone connecting these two areas is only marginally significant but coherent. The whole zone corresponds roughly to the geothermal area if the Grensdalur central volcano region is ignored (figure 2.13). Relatively low densities in this zone are to be expected from lithological contrast with the neighbouring intrusive sites of Grensdalur and Husmuli and from geothermal phenomena, e.g. the presence of steam or geothermal alteration of the rocks to form clay minerals or other low density materials.

The residual anomaly field is systematic, and so it must arise from an unmodelled systematic effect. Possibilities are: (i) deviations of surface rock density within the area from the Bouguer density; (ii) the velocity-density relationship varied within the area; and (iii) infidelity in the velocity structure.

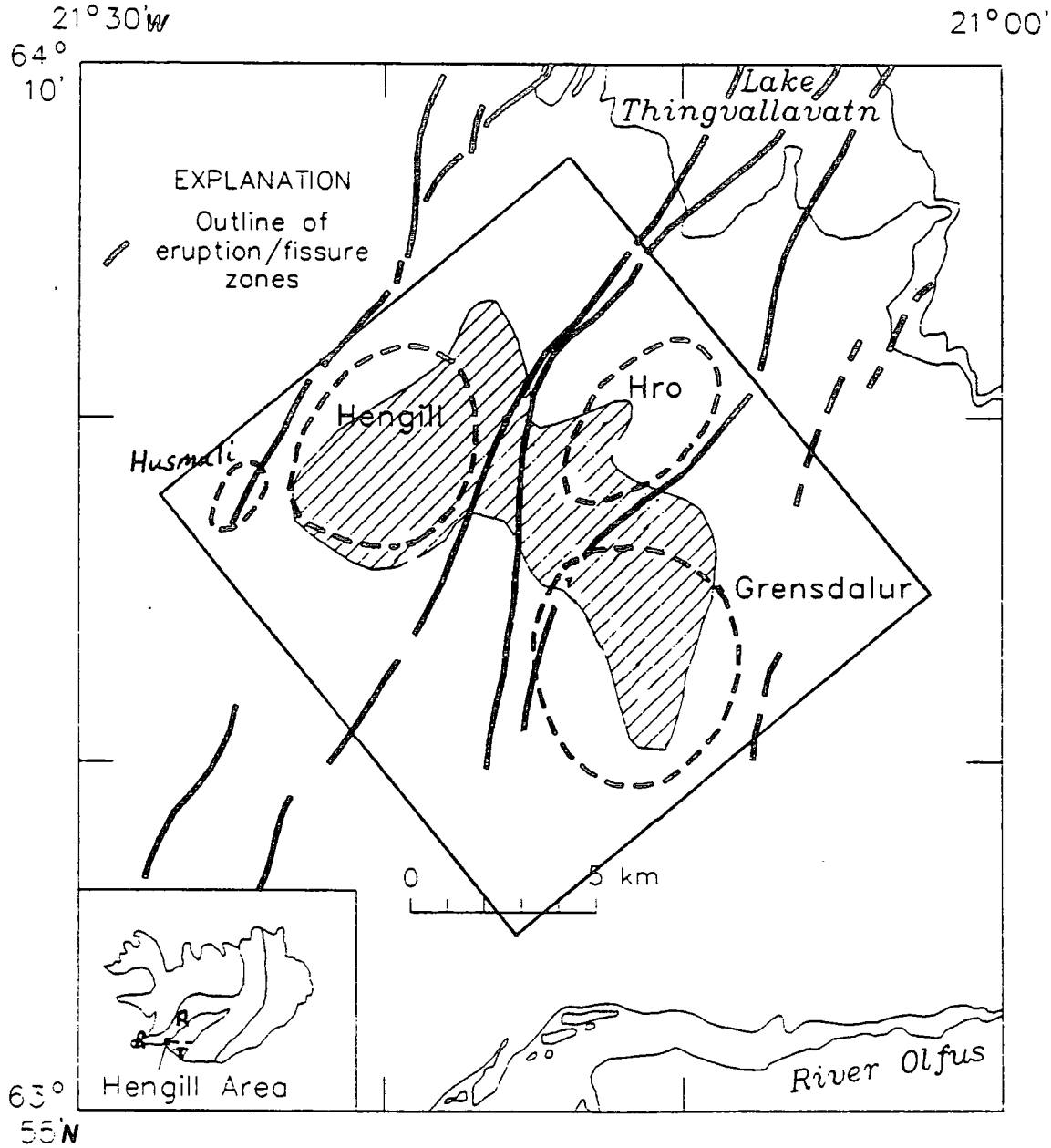

Figure. 2.13 Schematic tectonic map of the Hengill-Grensdalur spreading segment. The high-temperature geothermal area is shaded. Inset shows location of the area within Iceland.

A systematically low Bouguer density in the geothermal area seems unlikely since the residual field does not correlate with topography and unrealistic Bouguer densities of up to several hundred kg m^{-3} less than the value used would be required. A systematic difference in the appropriate velocity-density relationship for rocks in the geothermal area is a possible partial explanation. A gradient for this relationship for the rocks within the geothermal area approximately 15% lower than the one used would account for the residual field everywhere except for small areas south of Hengill and in the neighbourhood of Mt. Hrómundartindur. Those areas of large amplitude residuals are of small extent and could be partially explained by low Bouguer densities in those areas.

Infidelity in the velocity structure in the form of a systematic underestimate of the amplitude and extent of low-velocity volumes is also a possible explanation. Seismic tomography may be poorer at imaging low-velocity volumes than high-velocity volumes because rays follow minimum time-paths avoiding low-velocity material.

The maximum depth rules (Bott and Smith, 1958) were applied to the residual field to estimate the maximum depth to the low-density material within the area which does not correspond to the velocity structure. Five profiles across the zone of low gravity were averaged (figure 2.14). A "maximum depth" to the body of 2.5-3.0 km is suggested, depending on whether profile 3, which crosses the least reliable part of the residual gravity field (figure 2.8d), is included. Inclusion of profile 3 broadens the average profile and gives the deeper estimate of maximum depth.

The residual gravity field has been modelled as a low-density graben-shaped structure that outcrops at the surface (figure 2.15). Because of the ambiguity problem, a set of different shaped structures with different density contrasts will fit the anomaly equally well. Three models with density contrasts of -50, -75 and -100 kg m^{-3} and extending to about 3.0, 1.5 and 1.0 km are illustrated in figures 2.15a,b and c.

If the residual results from the rocks within the geothermal area having a different velocity-density relationship from those in other areas, the gravity residual would result from contributions throughout the depth range to which the surface gravity field is sensitive, which is a few kilometres. If the residual results from limited ability of the tomography to detect low-velocity bodies, then the body probably represents either a large volume whose velocity is slightly systematically overestimated, or a volume with a large low-velocity anomaly that is smaller than the limit of resolution of the tomography. A body a few hundred metres in width would require a density contrast of up to 1000

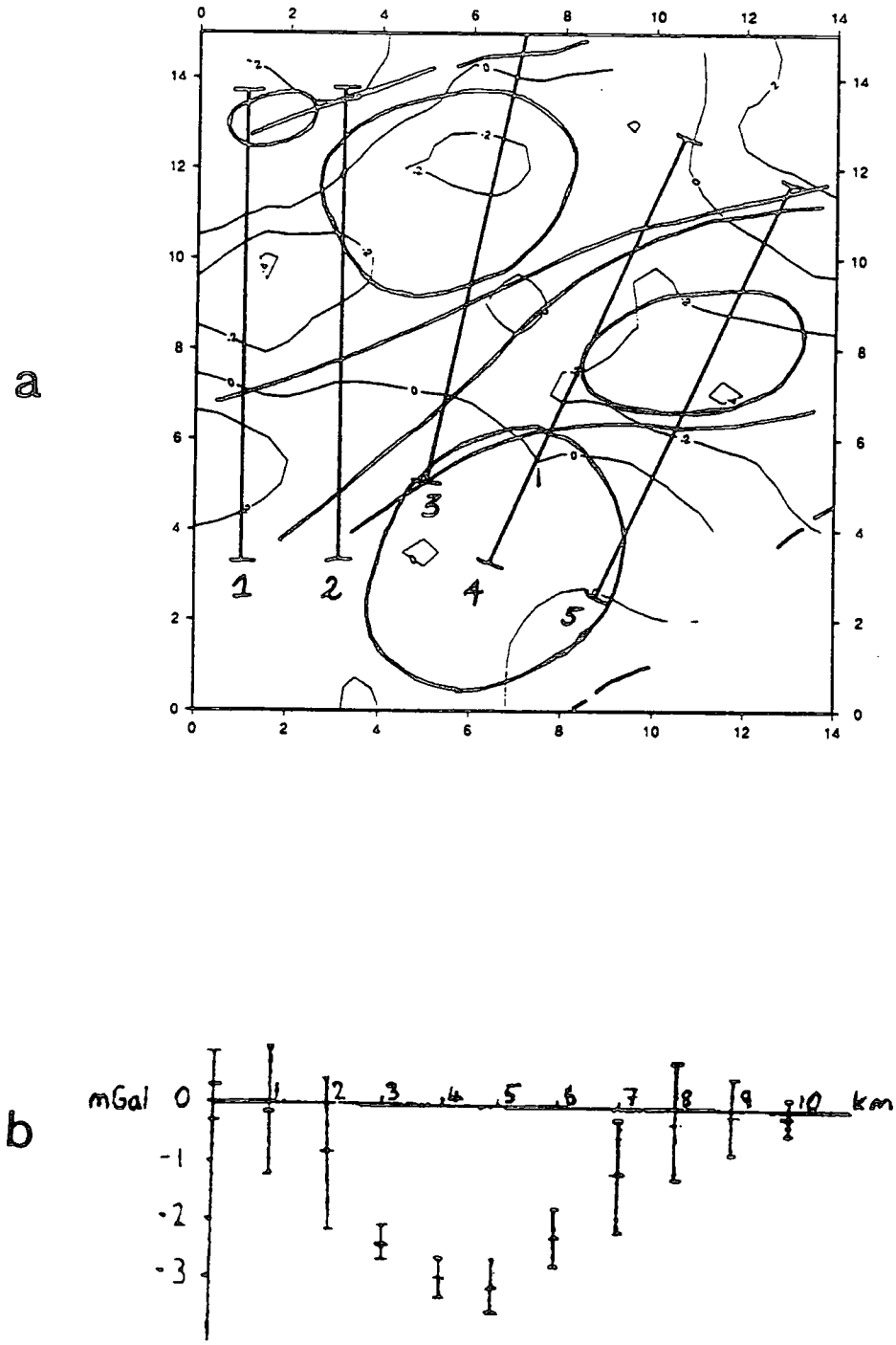

Figure 2.14.(a) Map of the study area showing the locations of profiles made crossing the residual low-gravity zone. (b) Combined gravity cross-section across the residual low-gravity zone obtained by averaging the five profiles shown in (a). 1σ error bars are shown.

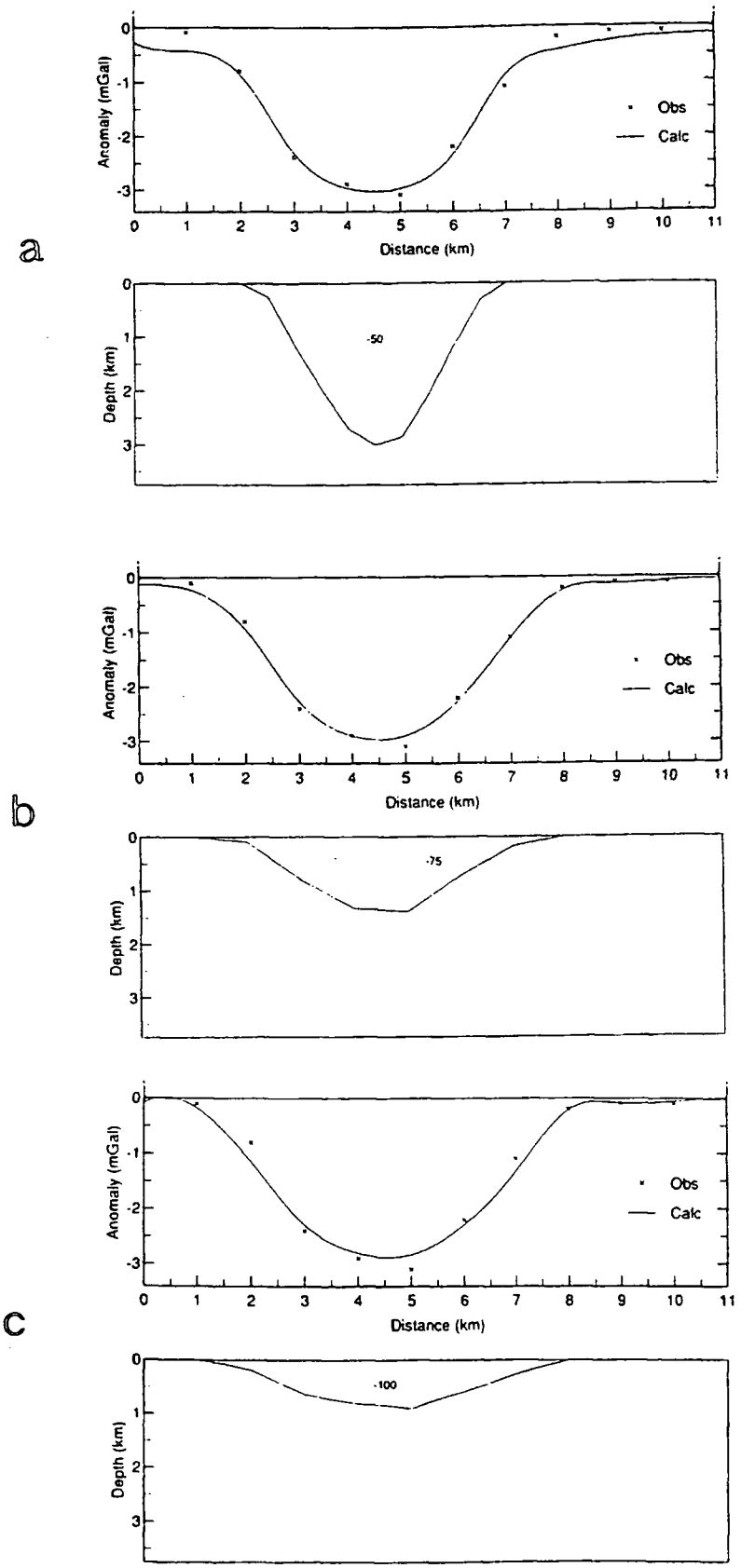

Figure 2.15. Candidate interpretations of the residual low-gravity zone in the geothermal area. Graben-shaped structures with various density contrasts and extending to various depths are modelled. (a) Density contrast -50 kg m^{-3}, extending to depth of approximately 3.0 km, (b) density contrast -75 kg m^{-3}, extending to depth of approximately 1.5 km, (c) density contrast -100 kg m^{-3}, extending to depth of approximately 1.0 km.

kg m^{-3} to generate the residual Bouguer anomaly calculated, which seems unlikely. A large body with small density contrast is therefore a more likely explanation and the model presented in figure 2.15a is reasonable. A density contrast of about 50 kg m^{-3}, or 2%, corresponds to a velocity decrease of about 0.2 km s^{-1}, or 4%. A systematic underestimate of low velocities of this small magnitude might reasonably be expected to occur.

A low-velocity body was detected by the tomography beneath the north flank of Mt. Hengill. If the tomographic analysis systematically underdetected low-velocity bodies, then this volume, interpreted as possibly representing a partial melt body with a volume of about 5 km^3 (Foulger and Toomey, 1989), may be larger than was previously thought. However, addition of gravity data to the body of data concerning the structure of the Hengill-Grensdalur area provides no evidence for an extensive low density body possibly associated with melt or an extensive steam reservoir underlying Mt. Hengill at shallow depth. This is consistent with the hypothesis that Mt. Hengill is not a central volcano underlain by a long-lived magma chamber in the shallow crust.

The low-density zone correlates well with the geothermal area outside the Grensdalur area. Likely explanations for the relatively low densities are lithological contrasts and the presence of steam and clay minerals as a result of geothermal processes. Another possibility is that heat expansion could give rise to the zone of anomalous density. All these effects probably contribute.

2.4 The Krafla Spreading Segment

2.4.1 Introduction

The Krafla volcanic system is marked by a 10 km wide, 100 km long fissure swarm extending south from the Tjörnes Fracture Zone. The central volcano at Krafla has a low relief caldera measuring 10 km in the east-west direction and 8 km in the north-south direction. Björnsson et al. (1977) suggest that the caldera was formed along with sub-parallel dykes and eruptive fissures and that the presence of outward dipping lavas and breccias imply the existence of an earlier shield volcano of at least 20 km in diameter.

The Krafla spreading segment undergoes an eruptive cycle of approximately 500 years, 35 eruptions being documented in post-glacial times, giving rise to basaltic, intermediate and acidic material which has been mostly erupted either within or just south of the caldera. Sub-glacial eruptions also resulted in the creation of hyaloclastite ridges running

north and south from within the caldera of which mount Krafla is part, standing 700 m above sea level. Most of the caldera lies at greater than 500 m above sea level. The ring fault itself is externally bordered by rhyolitic extrusives.

From 1975 to 1985 the Krafla fissure swarm experienced a spreading episode. Twenty rifting events occurred resulting in the flow of lava originating from a mid-crustal magma chamber and associated seismicity. In the intervening months between lava outflows, the caldera inflated due to the influx of material into the magma chamber from below. The first event in 1975, at Leirhnjúkur, gave rise to a horizontal spreading of 70 cm in the Krafla area and 1 - 1.5 m in the Axarfjördur area (Björnsson et al., 1977; Sigurdsson, 1980) (figures 2.16, 1.3). It was also revealed in 1976 that a total subsidence of ~ 2.1 m had occurred in the caldera relative to a point to the north of Lake Mývatn since 1974 (Björnsson et al., 1977). Trygvasson (1978) carried out tiltmeter readings within and around the caldera and noted that uplift was greatest at the centre of the caldera. The observed ground motion was consistent with that predicted to be produced by an inflating spherical body at a depth of 3 km (the magma chamber). In the ten years of active rifting, which occurred when the caldera was elevated above its previous maximum altitude, general widening and subsidence of the active fissure swarm associated with compression and uplift of the flanks was reported (Björnsson et al., 1977). These events underwent a cyclic pattern of inflation and deflation events. Of the twenty rifting events, only nine were accompanied by basaltic fissure eruptions.

At the end of the rifting episode a total of up to 8 m of extension had occurred within the centre 2-3 km of the rift zone to the north of the caldera (Trygvasson, 1984; Wendt et al., 1985). However, compression at the flanks resulted in only ~ 1 m of net extension over a 90 km wide zone (Möller and Ritter, 1980).

The model describing this type of episodic rifting is simple (Björnsson, 1985). Over time, divergence of the plate results in an increase in the strain at the rift zone. The crust gradually thins and subsides until the stress is released in the form of rifting. At this point new fissures may form and dyke injection may occur (Einarsson and Bransdottir, 1980) until the pressure inside the magma chamber is reduced to a sufficient level at which it is unable to support such activity (Björnsson et al., 1979).

Drilling within the area has been carried out primarily to assess the exploitable properties of the geothermal system and has shown that the first 300-400 m below the surface is dominated by hyaloclastite and basalt. Below this layer hydrothermally altered rock becomes dominant with the maximum steam discharge occurring in the borehole at

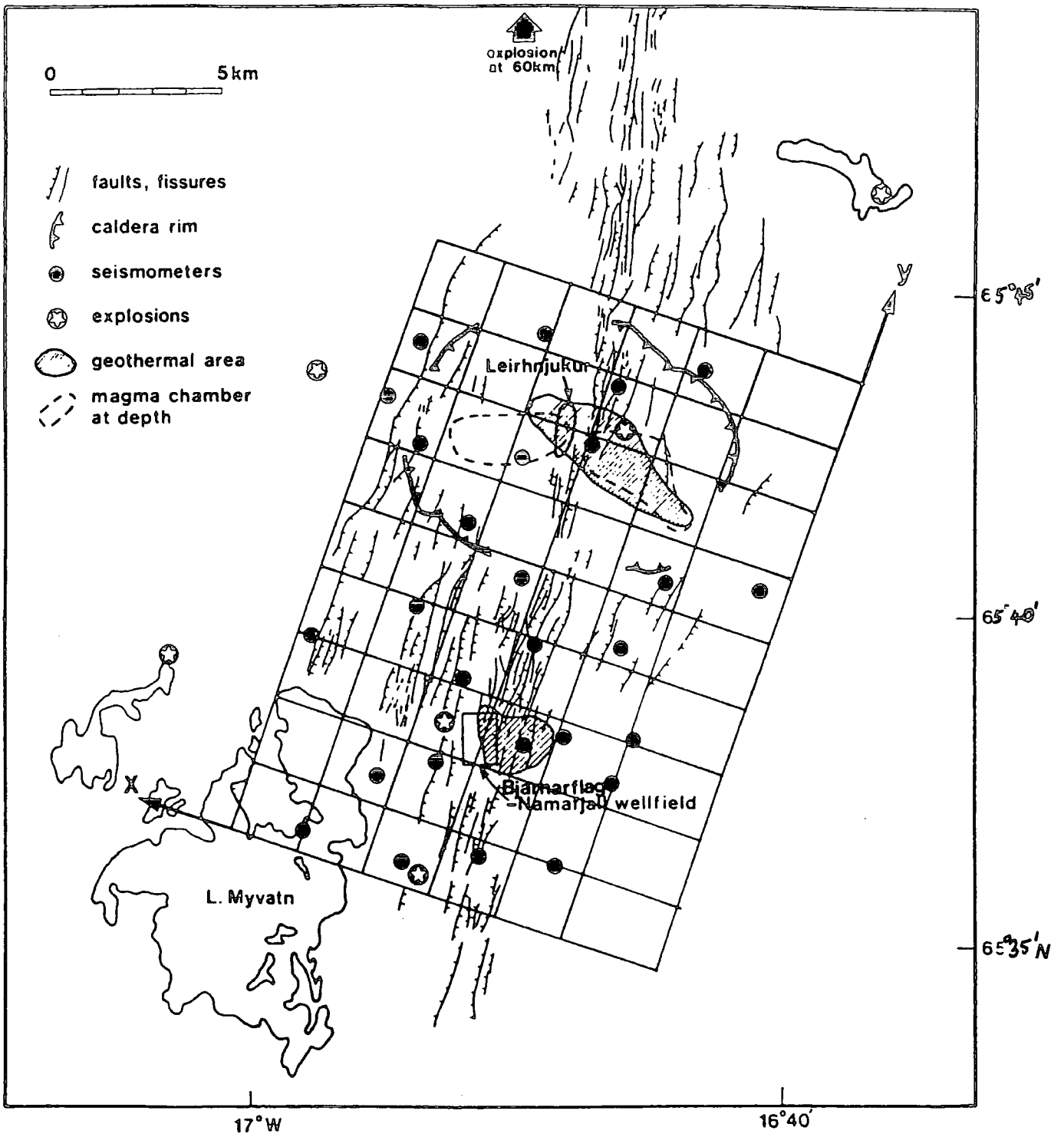

Figure 2.16. Area covered by the Krafla local earthquake tomography experiment, the positioning of the 27 seismometers (black circles) and the coordinate system used for the Krafla study (the gridded box) are shown. The diagram also gives relevant place names. After Arnott (1990).

depths of ~660 m and ~1150 m (Armannsson et al., 1987). Below 1300 m intrusives become dominant. Drilling results indicate that the hyaloclastite bottoms out at about 1 km below the surface, suggesting the throw of the caldera ring fault. Cross-sections created from the drill records also show zones of hydrothermal alteration indicating updoming at the Sudurhlidar and Hvitholar geothermal fields. The reservoir temperature at Sudurhlidar is ~300°C while that at Hvitholar is 250°C.

Geophysical investigations provide further evidence of the position and existence of Krafla's geothermal resources. Resistivity sounding results at 600 m below the surface (Stefansson, 1981) characterise the reservoir with a large resistivity low towards the eastern part of the caldera. The energy for this reservoir is ultimately drawn from the partial melt below. The magnetotelluric method used by Beblo et al. (1983) in a profile across the NVZ suggests that partial melt (inferred from the low resistivity) could be within 8 km of the surface at the axis, deepening to ~ 20 km at 40 km from the axis. The additional presence of a low resistivity zone at 5 km below the surface is thought to indicate the location of a magma chamber. These observations are also supported by the seismic evidence of Zverev et al (1980) observing an homogenous body below ~8 km from the surface, and Einarsson (1978) who infers a partial melt zone between 3-7 km beneath the caldera on the basis of an observed S-wave shadow. Further evidence for the position and existence of a mid-crustal magma chamber at Krafla is provided by geodetic observations of ground deformation. Ewart et al. (1991) suggest that geodetic observations indicate a magma reservoir lies in 2-5 km depth range.

Ward and Björnsson (1971) report hypocentre locations between 0-4 km depth. Arnott (1990) gives solutions within the depth range of 1-3 km and locates earthquakes clustered beneath Leirhnjúkur. This is believed to be a frozen magma conduit that originally fed the 1727-29 fissure eruption at Leirhnjúkur during the 'Mývatn Fires' and the site of the 1975 eruption (Björnsson et al., 1977). The source of the seismicity is thought to be due to water causing rapid cooling of the magma conduit inducing fracturing as is proposed to be the mechanism at Hengill-Grensdalur (Foulger and Long, 1984; Foulger 1988b). As at Hengill-Grensdalur, the detailed crustal structure of the Krafla area was revealed with a tomographic study (Arnott, 1990).

2.4.2 The Krafla Tomography Study

2.4.2.1 The Tomographic Inversion

The volume in which the Krafla tomographic inversion took place was 13 x 18 km in horizontal extent and 4 km deep (figure 2.16). Six controlled explosions and 105 of the best located and distributed earthquakes, gave rise to 1771 P-wave arrivals recorded on a 27 station network array optimally designed for events at 4 km depth, which may have been too sparse for the relatively shallow earthquake incidence (Arnott, 1990). These were used in the inversion method of Thurber (1983). The inversion was carried out in a very similar manner to that of the Hengill-Grensdalur dataset. The final RMS residual arrival time was 0.027 s reduced from 0.066 s.

2.4.2.2 Tomographic Results from the Krafla Area

Figure 2.17 depicts the well constrained linearly interpolated final velocity solution for the Krafla area. Most noticeable about the structure are the high velocity bodies that exist around the north, west, east of the caldera ring fault and the low velocity bodies, one within the caldera and the other corresponding to the Námafjall geothermal zone to the south of the caldera.

There are three high velocity bodies, mentioned above, which are encompassed by the gravity coverage. The western one is located at approximately (11,14,1) and exhibits a velocity increase relative to the surrounding crust of up to 2 km s^{-1}, which is a velocity perturbation of the order of 45 %. The anomaly to the east (3,10,0) deepens towards the north until it reaches a maximum value of ~ 2 km s^{-1} at (3,16,2). The anomaly in the north (6,16,1) has a velocity contrast of ~ 1.5 km s^{-1} and at a depth of ~ 2 km merges with the eastern anomaly. These zones of high velocity located near the caldera ring fault are interpreted as probably being high density gabbros which may have been formed by intrusion at the time of caldera collapse (Arnott, 1990).

One of the low velocity bodies observed, extending from 0 to 2 km depth from (9,16,2) to (5,13,2) exhibits a velocity contrast of up to -1 km s^{-1}. The other zone of low velocity extends from (7,4,0) to (7,7,0) continuing towards the west (12,0,1) at a depth of 1 km. The whole area to the south of the caldera generally exhibits a negative velocity contrast. These regions of low velocity are interpreted as volumes of hydrothermal alteration resulting from flux of geothermal fluids causing dissolution and removal of minerals or alteration of the caldera infill to clay facies.

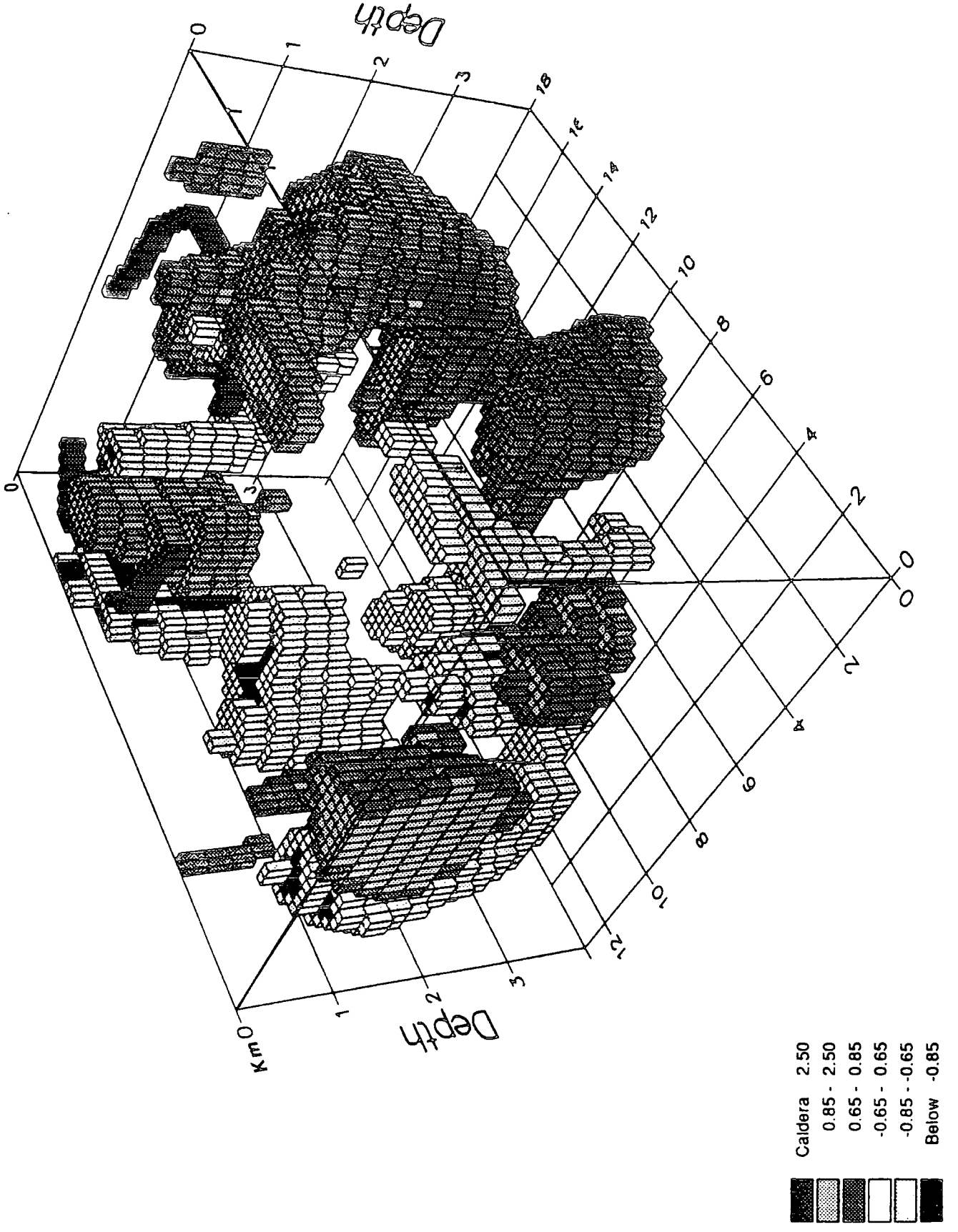

Figure 2.17. Three dimensional image of the final tomographic velocity model for the Krafla region (Arnott, 1990) and used for forward modelling. View is from the south. Each cube has a volume of 0.25 km^3. All velocity volumes shown have a DWS > 50 (see text). Light coloured blocks represent volumes with low velocity, and dark coloured blocks represent high velocity volumes. From Arnott (1990).

2.4.3 Forward Modelling of the Tomographic Solution

The Krafla velocity solution has been forward modelled to obtain the predicted gravity field for the Krafla area in the same way as for the Hengill-Grensdalur dataset. This was to allow comparison with the actual gravity data. The final velocity model was linearly interpolated into 250 m cubes. The velocity contrast within each cube was transformed to a density contrast and the combined gravitational effect of the assembly of masses was computed at both the gravity station positions and onto a horizontal plane, 1 km above sea level.

Large velocity contrasts in the final velocity structure were found in regions in the solution known to be not well constrained. In view of this it was decided that the badly constrained velocity contrasts would be omitted from the forward modelling procedure so as not to falsely bias the outcome of the processing. A threshold value for the DWS was chosen by both Toomey and Foulger (1989) and Arnott (1990). Using this value the tomography solution was sorted so that only well constrained (DWS > 50) volumes were used in the forward model.

2.4.4 The Krafla Gravity Dataset

2.4.4.1 Acquisition

A gravity survey of the Krafla area was carried out between 1976 and 1978 (Karlsdöttir et al., 1978). A LaCoste and Romberg gravimeter was used and the measured gravity values were tied to the Iceland-wide gravity net (Pálmason et al., 1973). Karlsdöttir et al. (1978) carried out height, Bouguer, terrain, and tidal corrections for all of the surveyed points. They estimate an error of 0.5 mGal for the readings based on possible errors associated with the original readings and the subsequent reductions. The corrections were supplied with the gravity data so that it would be possible to use other Bouguer reduction densities if necessary. Figure 2.18 indicates the coverage for 393 stations in the survey. Unfortunately the survey was originally designed to monitor local sub-surface effects caused by geothermal exploitation. Hence, the stations were clustered around the geothermal areas.

No interpretation was made by Karlsdöttir et al. (1978), but a brief description was given of the results. They found that the gravity map showed increasing gravity from south to

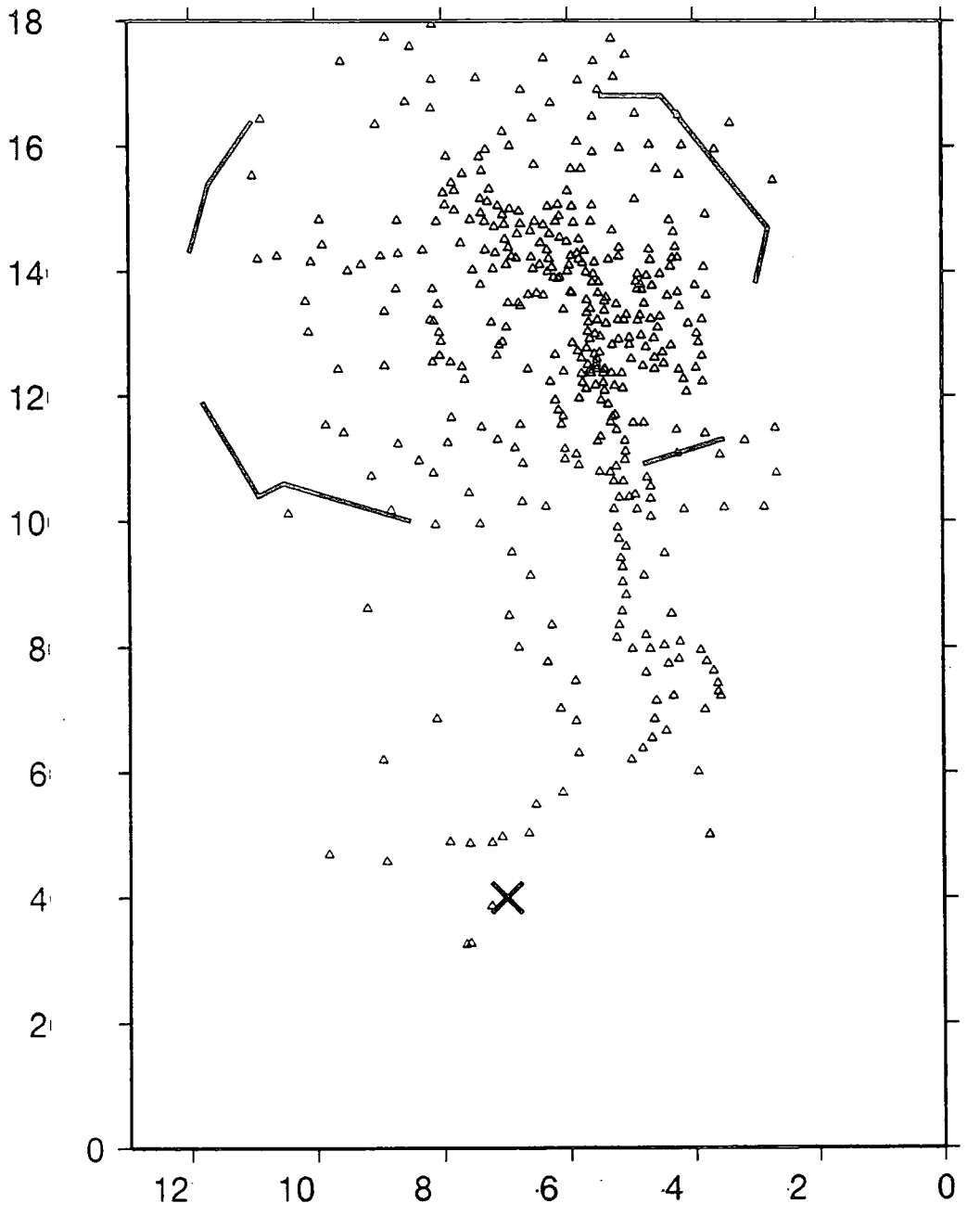

Figure 2.18. Gravity station coverage (triangles) for the Krafla area. The black lines represent the caldera ring fault, and the cross is the position of the Námafjall well field.

north and that more irregularities exist within the caldera than to the south (although this could be a function of the amount of station coverage).

The original gravity map of the area was computed using the 1930 International Gravity Formula. In this chapter the Geodetic Reference System 1980 (Torge, 1989) has been used to compute the theoretical gravity.

2.4.4.2 Bouguer Reduction Density

The surface geology in the Krafla region comprises of rhyolitic extrusives, hyaloclastite, pumice, tuffs, hydothermally altered caldera infill and lava under various stages of erosion. Rock samples were not available for analysis to obtain their bulk wet density. However, previously Schleusener et al. (1976) used 2300 kg m^{-3} for the Krafla area as did Karlsdöttir et al. (1978). Using Parasnis' method on the data available yielded an estimate for the appropriate reduction density of 2300 kg m^{-3} . Therefore 2300 ($\pm$ 100) kg m^{-3} was chosen as the reduction density. Figure 2.19a shows the Bouguer gravity field for a reduction density of 2300 kg m^{-3} .

2.4.4.3 Removal of the Regional

The station coverage of the area was not extensive enough to make a regional gradient very obvious, but Schleusener et al. (1976) report a regional gradient of 0.5 mGal km^{-1} for a region which includes the Krafla area. A gradient of this magnitude can also be seen in the relevant portion of Einarsson's (1954) Bouguer anomaly map for Iceland. A gradient of 0.5 mGal km^{-1} was therefore removed and a 'dc' shift of the data was performed to give the dataset a mean of zero. Figure 2.19b shows the de-trended gravity field.

2.4.4.2 Continuation of the Gravity Field

The gravity field was also upward continued onto a horizontal plane 1 km above sea level using equivalent sources arrayed at sea level (figure 2.20a). Because of the extremely close spacing of gravity stations the gravity readings were resampled onto a 200 x 200 m grid to prevent instabilities in the continuation procedure. It was felt that as the results would be output onto a grid of nodal spacing ~ 400 x 560 m that re-sampling would not have too strong an effect on the result of the continuation.

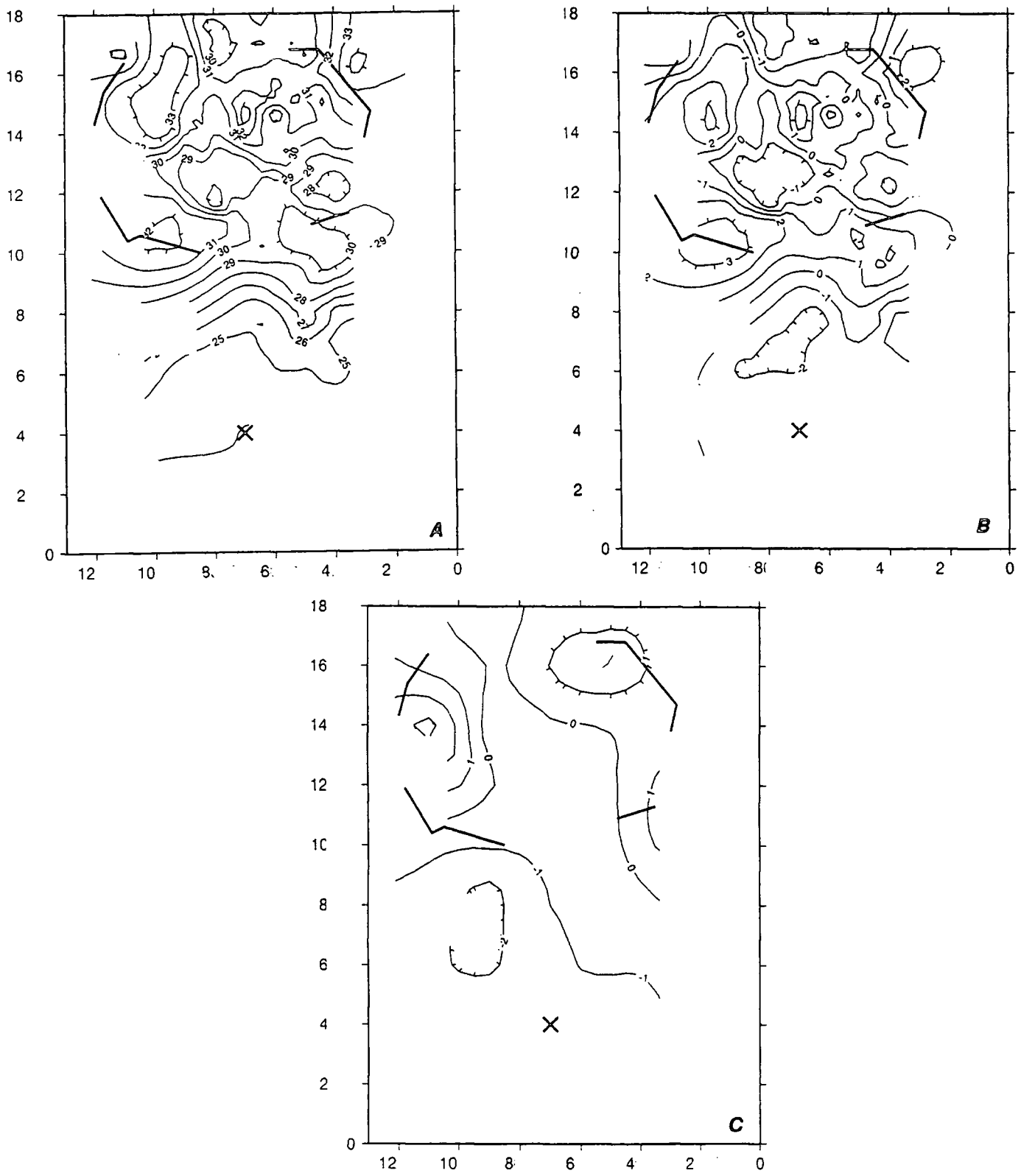

Figure 2.19. (a) The Bouguer gravity field for the Krafla region reduced with a density of 2300 kg m^{-3}. The contour interval is 1 mGal. (b) The de-trended Bouguer gravity field after the removal of a regional gradient of 0.5 mGal km^{-1} to the north. The mean of the data is 0 mGal. The contour interval is 1 mGal. (c) The forward modelled 'predicted' gravity field from the tomography results. This is the gravitational effect computed for the actual gravity station positions. The contour interval is 1 mGal. The field has a mean of 0 mGal.

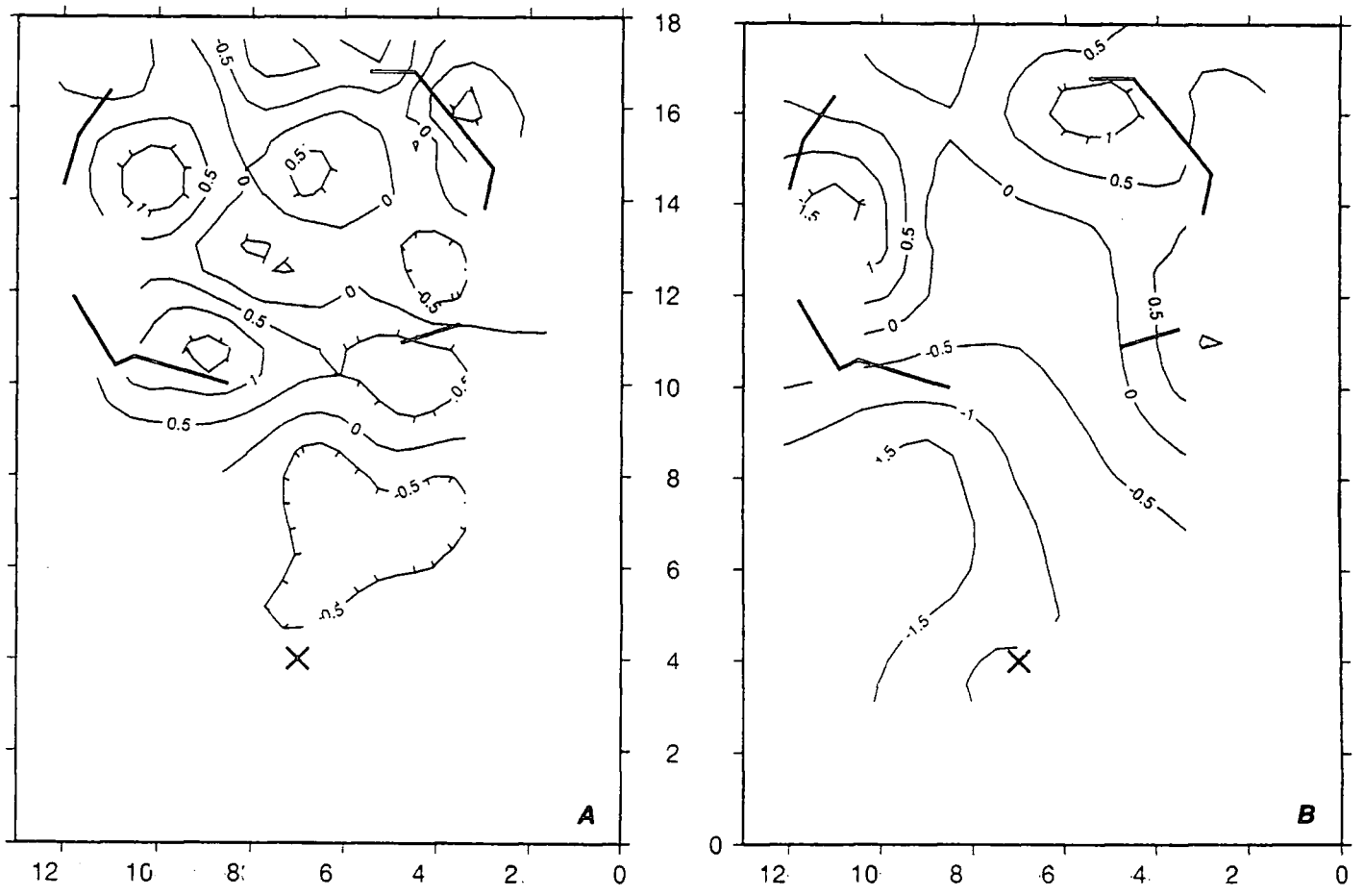

Figure 2.20. (a) The upward continued gravity field from figure 2.19b. The continuation plane is at an altitude of 1 km above sea level. The contour interval is 0.5 mGal. (b) The forward modelled 'predicted' gravity field from the tomography results. This is the gravitational field on a horizontal plane 1 km above sea level. The contour interval is 0.5 mGal. The field has a mean of 0 mGal.

2.4.5 Comparison of the Predicted and Real Bouguer Anomaly Fields

The real gravity field corresponds quite well with the known geological structure of the area. With reference to figure 2.19b, the main features are:

(a) High gravity zones approximately mark the edge of the caldera at (10,15), (3,16), (10,10), having a magnitude of 3-4 mGal relative to the centre of the caldera;
(b) Another relative gravity high can be seen just to the north of the centre of the caldera (7,15), the site of the 1727 and 1975 fissure eruptions at Leirhnjúkur, which is now marked by a cinder cone.

The forward modelled gravity fields have received a 'dc' shift to give them a mean of zero mGal so that the predicted fields could be directly compared with the actual de-trended Bouguer field.

The gravity field depicted in figure 2.19c is that of the forward modelled tomography solution onto the actual gravity station positions. The amplitude of the field is ~5 mGal. This synthetic gravity map displays a relative gravity high just inside the north west caldera fault (11,14). Another relative gravity high also associated with the caldera is to the northeast (5,16). A slight hint of high gravity is seen at around (3,11), but is outside of the gravity coverage. To the south of the caldera the gravity field exhibits a negative character reaching a low at (9,7). The forward modelled field at an altitude of 1 km (figure 2.20b) displays essentially the same behaviour as figure 2.19c, but the amplitude of the field is reduced to about 3 mGal.

The de-trended Bouguer gravity field (figure 2.19b) contains more irregularities and steeper horizontal gravity gradients than the synthetic gravity map (figure 2.19c). This implies a strong influence on the gravity field derived from shallow bodies. Upward continuation of the gravity data produced a smoother map (figure 2.20a). This map was compared with the predicted gravity map for the forward model onto a plane at 1 km above sea level. It was noted that the difference in amplitudes of the two fields (2 mGal for the gravity map versus 3 mGal for the predicted field) could be a result of an incorrect velocity-density conversion factor being used.

The gravity anomaly at (10,15) correlates well with the tomography forward model. The relative gravity high in the predicted map at (5,16) falls between two relative highs in the gravity map situated nearly 4 km apart (7,15; 3,16). The relative low to the south of the

caldera seems to be partially explained by the forward model, but displaced towards the west. The forward modelled predicted gravity map shows no high gravity at the southwestern caldera fault (9,11), or in the centre of the caldera (7,15). Overall the forward model only correlates to the extent of there being relatively higher gravity in the caldera than to the south, but otherwise does not seem to reproduce all of the relative gravity highs observed in the actual gravity map.

Because of the lack of good spatial correlation between the predicted and the actual gravity field it was decided that, instead of interpreting the residual (which was found to have a greater RMS than the original de-trended Bouguer anomaly), an inversion of the gravity data would be performed to allow comparison of a gravity derived sub-surface structure with the tomography model. The continued gravity map was used for the inversion.

2.4.6 Assessment of Errors

All of the gravity stations were above ~300 m in the Krafla area which means that errors due to an incorrect Bouguer reduction density, assumed to be within the range of $\pm$ 100 kg m^{-3}, will only be caused by topographic variations above this height. Combining this error with the errors encountered in the gravity data yields an RMS error of 1.1 mGal. Thus the positive anomalies around the caldera and at Leirhnjúkur can all be considered significant. It was felt unnecessary to produce an error map including the forward modelling errors as a residual gravity field has not been used.

2.4.7 Gravity Inversion

2.4.7.1 Density Distribution Within a Horizontal Slab

The inversion method used calculates the density distribution required throughout a horizontal slab of a given thickness and depth below the observation plane to reproduce the observe gravity field. This has previously been described by Granser (1985). The density distribution, $\rho(x,y)$, is obtained by applying this expression:

$$\rho(x,y) = \frac{1}{2\pi G} F^{-1}\left[\frac{|\mathbf{k}|\exp\left(+|\mathbf{k}|h_1\right)}{1-\exp\left(-|\mathbf{k}|t\right)} F[g(x,y)]\right] \qquad (2.17)$$

where $t = (h_1 - h_2)$, the thickness of the slab, $\mathbf{k}$ is the wave vector, h_1 is the depth to the top of the slab, h_2 is the depth to the bottom of the slab and $g(x,y)$ are the gravity observations. F and F^{-1} are the forward and inverse two-dimensional Fourier transforms.

Equation 2.17 has been encoded by the author in a program (INVRHO, see appendix). Figure 2.21a represents the gravity field on a grid measuring 128 x 128 km produced by an extensive block at 10 km depth and of x, y, z dimensions 400, 400, 2 km, respectively with a density contrast of 500 kg m^{-3}. The grid was positioned such that only half of it overlapped the block. By using this gravity field as the input data for INVRHO, the density distribution for a slab 2 km thick at a depth of 10 km is illustrated in figure 2.21b. The density contrast is around 500 kg m^{-3} and the extends approximately over half of the test area in agreement with the properties of the initial perturbing body.

2.4.7.2 The Inversion Parameters

To perform the inversion three parameters must be selected: (i) a depth to the top of the slab; (ii) a thickness for the slab; and (iii) a cut-off wavelength so that high wavenumber instabilities inherent in downward continuation are avoided.

The depth to the top of the slab can be estimated from the power spectrum of the gravity field.

Power Spectrum Maximal Depth Estimates.
Granser et al. (1989) utilised an equation which can be written as:

$$\ln E(\mathbf{k}) = [A_0(\mathbf{k})]^2 - 2|\mathbf{k}|z_0 \qquad (2.18)$$

where $E(\mathbf{k})$ is the power spectrum, z_0 is the maximal source depth, $A_0(\mathbf{k})$ is the spectrum continued to the maximal source depth and $\mathbf{k}$ is the wavenumber vector. To estimate the depth of the sources, the natural logarithm of the power spectrum is plotted against wavenumber to which a straight line may be fitted with a gradient of $-2z_0$. A gradient of zero would have resulted if the data had already been downward continued to a depth of z_0 and the spectrum of the downward continued field would have then been white. If two distinct source depths had been present then the plot would have been split into two line segments.

It was decided to synthetically test this method so as to understand what the depth estimate means. Three test cases have been presented below.

The vertical component of gravitational acceleration due to sets of bodies below a measurement plane were calculated. The plane measured 128 x 128 with a nodal spacing of 1 km. All the bodies used were parallelepipeds that had a horizontal cross-sectional area of 2 x 2 km^2 and a density of 500 kg m^{-3}. Three cases considered were:

(a) Three bodies, all with their top surface at 5 km depth. The lengths of the bodies were 10 km, 4 km , and 2 km;
(b) Exactly as for (a) except that all of the top surfaces were placed at 2 km depth; and
(c) Exactly as for (b) apart from the addition of two shallower bodies. They both were placed with their top surfaces 1 km below the surface and had a length of 2 km.

The power spectra for the three cases were calculated and plotted versus wavenumber (figure 2.22). The estimates of depths obtained are given in the table 2.2 below.

Case.	Depth range of bodies.	Depth estimate, z_o
a	5 - 15 km	5.2 km
b	2 - 12 km	2.6 km
c	1 - 12 km	1.8 km

Table 2.2. Tabulation of the results from testing source depth determination from a plot of ln E(k) (power spectrum) versus wavenumber.

The results show that the depth estimate derived from the power spectrum method is a slight over-estimate of the actual depth to the top of the sources.

Parameters

A plot of the continued gravity field's power spectrum yielded a depth estimate of 700 m below the datum plane (figure 2.23). The top of the slab was set at 300 m above sea level. The thickness of the slab was set at 1 km to correspond to the assumed thickness of the caldera infill obtained from drilling. The short wavelength cut-off was set at 1.5 km which is where the power spectrum of the gravity field goes white (figure 2.23).

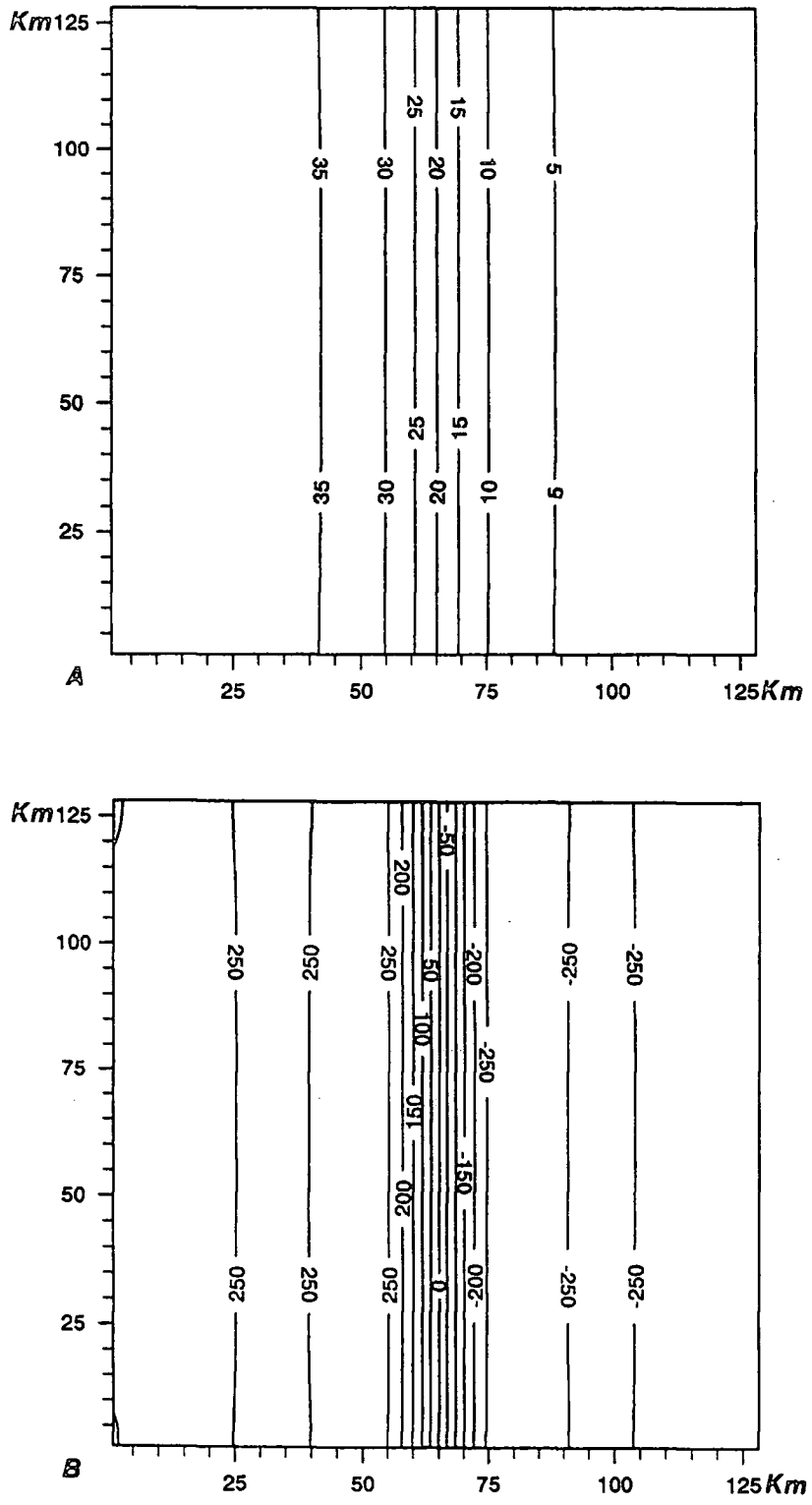

Figure 2.21. Testing the inversion program, INVRHO. (a) Gravity field generated by a 'semi-infinite' slab 2km thick, at a depth of 12 km and density 500 kg m^{-3}. The contours are at 5 mGal intervals. (b) The result of the inversion using (a) as the input. The contour interval is 50 kg m^{-3}.

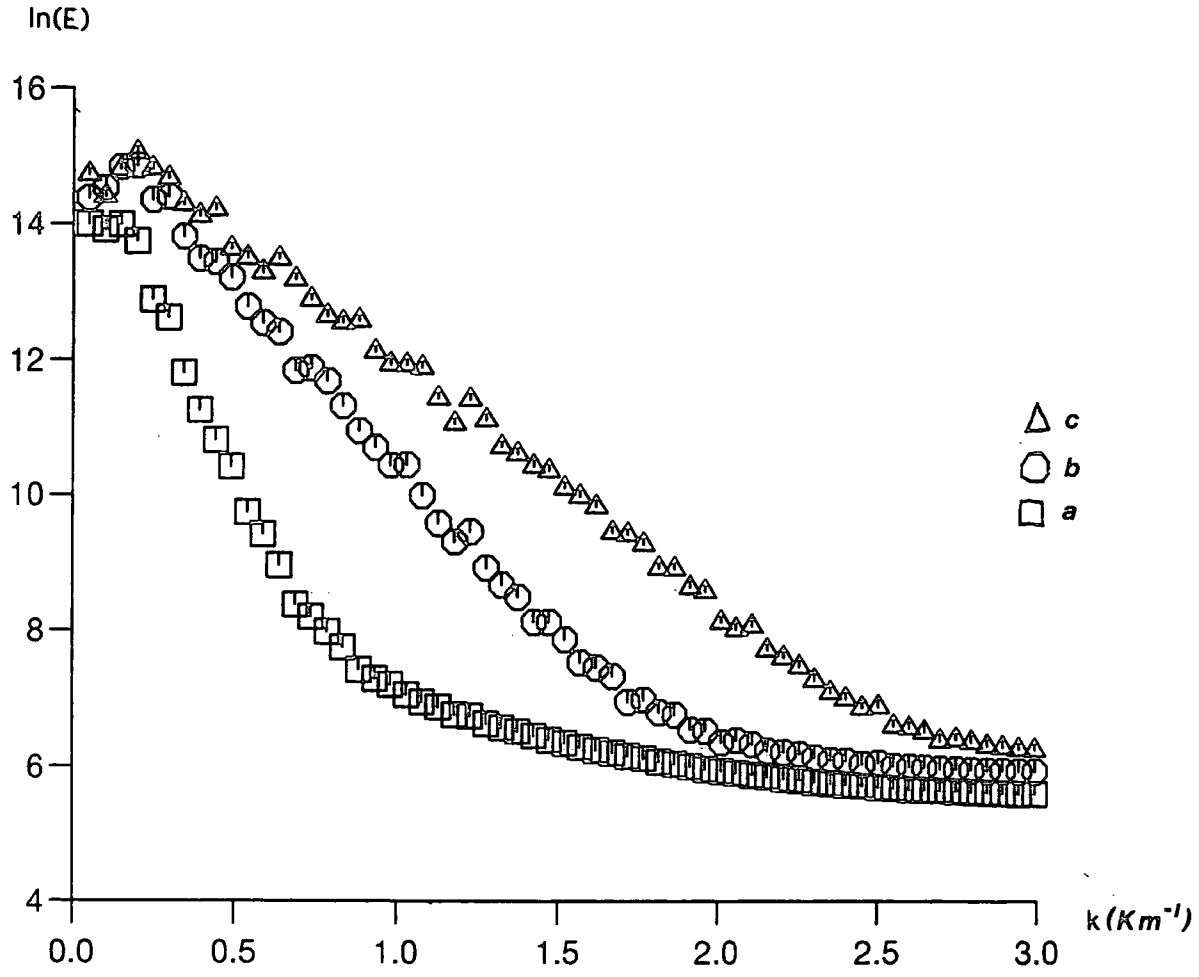

Figure 2.22. Plots of the natural logarithm of the power spectrum versus wave number for three synthetically generated gravity maps. Letters a, b, c, refer to case a, b, c in Table 2.2.

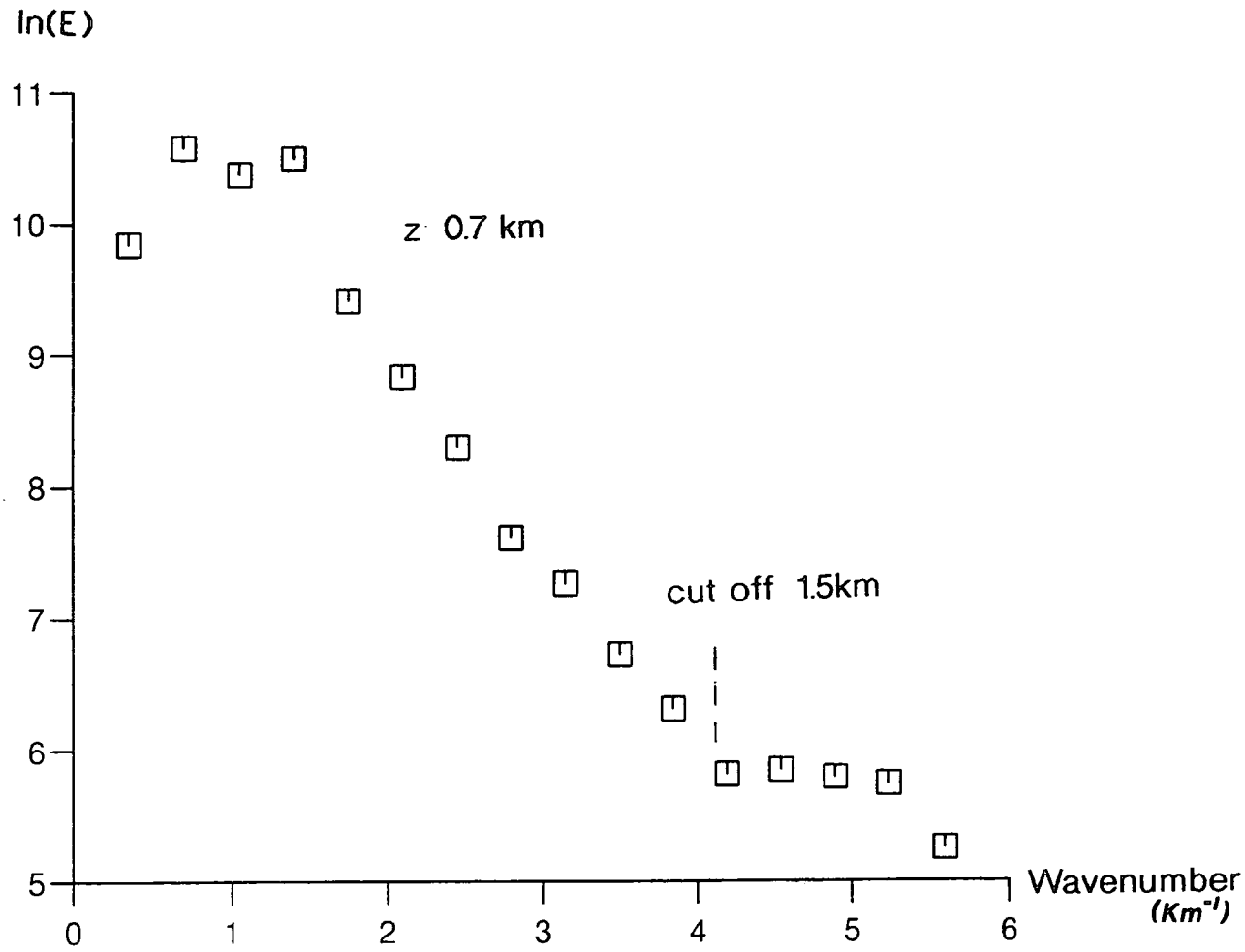

Figure 2.23. A plot of the natural logarithm of the power spectrum versus wave number for the upward continued gravity field.

2.4.7.3 Result of the Inversion

A gravity inversion was carried out to investigate the density distribution within a 1 km thick slab with its top surface set at sea level which could produce the observed gravity anomaly. Figure 2.24 depicts the results of the inversion. Regions of density in excess of 50 kg m^{-3} have been shaded light grey and regions of density below -50 kg m^{-3} have been shaded dark grey. The densities are relative to an average crustal density. The amplitude of the density variation inferred from the inversion is 250 kg m^{-3} with most of the variation taking place within the caldera. Two other inversions were carried out using slabs of thicknesses 200 m and 2 km. The 200 m thick slab developed a density variation in excess of 1200 kg m^{-3} and is unlikely to represent the true distribution of mass in the Krafla area. The 2 km thick slab displayed density variations of the same form as the 1 km slab but with about 60% of the amplitude. The caldera ring faults are associated with regions of high density relative to the caldera infill. Four high density volumes mark the perimeter of the caldera displaying a positive density contrast of 250 kg m^{-3} relative to the hydrothermal areas within the caldera. Leirhnjúkur marks the site of a +200 kg m^{-3} density contrast relative to the caldera infill.

2.4.8 Interpretation of the Krafla Results

The gravity inversion revealed that relatively dense zones were associated with the caldera ring fault and Leirhnjúkur. The local earthquake tomography results for the same area showed that high velocity bodies were also associated with the caldera ring fault. However, forward modelling of the tomographic image to produce a predicted gravity map resulted in only partial correlation between tomography and gravity data.

A good correlation was seen between the high velocity body and the gravity high at (10,15) indicating the presence of a high density, high velocity body, interpreted as a gabbroic intrusive. A bad correlation was given by the lack of high velocity body below the caldera ring fault at (10,10), even though the gravity anomaly was similar in extent and magnitude to the one at (10,15). A possible reason for the lack of an imaged body may have been that the density (and presumably velocity) anomaly which gave rise to the gravity anomaly is very shallow, dense (~800 kg m^{-3} positive density contrast for a thickness of 200 m) and consequently quite thin. Such a body may not be resolved by seismic rays of several hundred metres wavelength. This would imply that high velocity bodies may be just as susceptible to underdetection as low velocity bodies by tomographic analysis. Alternatively, Birch's relationship may be different or may not

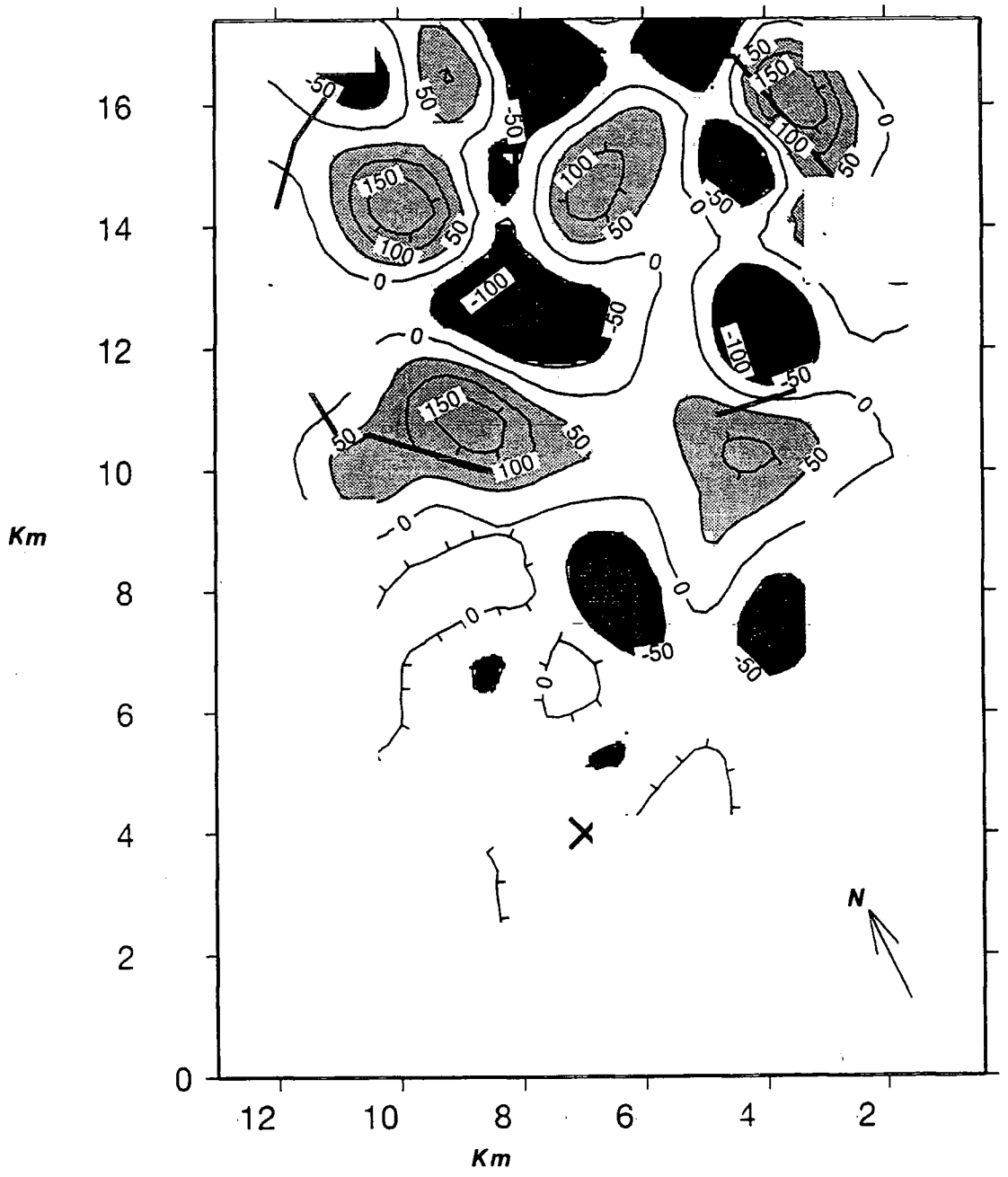

Figure 2.24. The result of a gravity inversion showing density variations within a slab of thickness 1 km. The contour interval is 50 kg m^{-3} .Dark grey areas represent densities less than -50 kg m^{-3} and light grey areas represent densities greater than 50 kg m^{-3} (than the average crustal density).

apply to this volume. The two discrete gravity highs at (7,15) and (3,16) are not reproduced in the predicted gravity field but are approximated by a smooth high which lies between them at (5,16). Again there is the possibility that one of the anomalous bodies was too small and shallow for the tomographic method to image. Due to the coarse resolution of seismic tomography relative to gravity, there is the possibility that the two discrete bodies have been combined or averaged in some way by the tomography to result in a wider anomaly lying roughly midway between the two actual gravity anomalies.

Tomography indicated the presence of gabbroic intrusives around the northern half of the caldera. The addition of gravity data infers that gabbroic intrusives are located within the crust around the periphery of the caldera correlating well with all the caldera ring faults.

The Leirhnjúkur anomaly (7,15) is probably associated with a vertical zone of cooled intrusives within the fissure that originally fed the fissure eruptions of 1727 and 1975 and is not contemporaneous with the caldera fault intrusions. The volume of the conduit is probably about 5 km^3, if the 50 kg m^{-3} contour (figure 2.24) is taken as its areal extent.

The crust in the geothermal areas of the caldera may experience increases or decreases in density due to hydrothermal alteration. The proximity of the massive intrusions in the Krafla area make it difficult to assess the effects of alteration upon density.

2.5 Discussion

The activity at both Hengill and Krafla in the recent past has presumably been fed by a crustal or sub-crustal magma supply. At Mt. Hengill a compact low velocity body was resolved with tomography and interpreted as an accumulation of partial melt. The gravitational effect of such a body (5 km^3) is small at a depth of 3 km. An anomaly of ~-1 mGal would be expected if a density contrast of -300 kg m^{-3} is assumed. The gravity field does not show any indication of a large body having a negative density contrast at depth, providing further evidence that the Hengill system may have been fed from a deeper source.

The Krafla caldera is thought to overlie a magma chamber at a depth of ~4 km. This has been inferred from seismic results, geodetic work and the presence of a caldera. Making the assumption that the magma chamber is spherical, has a radius of 1.5 km and a density contrast of ~-300 kg m^{-3} this would result in an anomaly of ~-2 mGal. This anomaly may be present in the Krafla gravity anomaly, but the proximity of near surface

perturbing bodies such as the caldera intrusions and variations within the caldera due to hydrothermal processes render it difficult to observe.

The geothermal areas within the Hengill-Grensdalur and Krafla areas generally correlate with lower gravity, but this is probably the combination of alteration effects and the close proximity of relatively high density bodies such as the gabbroic caldera intrusions at Krafla and the eroded Grensdalur volcano.

Near Mt. Krafla and Mt. Hengill, volumes interpreted as frozen magma conduits are overlain by positive gravity anomalies. In the case of Husmuli (southwest flank of Mt. Hengill) the inferred magma conduit was imaged directly with tomography, whereas at Leirhnjúkur (west of Mt. Krafla), the existence of a cooling conduit was hypothesised on the basis of clustered hypocentre locations, rather than being directly imaged by the tomography. A significant high density body located near the southwest fault of the Krafla caldera and a shallow low density zone running from south of Mt. Hengill to Hrómundartindur, inferred from gravity observations, were also unobserved by the tomographic analysis.

In both of the studies presented in this chapter, the gravity field has indicated the possibility of additional shallow structure in addition to that resolved by the tomographic method. The resolution of the tomographic method is controlled not only by the ray geometry and wavelength of the seismic waves, but also the uncertainty in P-wave arrival time. For both the Hengill-Grensdalur and Krafla studies the travel times were deemed accurate to 0.03 s. If it is assumed that a perturbing body that gives rise to a change in travel time of 0.03 s, or less, is invisible to the tomographic analysis, some estimates of the size or velocity of these bodies can be made.

Consider a ray travelling a distance Y, with a speed v_1, and a neighbouring ray which travels the same distance, but passes through a perturbing body of thickness X, and at a speed v_2 (figure 2.25).

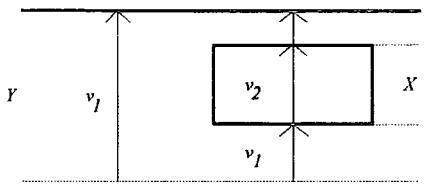

Figure 2.25. Two adjacent rays travelling a distance Y through a medium allowing a wave speed of v_1. The left hand ray travels unperturbed but the right hand ray passes through a body of width X that allows a wave speed of v_2.

The change in travel time, Δt, caused by the perturbing body is:

$$\Delta t = \frac{X}{v_1} - \frac{X}{v_2} \tag{2.19}$$

which when rearranged gives:

$$X = \left| \frac{\Delta t \left(v_1 \Delta v + v_1^2 \right)}{\Delta v} \right| \tag{2.20}$$

where $\Delta v = v_2 - v_1$.

So by setting Δt equal to 0.03 s, Table 2.3 has been constructed.

	Δv	0.2	0.4	0.8	1.2	km s^{-1}
$\Delta\rho = 230\ \Delta v$	$\Delta\rho$	46	92	184	276	kg m^{-3}
$v_1 = 4$ km s^{-1}	X	2.5	1.3	0.7	0.5	km
$v_1 = 6$ km s^{-1}	X	5.6	2.9	1.5	1.1	km
Δg		1.6	1.6	1.8	1.9	mGal

Table 2.3. Table of anomalous body thickness that would be invisible to the tomographic method, where Δv are velocity perturbations within the anomalous body, $\Delta\rho$ are the density contrasts expected using the conversion: $\Delta\rho = 230\ \Delta v$, X is the thickness of the anomalous body that causes a perturbation, Δv, relative to a velocity v_1, that would be invisible to the tomographic method. Δg is the magnitude of the gravitational effect of a sphere of diameter X for $v_1 = 4$ km s^{-1} which is centred one radius below the surface.

For the P-wave velocities encountered in the Icelandic shallow crust, Table 2.3 illustrates that the tomographic method will have difficulty in imaging bodies smaller that ~ 2 km in extent and of density contrast less than ~100 kg m^{-3}. The possible existence of crustal structure in addition to that resolved with tomography, as inferred from the gravity anomalies, supports this theory. Thus, it can be seen that the uncertainty in arrival time is

crucial to the success of local earthquake tomography. In order to approach the limits set by ray geometry and seismic ray wavelength, the arrival time uncertainty needs to be reduced significantly.

In absolute terms, correlation between gravity and tomography is poor and only qualitative similarities link the two. The reason for this is probably due to imperfect source and receiver coverage for the tomography experiment which can lead to distortions in the predicted three dimensional structure. This will result in a mismatch between the more accurate horizontal location properties of gravity data and the greater depth indication abilities of tomography. The magnitude of this effect can be gauged by referring to figure 2.9 which shows that the mismatch between the gravity and tomography is of the same order as the predicted gravity.

2.6 Summary

1. Material underlying the geothermal area in the southern part of the Hengill system and in the Hrómundartindur system has lower densities than predicted by a three-dimensional seismic velocity field obtained from local earthquake tomography.

2. Volumes underlying all of the Krafla caldera faults display positive density anomalies even where the velocity field obtained from local earthquake tomography inferred the absence of anomalous bodies.

3. Material underlying the Leirnjukur cinder cone in the Krafla caldera has a higher density than predicted by local earthquake tomography.

4. These discrepancies could be explained by either: a) a different velocity-density relationship for the volumes that were undetected from that of neighbouring areas; or more likely b) failure to detect anomalous bodies with tomography due to ray geometry, wavelength and uncertainty in P-wave arrival time.

5. Relatively low densities in the Hengill-Hrómundartindur zone are expected from lithological contrast with the neighbouring Grensdalur and Husmuli areas, and geothermal processes that replace groundwater with steam and increase the percentage of clay minerals.

6. The addition of the gravity data to the seismic tomography results provides no evidence for an extensive volume of partial melt or a steam reservoir at shallow depth beneath Mt. Hengill.

Chapter 3

Analysis of the Icelandic Gravity Field

3.1 Introduction

3.1.1 Components of the Icelandic Gravity Field

Theories concerning Iceland's evolution, morphology and geology closely concern the interplay between the Mid-Atlantic Ridge and the hypothesised North Atlantic Tertiary mantle plume. Presumably, the gravitational effects of these two phenomena are superimposed upon one another. Einarsson (1954) first recognised the Bouguer gravity 'bowl-shaped' low centred over the island and interpreted it as isostatic compensation of the Icelandic topography through crustal thickening. Since then, a combination of evidence from geochemistry (Schilling, 1973), seismic P-wave travel time delays (e.g. Long and Mitchell, 1970; Tryggvason et al., 1983; Gebrande et al., 1980), geoid and free air gravity highs (Bott, 1988) have led to the hypothesis that the mantle below Iceland contains a mantle plume. The Icelandic rift system is thought to be analogous to the oceanic rift systems and represents the continuation of the Mid-Atlantic Ridge on land (e.g. Pálmason and Sæmundsson, 1974), and as such should experience a lithospheric thermal effect, whereby the presence of 'hot' lithospheric material at the spreading axis thermally expands axial material to a greater degree than cooler lithosphere at a greater distance. This would give rise to lower gravity at the axes of Iceland's rift system due to the thermally expanded lithosphere having a lower relative density. Pálmason's (1980) proposed kinematic model for accretion at Iceland's rift axes results in a ridge-perpendicular cross-section which has recent eruptive and intrusive products at the axis, giving way to eroded metamorphosed facies at distance from the axis within older volcanic successions. In addition, volcanism has occurred in sub-glacial, sub-aerial and in some cases sub-marine environments leading to eruptive products of differing bulk physical properties and hence a diversity in shallow crustal rocks. In this chapter an attempt is made to separate the constituent crustal and mantle plume components from the gravity field, attributing physical parameters to the sources of these anomalies where possible.

3.1.2 A Mantle Plume

In order to assess the effect of a mantle plume on Iceland's gravity field it is necessary to assume a plume evolution and geometry which is consistent with geological and geophysical observations. Mantle plumes have been described by Hill (1993) and Campbell and Griffiths (1990) and others (e.g. Sleep, 1990). There appears to be three stages associated with plume behaviour. Stage one (figure 3.1a) is the initiation of the plume. The ascending plume has a tail and a bulbous head of entrained lower mantle material. Stage two (figure 3.1b) is the impact of the bulbous head with the base of the lithosphere. The head spreads out and causes wide-scale volcanism (e.g. continental flood basalts) over areas of ~1000-2000 km in diameter. After about 20 Ma of extensive volcanism, activity is reduced and becomes more localised over a smaller area (diameter ~100-300 km) above the axis of the plume. If there is continued supply along the plume conduit then the plume has reached steady state: stage three.

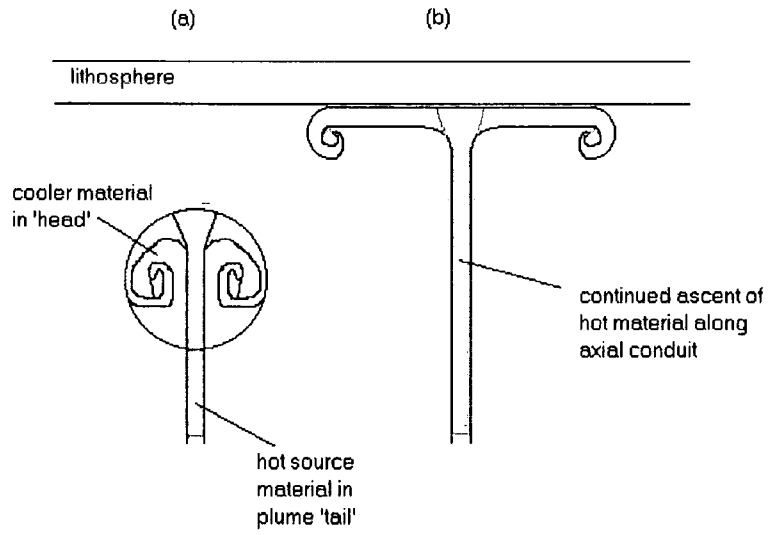

Fig 3.1. The first two stages of a hypothetical plume's evolution.

Stage three is described by Sleep's (1990) plume model (figure 3.2). A vertically ascending plume is fed from below, passes through relatively high viscosity material, and then spreads out radially into the asthenosphere.

In Sleep's (1990) model the horizontal velocity of the plume material which is now spreading horizontally is zero for material at the base of the asthenosphere increasing linearly to plate velocity for material in contact with the lithosphere. The model depicted in figure 3.2 may be representative of the present state of the plume with respect to the Icelandic zones of rifting.

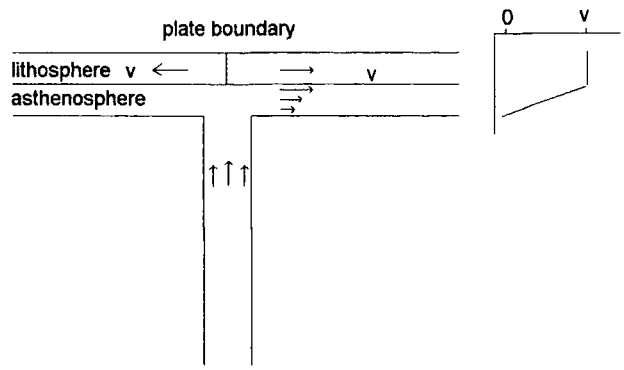

Fig. 3.2 . Sleep's (1990) plume model. The upwelling material is centred on a spreading plate boundary. Horizontally spreading asthenosphere in contact with the lithospheric plate has the plate velocity. Material at the base of the lithosphere has zero horizontal velocity (refer to graph on the right).

In reality the plume may undergo variations in rate of discharge, but at present may be in a stabilised state (Vogt, 1972 and 1974). The plume is assumed to have a three-dimensional circularly symmetric structure and be upwelling as a result of a thermal anomaly at depth within the mantle. Of importance to analysis of the gravity field is the extent of the density anomaly associated with the plume. Below the base of the asthenosphere the plume stem is cylindrical and so can be approximated by a cylindrical density anomaly. Within the asthenosphere the plume material's vertical motion is transformed to horizontal motion. Numerical models of circularly symmetric plumes (e.g. Parmentier et al., 1975) exhibit a mushroom head formed by the impact of upwelling plume material onto the base of the lithosphere (figure 3.3). A density anomaly of this form would contain many variables such as the radius, density and thickness of the mushroom head as well as the radius and density of the plume stem, leaving it with many degrees of freedom (figure 3.4). There are three mechanisms for providing a negative density contrast within the plume relative to the surrounding mantle: (i) thermal expansion of plume material leads to a lower density; (ii) solid-solid phase changes occur deeper than is normal because of the thermal anomaly which allows the existence of lower density phases of the material at greater depths (Hermance, 1981a); and (iii) the vertical migration of partial melt results in depleted mantle of lower density than undepleted mantle at depth. Combining these density effects with a plume model may result in a hybrid model. Mantle ascends along vertical trajectories undergoing solid-solid phase changes and eventually begins to melt at depth within the asthenosphere. Depleted mantle continues to be transported along the mantle trajectories, which eventually become horizontal. The phase changes which occur in the plume absorb heat energy and may reduce the extent of the thermal mushroom head. In the case of Iceland, the plume head may also be modified by the fact that plume material is incorporated into the lithosphere, inhibiting the extent of

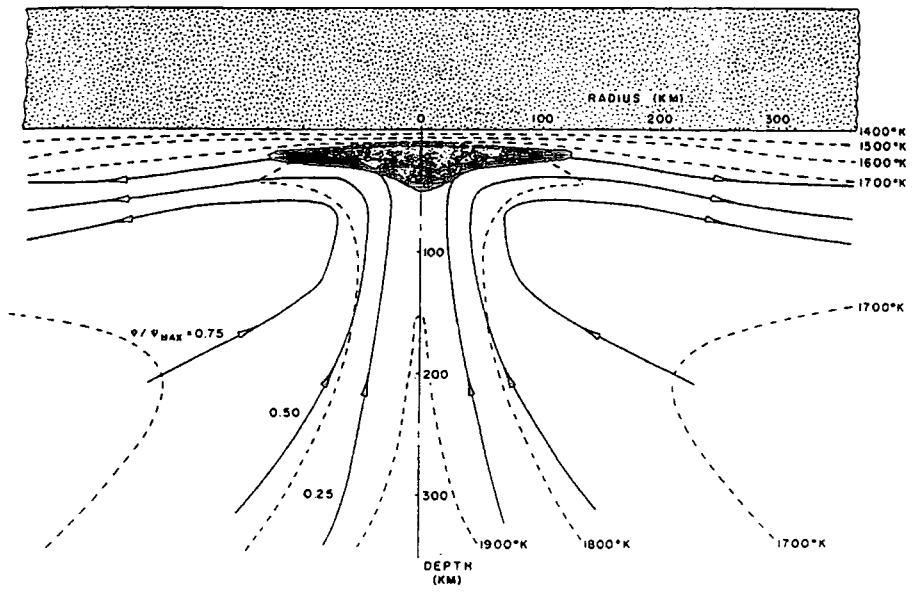

Figure 3.3. Structure of a thermal plume impinging on the base of a rigid 100 km thick lithosphere. Lithosphere moves to the right in the figure in relation to the plume with a velocity of 10 cm a^{-1} at Hawaii. The shape of the geotherm is shown schematically. The zone of partial melting is shaded. After Parmentier et al. (1975).

'mushrooming' of the plume and possibly creating a more cylindrical feature. For simplicity the effect of a plume on the gravity field of Iceland has been assumed to be that of a cylinder of anomalous mantle density, which has only three variables: density, radius, and depth to its top surface. In reality, there is likely to be a radial density gradient rather than the density step suggested by a cylinder model.

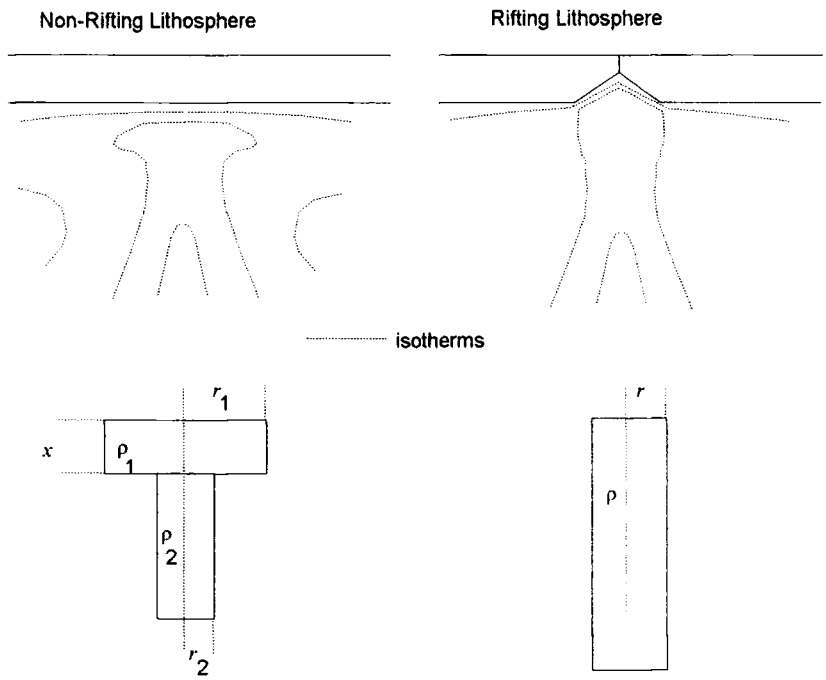

Figure 3.4. Schematic diagrams representing the possible thermal structure of a plume below a rifting and non-rifting lithosphere (top), and corresponding simple physical geometric models (bottom). r_1 and r_2 are the radii of the top and bottom cylinders (left). ρ_1 and ρ_2 are the densities of the top and bottom cylinders (left). x is the thickness of the top cylinder (left). ρ and r are the density and radius of the cylinder (right).

3.1.3 The Lithospheric Thermal Effect

The creation of a lithospheric plate at a spreading axis and the subsequent cooling of the plate as it moves away from the axis give rise to a laterally varying thermal expansion effect. In the simplest models the isotherms and hence isodensities form parabolas. The magnitude of the gravitational effect due to thermal expansion depends upon the thickness of the evolved lithosphere. Flóvenz and Sæmundsson (1993) produced depth estimates to the basalt solidus in Iceland from drill results. If the basalt solidus defines the lithosphere-asthenosphere boundary then in Iceland the lithosphere

is 20-25 km thick around the periphery of the island. The proximity of an extensive thermal anomaly associated with the Iceland mantle plume probably inhibits the normal evolution of the lithosphere across the whole of the island giving rise to a sub-crustal thermal structure dominated by the hotspot rather than a ridge thermal structure (figure 3.5). It is only exterior to the Icelandic insular shelf that normal cooling probably begins to take effect as evidenced by earthquake events originating on the insular shelf off eastern and south eastern Iceland. One explanation for these events is that different cooling rates are present either side of the shelf edge (Einarsson, 1991).

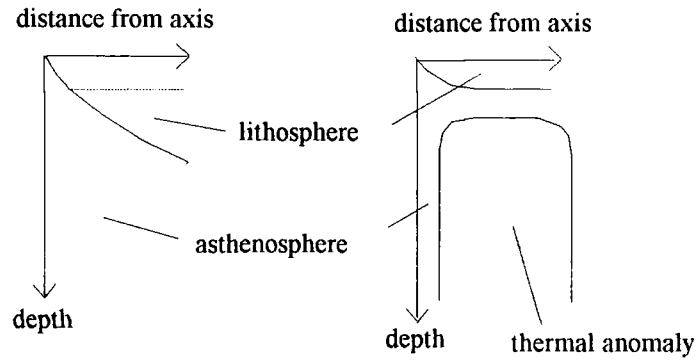

Figure 3.5. Perturbing of the basalt solidus from the normal 'parabola' shaped curve (left) to the near horizontal due to the proximity of an extensive thermal anomaly (right).

3.1.4 Previous Gravity Work

The only previous regional interpretation of a gravity survey of Iceland was made by Einarsson (1954). This survey consisted of 900 stations sparsely distributed throughout most parts of the country. The survey was completed between 1950 and 1954. The Bouguer map of Iceland which resulted from these observations displayed a "bowl-shaped" structure varying from 40-50 mGal at the shores to -30 mGal at the interior of the country. Einarsson (1954) proposed that the ~75 mGal bowl was a result of compensation for the elevation of the central country and went on to describe the nature of the compensation as possibly being a low density sialic layer which thickened beneath central Iceland. In the light of present day tectonic theory and geophysical evidence this explanation does not seem too likely. The observations are still valid and Einarsson further points out that details within the Bouguer field are probably caused by density inhomogeneities no deeper than 5 km.

A gravity investigation of SW Iceland has also previously been carried out by Thorarinsson et al. (1989). Their results are derived from a subset of the data used in this

thesis. A second order polynomial was removed from the Bouguer map resulting in a residual anomaly that displayed a gravity low centred over the WVZ. They also noted a low, presumably related to the EVZ, centred over the Hekla volcano. Their explanation of the observed residual field included the view that an inaccurate choice of Bouguer density would lead to an under or over-estimated elevation correction and hence contribute towards the anomalies. An additional explanation was offered which cited the existence of extinct volcanoes adjacent to the rift zone as being the source of positive anomalies.

Schleusener et al. (1976) carried out a regional survey stretching from 65.5° to 66°N in latitude and 344° to 342° W in longitude straddling the NVZ. The reduction densities they used varied according to the geology. The results of the survey showed part of the island-wide Bouguer low observed by Einarsson (1954). The Bouguer anomaly gradually becomes more negative towards the south (~0.5 mGal/km). They also observed minima at Eyjafjördur (near Akureyri) which they attribute to the presence of low density sediments in coastal valleys. A 5 mGal minimum was seen 15-25 km east of Mývatn within the active volcanic zone. Schleusener et al. (1976) propose that the relative minimum found over young volcanic rocks was produced by thickening of this layer of low density young volcanic rock in the active volcanic zone, as seismic evidence suggested.

3.2 Methodology

In this chapter the gravity data is reduced to the Free Air Anomaly and two Bouguer anomalies by applying two separate Bouguer corrections. One correction uses a single Bouguer density for the whole area, while the other assigns stations one of two different Bouguer densities, the choice of which is dependent upon the geology about the station. Both Bouguer anomaly fields are continued onto a plane 1 km above sea level where the gravity field is separated into long and short wavelength components. These are then interpreted.

3.3 The Gravity Dataset

3.3.1 Description of the Data

The data used in this chapter were originally compiled between 1967 and 1985 (Thorbergsson et al., 1990). The gravity data comprised latitude, longitude, height, gravity, terrain correction, and topographic correction and were tied to the IGSN71

reference system. The terrain corrections for stations on land were made using Hammer tables (Hammer, 1939) out to a distance of 9903 m whereafter a topographic correction was calculated out to a distance of 167 km. For the sea data the terrain correction was carried out to a distance of 6653 m and the topographic correction out to a distance of 167 km. The topographic correction was made by correcting for the effect of mass above sea level or absence of mass below sea level. The average data spacing on land was of the order of 10 km. Figure 3.6 depicts the station positions within the study region chosen. The size of the region was decided upon by consideration of the amount of memory required by the computer to continue the data using the EQSM program (chapter 2). The 2602 points within the region are near the maximum number that could be handled by the computers that were available.

3.3.2 Assessment of Data Errors

The uncertainty quoted by Thorbergsson et al. (1990) for the gravity data due to combined uncertainties in the corrections made and the height of the stations used is 1 mGal, although some stations at high altitude within the interior of the country were quoted as being possibly up to 10 mGal in error. As an added measure of possible error the total Bouguer correction was calculated for a density of 200 kg m^{-3} so as to estimate the possible error due to an incorrect choice of Bouguer reduction density. Figure 3.7 shows that locally the error in the anomalies is of the order of 2-3 mGal. However, variations of up to 10 mGal could occur between coastal stations and those in the interior due to an incorrect choice of Bouguer density. It should also be noted that the spacing of the stations in this survey is ~10 km, which is the scale of the surveys covered in chapter 2. In the studies at Hengill-Grensdalur and Krafla it was seen that gravity anomalies can vary by ~5 mGal. This variation could be interpreted as 'noise' in a large scale survey. With the gravity map continued to an altitude of 1 km above sea level, 5 mGal is probably a good estimate of the 'noise' present in the gravity fields presented here.

3.4 Reduction of the Gravity Data

3.4.1 The Free Air Anomaly over Iceland

The Free Air Anomaly (FAA) was produced from the gravity readings in the usual way by means of removal of the theoretical gravity and the first vertical derivative of the theoretical gravity: the free air reduction (figure 3.8).

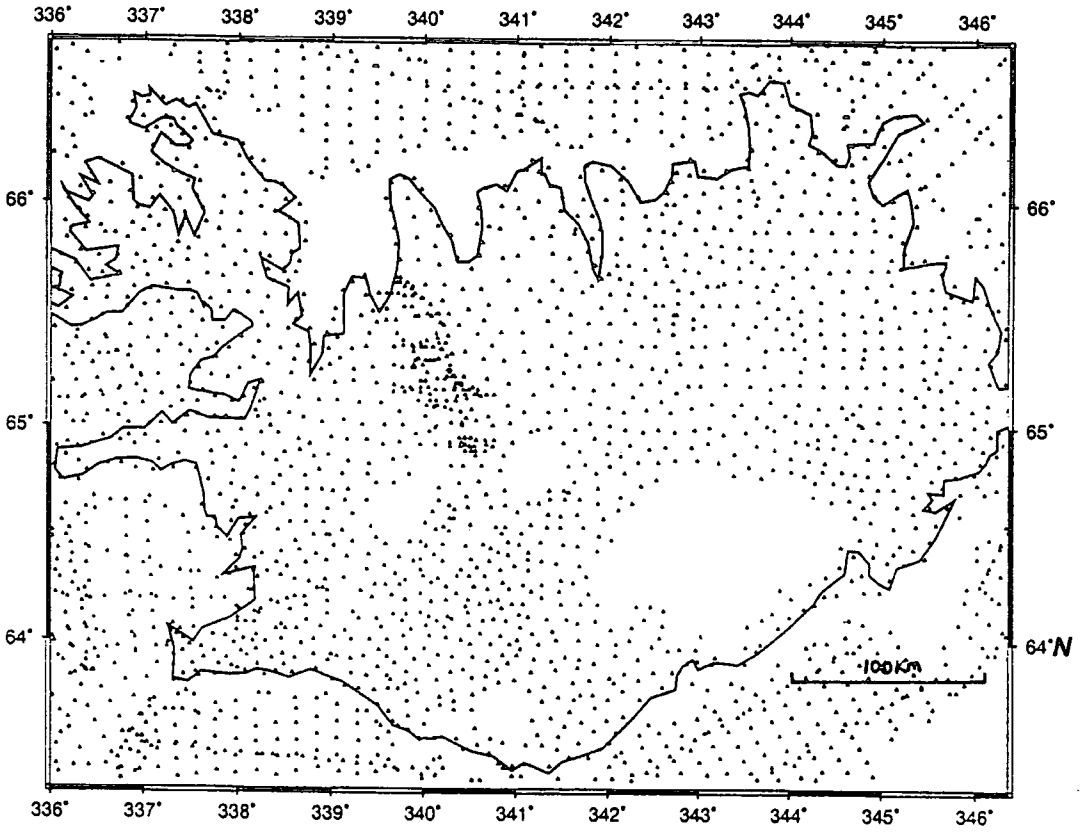

Figure 3.6. The position of gravity stations used in this chapter. Each triangles represents a station.

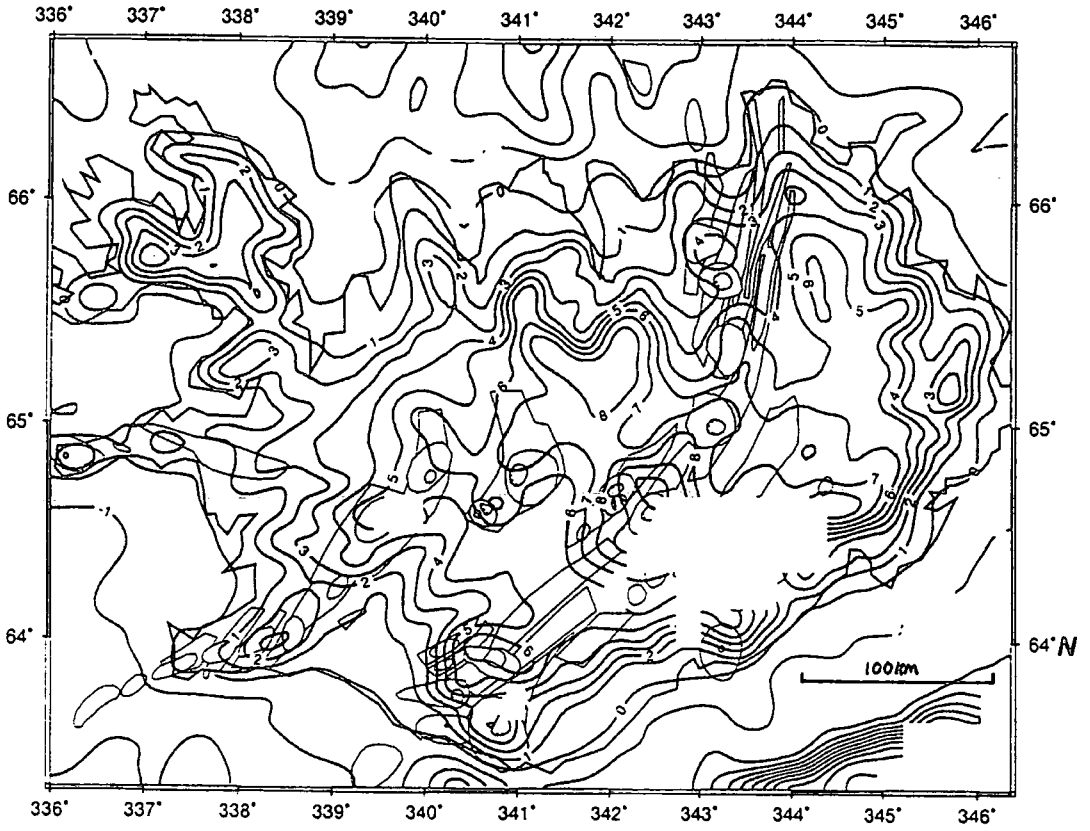

Figure 3.7. An error map constructed to show the effect of an incorrect choice of the Bouguer reduction. The error in reduction density is 200 kg m^{-3}. The contour interval is 1 mGal. The tectonic units are marked on for reference.

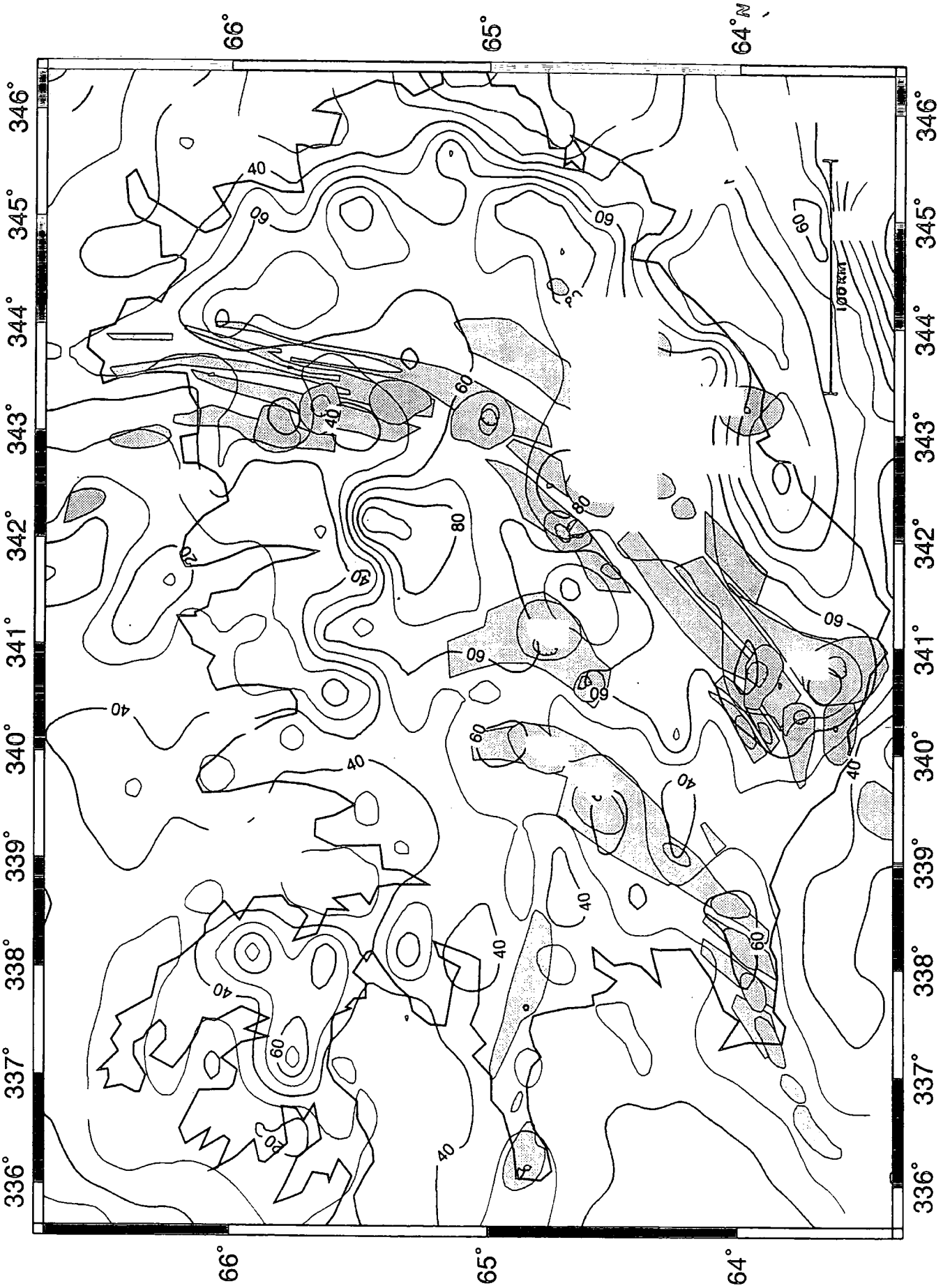

Figure 3.8. The Free Air Anomaly map for Iceland gridded using splines in tension (Smith and Wessel, 1990).The contour interval is 10 mGal. Tectonic units are shown as shaded polygons.

3.4.2 Bouguer Correction

The Bouguer correction attempts to account for the rock mass above the reference plane (usually sea level). In making this correction a choice for the density of the rock above sea level must be made. In Iceland, numerous authors have made use of different densities depending upon their perception of the geology of the area surrounding the stations. Table 3.1, below, is a summary of reduction densities previously used in gravity work on Iceland.

Reference:	Rock Type:	Density:	Region:	
Einarsson (1954)	Hyaloclastite Tertiary	2200 kg m^{-3} 2600-2700 kg m^{-3}	All of Iceland	*
Schleusener et al. (1976)	Hyaloclastite Intermediate Tertiary	2300 kg m^{-3} 2500 kg m^{-3} 2700 kg m^{-3}	North Iceland incl. NVZ	+*
Thorarinsson et al. (1989)	SW Iceland	2500 kg m^{-3}	SW Iceland incl. WVZ	+
Thorbergsson et al. (1990)	All	2600 kg m^{-3}	All Iceland	
Schoenharting and Pálmason (1982)	Tertiary	2700 kg m^{-3}	Reydarfjordur	*
chapter 2	WVZ	2450 kg m^{-3} 2400 kg m^{-3}	Hengill area	* +
chapter 2	NVZ	2300 kg m^{-3}	Krafla	+

Table 3.1. Summary of the Bouguer reduction densities used in the references cited for gravity work on Iceland.

These densities were determined either by experiment upon samples (*) or by statistical analyses (+) of the data using methods proposed by Nettleton (1939) or Parasnis (1962).

Selecting the correct reduction density is critical to gravity analysis. There are two extreme cases for the assigning of Bouguer reduction densities. Either, one reduction density is used throughout the whole area or, each station is assigned an individual

density according to the surrounding geology (e.g. Einarsson, 1954). This second case may seem most accurate, but it is hampered by the fact that matching each station to its lithology would be very time consuming and that densities can also change quite drastically within a lithology.

A compromise was sought. The highlands, which usually undergo the greatest terrain correction, tend to be composed of low density hyaloclastite material in contrast to the higher density Tertiary 'lowlands'. It was decided that two reduction densities would be used. An area approximately coinciding with the neovolcanic zone was digitised (figure 3.9) and a computer program was written to assign all those stations within the zone a density of 2300 kg m^{-3}. A value of 2300 kg m^{-3} was used as it was the median value for rock densities of the axial neovolcanic zone. Everywhere outside of the zones was assigned a density of 2600 kg m^{-3}. The value of 2600 kg m^{-3} rather than 2700 kg m^{-3} was chosen because it would not contrast too much with intermediate rocks, but still be representative of the Tertiary rocks. The bounds of the zone were chosen so as to approximately fall midway between the Pleistocene and Plio-Pleistocene stratigraphic boundaries.

For the purpose of this chapter, two Bouguer reductions were carried out: i) a single reduction density of 2600 kg m^{-3}; and ii) a reduction density of 2300 kg m^{-3} within the axial neovolcanic zones and 2600 kg m^{-3} outside.

3.4.3 Continuation of the Bouguer Anomalies

The irregularly spaced Bouguer anomalies were continued onto a plane using the equivalent source method (section 2.3.5.3) to allow investigation with Fourier methods. The parameters required for the continuation of the Bouguer anomalies with the program EQSM are: depth to the equivalent sources and altitude of the horizontal continuation plane. Section 2.3.5.4 described how it was possible to choose the optimum depth for the equivalent source layer by plotting the RMS of the continued field against the depth to the equivalent sources. This was done for a subset of the Iceland dataset and the result is shown in figure 3.10. It was seen that a plateau region exists, stretching between 8-23 km with its centre at 16 km, hence a depth to the equivalent source layer of 16 km was chosen. A horizontal continuation plane at an altitude of 1 km was chosen on the basis that it was above most of the data, but not so far away that errors creep in (section 2.3.5.4). The data, after continuation, were to be regularly spaced onto a 128x128 grid to allow direct input into 'Fast

Figure 3.9. Map depicting the density zoning used for assigning different Bouguer reduction densities to the Icelandic gravity stations. Stations within the stippled area were reduced with a Bouguer density of 2300 kg m^{-3}. Stations outside of the stippled zone were reduced with a Bouguer density of 2600 kg m^{-3}.

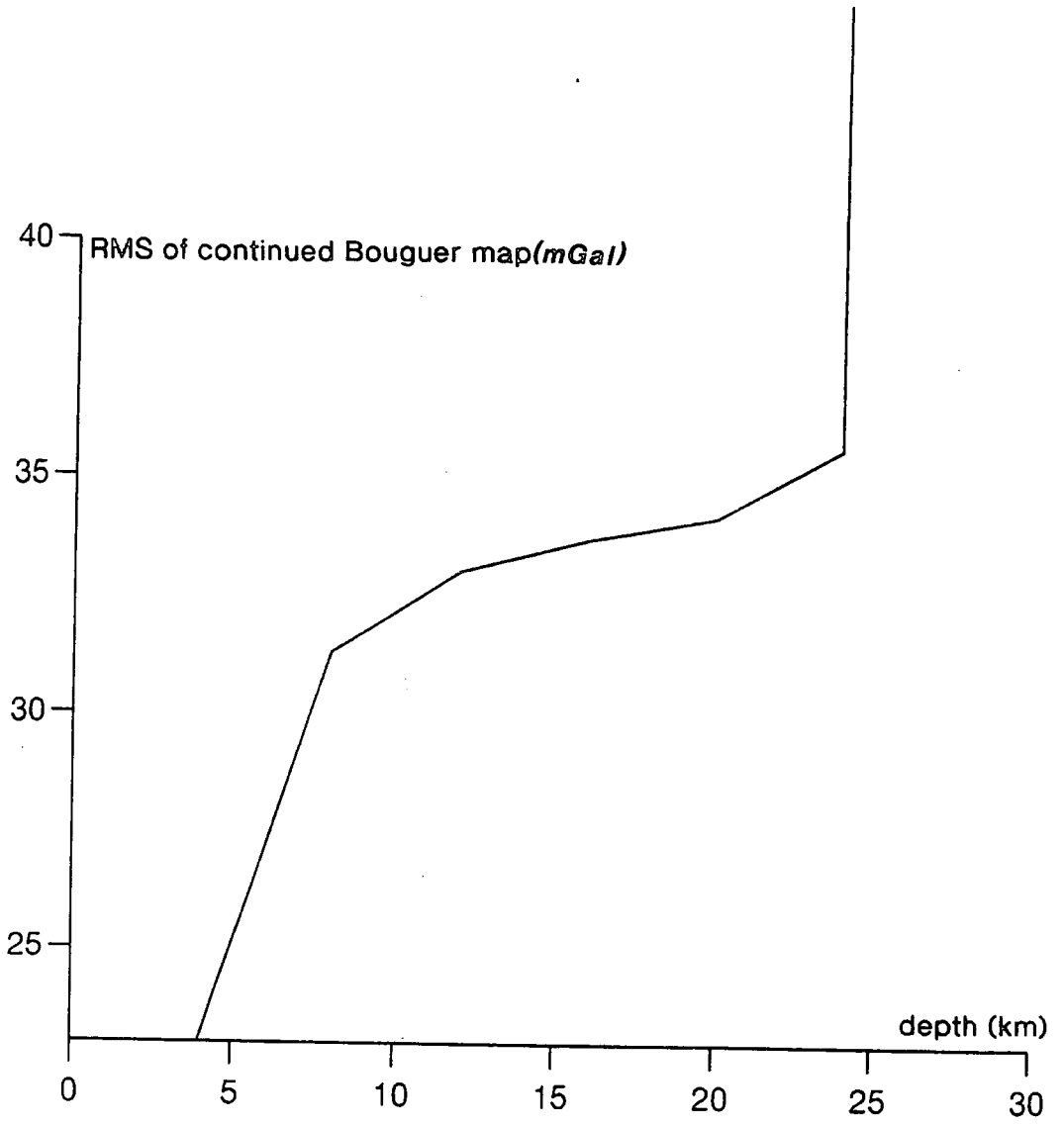

Figure 3.10. The RMS signal (in mGal), of a subset of the whole Iceland dataset which has been continued using EQSM, versus depth to the equivalent source layer used for the continuation.

Fourier Transform' routines. By applying these parameters the Bouguer values were continued onto a plane 1 km above sea level. The continued Bouguer anomaly resulting from the single density Bouguer reduction is referred to as CBA1 (figure 3.11), while the continued Bouguer anomaly resulting from the dual density reduction is referred to as CBA2 (figure 3.12).

3.4.4 Separation of the Long and Short Wavelength Components of the Continued Bouguer Field

The radial power spectrum (un-normalised) of CBA1 was obtained through the *grdfft* routine (GMTsystem: Wessel and Smith, 1991) (figure 3.13a). It was immediately apparent that the spectrum was dominated by components of the signal of wavelength greater than ~200 km. Figure 3.13b is detail of 3.13a showing the character of the power spectrum for the sub-200 km wavelength components.

The assumption is made that short wavelength anomalies are derived from shallow sources while long wavelength anomalies are derived from deep sources. For point masses this is a valid assumption, but extensive shallow mass distributions will be mis-interpreted as deeper, less extensive anomalies. This is part of the inherent ambiguity of interpreting gravity data. It is further assumed that the Iceland mantle plume will be responsible for the long wavelength anomaly, while the short wavelength anomalies in the gravity field are due to crustal or lithospheric density anomalies. Maximum depth estimates were made for the sources of these two components of the gravity field using the method of source depth estimation (Granser et al., 1989) as described in section 2.4.7.2.

The regularly spaced data from CBA1 was used to produce the graph in figure 3.14. A straight line is depicted which seems to asymptote at either end. A 'white tail' is seen at high wavenumbers corresponding to wavelengths less than 10 km, the approximate spacing of the original data. The main line produces a maximum depth estimate of 5 km up to wavelengths of ~150 km. At wavelengths in excess of 150-200 km, a maximum depth is not well constrained but is very probably at depth and within the mantle ~40 km. Using this method leads to the conclusion that anomalies of wavelength less than 150 km are probably due to a source which has a top surface most likely shallower than 5 km. Anomalies of wavelength in excess of 200 km could be due mainly to a deep source beginning at a depth of approximately 40 km. This does not rule out the possibility of arealy extensive shallow bodies being responsible for the long wavelength anomalies also.

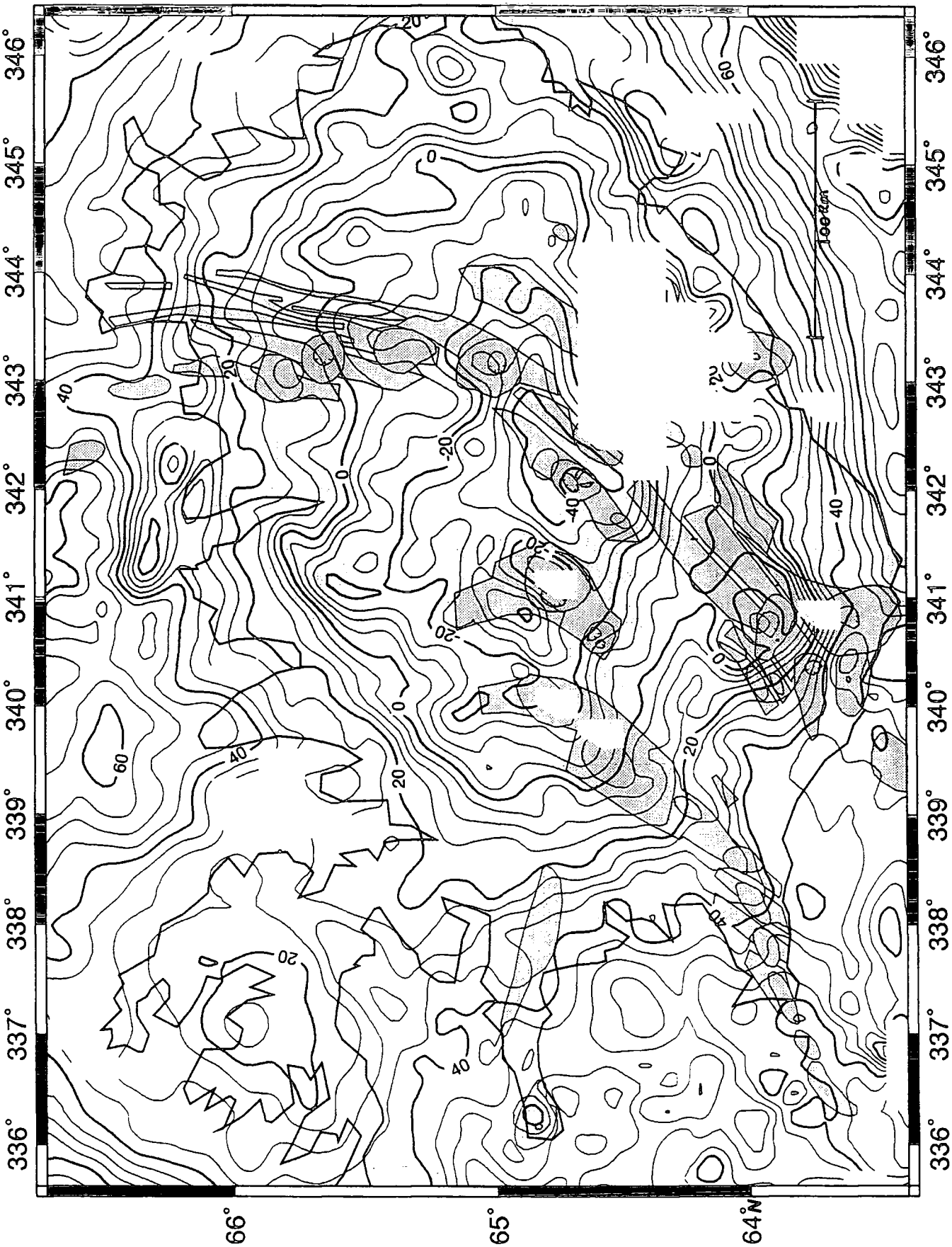

Figure 3.11. CBA1. Contour map of the continued Bouguer gravity anomalies for the single density (2600 kg m^{-3}) reduction using EQSM. The data values are on a 128x128 grid with a nodal spacing of 4.1471 km in the east-west direction and 2.9613 km in the north-south direction. The grid is 1 km above sea level and the equivalent sources are at 16 km below sea level. The tectonic units are marked as shaded polygons. The contour interval is 5 mGal.

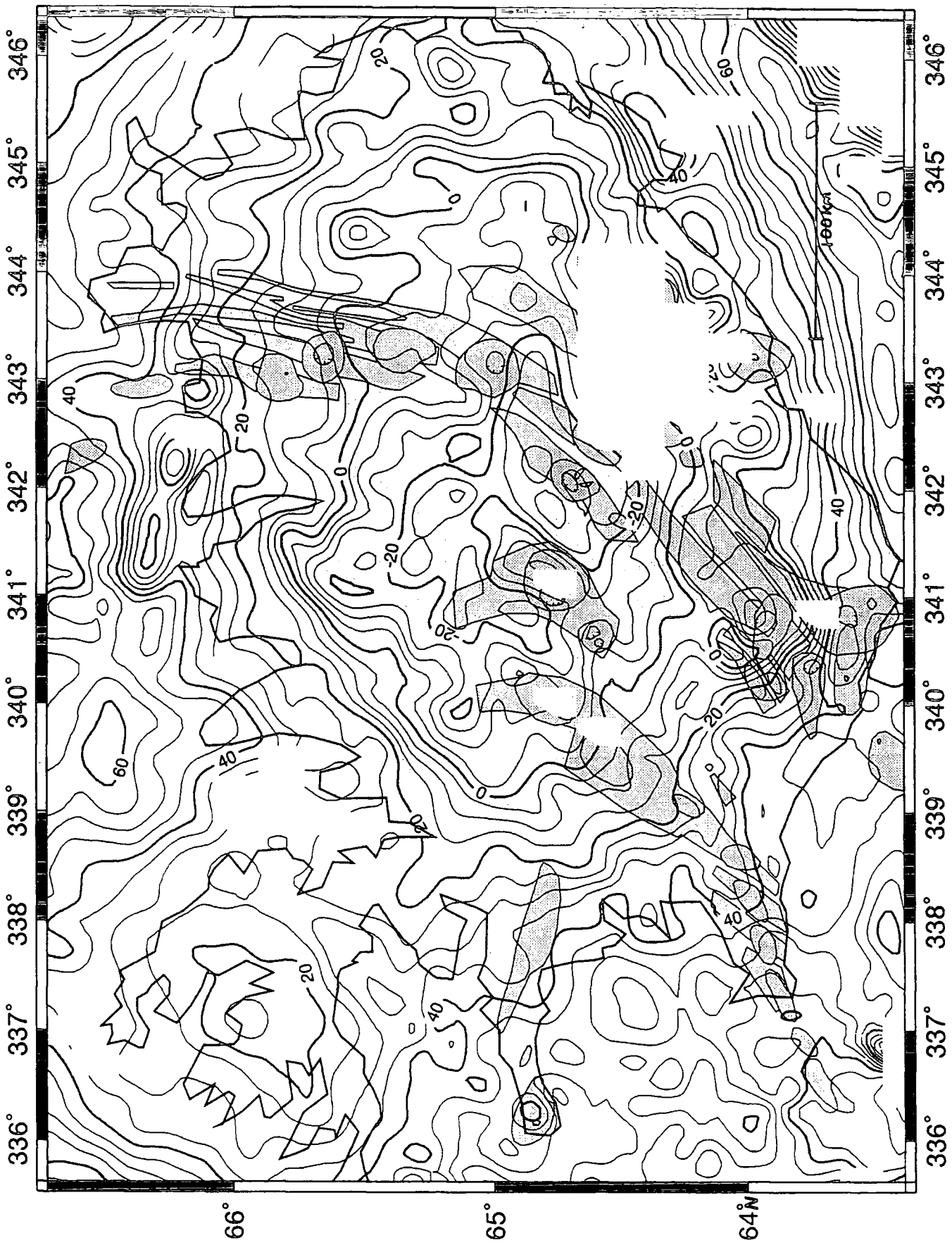

Figure 3.12. CBA2. Contour map of the continued Bouguer gravity anomalies (using EQSM) for the dual density (2300 and 2600 kg m^{-3}) reduction. The data values are on a 128x128 grid with a nodal spacing of 4.1471 km in the east-west direction and 2.9613 km in the north-south direction. The grid is 1 km above sea level and the equivalent sources are at 16 km below sea level. The tectonic units are marked as shaded polygons. The contour interval is 5 mGal.

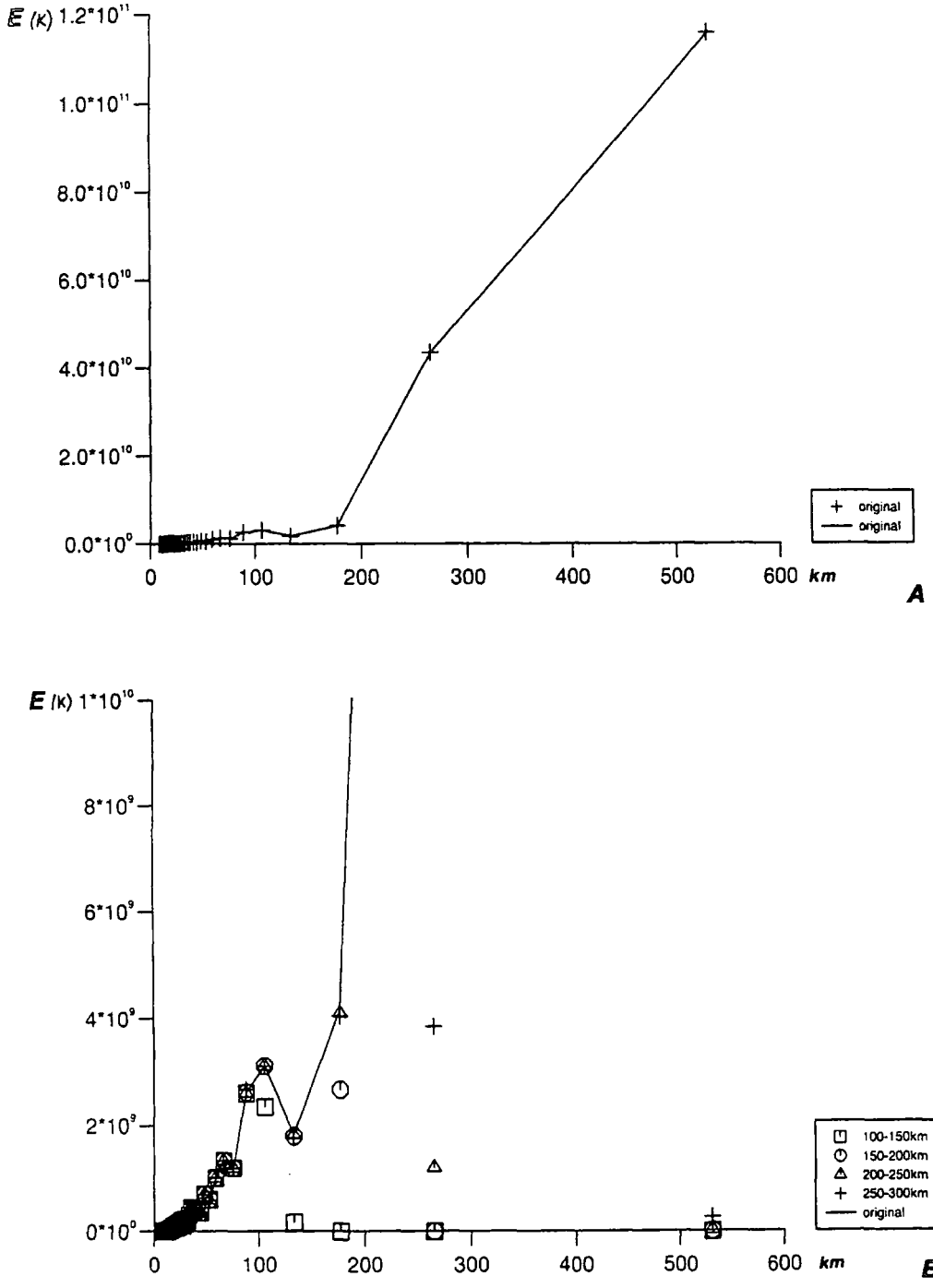

Figure 3.13. a) Un-normalised radial power spectrum for CBA1 as a function of wavelength in km. b) Detail of (a) (the solid line). Also shown are power spectra after CBA1 was filtered with high pass filters, versus wavelength in km. The legend refers to the filter parameters: high pass, high cut.

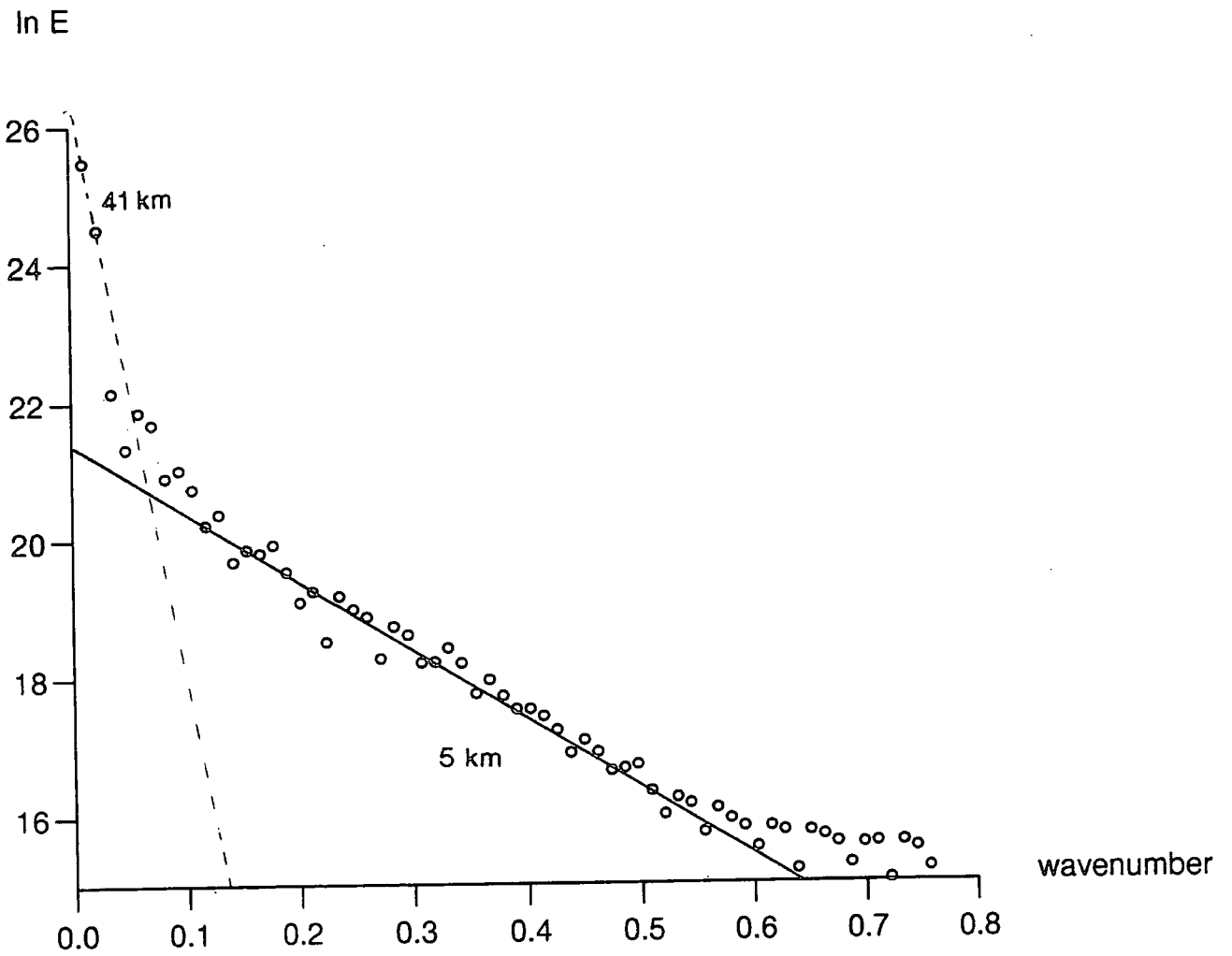

Figure 3.14. A plot of the natural logarithm of the power spectrum versus wavenumber (2π/wavelength) for CBA1 (see Granser et al., 1989). Maximum depth estimate for anomalous bodies of 5 and 41 km are obtained for CBA1.

Separation of the long and short wavelength components of the continued Bouguer anomalies was achieved through the application of cosine tapers in the Fourier domain (using the *grdfft* routine; Wessel and Smith, 1991). To obtain the short wavelength component various high pass filters were tried. Each filter had the characteristic that between two specified wavelengths, high cut and high pass, tapering occurs; wavelengths greater than high cut are eliminated; wavelengths smaller than high pass are unaffected. Figure 3.13b shows post-filtered radial power spectra of CBA1 superimposed upon the original radial power spectrum of CBA1 (the solid line). Comparing each of the filtered spectra in turn with the original power spectrum revealed that the 200-250 km filter still retained the character of the short wavelength component of the power spectrum, while successfully eliminating the long wavelength component. On this basis it was decided that the 200-250 km filter was the most effective. To obtain the long wavelength component of the gravity field, a low pass filter with a low cut of 200 km and a low pass of 250 km was used.

3.5 Results: The Gravity Anomalies

3.5.1 Free Air Anomaly

The FAA reaches a high of 70-80 mGal over the Vatnajökull region (figure 3.8). Regions of high FAA extend north and west from Vatnajökull approximately encompassing the EVZ (60 mGal) and to the east of the NVZ. The WVZ and EVZ exhibit a local free air anomaly of 10-20 mGal. To the south of Akureyri the anomaly again approaches 80 mGal, and in the northwest a 60 mGal high exists over the peninsula. To the south and southeast of Iceland a steep step of ~ 50mGal can be seen coinciding with the bathymetric step there. Overall though, the Iceland plateau has a FAA of the order of 50 mGal.

3.5.2 The Continued Bouguer Fields

Two continued maps were considered, the first was the map derived from the single density elevation correction (CBA1: continued Bouguer anomaly 1, i.e. the result of continuing the single density reduction Bouguer map.) and the second was for the map derived from the dual density reduction (CBA2). These two cases and the results derived from both have been pursued throughout the rest of the chapter.

CBA1 (figure 3.11): The map was contoured at 5 mGal intervals. The tectonic and volcanic features were also included for reference. The general shape of the field is an elliptical bowl sloping down from ~40 mGal near the coast to ~ -45 mGal in the interior. The NW peninsula mimics the main Icelandic gravity structure, exhibiting a negative bowl of the order of 20 mGal. Closer inspection of CBA1 reveals a number of smaller scale anomalies. The bathymetric deep of the Tjörnes Fracture Zone displays a relative low of ~20 mGal. The Torfajökull-Hekla area is the site of a curious circular low of ~20 mGal. The axial neovolcanic zones have indications of attendant gravity lows evidenced by the way the contour lines buckle outwards to encompass the neovolcanic zones.

CBA2 (figure 3.12): The only obvious difference between CBA1 and CBA2 is that the bowl-shaped low only approaches ~-30 mGal in the middle of the island in contrast to ~-45 mGal for CBA1. This is because of the different Bouguer corrections made to the original data. Further differences arise along the axial neovolcanic zones, but are quite subtle. For example, along the WVZ the 30 and 10 mGal contours are not as buckled in CBA2 as they are in CBA1. The same is true of the 0 and 20 mGal contours across the NVZ and the 40 mGal contour across the EVZ. This result is as expected and due to the fact that the lower density of these regions in CBA2 gives rise to a smaller Bouguer reduction and reduces the apparent gravity anomaly across the axial neovolcanic zones.

It was obvious from inspection that the upward continued Bouguer maps both had a long wavelength (the negative bowl) and short wavelength (e.g. the Torfajökull region) component. Normally the long wavelength component in gravity work is treated as the regional and removed before local anomalies are interpreted. In this chapter the long wavelength component was thought to be a manifestation of the mantle plume beneath Iceland.

3.5.3 Long Wavelength Anomaly

The bowl-shaped negative anomaly over Iceland is now readily apparent in figures 3.15 and 3.16 depicting the long wavelength gravity component. The anomaly (in both figures) is centred on 342°W 65°N, some 40 km due east of Hofsjökull. It is elliptical with its major axis striking 025°. The two figures (3.15 and 3.16) are derived from CBA1 and CBA2, respectively, and bear close resemblance to one another although offset by ~10 mGal.

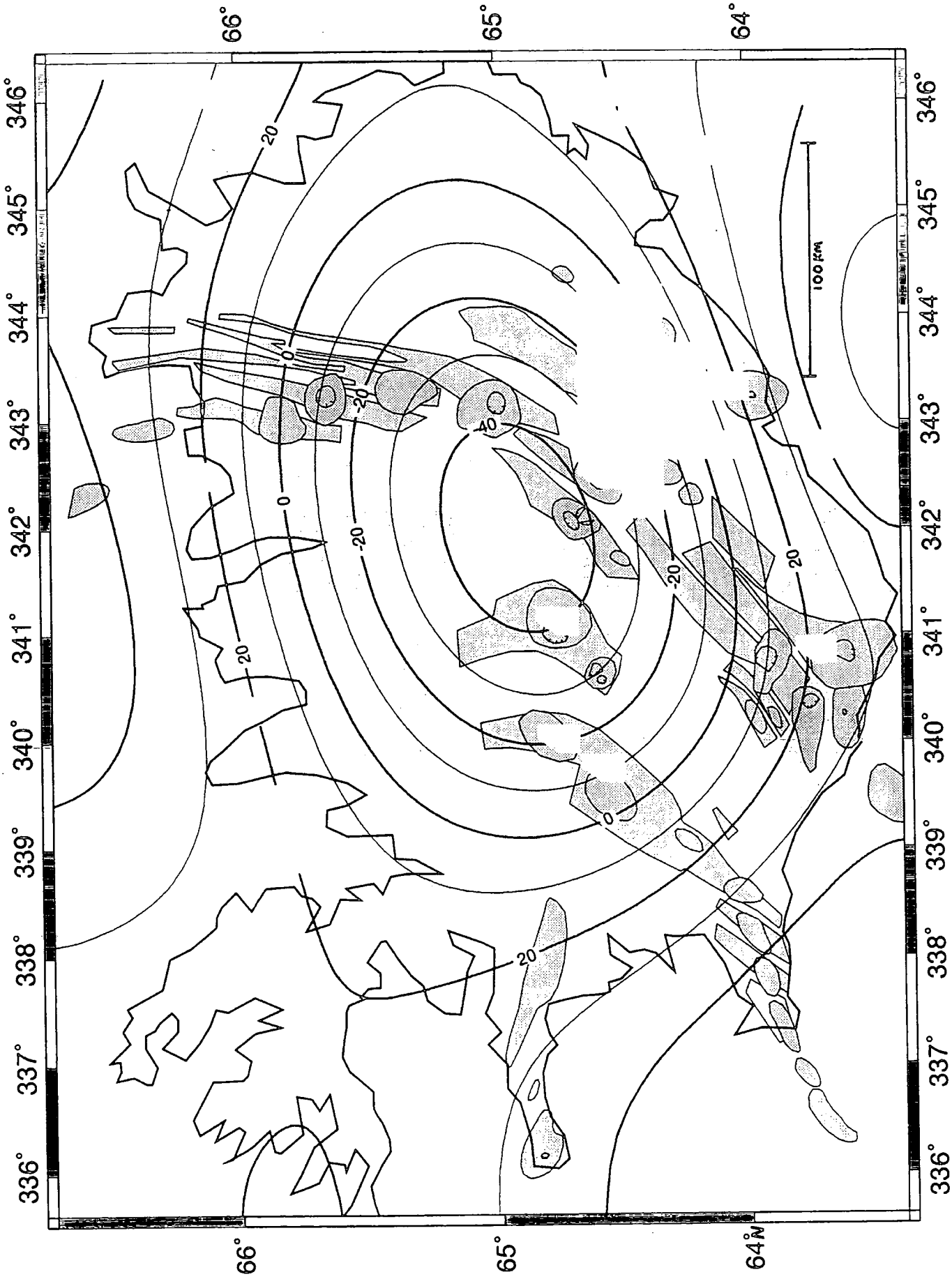

Figure 3.15. The long wavelength component of the Icelandic gravity field. The result of applying a 200-250 km low pass filter to CBA1. The contour interval is 10 mGal. The tectonic units are shown as shaded polygons.

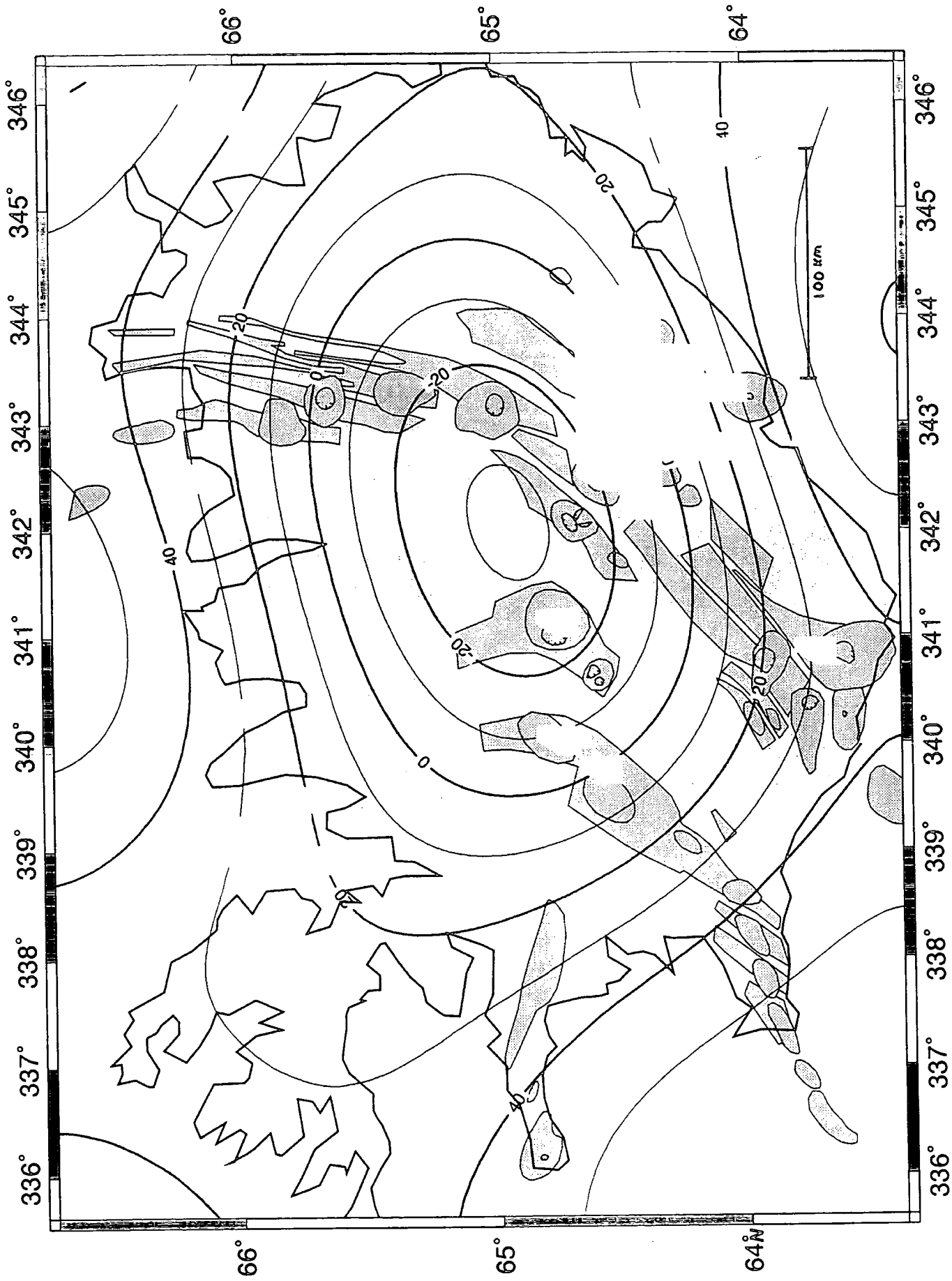

Figure 3.16. The long wavelength component of the Icelandic gravity field. The result of applying a 200-250 km low pass filter to CBA2. The contour interval is 10 mGal. The tectonic units are shown as shaded polygons.

3.5.4 Short Wavelength Anomaly

The short wavelength components of the gravity field over Iceland were interpreted as being mainly due to crustal density inhomogeneities. Again, there were two results caused by making two different Bouguer corrections and the result derived from the single density reduction has been described first followed by pointing out any differences that arose due to the dual density reduction.

The peak to peak amplitude of the residual map is ~30 mGal on Iceland itself (the south east high of 30 mGal is very close to the edge of the data and so is not well constrained) (figure 3.17). It can be seen that the gravity lows mentioned in connection with the CBAs are now well pronounced with the removal of the regional. The local low over the Tjörnes Fracture Zone is ~20 mGal. The Hekla-Torfajökull region is the site of a pronounced horseshoe-shaped negative anomaly. The WVZ now displays a northeast striking relative gravity low of ~20-30 mGal, stretching from Reykjanes to Langjökull. The NVZ also displays a relative gravity low, but is it is not very coherent. It can be traced from 344°W, 66°N running south along the NVZ to about 65.5°N. A more pronounced relative gravity low is ½° to the east, running parallel to the NVZ low. A halo of low gravity surrounds the Vatnajökull ice cap running along the shores of the island in the south. The NW peninsula exhibits a gravity low of ~10 mGal and is about 100 km in diameter. The Snaefell volcano is located near the site of a roughly circular low. In the north of the island there is a substantial low just to the west of Akureyri within the Tertiary flood basalts, but not associated with any obvious tectonic feature.

The residual anomaly derived from the dual density reduction is seen in figure 3.18. As expected the only differences in the magnitudes of the anomalies occur over the volcanic zones where different reduction densities were used. The magnitude of the local low over the WVZ is now only ~15 mGal, reduced by ~25-30%. In the NVZ the magnitude of the anomaly is reduced slightly. Following a profile along 65.6°N from 342.5°W to 344°W sees a change in anomaly from greater than 10 to less than 0 mGal in the residual derived from CBA1 compared to greater than 10 to less than 5 mGal for the residual derived from CBA2

These residual anomalies compare favourably with Einarsson's (1954) isostatic anomaly for Iceland (figure 1.9) in which he identifies a northeast-southwest trending anomaly in the WVZ, a low gravity region just to the north of Torfajökull, the NW peninsula

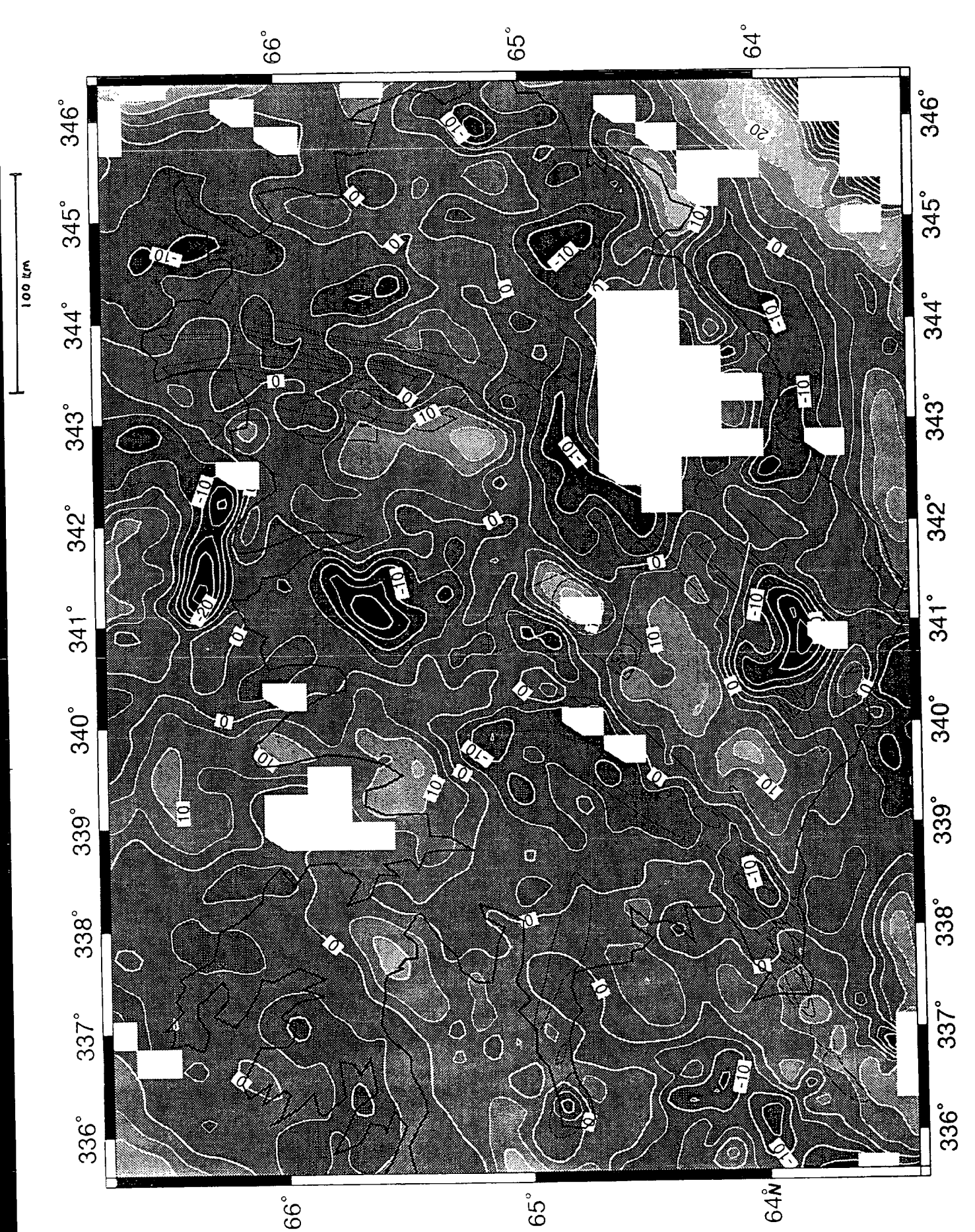

Figure 3.17. The short wavelength component of the Icelandic gravity field. The result of applying a 250-200 km high pass filter to CBA1. The white contour interval is 5 mGal. The shaded scale goes from dark to light in 5 mGal steps. The tectonic units are shown as thin black lines.

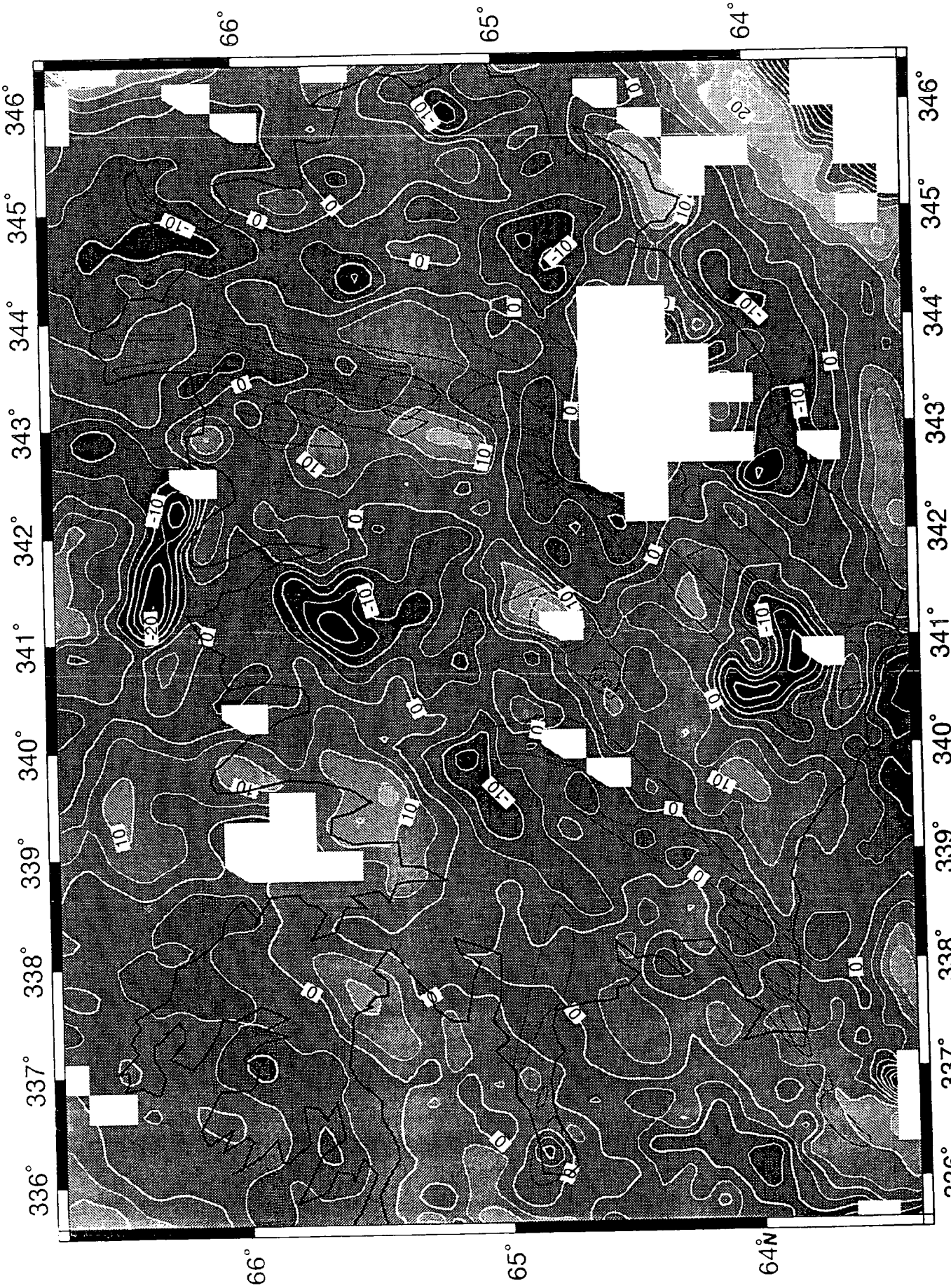

Figure 3.18. The short wavelength component of the Icelandic gravity field. The result of applying a 250-200 km high pass filter to CBA2. The white contour interval is 5 mGal. The shaded scale goes from dark to light in 5 mGal steps. The tectonic units are shown as thin black lines.

relative gravity low and a relative gravity low in the region between the Skagi peninsula and Krafla.

3.6 Interpretation

3.6.1 The Long Wavelength Component

3.6.1.1 Introduction

It is noticeable that the long wavelength anomalies correlate with the general shape of the island. There are four possible explanations for this: (i) the reduction density applied to the gravity data was too great for the coastal areas where shallow marine and fluvial deposits can be found; (ii) a halo of low density sediment exists just off the coast of the island that have significant thickness and lateral extent to affect the long wavelength anomaly; (iii) crustal thickness variations (if it is assumed that there exists a significant density contrast between the crust and upper mantle below Iceland); and (iv) there is an elliptical low density mantle source.

3.6.1.2 Crustal Thickness Variations

The question of crustal thickness variations giving rise to the long wavelength gravity anomaly has been investigated further. The shape of the long wavelength anomaly matches the shape of Iceland quite closely. This leads to the possibility that variations in crustal thickness are responsible for a large part of the anomaly. It was assumed that a significant density contrast existed at the Iceland crust-mantle interface, which was totally responsible for the long wavelength anomaly, and a program by B. Kuo (see section 4.2.2.3 for details) was used to derive the crust-mantle relief at a depth of 25 km. Figure 3.19 represents the crust-mantle relief at 25 km depth for a 300 kg m^{-3} density contrast between the crust and mantle. A thickening of the crust by 8 km at the island's centre relative to the coast was found to account for the long wavelength anomaly. Taking isostasy into account, it would be expected that an 8 km root, relative to the coast, with a density contrast of 300 kg m^{-3} would be able to support 900 m of crust with a density of 2600 kg m^{-3} at the centre of the island. This is the approximate altitude of the plateau there.

One important problem with the model above is that plate motion has been ignored. Unless there has been a temporal variation in crustal thickness, with maximum crustal thickness coincident with the present, then a dome-shaped crust seems unlikely.

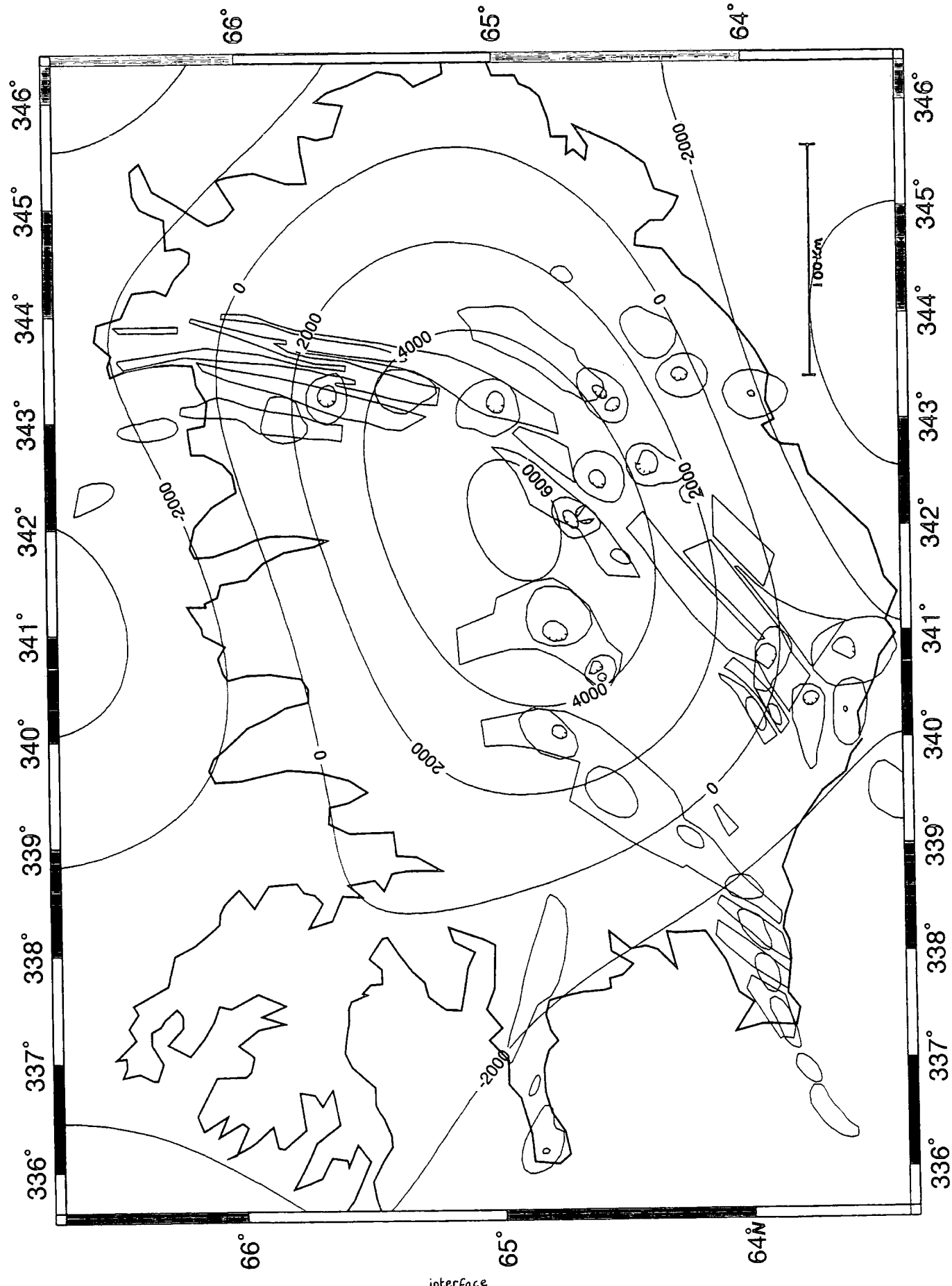

interface

Figure 3.19. Contour map of the crust-mantle beneath Iceland at a depth of 25 km for a density contrast of 300 kg m^{-3}, assuming that the long wavelength component of the gravity field is due a thickening of the crust. Contour interval is 1000 m. Tectonic units are also shown.

Instead, the expected crustal shape would be more two dimensional, with variations occurring perpendicular to the spreading direction.

Figure 3.19 suggests that if all of the anomaly is attributed to the shape of the crust-mantle interface the dome shaped gravity anomaly is caused by a dome shaped interface. It should be borne in mind that during the inversion of the gravity signal short wavelength information is eliminated. This means that using this inversion procedure will not produce a result which contains short wavelength information such as if there were a step feature present in the crust-mantle interface, and the remaining wavelengths will only be able to generate broad low frequency structures. Hence , although the dome shape may be true to some extent it lacks resolution.

Using a simple Bouguer slab model for an anomaly of 80 mGal with a density contrast between crust and mantle of 300 kg m-3 indicates that a thickening of about 6.5 km of crust relative to the neighbouring oceanic crust may occur. However, if the crust-mantle interface were simply a step function i.e. an additional slab of crust of uniform thickness below Iceland only, the resulting Bouguer anomaly, for a crust-mantle relief cause alone, would be a bowl with a flatter bottom and steeper sides than the observed anomaly.

3.6.1.3 Sub-Crustal Density Structure

To calculate the density structure of a deep slab, removal of the shorter wavelengths was carried out using cosine tapering in the Fourier domain. The filters used were low pass: between two specified wavelengths, low cut and low pass, tapering occurs; wavelengths smaller than low cut are eliminated; wavelengths greater than low pass are unaffected. The filtered signal was then converted into a density structure within a constant thickness slab at depth (section 2.4.7). To test the sensitivity of the results to slab thickness and depth to the top of the slab, two plots were made. One shows the peak to trough variation in density of the final model versus the thickness of the slab (figure 3.20a). A second shows again the peak to trough variation in density but this time versus depth to the top of the slab (figure 3.20b). Changes in slab thickness greater than 200 km have little effect upon the density structure of the slab causing less than 2 kg m^{-3} (~4%) of change for an increase in thickness of 600 km. Conversely, the peak to trough change in density is quite sensitive to the depth to the top of the slab; a change of 5 km producing a corresponding change of ~5 kg m^{-3} (~10%).

The slab thickness was chosen to be 200 km and the depth to the top of the slab was chosen to be 25 km on the basis of magnetotelluric (e.g. Beblo et al., 1983), geothermal (Flóvenz and Sæmundsson, 1993) and seismic evidence (Bjarnason et al., 1993; Evans and Sacks, 1979).

The density structures derived for the deep slab are depicted in figures 3.21 and 3.22. The values given in these figures can only be considered as relative, and to some extent are influenced by edge effects. The values given by the contours are anomalous density contrasts relative to the average mantle density throughout a 200 km thick slab. By inspection, it can be seen that both density structures are very much alike down to the -

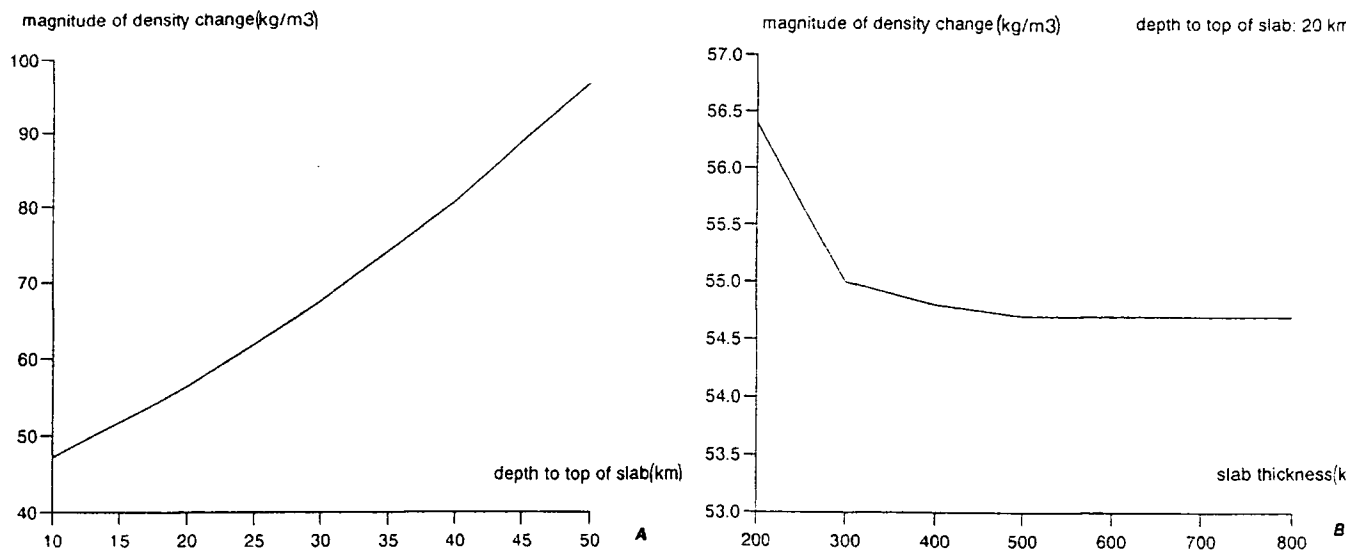

Figure 3.20. Testing the effect of different parameters on a constant thickness slab that has laterally varying density . The variation of density in the slab accounts for the long wavelength gravity component of the Icelandic gravity field. a) Amplitude of density variation within a 200 km thick slab versus depth to the top of the slab. b) Amplitude of density variation within a slab at a depth of 20 km versus the thickness of the slab.

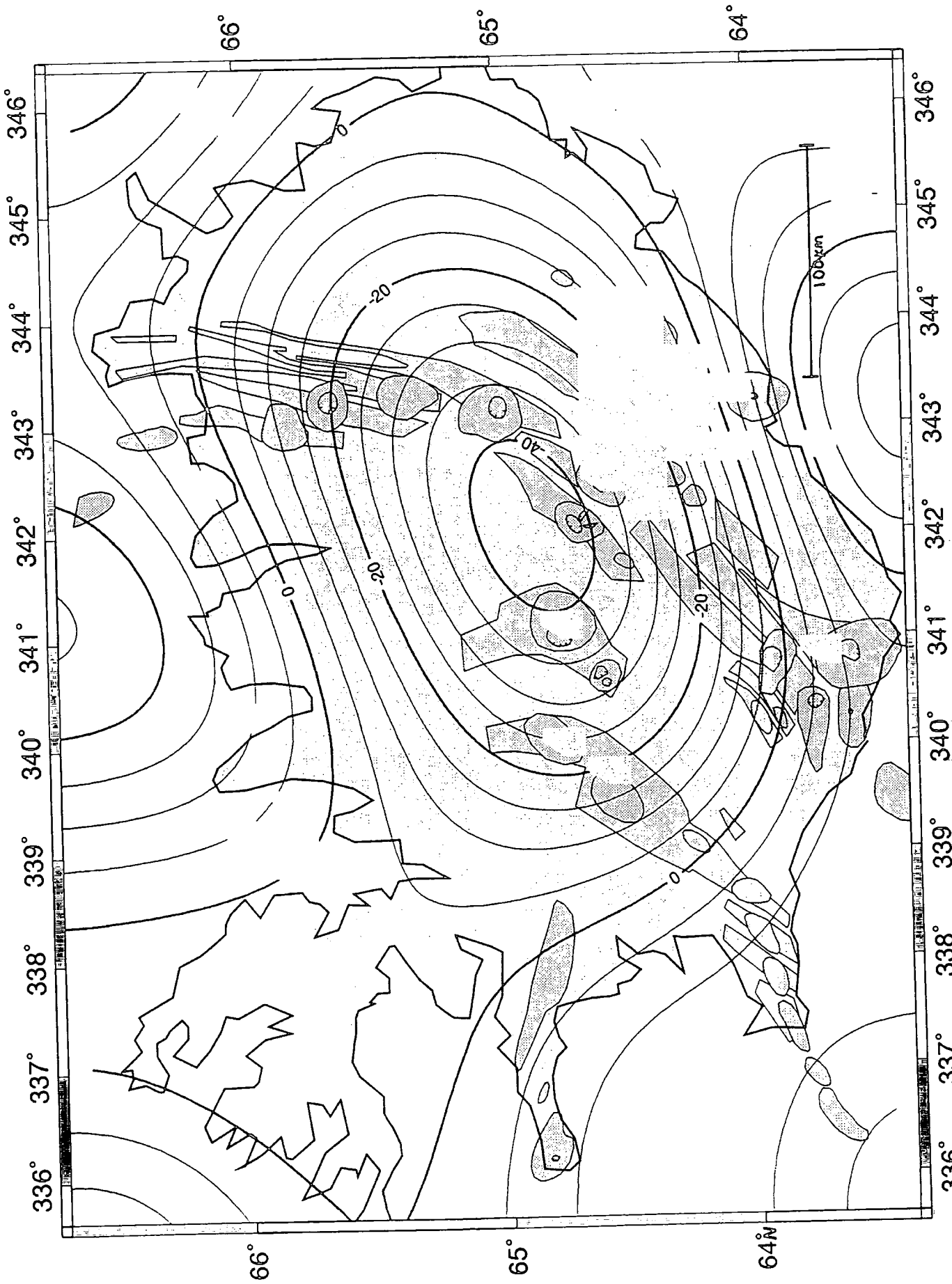

Figure 3.21. Density distribution within a 200 km thick slab at a depth of 25 km. This map was derived from CBA1. The contour interval is 5 kg m^{-3}. The tectonic units are shown as shaded polygons.

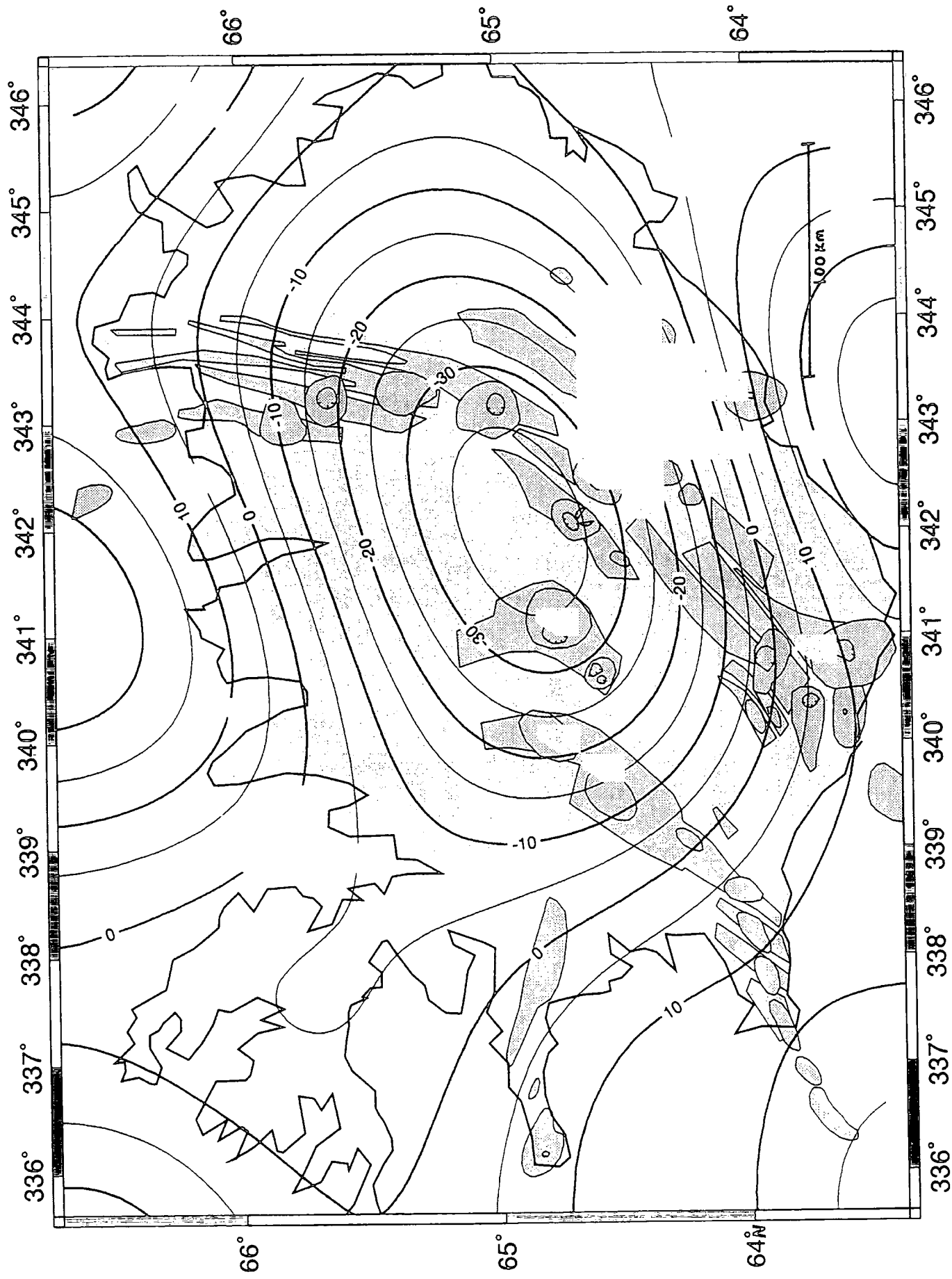

Figure 3.22. Density distribution within a 200 km thick slab at a depth of 25 km. This map was derived from CBA2. The contour interval is 5 kg m^{-3}. The tectonic units are shown as shaded polygons.

20 kg m^{-3} contour. At density contrasts more negative than this the structure derived from CBA1 achieves a more negative centre than that of CBA2 i.e. -40 kg m^{-3} rather than -30 kg m^{-3}.

It is possible that a temperature anomaly is responsible for the concentric variation in density by means of thermal expansion. If the temperature anomaly is a product of an upwelling mantle plume then temperature contours beneath Iceland will be controlled by a combination of conduction and advection of mantle material. Material moving perpendicular to the plate separation vector will be relatively unaffected whereas material moving parallel to the plate motion vector will acquire extra velocity, i.e. material of similar density will be transported further in the separation direction, and so deform an originally bull's eye pattern into an elliptical one.

3.6.1.4 Cylinder Model

If all the ellipticity is ignored, the long wavelength component of the gravity field can be approximated by a radially symmetric anomaly that is generated by a cylindrical density anomaly. If this cylinder is taken to represent a simplified mantle plume then estimates of some physical properties may be found. It was decided to model the plume beneath Iceland to a first approximation by a cylinder of infinite length with the top of the cylinder set 25 km below the surface. In the first instance two points in the long wavelength gravity field were fitted to a plume model, but later forward modelling of this result showed it to be an adequate fit to the rest of the field.

It is possible to compute the gravity field for a cylinder given that a radius, length, depth to the top of the cylinder and density have been assumed. Alternatively, which was done here, the density of the cylinder may be computed by varying the radius of the cylinder when the other parameters are fixed and the gravitational effect is known. The method used was to first, by inspection of the long wavelength anomaly, estimate the change in the gravity field, Δg, at some point (P) relative to the axis. Then, by calculating the gravitational attraction (vertical component) of a unit density cylinder of given radius at the axis (G_1) and at P (G_2) the density, ρ, could be found:

$$\rho = \Delta g \; / \; (G_1 - G_2) \qquad (3.1)$$

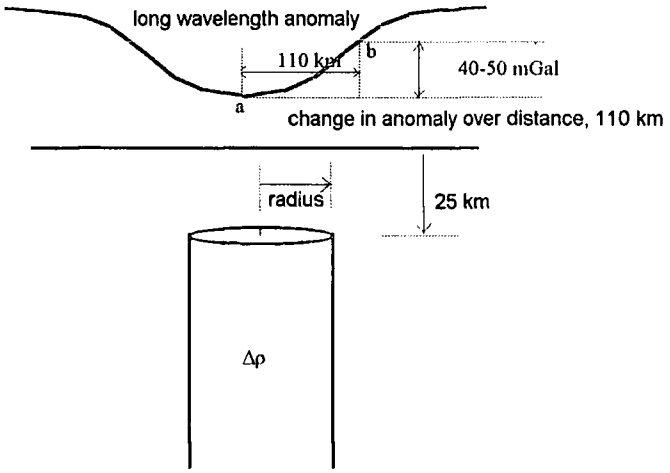

Figure 3.23. The cylinder model. The gravity effect of a cylinder of given radius, length (infinite), depth (25 km) and density (Δρ) is fitted to two points in the gravity field (a, b).

The change in gravitational attraction was taken to be between 40-50 mGal over a distance of 110 km from the axis of the cylinder (figure 3.23), where this number was an average taken by inspection of the long wavelength anomaly. The anomaly is assumed to be circularly symmetric and completely due to the effect of the underlying cylinder. This assumption gives rise to a maximum estimate of density contrast, within a single density cylinder of given radius, as any temperature anomaly would tend to heat the crust and surrounding mantle yielding additional negative density contrasts. Figure 3.24 shows the results of varying the radius of a cylinder of infinite length set 25 km below the surface. These results were calculated by making use of tables computed for a cylindrical body (Talwani, 1973). It can be seen that a radius of ~80-100 km produces the desired gravity anomaly for a minimum density contrast of -35 kg m^{-3}.

Plotting the forward modelled profile of a cylinder of radius 90 km, density contrast -35 kg m^{-3} and of thickness 600 km (large enough to give a similar answer to an infinite thickness) with approximately north-south and east-west profiles taken across the long wavelength gravity anomaly resulting from CBA2 shows a good fit (figure 3.25).

If -35 kg m^{-3} is assumed to be the density contrast of such a cylinder (~100 km radius) then the whole anomaly it gives rise to is ~-100 mGal, which is much smaller than Bott (1988) had previously predicted. However, Hermance (1981a and b) proposes that if underplating of the Icelandic crust occurs producing a crustal thickness of ~25 km, then the mantle contribution would be reduced to -100-150 mGal. Thus, an

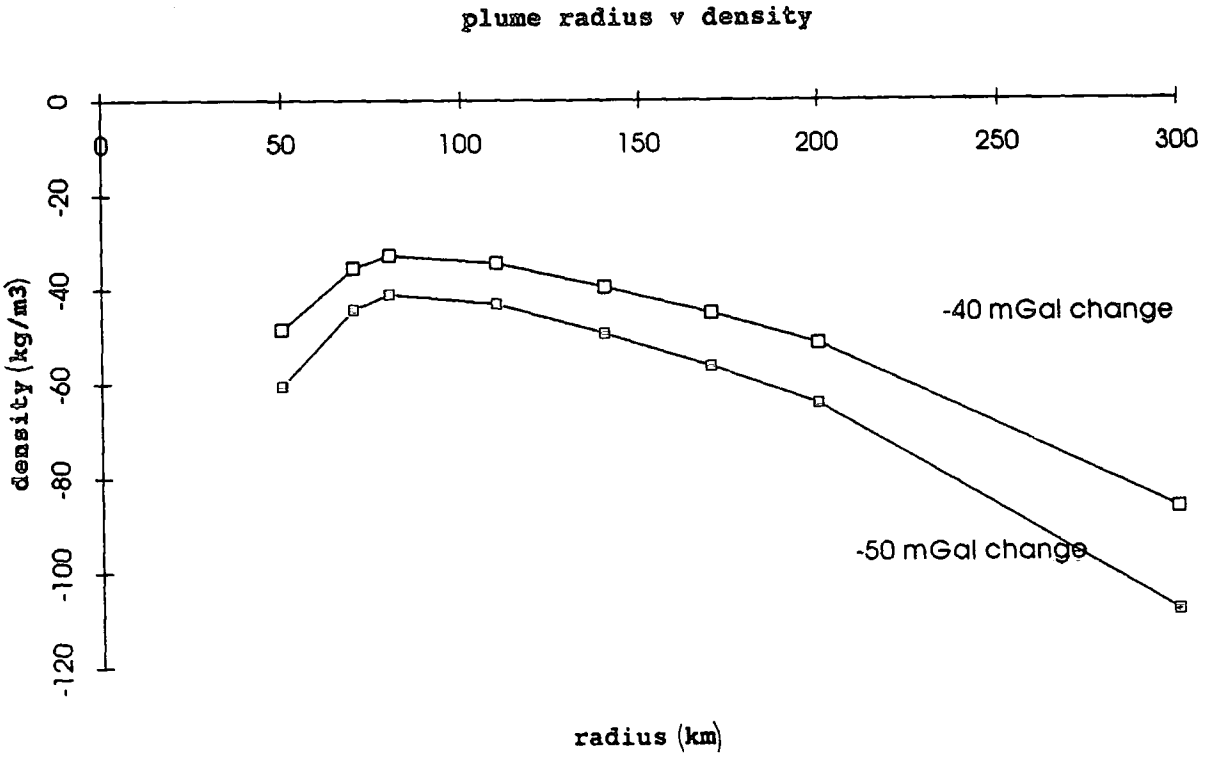

Figure 3.24. Anomalous density required by an infinitely long cylinder, of a given radius, at a depth of 25 km to produce a radial change in gravity of -40 mGal (white squares) or -50 mGal (black squares) over 110 km from the axis. Squares represent calculated values.

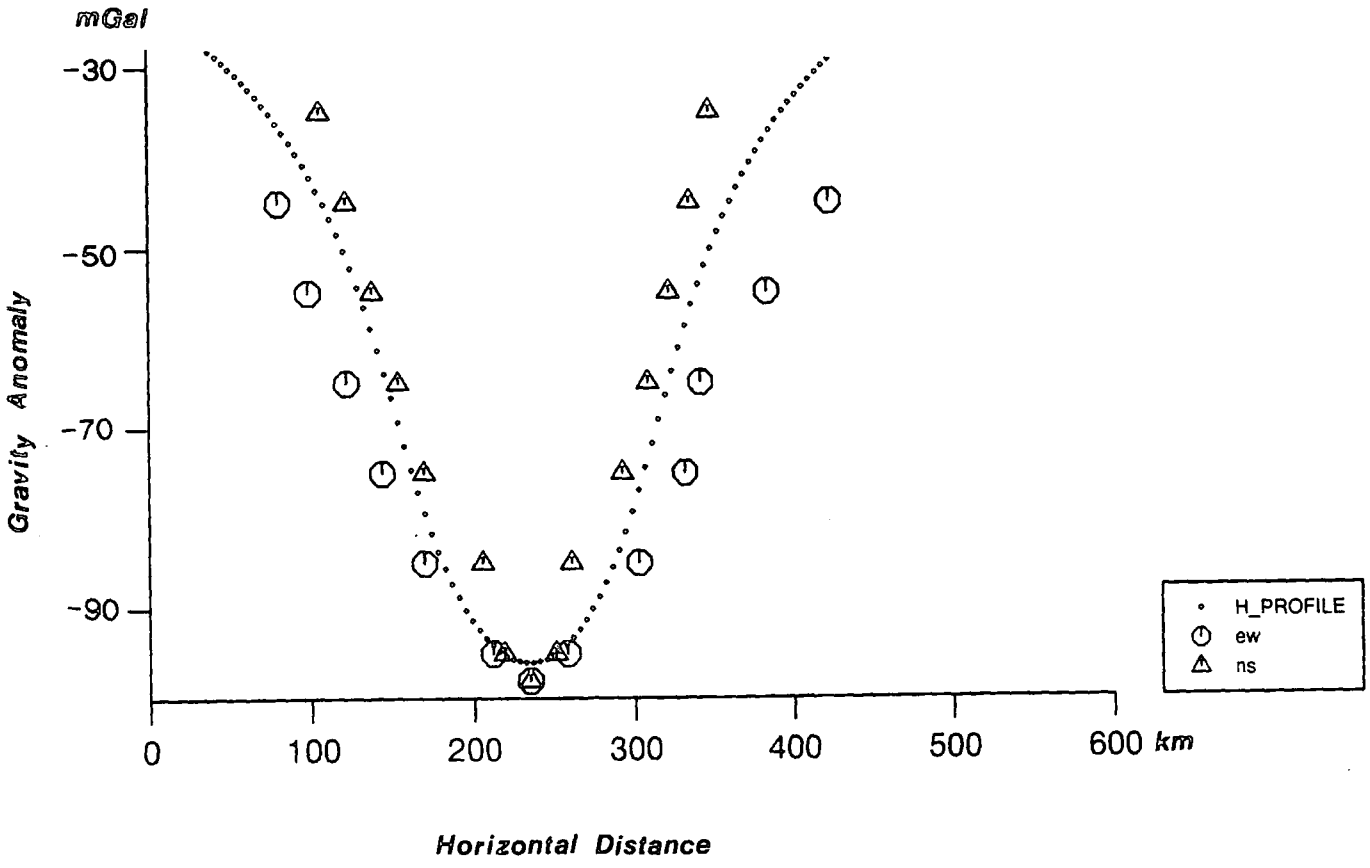

Figure 3.25. Octagons represent an approximate east-west traverse across the long wavelength component of CBA2. Triangles represent an approximate north-south traverse across the long wavelength component of CBA2. The dots are a profile above the axis of a 3D model of a cylinder set at 25 km depth, 600 km long, and 90 km in radius.

infinitely long cylinder that has a radius and density of ~100 km and -35 kg m^{-3} may represent a lower constraint for the physical properties of the Icelandic mantle plume.

All that is necessary now is a mechanism for producing the required -35 kg m^{-3} density contrast. If it is assumed that the plume exists at an average excess temperature of 250°C, within the cylinder, and that the thermal expansion coefficient is ~$4x10^{-5}°C^{-1}$, then this would give rise to about -33 kg m^{-3} for a mantle density of 3300 kg m^{-3}. This is a maximum average temperature estimate as other negative density contributions may come from solid-solid transitions (Hermance 1981a). One other very important contribution is that of partial melt. Partial melt will only be present at depths shallower than 60 km (Ahern and Turcotte, 1979), but a partial melt fraction of 10 % could provide a density contrast of -30 kg m^{-3} (Bott, 1988).

In summary, a cylindrical mantle plume of ~100 km radius extending from 25 km below sea level to infinity at a temperature of 250°C could give rise to the observed bowl-shaped Bouguer low over Iceland. The required -35 kg m^{-3} density contrast could be caused by a combination of thermal expansion and solid-solid phase changes and occurrence of partial melt within the plume.

3.6.1.5 A Comparison of Regional Tomography and Gravity Observations over Iceland

This section attempts to compare the observed Bouguer low observed over Iceland (Einarsson, 1954) with tomographic evidence for mantle velocity structure beneath Iceland (Tryggvason et al., 1983) by means of a 'gravity-velocity' inversion.

Compressional wave travel time data were collected on Iceland and subjected to three dimensional tomographic inversion by Tryggvason et al. (1983). The data consisted of 61 events recorded at 39 stations (figure 3.26). The inversion resulted in a final model which reduced the RMS delay time by 18%, leaving some 0.38s of RMS delay time unaccounted for and presumably due to observational errors. The velocity structure was calculated at four levels down to a depth of 375 km, with layer one having a thickness of 75 km and layers two, three, and four having a thickness of 100 km. Each of the layers was divided into blocks approximately 144 x 66 km^2 in horizontal extent.

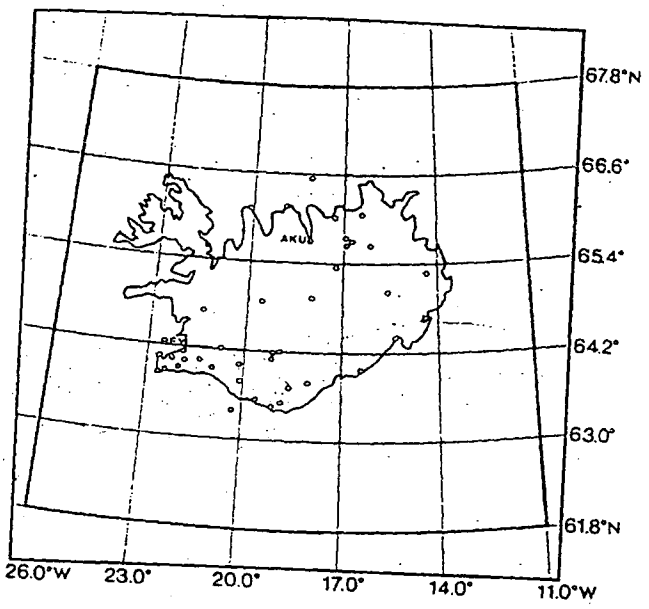

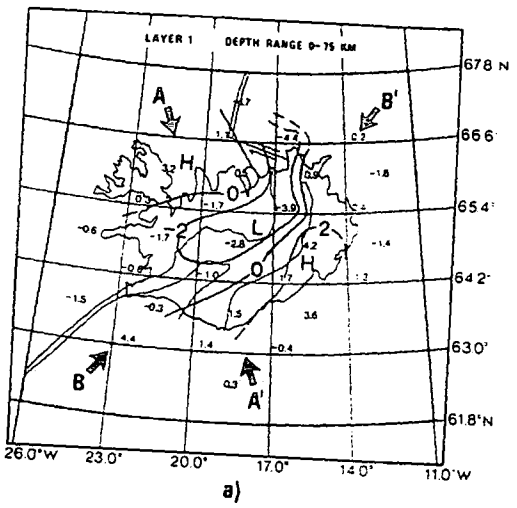

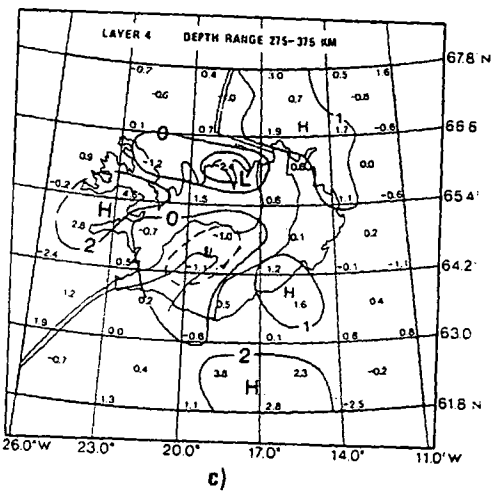

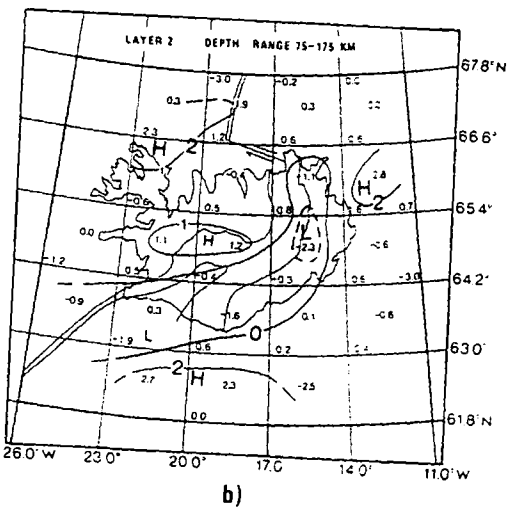

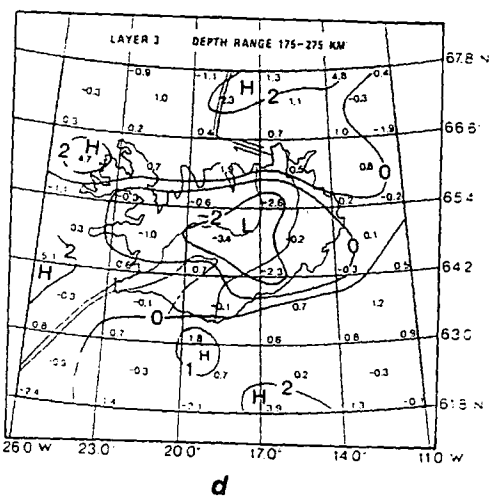

Figure 3.26. (top) Icelandic network of 39 seismograph stations used in the tomographic analysis of Tryggvason et al. (1983). The model box is circumscribed with heavy lines. a) Velocity perturbations (%) for layer 1. Areas of high and low velocities are indicated by capital letters H and L. b), c), and d) are the same as a) for their respective layers. From Tryggvason et al.(1983).

The results of the inversion provided a seismic image of the Icelandic mantle (figures 3.26a,b,c and d) and were as follows. In the uppermost layer (0-75 km) a velocity low, of the order of 2%, was found to extend from the Tjörnes Fracture Zone (TFZ), south-westwards towards Snaefellnes and Reykjanes. The observed low roughly corresponds with the neovolcanic zone with the TFZ and Krafla marking pronounced velocity lows (~4%). In the three deeper layers the low velocity volumes are seen to lie further south eventually becoming more centralised with respect to Iceland. Tryggvason et al. (1983) interpret the results as indicating the presence of a hotspot beneath Iceland to a depth greater than 300 km in support of the plume hypothesis.

The 'bowl-shaped' Bouguer low first reported by Einarsson (1954) may also be interpreted as being the result of upwelling 'hot' mantle. To test if the results of the tomography are consistent with the gravity observations the two sets of data need to be coupled in some way. Empirically, it is seen that rock density is approximately linearly related to velocity (Birch, 1961) (section 2.3.3.1). If the generalised Birch relationship is adopted: $\rho = \alpha V_p + \beta$ (equation 2.2), where ρ is the density, V_p is the P-wave velocity, and α, β are constants, then it becomes possible to use the velocity and gravity observations to obtain α:

The gravitational effect, g, of an assemblage of n perturbing bodies can be written as:

$$g = \sum_{i=1}^{n} B_i \Delta\rho_i \qquad (3.2)$$

where B_i is the vertical component of the gravitational effect of a unit density perturbing body, $\Delta\rho_i$ is the density contrast of each perturbing body. From equation 2.2 it can be seen that $\Delta\rho = \alpha\Delta V_p$, where ΔV_p is the velocity perturbation, and so equation 3.2 becomes:

$$g = \alpha \sum_{i=1}^{n} B_i \Delta V_{p_i} \qquad (3.3)$$

Therefore, if g and the appropriate summation is known for all stations, then α may be found by linear regression. The 'inversion' was carried out using the percentage velocity perturbation rather than an actual velocity perturbation. The P-wave velocity only varies between ~ 8 - 9 km s^{-1} in the top 500 km of the Earth (Bullen and Bolt, 1985), so there will not be much difference in actual velocity perturbations for the same percentage perturbation at different depths. The result is that α will be multiplied by another

constant factor. The gravitating masses were treated as cells of 140x66x75 km (WxNxZ) or 100 km (Z) depending on layer. To reiterate, when the combined gravitational attraction of all the cells (figure 3.26), are calculated at each gravity station and plotted against the observed gravity at that station, then if there is a linear relationship between density and velocity, the points will plot on or near a straight line. Figure 3.27 depicts such a plot. The straight line is the least squares best fit. The scatter graph has a correlation coefficient of 0.19 which seems very poor. The only semblance of correlation seems to occur in the bottom left hand of the plot which is probably due to the velocity low coinciding with the central Bouguer low. Although there is usually a lot of scatter observed for empirical velocity-density plots, figure 3.27 looks unusually scattered. Possible causes for such a lack of correlation are:

(i) The gravity observations are wrong;
(ii) The results of the tomography are wrong;
(iii) A superposition of many velocity-density relationships is occurring; and
(iv) No simple velocity-density relationship exists for these data.

It seems unlikely that (i) is the case. Subsequent to Einarsson's (1954) initial discovery of the Bouguer low a more densely surveyed gravity map has supported this observation (Thorbergsson et al., 1990), and is the data used in this study. Case (ii) is open to debate. Tryggvason et al. (1983) quote an RMS time of 0.38s which they attribute to observational errors and the final reduction in the time residual variance was only 33% compared to 87% for a similar study of the Kilauea Volcano, Hawaii (Ellsworth and Koyanagi, 1977). Even if case (ii) were only partly true, cases (iii) (iv) would still further confuse the picture. The hint of correlation in the bottom left hand corner of figure 3.27 may be an indication that case (iii) has a strong influence. A possible source of error is in the fact that most of the stations used in the tomography study were located over regions where partial melt is inferred to exist and Birch's law does not apply. It is possible that the time delay caused by this relatively thin layer has been averaged over the complete thickness of the of the top cells i.e. 75 km.

In conclusion, the results of the tomographic inversion were not very consistent with the observed Bouguer gravity. This could be due to a combination of error within the tomographic results coupled with the effect of multiple velocity-density relationships and the presence of partial melt.

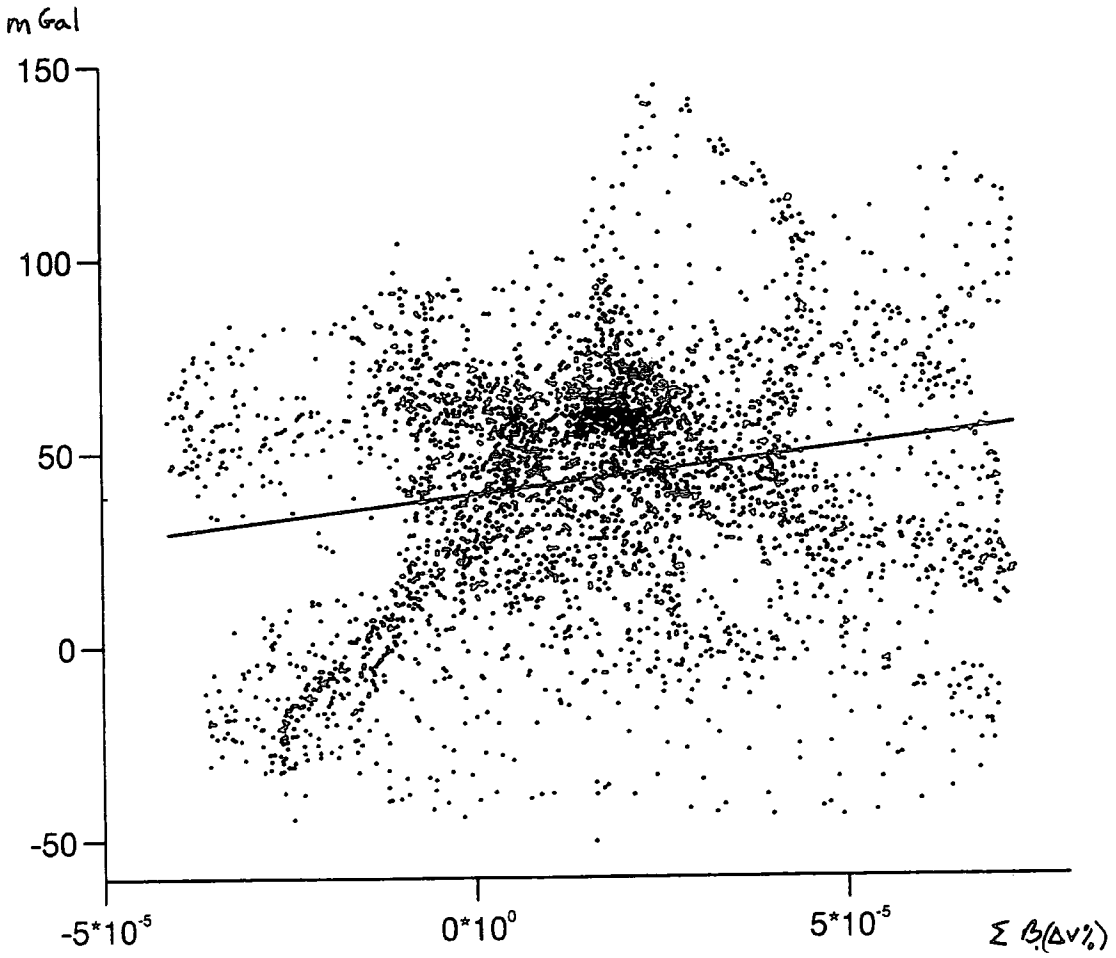

Figure 3.27. Bouguer anomaly values for Iceland (single density reduction of 2600 kg m^{-3}) versus Σ B (velocity perturbation %) (see section 3.6.1.5). The vertical axis is in mGal.

3.6.2 The Short Wavelength Component

3.6.2.1 Introduction

In this section possible short wavelength gravity anomalies will be identified and the effects of some expected causes of gravity anomalies considered as sources. Anomalies which encompass many of the original gravity stations and have a magnitude in excess of 10 mGal are deemed to be real anomalies that require explanation.

The anomalies revealed in the residual maps are thought to be due to lateral density differences within the crust, or possibly at the base of the crust within the upper mantle. Crustal thickness variations seem an unlikely cause given that the maximal depth of the short wavelength anomalies is thought to be less than 5 km. In some cases crustal thickness variations would give erroneous results such as at the axis where greater crustal thickness would be required contrary to evidence provided by magnetotelluric and geothermal work. In this next section crustal rocks are considered to be able to vary laterally in density due either to their composition and/or thermal expansion. By assuming that densities varied laterally only, maps of density within a slab of given thickness were computed (section 2.4.7). This was done for slabs of thickness 1 km, 5 km, 10 km, 25 km (figures 3.28, 3.29, 3.30 and 3.31). For the 1 and 5 km thick slabs a filter which removed wavelengths smaller than the Nyquist wavelength, 20 km (for a station spacing of ~10 km) and then cosine tapered up to 30 km was used. For the 10 and 25 km thick slabs, high frequency instabilities were eliminated with a filter that removed wavelengths smaller than 30 km and then cosine tapered up to 40 km. It should be remembered that the density variations obtained for these slabs cannot be wholly applied to the sea areas as the slabs begin at sea level.

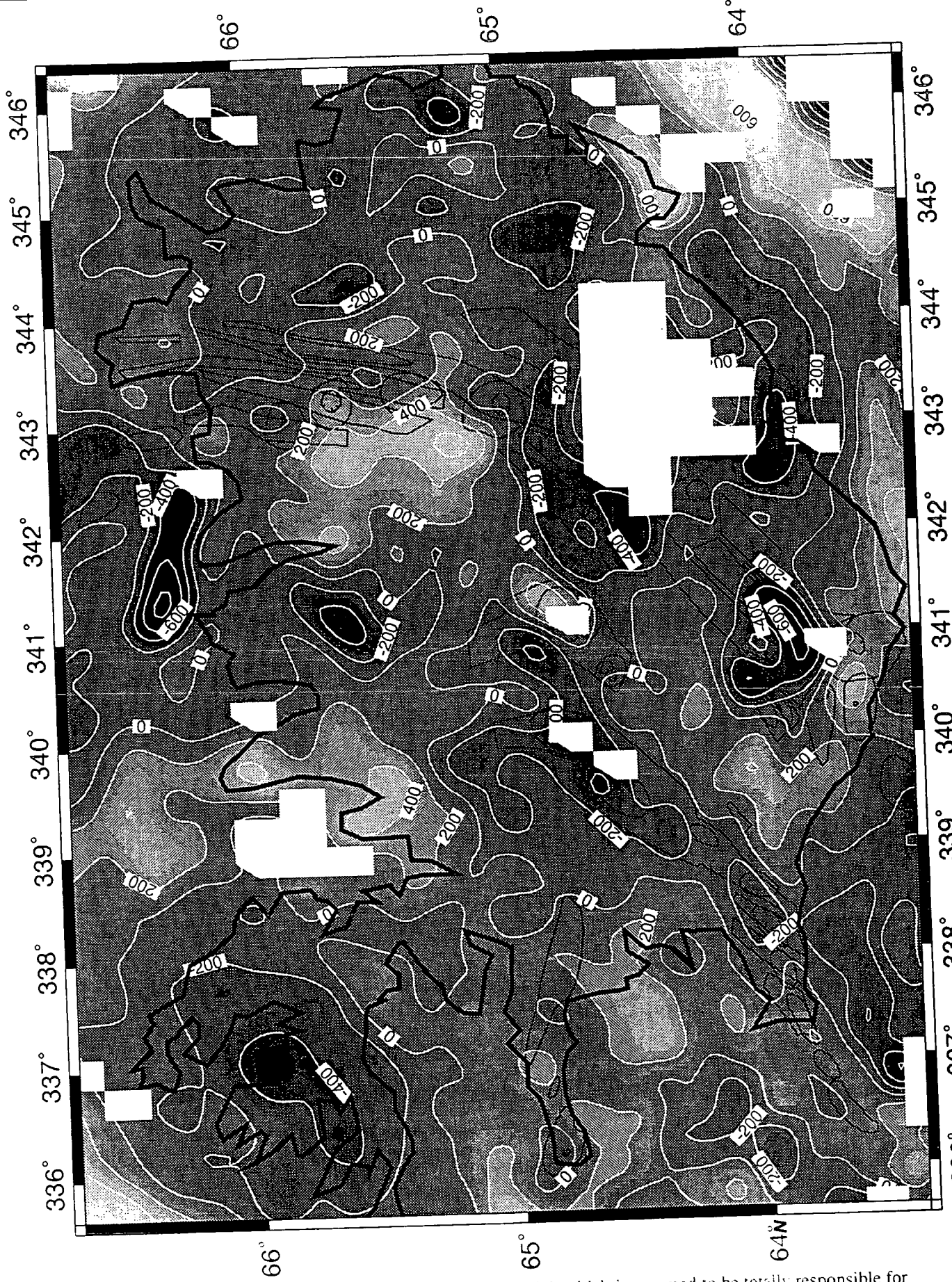

Figure 3.4.7a. Density distribution within a 1 km thick slab which is assumed to be totally responsible for the short wavelength component of CBA1. The white contour line interval is 200 kg m^{-3}. The shaded scale goes from dark (low) to light (high) in 100 kg m^{-3} steps. Tectonic units are marked as thin black lines.

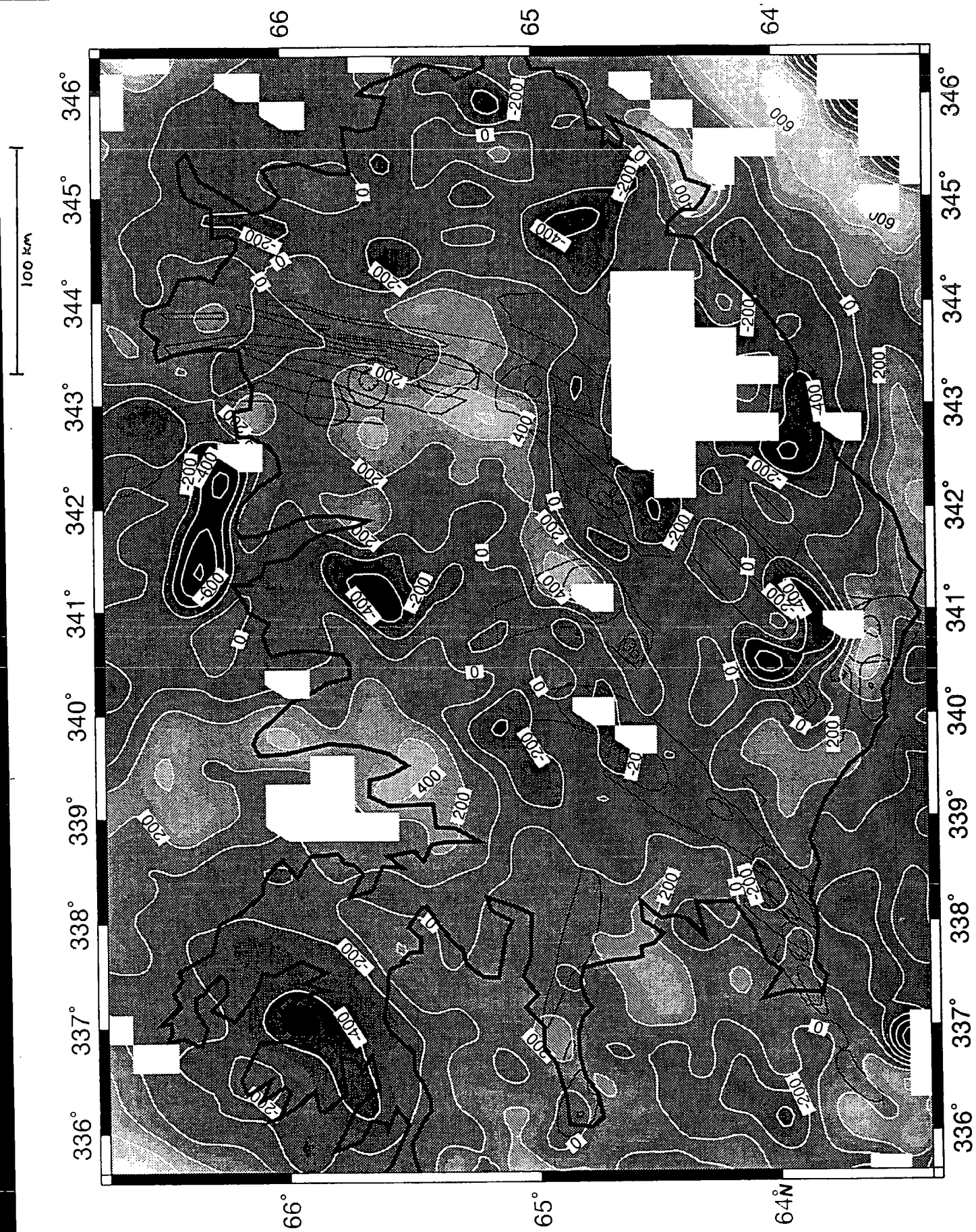

Figure 3. b. Density distribution within a 1 km thick slab which is assumed to be totally responsible for the short wavelength component of CBA2. The white contour line interval is 200 kg m^{-3}. The shaded scale goes from dark (low) to light (high) in 100 kg m^{-3} steps. Tectonic units are marked as thin black lines.

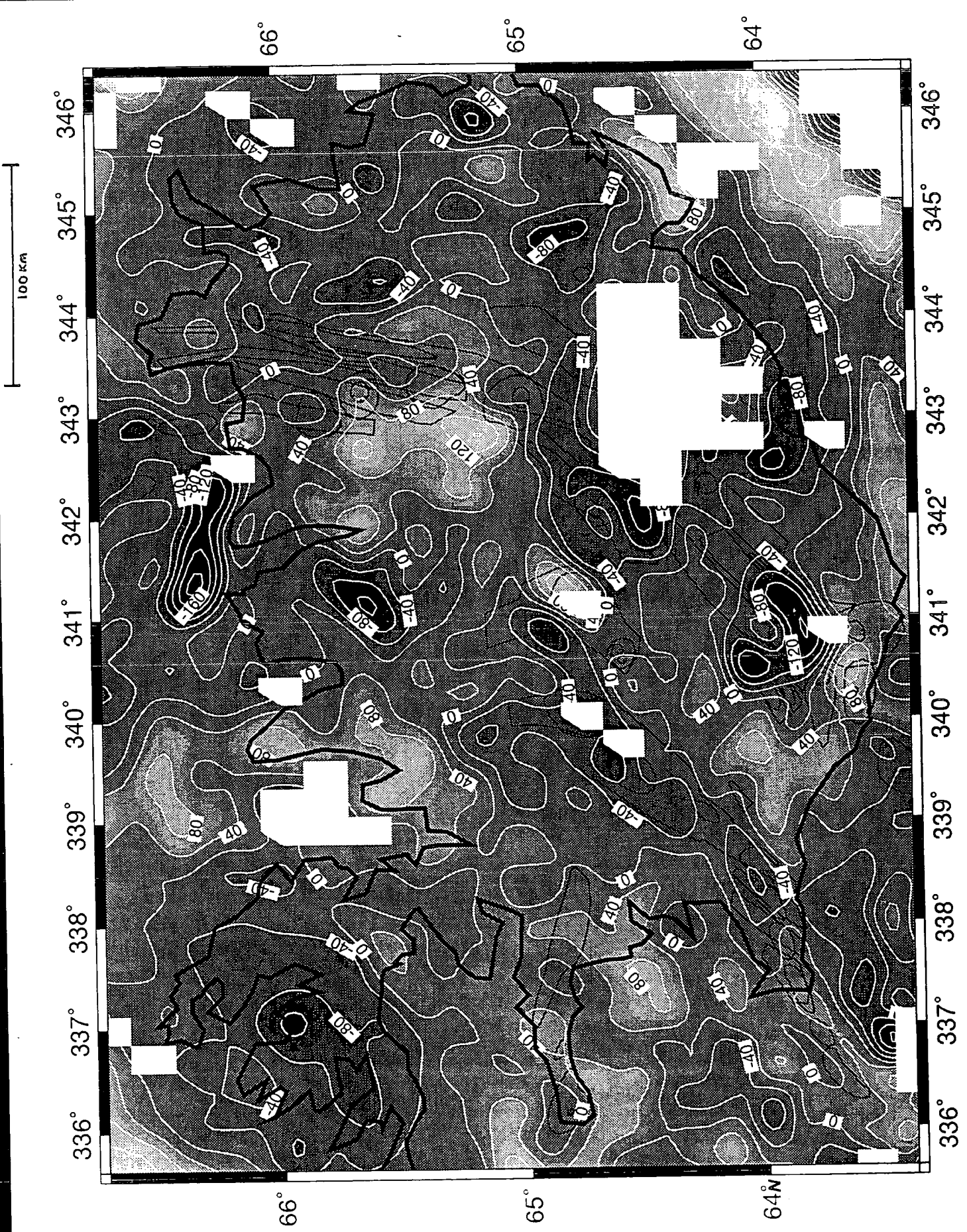

Figure 3.29 a. Density distribution within a 5 km thick slab which is assumed to be totally responsible for the short wavelength component of CBA1. The white contour line interval is 40 kg m^{-3}. The shaded scale goes from dark (low) to light (high) in 20 kg m^{-3} steps. Tectonic units are marked as thin black lines.

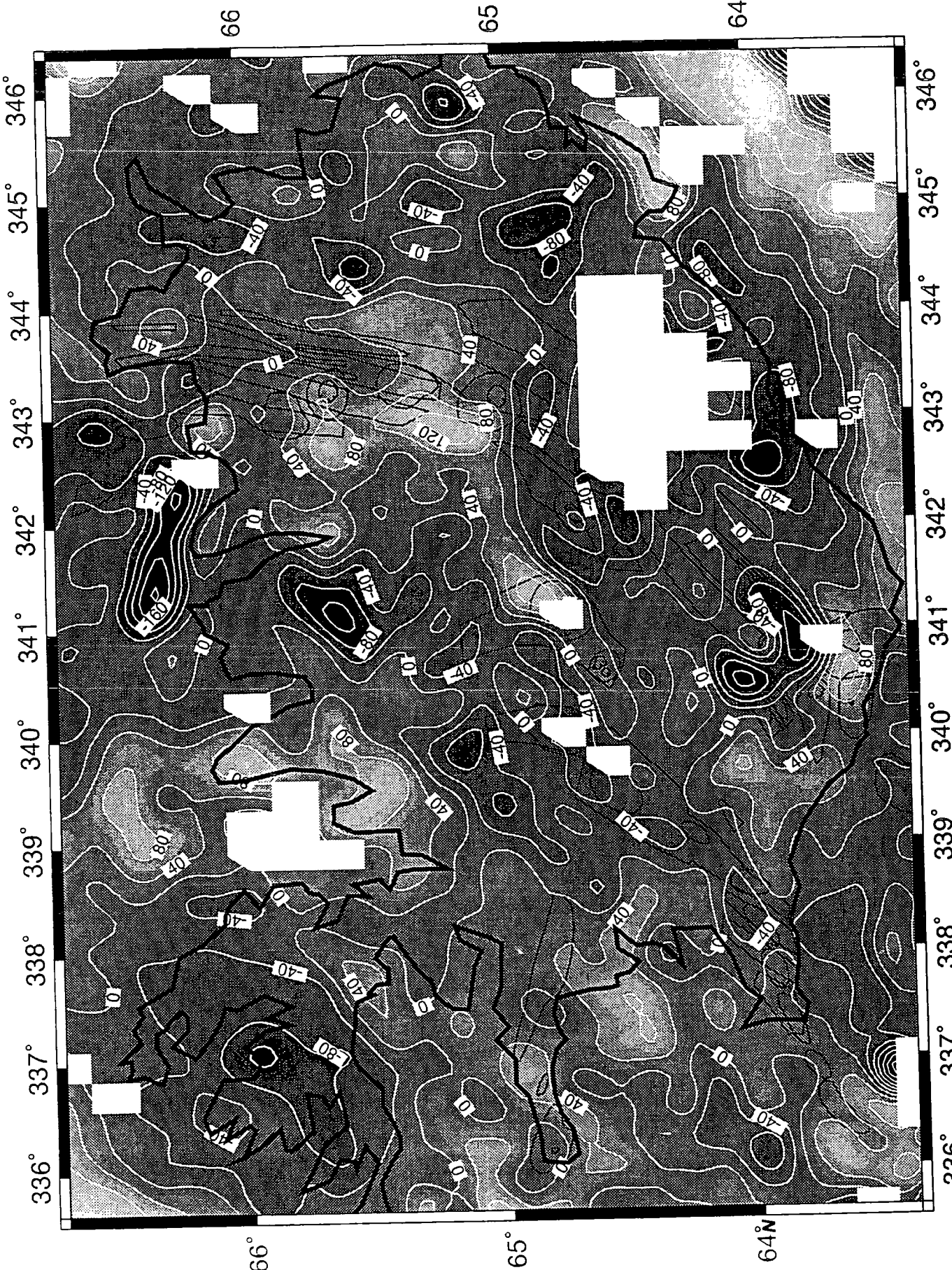

Figure 3.6 b. Density distribution within a 5 km thick slab which is assumed to be totally responsible for the short wavelength component of CBA2. The white contour line interval is 40 kg m^{-3}. The shaded scale goes from dark (low) to light (high) in 20 kg m^{-3} steps. Tectonic units are marked as thin black lines.

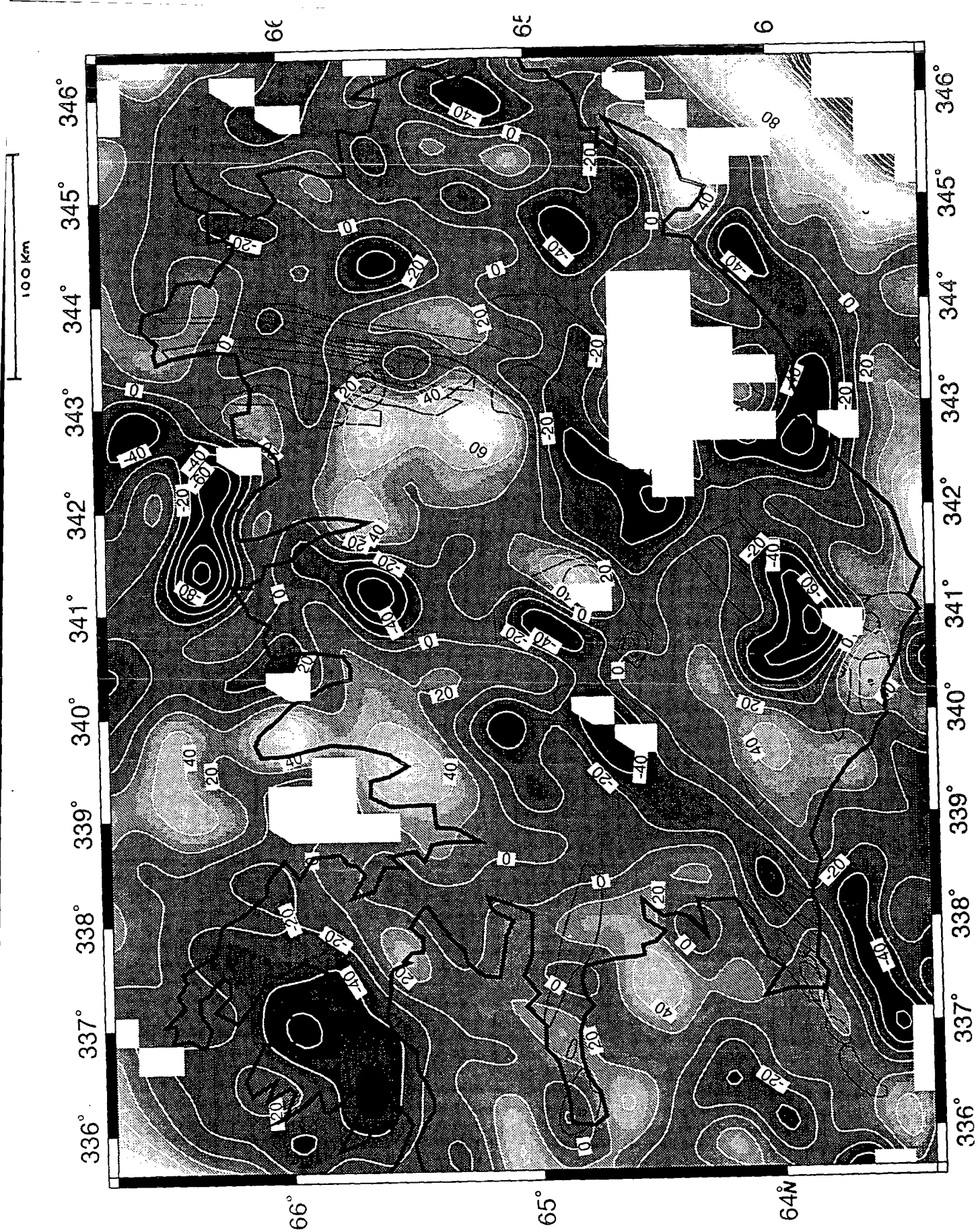

Figure 3.30 a. Density distribution within a 10 km thick slab which is assumed to be totally responsible for the short wavelength component of CBA1. The white contour line interval is 20 kg m^{-3}. The shaded scale goes from dark (low) to light (high) in 10 kg m^{-3} steps. Tectonic units are marked as thin black lines.

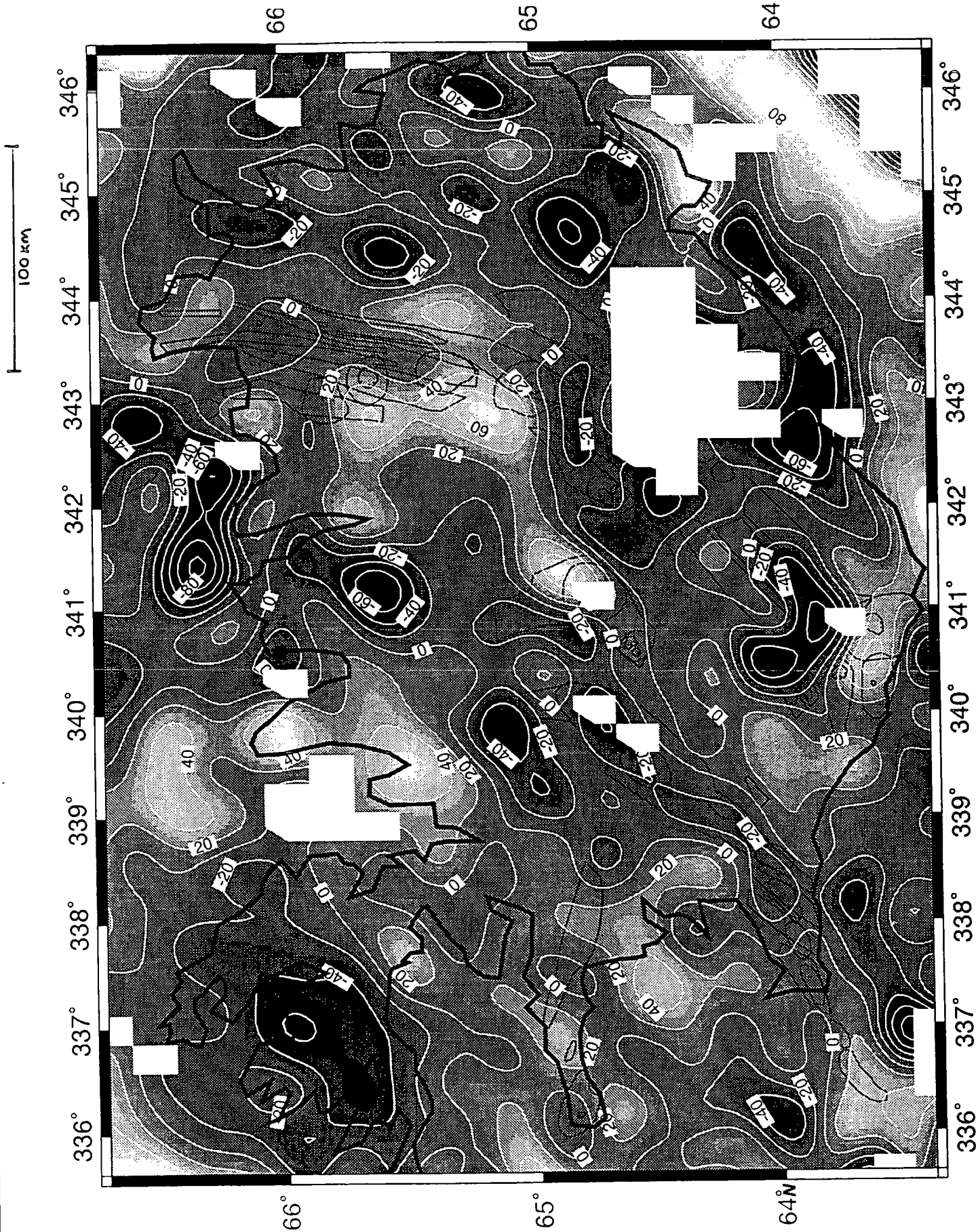

Figure 3.30.b. Density distribution within a 10 km thick slab which is assumed to be totally responsible for the short wavelength component of CBA2. The white contour line interval is 20 kg m^{-3}. The shaded scale goes from dark (low) to light (high) in 10 kg m^{-3} steps. Tectonic units are marked as thin black lines.

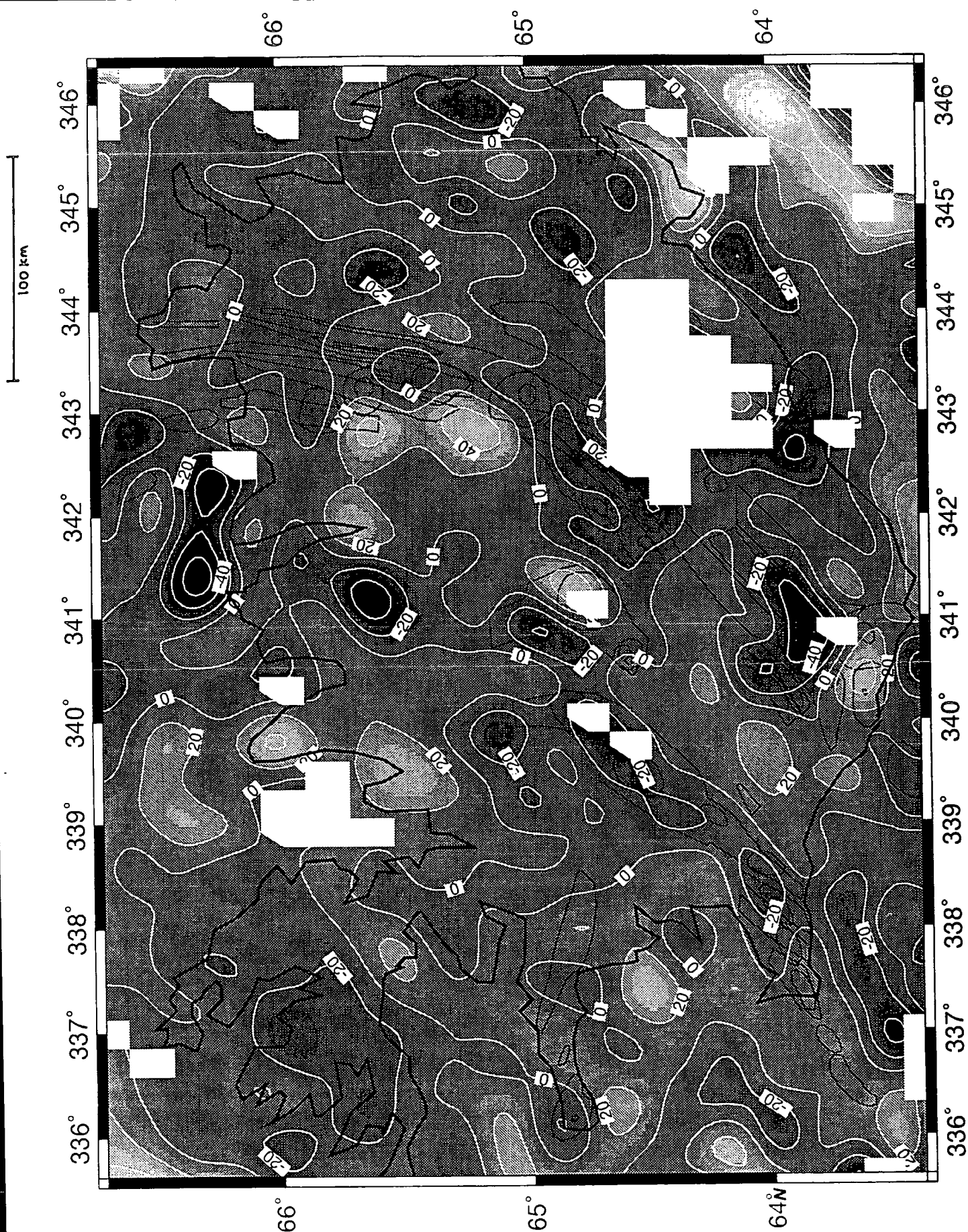

Figure 3.3: a. Density distribution within a 25 km thick slab which is assumed to be totally responsible for the short wavelength component of CBA1. The white contour line interval is 20 kg m^{-3}. The shaded scale goes from dark (low) to light (high) in 10 kg m^{-3} steps. Tectonic units are marked as thin black lines.

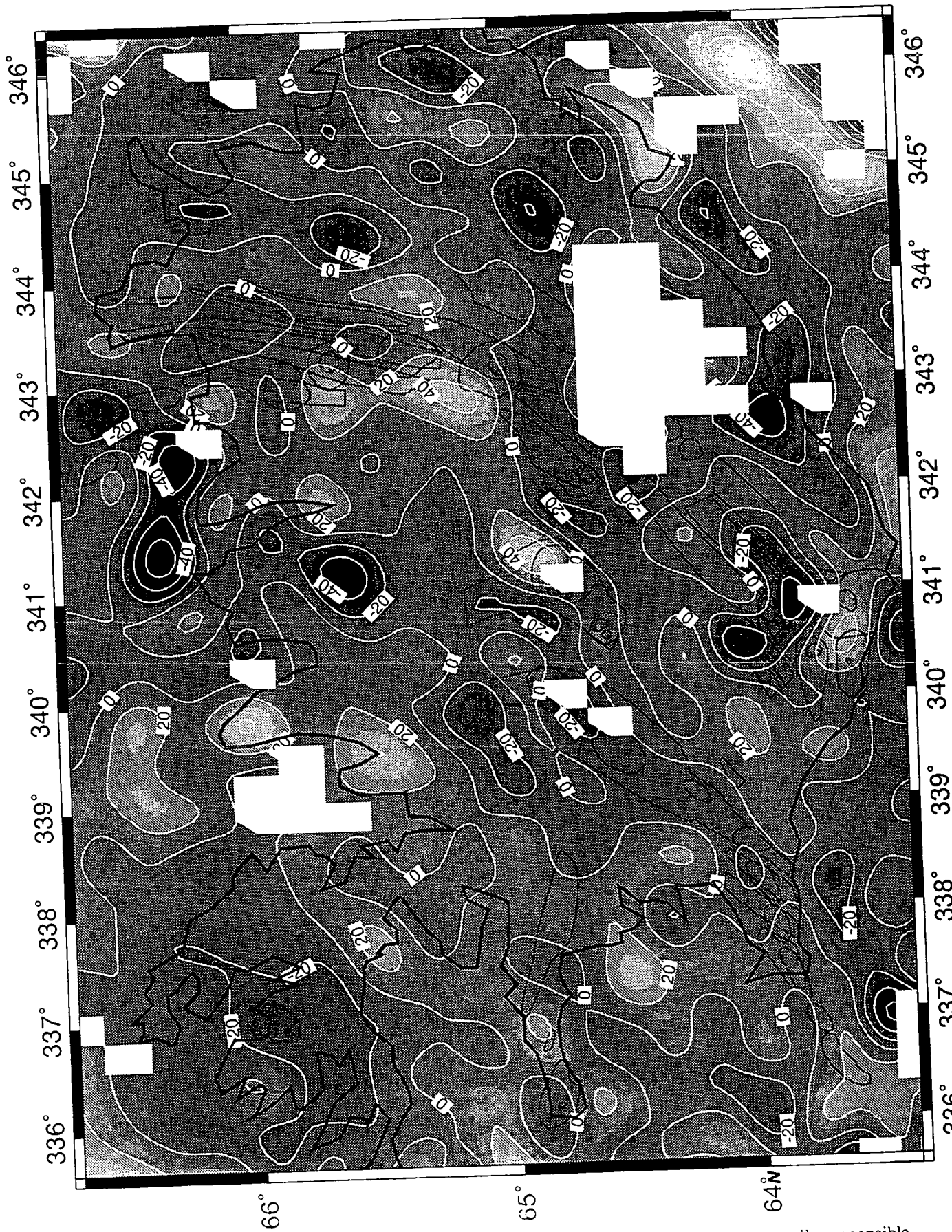

Figure 3.31b. Density distribution within a 25 km thick slab which is assumed to be totally responsible for the short wavelength component of CBA2. The white contour line interval is 20 kg m^{-3}. The shaded scale goes from dark (low) to light (high) in 10 kg m^{-3} steps. Tectonic units are marked as thin black lines.

3.6.2.2 Gravity Signature of Iceland's Spreading Plate Boundaries

Before looking at the anomalies in detail it was decided to calculate the gravity signature due to a spreading lithosphere, as encountered in the oceanic setting, to assess its contribution to Iceland's gravity field.

A thermal model which has been used by other workers (e.g. Morris and Detrick, 1991; Lin et al., 1990) is that of Morgan and Forsyth (1988). Their method makes use of a finite element model which is used to produce the thermal effects of more geometrically complex ridge-transform systems. Morgan and Forsyth (1988) solve for a uniform viscosity mantle flow in a half-space. The resulting three dimensional temperature distribution is converted to density and its gravitational effect at the surface is calculated. This is all done using a set of programs written by D. Forsyth and made available to R. Searle.

The gravity signature for Iceland's ridge system was computed using the set of programs supplied by Forsyth. The upper layer of the model was set at sea level and the base of the model was set at depths of 100 km and 25 km. The deeper depth is that usually used in marine gravity reductions and the shallower depth is the proposed thickness of the Icelandic lithosphere, i.e. the depth to the partial melt. The temperatures of the upper and lower boundary were 0°C and 1250°C, respectively. The nodal spacing of the model was ~8 x 6 km. Forsyth's set of programs do not allow for the possibility of overlapping ridge segments such as the WVZ and EVZ. As a compromise two models were created: one described the EVZ and NVZ and the other described the WVZ and the NVZ. Figure 3.32 depicts the ridge geometry used. The signals from each of the models was calculated at 1 km above sea level. The results from the 100 km thick model (figures 3.33a and b) show a variation of ~ 60 mGal over the whole region with lows centred over the neovolcanic zones as expected. Anomalies of this size and shape do not seem to be evident in the Bouguer gravity field of Iceland. The 25 km thick model exhibits a variation of ~ 4 mGal which is below the noise threshold of the gravity field (figures 3.33c and d). Thus, the apparent absence of a ridge gravity signature derived from a thermal expansion of the lithosphere may imply that a thermal effect of typical oceanic proportions does not exist below Iceland. The influence of the hotspot is a probable cause - its proximity perturbing isotherms into horizontal stratifications resulting in little lateral temperature contrast, and hence little density contrast. Another complication of Icelandic geodynamics is the frequent shifting of the plate boundaries (Helgason,

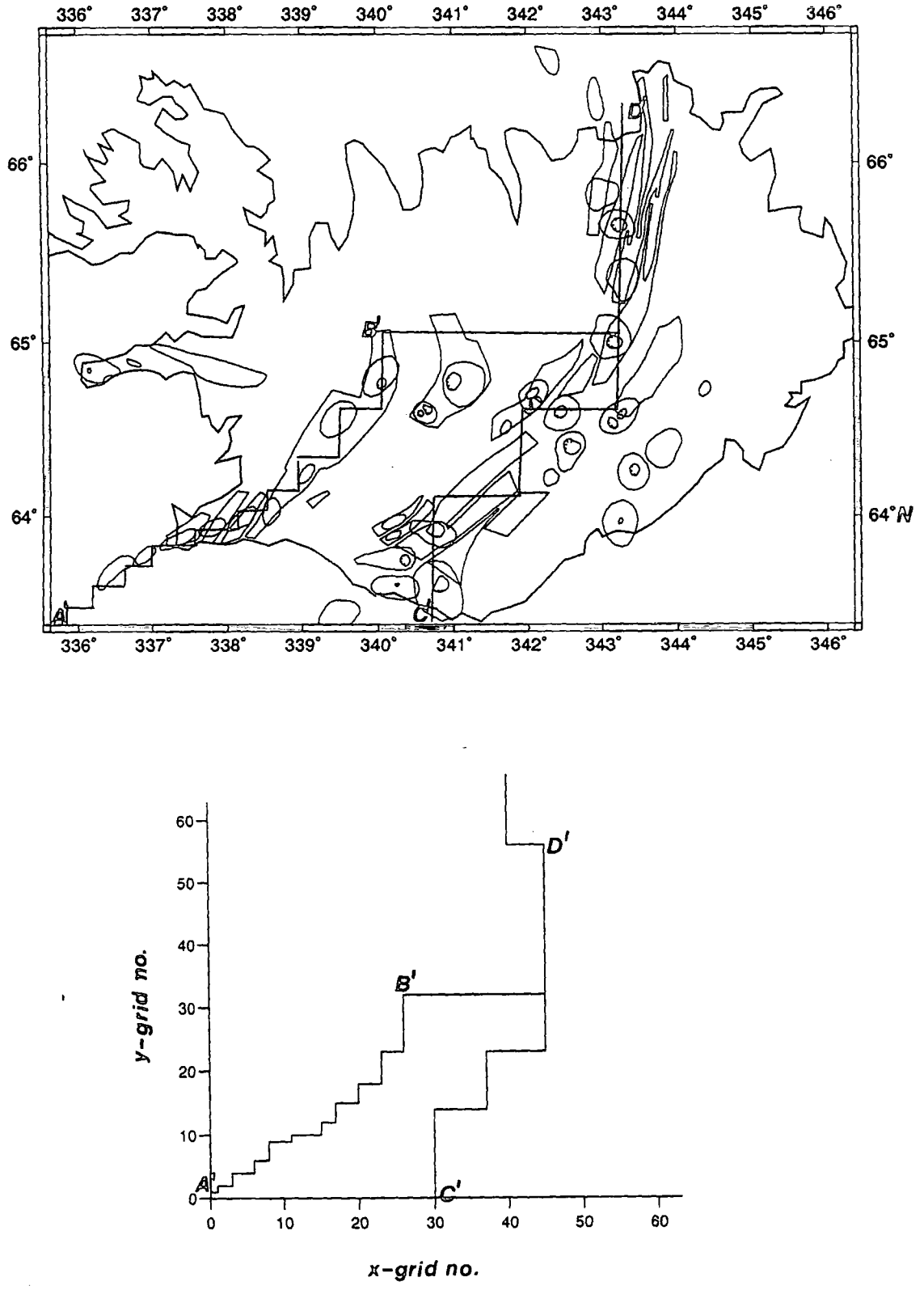

Figure 3.32. (top) Trace of the ridge geometry (orthogonal black lines) used for calculating the lithospheric cooling effect in Iceland (using a program written by D. Forsyth). The two separate geometry s are coincident north of ~65°N. (bottom) The ridge geometry on the 64 by 64 node grid. The grid spacing is 8.29 km (left-right) and 5.92 km (up-down).

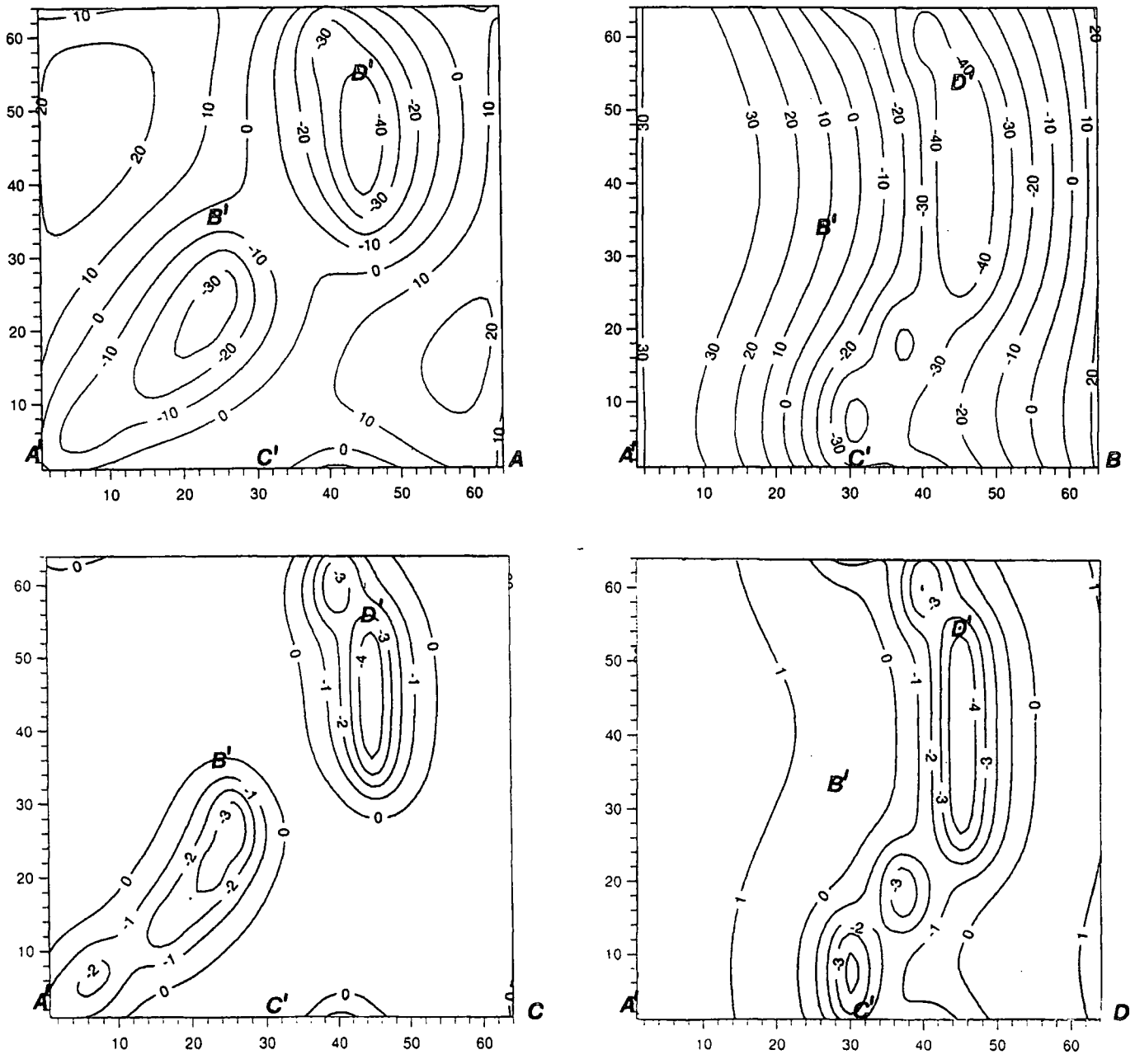

Figure 3.33. Gravitational effect of cooling lithospheric plates with the geometry shown in figure 3.32 a) The western and northern parts of the ridge geometry showing the gravitational effect of a 100 km thick lithosphere. The contours are labelled in mGal. b) The eastern and northern parts of the ridge geometry (100 km thick lithosphere). Contours in mGal. c) The same as (a) except the lithosphere is 25 km thick. d) The same as (b) except the lithosphere is 25 km thick.

1985 and 1985). Pálmason (1980) states that volcanic accretion has to be active in one place for several million years before the steady state properties described by his model are applicable. Therefore, Iceland's volcanic zones are unlikely to have a well matured thermal and gravity signature.

3.6.2.3 The Short Wavelength Gravity Anomalies

The Western Volcanic Zone (338°E, 64°N to 340°E, 64°50'N)

A pronounced gravity low, ~15-20 mGal (figure 3.18), correlating with shallow P-wave velocities (figure 1.8), is seen striking northeast, coincident with the volcanic zone. Even when the low density surface rocks in the zone were taken into account there was still an appreciable anomaly present. Possible reasons for the presence of the anomaly were that the density zoning used was not adequate or that the gravity effect seen here was derived from a crustal source. Possibly up to a third of this anomaly may be derived from a thermal expansion effect. Assuming that the anomaly was totally derived from a crustal source then density contrasts due to lithological changes and thermal effects can be considered.

As remarked in the introduction, sub-glacial volcanic activity gave rise to the creation of low density hyaloclastites at the accretion axis. Drilling results show that strong lithological contrasts exist for a thickness of ~ 1 km. Figure 3.34 depicts a geological cross-section that traverses the WVZ constructed from drill records. Also shown in figure 3.34 is a density profile taken from the density structure within a 1 km thick slab derived from inversion of the residual anomaly (figure 3.28b). The uncertainty of this density profile is probably of the order of 50 kg m^{-3}. The density profile exhibits a variation of ~ 300 kg m^{-3} which could be provided by the different lithologies present, i.e. new low density volcanics with numerous fractures and pores at the axis in contrast to closed fractures and filled pore spaces, or low porosity away from the axis. This shallow crustal density increase with distance from a spreading axis is thought to occur on the Juan de Fuca Ridge (Holmes and Johnson, 1993).

Hekla-Torfajökull Region (340°30'E, 63°55'N)

A roughly circular low of magnitude ~20-25 mGal (figure 3.18) correlates with a possible low shallow P-wave velocity (figure 1.8). Geodetic studies around Hekla infer a possible magma body at a depth of 7-10 km. In contrast to the WVZ, acid extrusives cover a large area and may contribute towards the negative anomaly. An areally extensive density anomaly would make it difficult to separate the effects of a

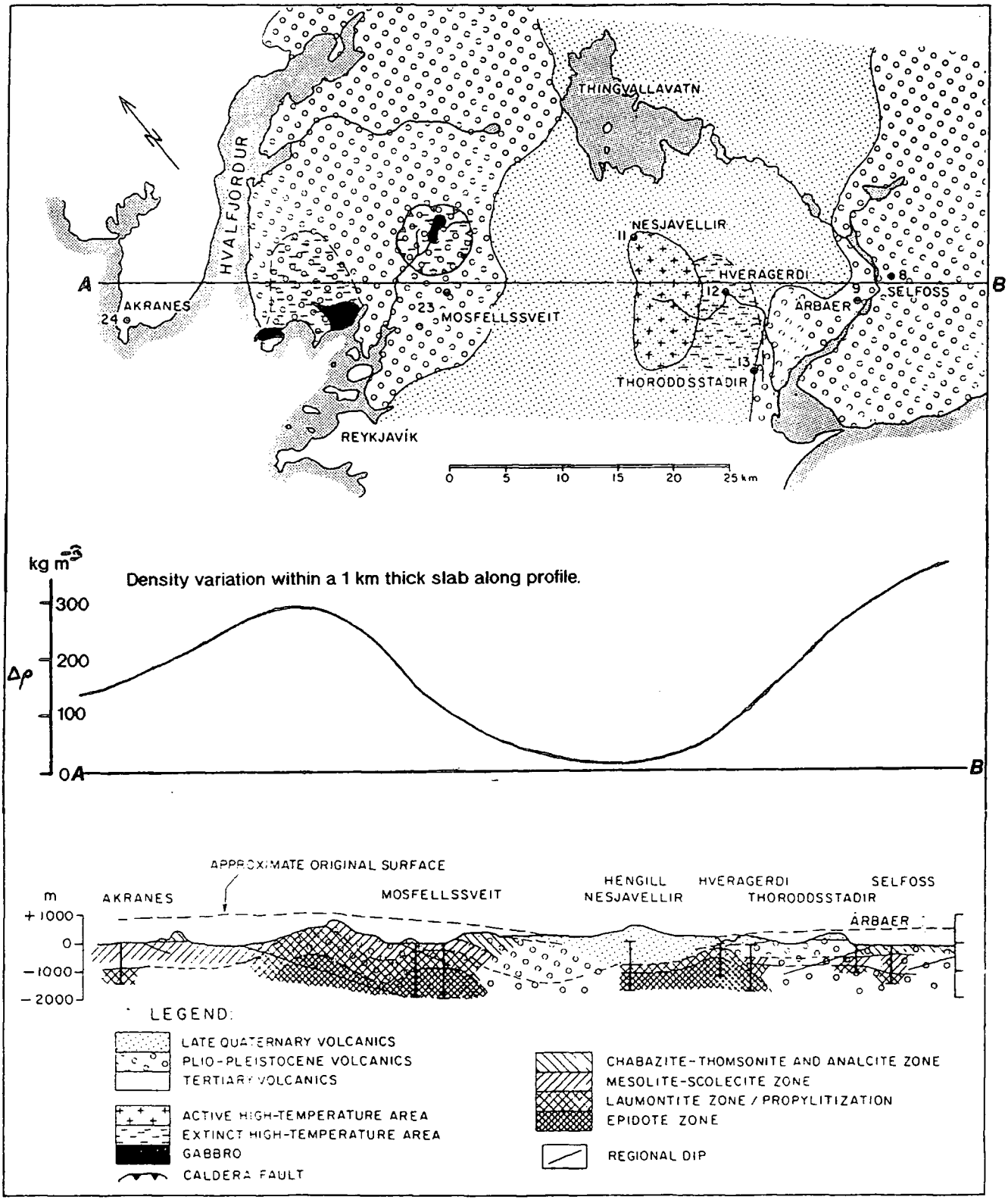

Figure 3.34. (top) Simplified geological map of area that straddles the WVZ. (middle) Density variation within the 1 km thick slab shown in figure 3.. /b along the profile in the geological map above. (bottom) Cross-section (along profile) through the WVZ in southwest Iceland and the surrounding Plio-Pleistocene and Tertiary rocks. The section shows the subsurface extension of alteration zones obtained from drillhole data. From Pálmason et al.(1979).

deeper source. All that can be said is that if the density anomaly is evenly distributed throughout a 10 km thick slab then it varies by about 80 kg m^{-3} over 50 km as indicated in figure 3.30b. If the density anomaly is distributed throughout a 5 km thick slab then the density variation is about twice that of the 10 km slab (figure 3.29b). For density variations within a slab of thickness 1 km, the density variation required would be ~ 500 kg m^{-3} over 50 km (figure 3.28b). Heat flow measurements around the EVZ suggest that the thermal system is not as well developed as that of the WVZ, exhibiting relatively low heat flow values (Flóvenz and Sæmundsson, 1993), although the anomaly still coincides with the high temperature region at Torfajökull which has subsurface temperatures in excess of 200°C at depths shallower than 1 km (Pálmason and Sæmundsson, 1974) and could also be responsible for lowering shallow crustal densities.

The Northern Volcanic Zone (343°30'E, 65°20'N to 343°30E, 66°N)

Immediately obvious is the linear low to the east of the volcanic zone (figure 3.18), which coincides with the extinct Fjallgarður Volcanic Zone (FVZ), a hyaloclastite ridge stretching ~150 km north from Kverkfjöll. Referring to figure 3.7, this shows that an error in reduction density of 200 kg m^{-3} would give rise to about 2 mGal locally and probably 3 mGal for 300 kg m^{-3}. With the dual density reduction this may rise to as much as 5-6 mGal locally. It is likely that most or all of the linear anomaly is due to the low density ridge. If the NVZ is now re-examined, ignoring the FVZ to the east it can be seen that a small roughly linear low exists near Krafla. Density variations of 200 - 300 kg m^{-3}, due to thickening of the top low velocity, low density layer, in the top kilometre of crust would produce a comparable anomaly. A coherent low associated with the NVZ, however, is still unclear and to some extent coastal sediments may effect it.

Snaefell Volcano (344°30'E, 64°50'N)

The Snaefell volcano is near a roughly circular gravity low (figure 3.18). At present the volcano is not associated with any seismic activity and there has been no post-glacial activity. The volcano, however, is close to the flanks of the Vatnajökull ice cap and is surrounded by extensive amounts of glacial drift. This stratovolcano is essentially a cone of hyaloclastite that sits on top of the Tertiary plateau. If the Snaefell volcano has been assigned an incorrect reduction density then an anomaly will result. To obtain an estimate of the likely error due to an incorrect choice of density, the gravitational effect felt at the apex of a cone has been calculated for a height of 800 m, radius of 7 km and a density contrast of -300 kg m^{-3}. These values result in an anomaly of magnitude ~ -9 mGal, which is very close to the residual anomaly of just in excess of -10 mGal. It is likely that the observed gravity low could be explained by more exact modelling of the surface features.

South of Vatnajökull (342°E, 63°50'N to 344°30'E, 64°10'N)

Flóvenz (1980) suggested that seismic refraction profiles along the south east coast of Iceland could be better interpreted by the inclusion of up to 700 m of sediments within the crustal velocity model. A 1 km thick slab requires a density contrast of ~ 500 kg m^{-3} to account for the gravity low seen there. This negative density contrast is possibly accommodated by the presence of sediments and is in agreement with the speculations of Flóvenz (1980).

West of Akureyri (341°E, 65°40'N)

The topography between Akureyri and the Skagi Peninsula lies in the Tertiary, is very rough and has experienced much glacial erosion exhibiting valleys eroded almost to sealevel. This area is associated with no known present tectonic feature. One explanation for the occurrence of this gravity low is that the density of the surface rocks is well below the value of 2600 kg m^{-3} either because of deep sediments within the valleys or through the presence of glacial drift. If it is assumed that the magnitude of the anomaly is ~ -20 mGal and is caused by a cylinder of thickness 1 km and radius 10 km then the density contrast required to give rise to the assumed anomaly at its top surface is -500 kg m^{-3}. This implies an average density in this area of ~2100 kg m^{-3}. A possibly better explanation is that of an increase in the depth to layer 3, the top of the lower crust, which on Pálmason's (1971) map (figure 3.35), corresponds quite well with the gravity low seen here. Pálmason (1971) gives a density contrast between layers 2 and 3 of 200 kg m^{-3} which would yield a gravity anomaly of ~ 10 mGal for a depth increase of 1.5 km. Possibly a combination of these two effects is present.

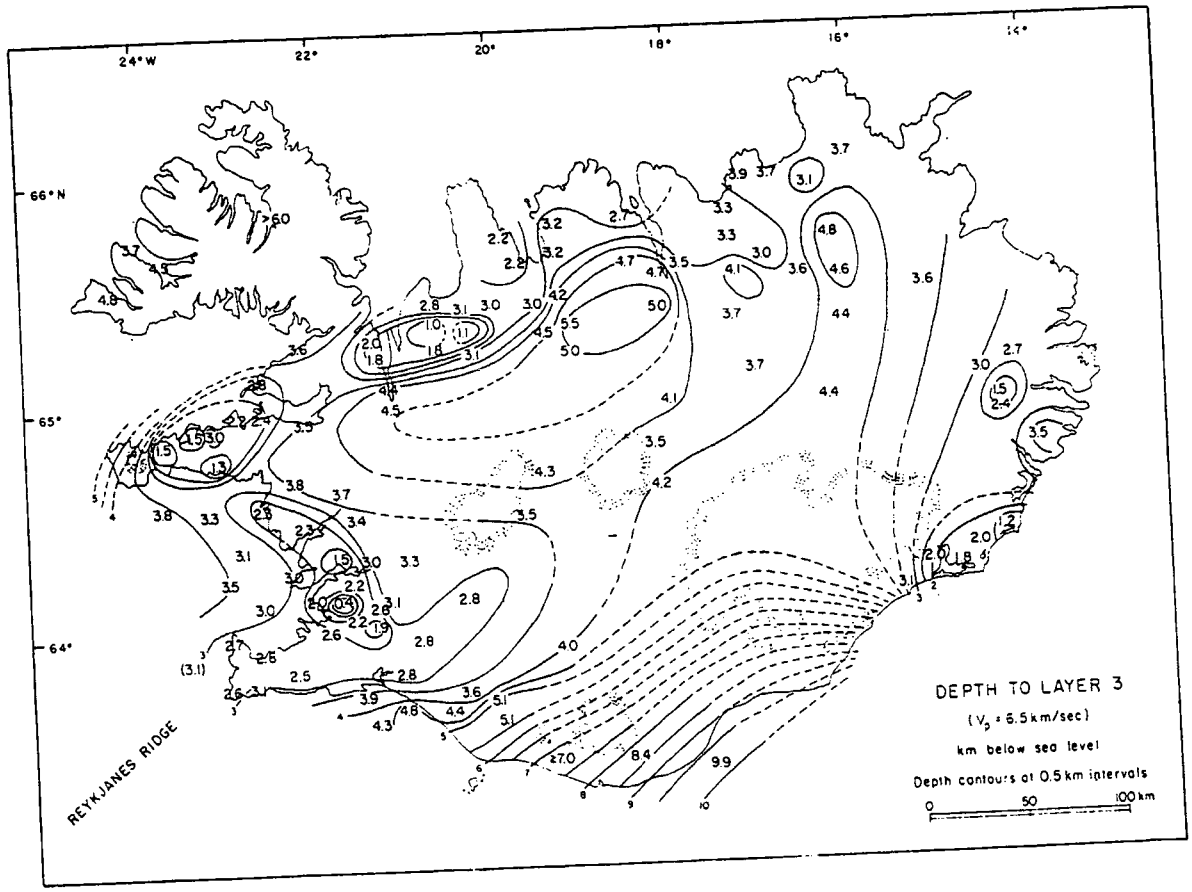

Figure 3.35. Map of the depth to the top of the lower crust (top of seismic layer 3) according to the layer model of Pálmason (1971). After Pálmason (1971).

NW Peninsula (337°E, 66°N)

The North West peninsula is on average 200 m above sea level. It may be the situation here that this isolated part of the country is independently isostatically supported. The Pratt mechanism for attaining isostatic equilibrium requires that any 'excess' topography is underlain by suitable negative density contrast for a constant depth of compensation. For the NW peninsula to support 200 m of crust of density 2700 kg m^{-3} a density contrast of -20 kg m^{-3} would be required throughout a thickness of 25 km of the underlying crust. The average density contrast for a 25 km thick slab is -20 kg m^{-3} (figure 3.31b), suggesting that the NW peninsula is in local isostatic equilibrium. Seismic refraction results (Pálmason, 1971; Flóvenz, 1980) suggest that the depth to layer 3 increases by at least 2 km from the edge to the centre of the peninsula. Using 200 kg m^{-3} as the density contrast, gives rise to a gravity anomaly of ~-15 mGal: similar to the residual anomaly.

3.7 Mantle Flow

Seismic P-wave time delays suggest anomalously slow mantle beneath Iceland to a depth of 200-300 km. P-S-wave velocity ratios imply that the anomalous mantle is also in a state of partial fusion. Gravity data in this chapter indicate that the top of the causative source for the long wavelength gravity anomaly is no deeper than 40 km below sea level. Together this geophysical evidence suggests that an anomalous body containing some partial melt extends from within 40 km of the surface to depths of the order of 300 km. It has been demonstrated that there are three ways of producing the long wavelength gravity signal: (i) crustal thickening; (ii) density variations within a constant thickness slab; and (iii) a vertical cylinder of anomalous density. Crustal thickening explains the gravity anomaly but does not extend for 300 km. Cases (ii) and (iii) can both explain the gravity anomaly and extend deep enough to give rise to the P-wave travel time delays (assuming that velocity is still proportional to density).

Plume material may rise in the form of Poissiulle flow if constantly fed from a deep source or possibly as discrete blobs detaching intermittently from some deep source.

The density contrast ($\Delta\rho$) of -35 kg m^{-3} within a cylinder of radius (r) 100 km is probably due to a combination of a temperature anomaly, solid-solid phase transitions and the presence of partial fusion which in turn give rise to a viscosity anomaly below Iceland. If these physical properties are assumed to be associated with the upwelling of discrete mantle blobs of approximately spherical shape (with r = 100 km) then the

vertical motion of the material can be approximated by the motion of a sphere in a viscous fluid, viscosity η, under the influence of gravity, g, then:

$$v_{vert} = \frac{2gr^2\Delta\rho}{9\eta} \tag{3.4}$$

where v_{vert} is the vertical velocity of the sphere. For a normal mantle viscosity outside the buoyant sphere of 10^{21} Pa s a vertical velocity of 25 mm a^{-1} results. From this estimate of vertical velocity of material an estimate can be made of the flux of material, i.e. $\pi r^2 v_{vert} \approx 0.8$ km^3 a^{-1}. If it is assumed that melt within this flux is responsible for the creation of Icelandic crust, then taking the volume of crust created annually as 350 km along strike (the approximate north-south extent of the insular shelf) multiplied by 15 km (8 km for the oceanic crust: Angenheister et. al., 1980) in thickness multiplied by a total spreading velocity of 20 mm a^{-1} gives a melt volume requirement of ~ 0.11 km^3 a^{-1}. This volume requirement implies a melt fraction of just less than 14 %. Given the uncertainties involved, e.g. viscosity estimates and how much of the crust that a hypothesised plume is actually responsible for, this result seems to show that a plume could quite possibly give rise to Iceland's anomalously thick crust. It is also implies that it is unlikely that much surplus melt will migrate along the Reykjanes Ridge, and if any mantle does it is likely to be depleted matrix as Strange (1991) suggests. An additional feature of a simple plume which has the dimensions as given above and is centred 40 km east of Hofsjökull, is that the Torfajökull-Vestmannaeyjar and Öraefajökull-Snaefell flank zones lie just outside its perimeter (figure 3.36).

An alternative to the buoyant sphere model, outlined above, is a simple pipe flow model. The maximum vertical velocity, v_{max}, of material in a vertical pipe which experiences a vertical pressure gradient (dp/dh) is (Turcotte and Schubert, 1982):

$$v_{max} = \frac{r^2}{4\eta} \cdot \frac{dp}{dh} = \frac{gr^2\Delta\rho}{4\eta} \tag{3.5}$$

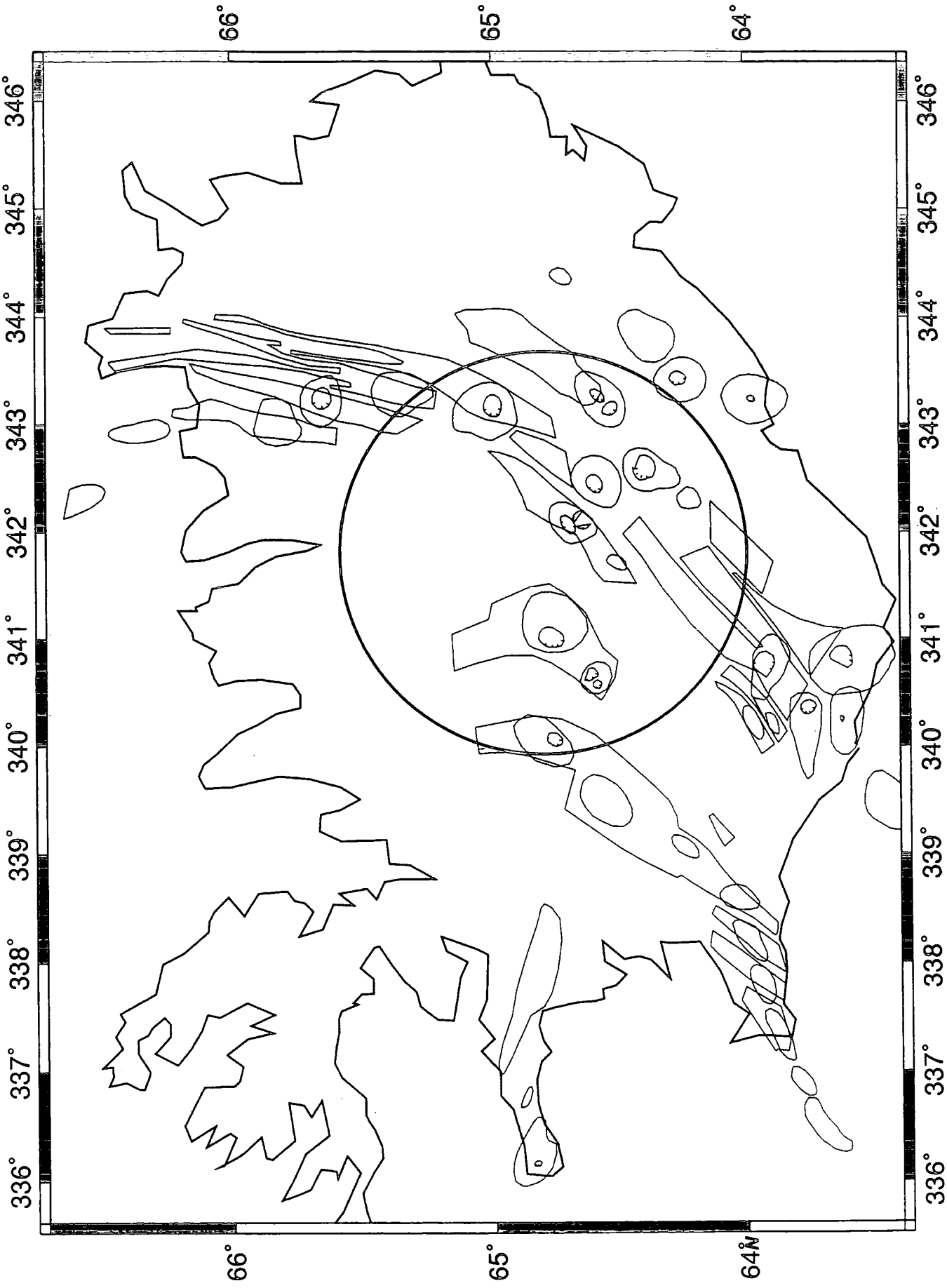

Figure 3.36. Spatial location of a mantle plume with a radius of 100 km centred ~ 40 km east of Hofsjökull (thick black circle). The tectonic units are shown as thin black lines.

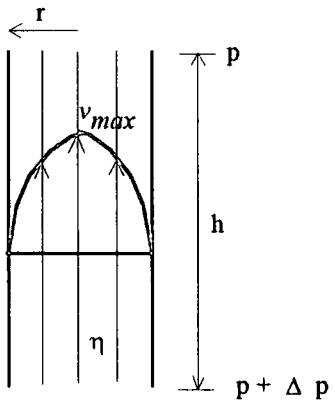

Figure 3.37. Flow within a pipe. There exists a pressure gradient $\Delta p/h$ which gives rise to the flow of material of viscosity η through the pipe of width r. Velocity is greatest at the centre of the pipe.

where the symbols are as above. Equation 3.4 looks similar to equation 3.5, but difficulties arise when a choice is made as to the value of viscosity to be used. From the diagram it would seem logical to use the viscosity of the plume i.e. 10^{19} Pa s, but this would result in v_{max} being 100 times larger than v_{vert}, and the resultant vertical flux of material would be very large. A near normal mantle viscosity within the plume would not be in keeping with experimental results (e.g. Foulger et al., 1992), or the effects of temperature which should reduce viscosity within the plume. Either a pipe model is too simple, because it does not take account of viscosity as a function of radial distance, or the Iceland plume is better described by a buoyant sphere model.

3.8 Discussion

Magnetotelluric and geothermic results suggest that much of Iceland may be underlain by partial melt in the 10 to 20-30 km depth range. The partial melt is inferred to be shallowest below the axis of the volcanic zones, gradually deepening below older crust. Hermance (1981b) interprets such an arrangement as indicating that the crust is ~10 km at zero age, produced by intrusion and extrusion, steadily increasing in thickness with increased age/distance from the axis. If it is assumed that the basalt solidus defines the lithosphere-asthenosphere boundary and that the zone of partial melt marks the crust-mantle interface then, in Iceland, the lithosphere and crust may be of the same thickness. Gravity results in this study imply that the Icelandic crust may be thicker than surrounding oceanic crust, which means that ~40% of the island's crust may be formed by freezing partial melt onto adjacent old cold crust, i.e. some method of underplating as Hermance (1981a and b) suggested.

Pálmason (1971) originally suggested that the depth to layer 3 (the lower crust) might correlate well with the short wavelength gravity anomalies. Comparing maps depicting the depth to layer 3 (figure 3.35) and the short wavelength gravity anomalies (figure 3.18) shows that correlation between gravity and seismic data is seen in the western Tertiary zone. This is evidenced by the increased depth to layer 3 beneath the NW peninsula and a region to the west of Akureyri which is accompanied by corresponding gravity lows. A correlation is also seen at the eastern end of the land bridge which joins the NW peninsula to the rest of Iceland: relative short wavelength gravity highs over the Snaefellsnes Peninsula and Húnaflói are separated by a relative gravity low, where the land bridge joins the island, in accordance with a shallower layer 3 beneath the Snaefellsnes Peninsula and Húnaflói. Slight correlation is also seen near the Krafla region of the NVZ. The correlation between residual gravity and the depth to layer 3 is not so good elsewhere. In the south and southeastern parts of the island, the depth map predicts a gravity low of perhaps three times the magnitude of the low seen over the NW peninsula which is not evident in the residual gravity map. If this effect was present it may have been included in the long wavelength anomaly because of its extensive nature. There is no northeast-southwest structure in the southwest of the depth map corresponding to the WVZ residual gravity low and many of the gravity lows in the east of the island are unpredicted by the depth map.

Shallow P-wave velocities in Iceland show good correlation with some of the younger Icelandic crust. Flóvenz et al. (1985) state that the P-wave velocities in figure 1.8 are for

crust 500 m below the surface (rather than sea level). Most of Iceland within 100 km of the coast is less than 500 m above sea level and so, there at least, the shallow P-wave velocities are representative of the shallow crust below sea level. Across the WVZ, inspection of the contours reveals a P-wave velocity change of ~1 km s^{-1} is equivalent to a density change of ~200-250 kg m^{-3}. This is similar to the conversion given by Christensen and Wilkins (1982) (equation 2.5).

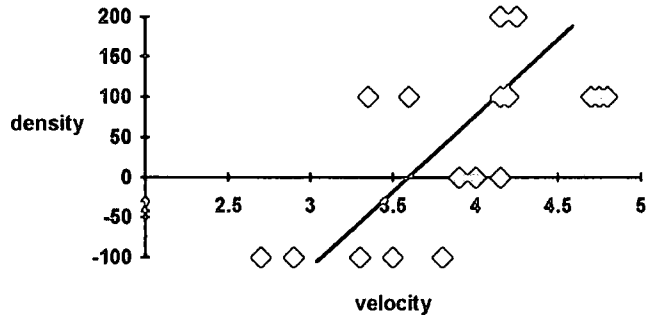

Figure 3.38. Plot of shallow (500 m below surface) P-wave velocity versus inferred density contrasts in the top 1 km of Icelandic crust across the WVZ. The vertical axis is in kg m^{-3}, and the horizontal axis is in km s^{-1}.

Figure 3.38 is a plot of hand picked velocity versus corresponding density changes within a 1 km thickness of crust inverted from CBA2, and so may be subject to inaccuracy. The diagonal line represents a gradient of ~ 200 kg m^{-4} s^{-1}, as stated above, in agreement with Christensen and Wilkins (1982). If the density variations within a thicker layer are used then the gradient of the line becomes much smaller. This is taken as tentative confirmation that only the top kilometre of crust is important to the local gravity field in Iceland over the volcanic zone. A similar correlation is seen across the NVZ but not to such a great degree. To the south and in the interior of the country, the shallow P-wave velocity observations are too sparse to make any comments about their correlation with the gravity data.

Unlike the oceanic lithosphere, Iceland does not appear to have a strong component of the gravity field due to thermal expansion of the lithosphere. Geothermal and

magnetotelluric studies suggest that a spreading plate thermal structure should exist below the WVZ, but calculations showed that the amplitude of the signal due to a lithospheric thermal effect would be ~ 4 mGal for a 25 km thick lithosphere, and therefore not be a major component of the anomaly. In the east of the country the locus of spreading has been migrating, east and west ~30-50 km, every 2 Ma or so (Helgason, 1984 and 1985) and recently (<700 Ka) shifted from the FVZ to the present NVZ. Such a frequent shifting of the plate boundary would lead to a variable distribution of volcanic products across time averaged plate boundaries and an ill-defined thermal structure. Below the lithosphere, as defined by the basalt solidus, the isotherms would need to be of large wavelength so as not to produce any small scale lateral density inhomogeneities. Thus the lack of observed ridge thermal gravity signature in Iceland may be indirect evidence for a sub-crustal long wavelength thermal anomaly such as a hotspot which dominates the sub-crustal thermal structure.

High heat flow, the presence of geothermal fields, high seismicity, strong magnetic signal, low shallow P-wave velocity and low crustal rock density along the WVZ imply that it is a region of crustal accretion. The coherent, stable gravity low that extends along the length of the WVZ is likely to be a product of continued spreading along a 'stationary' boundary for ~6 Ma which has created an orderly lateral stratigraphy of young, low density, fractured hyaloclastite at the axis flanked by higher density, sub-aerial volcanics. The coherency of the gravity field seen along the WVZ is not seen over the EVZ or NVZ, supporting the hypothesis that spreading in eastern Iceland has been occurring along many spreading centres over the past few million years.

3.9 Summary

1. Mantle compensation, in the form of a plume structure resembling a cylinder of ~100 km radius and -35 kg m^{-3} average density contrast, can account for the long wavelength, 'bowl-shaped' Bouguer gravity anomaly over Iceland if all of the Bouguer anomaly is attributed to a mantle source.

2. If all of the Bouguer anomaly is attributed to crustal thickening then a simple slab model suggests that on average an additional 7 km of crust is present uder Iceland relative to neighbouring oceanic crust, and, in the light of magnetotelluric evidence, lead to the conclusion that up to 40 % of the Icelandic crust may be formed by 'underplating'.

3. Depth to seismic layer 3 correlates quite well with the short wavelength residual anomalies in the western Tertiary zone and may be related to isostasy, but elsewhere such a relationship is unclear.

4. Shallow P-wave velocities correlate well with the WVZ and NVZ relative gravity lows and imply that density variations in the top kilometre of crust are responsible for the short wavelength component of the gravity field there.

5. The lack of an identifiable gravity signature for the ridge axis cooling effect implies that Icelandic sub-crustal thermal structure is dominated by an extensive thermal anomaly, in agreement with the hotspot hypothesis.

Chapter 4

The Reykjanes Ridge at 58°N

4.1 The Oceanic Spreading Boundary

4.1.1 Introduction

The EW9008 cruise aboard the R/V Maurice Ewing took place in October 1990 on the Reykjanes Ridge in the North Atlantic (figure 4.1). The aims of the cruise were to study the tectonics and segmentation of an obliquely spreading mid-ocean ridge and the change in morphology of the ridge as the effect of the Iceland hotspot decreased with increasing distance from Iceland.

The Reykjanes Ridge is part of the world-wide mid-ocean ridge system and extends along a strike of 216° from southwest Iceland (64°N) to the Bight Fracture Zone (57°N). The ridge itself is spreading obliquely with a half rate of 10 mm a^{-1} (Talwani et al., 1971) along a spreading direction of 096° (De Mets et al., 1990). Before considering the Reykjanes Ridge, mid-ocean ridges in general should be introduced.

The mid-ocean ridges mark constructional boundaries between tectonic plates. Here, 'hot' material from the asthenosphere upwells and fills the volume left by the separating plates, adding to them as it cools. The gross morphology of the 60 000 km of mid-ocean ridge exhibits a ridge axis high or a median valley which were initially thought to be controlled by plate spreading velocity (Small and Sandwell, 1989). However, more recent investigations propose that this morphology is also controlled by crustal thickness and mantle temperature (Chen and Morgan, 1990a and b; Small and Sandwell, 1994). Superimposed upon this two dimensional morphology is an along-axis segmentation effect. Macdonald et al. (1988) have defined four orders of segmentation that are now seen as a global phenomenon (Whitehead et al., 1984; Schouten et al., 1985). First order discontinuities are strike-slip zones oriented approximately normal to the spreading axis and offsetting it by up to several hundred kilometres. These structures are known as *transform faults*, occur at 300-500 km intervals along mid-ocean ridges and exhibit axial bathymetric anomalies of 500-3000 m. Second order discontinuities are characterised by offsets of 3-5 km with an associated depth anomaly of several hundred metres. They occur at 50-300 km intervals along the axis and are often termed *non-transform offsets*. Third order discontinuities display hardly any ridge axis offset (0.5-3 km), while fourth

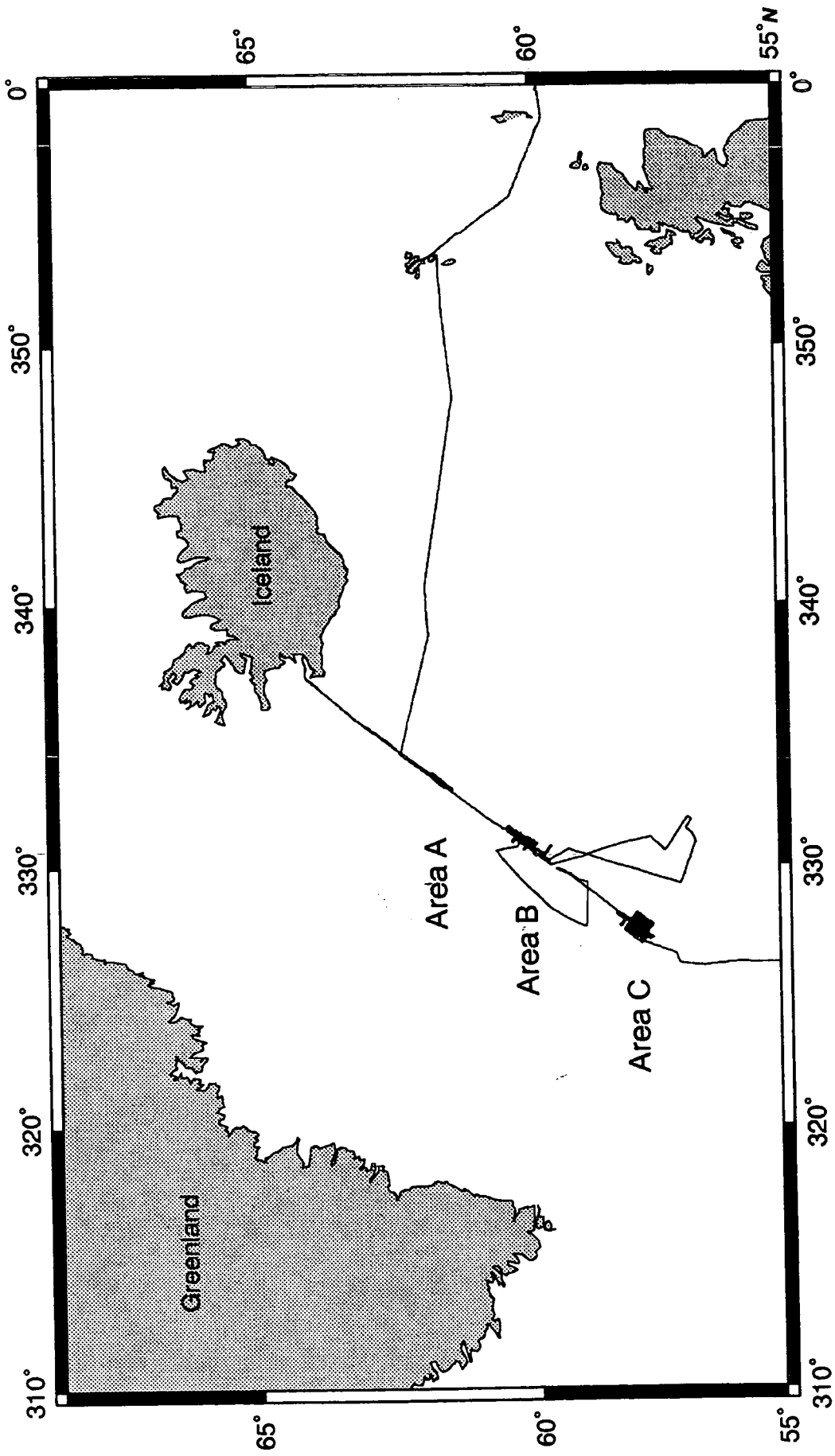

Figure 4.1. Shiptracks for the EW9008 cruise in the North Atlantic. Survey areas A, B, and C are depicted. Area C is covered in this chapter.

order discontinuities can be seen only as deviations in axial linearity (or even geochemical differences) and can appear at slower spreading ridges as the regions between volcanoes in the neovolcanic zone. These bathymetric observations, in conjunction with gravity and magnetic results, have led to the hypothesis that crustal accretion at spreading axes is fully three dimensional in that it varies along axis as well as across it (e.g. Lin et al., 1990; Macdonald et al., 1988). Whitehead et al. (1984) proposed that the cellular nature of spreading plate boundaries could be attributed to a Rayleigh-Taylor type of gravitational instability. Figure 4.2 is a cartoon of events on an along-axis section according to this model. This hypothesis is supported by the gravity work done by Lin et al. (1990) and Kuo and Forsyth (1988).

The Reykjanes Ridge can now be viewed with this global perspective in mind. In seven degrees of latitude the average axial depth changes from 0 m to 2300 m below sea level. Comparing ridge normal profiles of bathymetry, Figure 4.3 shows that at about 59°N the large scale morphology of the ridge changes from that of a ridge axis high (more usually seen on fast spreading ridges, e.g. East Pacific Rise) to that of an axial graben as is more commonly observed along the Mid-Atlantic Ridge (Macdonald, 1982). The Seasat gravity map (Haxby et al., 1983), which depicts free air gravity anomalies over the world's oceanic regions, correlates well with the bathymetry and shows the morphological transition at 59°N (figure 4.4). Also visible in figure 4.4, south of 60°N, are temporally persistant gravity lows (horizontal dark lines) similar in appearance to the Bight Fracture Zone's off-axis trace. It appears then that south of ~ 59°N, mid-ocean ridge dynamics display a marked change in behaviour: a ridge axis high is replaced by a median valley and offset traces (that are probably related to large bathymetric anomalies) become observable. The area studied in this chapter lies very close to this transition latitude and relating it to the global mid-ocean ridge perspective could provide constraints for future models of ridge dynamics.

4.1.2 The Oceanic Crust

In this chapter an attempt to model the crust is presented. The structure of oceanic crust has mainly been inferred from seismic refraction work revealing approximately horizontal zones of differing velocities (Raitt, 1963). Drilling has provided ground truth about the interpretation of the upper layers (e.g. Becker et al., 1989) (figure 4.5a) and ophiolites have been used to infer the physical nature of the deeper layers (Moores and Vine, 1971) (figure 4.5b). It should be borne in mind that ophiolites are thought to be a product of back-arc spreading centres rather than mid-ocean ridges and so may not be directly applicable. These investigations give a good picture of the evolved

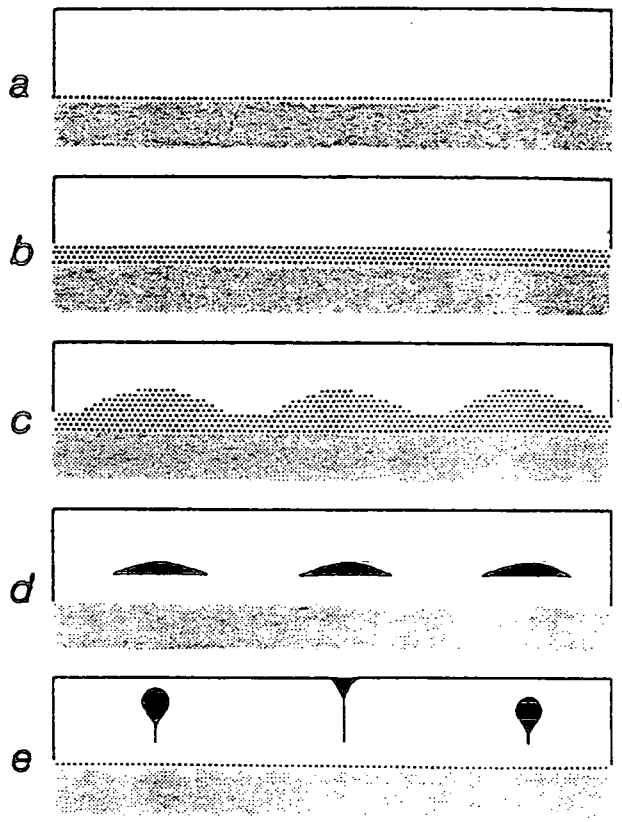

Figure 4.2. A model representing the life cycle of Rayleigh-Taylor instability initiated diapirs. Partially molten mantle collects at the base of the depleted mantle which is of lower viscosity and density than the surrounding material (a,b). The lower density material is unstable and forms regularly spaced domes (c). Partial melt accumulates at the top of the domes (d), and then rises towards the crust (e). From Whitehead et al. (1984).

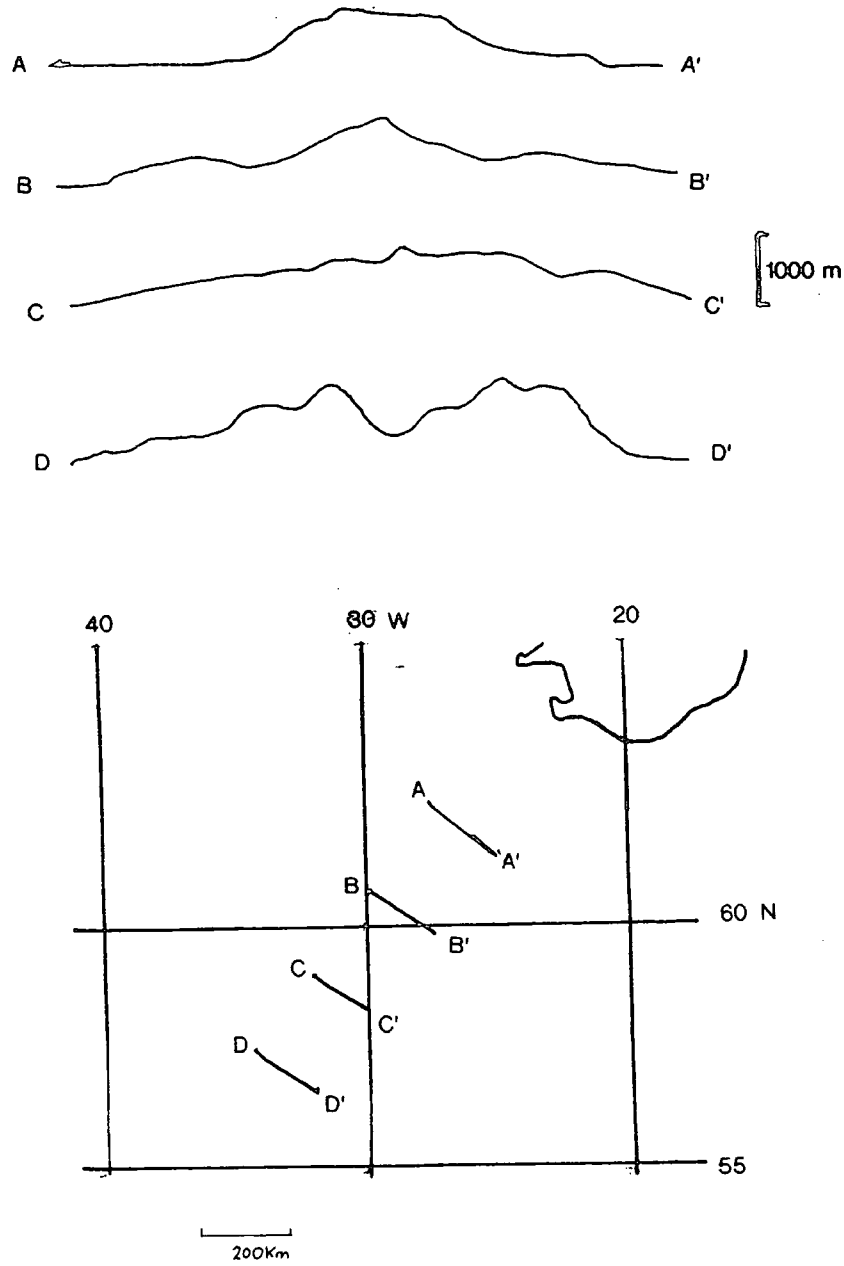

Figure 4.3. A plot of four ridge normal bathymetric profiles from the Mid-Atlantic Ridge. The profile positions are shown on the location map.

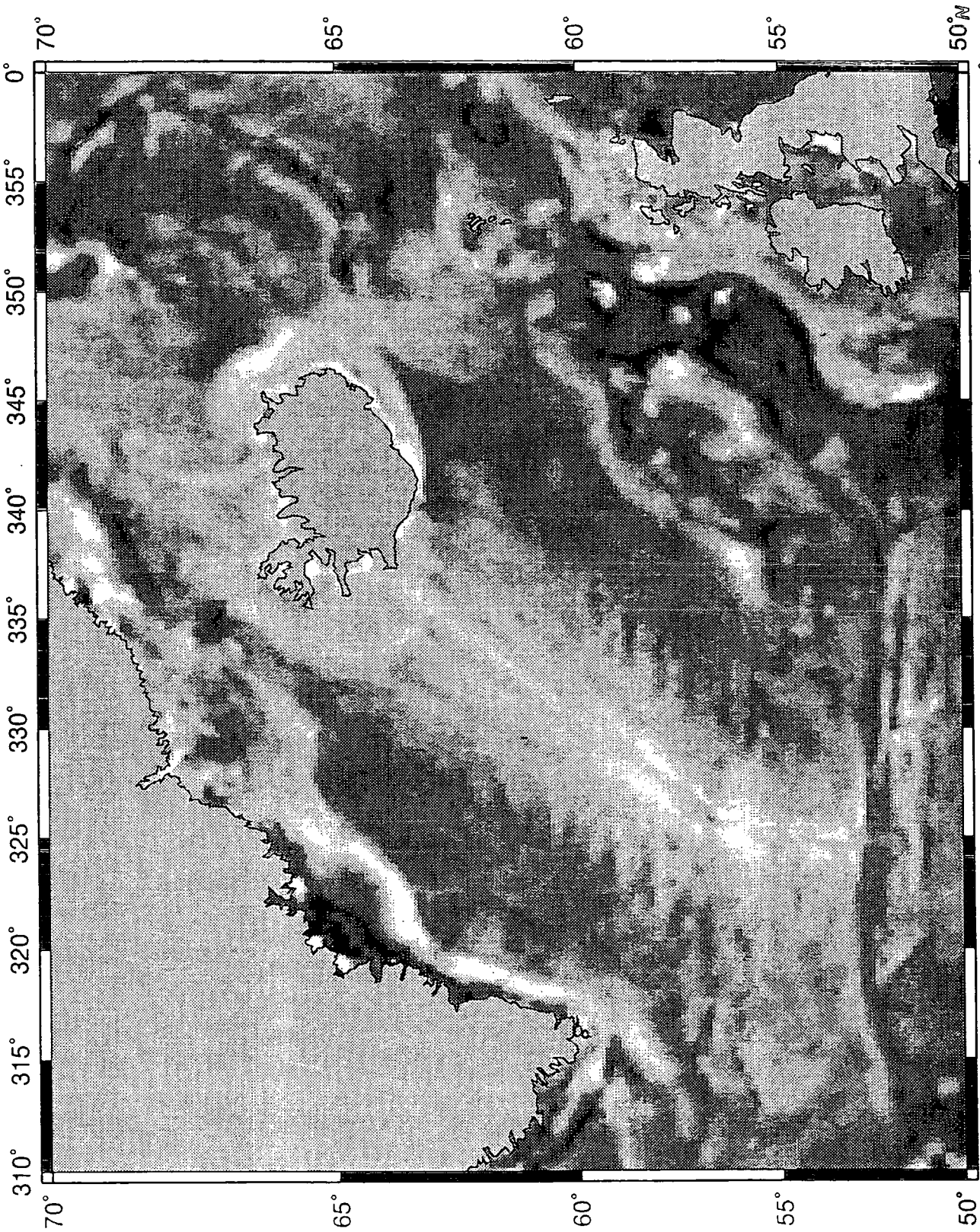

Figure 4.4. A black and white representation of Haxby et al. (1983) Free Air Anomaly map for the world's oceans from SEASAT. The shaded scale goes from low gravity (black) to high gravity (white).

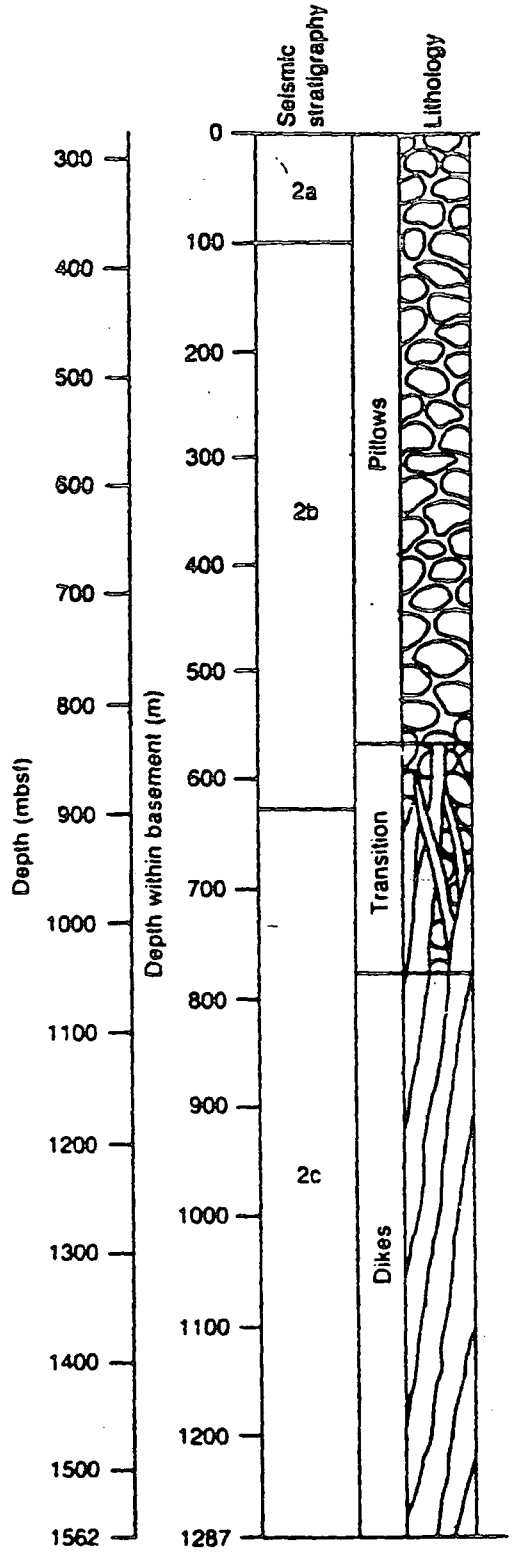

Figure 4.5a. Diagram repesenting the lithologies encountered in hole 504B as a function of depth with seismic layering for reference. From Becker et al.(1989).

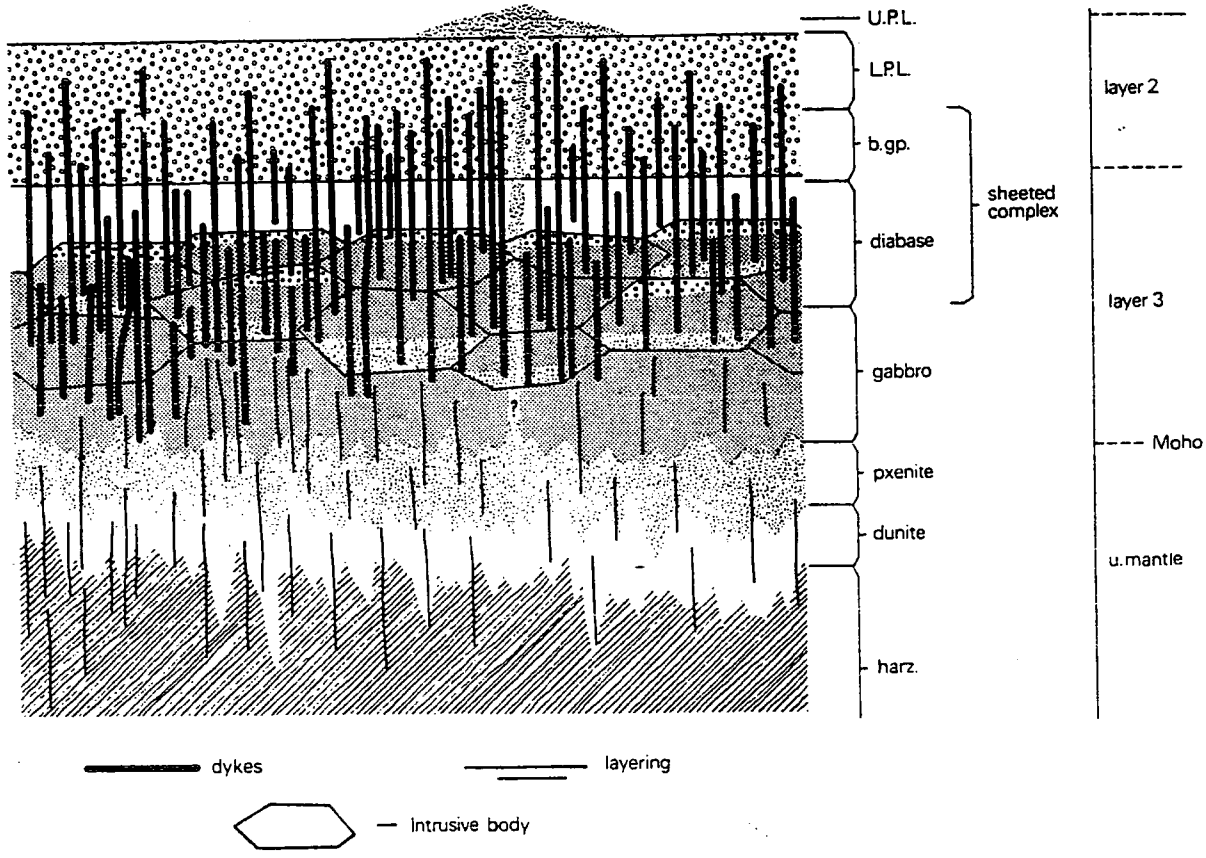

Figure 4.5b. A schematic cross-section through an ophiolite. U.P.L: upper pillow lavas, L.P.L: lower pillow lavas. The lithologies are given as a function of depth. Alongside is the oceanic seismic layer system for reference. From Moores and Vine (1971).

structure of the oceanic crust, but for explanations of its genesis and possible structure at the axis, it becomes necessary to turn to numerical models. These points have been examined below.

The oceanic crust is conventionally subdivided into 3 layers, after Raitt (1963).

Layer 1: This layer comprises the oceanic sediments, having an average thickness of 0.5 km but ranging from a few kilometres at passive margins to zero at ridge crests, apart from local basins. Talwani et al. (1971) confirm the lack of ridge axis sediment cover within 30 km of the Reykjanes Ridge axis. The area studied in this chapter only extends some 25 km either side of the axis and so the effects of sediments have been ignored.

Layer 2: This is the beginning of the igneous crust. Houtz and Ewing (1976) claim that their refraction results show that the velocity of the upper part of layer 2 increases with age due to pores being infilled with sediments and hydrothermal deposits. Bunch and Kennet (1980) confirm this observation noting an increase in P-wave velocity for the upper part of layer 2 of 2.2-3.8 km s^{-1} in 9 Ma for the Reykjanes Ridge at 59°30'N. The upper part of layer 2, is thought to be porous allowing extensive hydrothermal circulation (e.g. White, 1984). Results from hole 504b of the Ocean Drilling Program, which penetrates 1288 m into the igneous crust, suggest that the porosity is ~ 10 % or more for the top of layer 2 and reduces to 6-10 % at deeper levels within the layer where the onset of dykes is encountered (Becker et al., 1989). These drill results also explain why P-wave velocities within layer 2 experience a continuous increase as porosity and fractures decrease with increasing depth and pillow lavas eventually grade down into dykes. Ophiolitic studies lend further weight to this view of layer 2, with work of Moores and Vine (1971) revealing a stratigraphy of upper and lower pillow basalts which are eventually replaced by dykes with increasing depth.

Layer 3: In contrast to layer 2, layer 3 exhibits a nearly constant P-wave velocity of ~6.75 km s^{-1}. Layer 3 is now thought, on the basis of ophiolite studies (Moores and Vine, 1971), to consist of isotropic gabbros lying on top of cumulate gabbros and including metamorphic derivatives .

Overall, the crust at the ridge crest has an average thickness of ~6 km (Spudich and Orcutt, 1980; White, 1984) which varies by a few kilometers depending upon spreading rate and temperature of the underlying mantle.

Mohorovicic Discontinuity (Moho): This lies below layer 3, and is defined by a sharp increase in seismic P-wave velocity. Again, this is thought to be a zone of transition rather than a distinct boundary (Spudich and Orcutt, 1980). Below the Moho the upper mantle consists of peridotitic rocks. It should be noted however that seismic refraction work by Fowler (1976) and Bunch and Kennet (1980), is interpreted as indicating an absence of seismic Moho at the ridge axis. The onset of 'normal' velocity profiles is evident when 2 Ma crust is examined. In particular, Bunch and Kennet's (1980) results show that transition to the maximum P-wave velocity observed occurs at a crustal thickness of just under 7 km at the axis and ~8.5 km for 9 Ma crust.

Crustal rocks within the area studied in this chapter are mostly younger than 2 Ma and roughly a third of the area rests in the median valley. Hence an introduction should also be given to some ridge axis models that attempt to reproduce axial morphology. This is the subject of the next section.

4.1.3 Ridge Axis Models

The formation of oceanic crust is thought to involve the cooling of upwelled molten material from the mantle that infills the volume left by separating tectonic plates. Examining the process in more detail reveals that this global model is a time averaging of discrete physical events. Rifting episodes at Krafla, Iceland, may be a good indication of how plate spreading occurs. Every few hundred years, a zone 10-15 km wide, centred on the ridge axis, is activated and dykes several tens of kilometres long and several metres wide are intruded. The newly created dykes form new crust as they cool. At slow spreading ridges accretion usually occurs within the median valley, a local bathymetric low on the ridge crest.

Attempts have been made to explain the presence of large normal faults and a rift valley at the axis of slow spreading ridges, with the aid of models. Tapponier and Francheteau (1978) propose the mechanism of steady state necking of the lithosphere. The presence and structure of rift valleys are mainly controlled by the response of a strong solid axial layer of crust, which is stronger than an underlying region, to tectonic extension (necking). They believe that tectonic extension is the cause of most continental grabens and the structure observed at slow spreading ridges. The necking mechanism implies that faults only cut through the upper brittle layer but do not penetrate the plastic flow (steady state creep) layer below. Because the median valley is a steady state feature of a ridge, the extension cannot be taken to its ultimate conclusion (figure 4.6), that of zero

thickness crust. Instead, the crust at the axis is always replenished with lava accumulating at the top and mantle cooling from below, keeping the crust ~ 5 km thick.

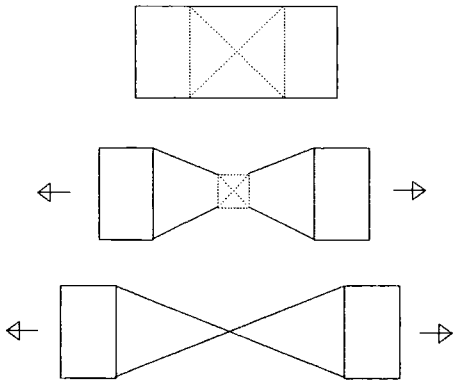

Figure. 4.6. An example of necking where the plastic deformation is spread continuously throughout a thick zone of initial length equal to the thickness of the bar. If necking is taken to its ultimate conclusion, the zone attains zero thickness.

Water replacing the basalt at the surface, due to the graben structure (figure 4.7a), gives rise to a net upward force. The upper layer is strong, so compensation within the elastic core takes place over a longer wavelength than the extent of the graben structure. The result is a bathymetric profile that resembles what is actually observed. This warping of the brittle layer causes vertical shear stresses which are maximum at ~7-8 km from the axis. Combining this result with a synthesis of steady state creep experiments for the brittle and ductile layers with the thermal structure of the lithosphere to obtain an estimate of lithospheric strength, shows that at 7-8 km from the axis the shear stresses are greater than the strength of the lithosphere. This gives rise to large normal faulting within the brittle layer.

In summary, the Tapponier and Francheteau (1978) model explains the presence of a rift valley, normal faulting and tilted fault walls which are observed at the axis of slow spreading ridges, by invoking the mechanism of necking of the lithosphere in the central part of the rift valley.

Chen and Morgan (1990a and b) investigate a model which reduces to the Tapponier and Francheteau (1978) model for slow spreading ridges, but also explains the axial ridge high for fast spreading ridges. The model that they develop has a zone of failure at the axis

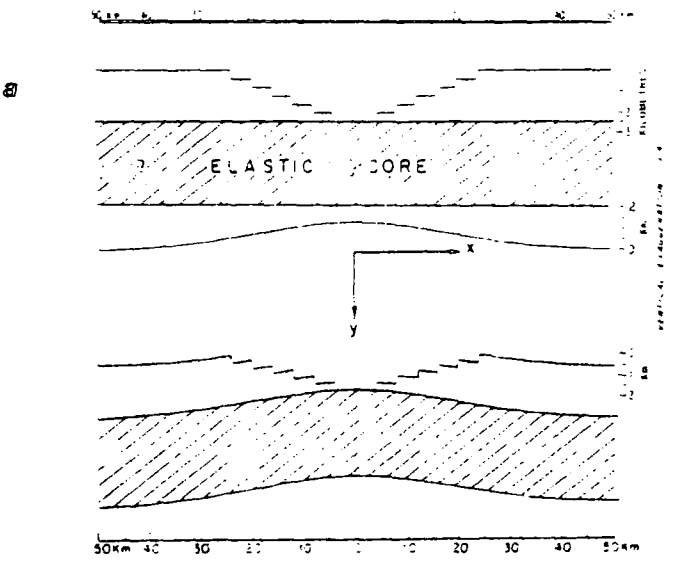

Figure 4.7a. Tapponier and Francheteau's ridge axis model. This sketch depicts how the 'elastic core' buckles upwards to accommodate for the absence of mass caused by successive normal faulting (the staircase pattern). After Tapponier and Francheteau (1978).

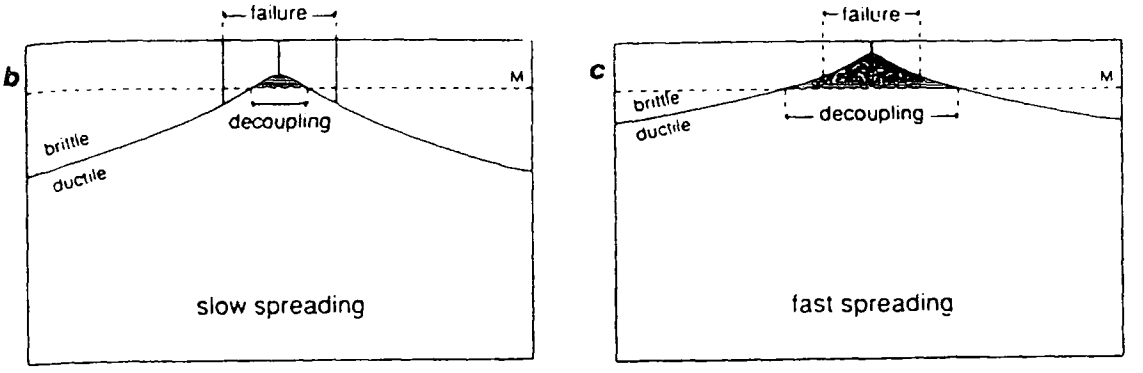

Figure 4.7b. Chen and Morgan's mechanism for creating a median valley at the axis of a slow spreading ridge: The buoyant zone (black) is unable to support the failed volume and the decoupling allows the block to sink forming a ridge valley. c. Chen and Morgan's mechanism for creating a ridge axis high: the buoyant region is great enough to push up the volume within the zone of failure and create a ridge axis high. After Chen and Morgan (1990a).

where the shear stress of the underlying viscous layer exceeds the yield strength of the brittle plate. Figure 4.7b and c shows the cases for fast and slow spreading ridges respectively. The brittle-ductile interface follows the 750°C isotherm (the ductile layer undergoes olivine creep). Between the two layers near the axis there is assumed to be a region of low viscosity (partial melt), which can withstand only low stresses for a given spreading velocity and so decouples the upper brittle layer from the stretching layer below. If the decoupling region is wider than the failure zone then no median valley forms. The buoyancy force from the soft decoupling region raises the decoupled brittle material up into an axial high as observed at fast spreading ridges (figure 4.7b). If the decoupling region is narrower than the failure zone then the mechanism would revert to that described by Tapponier and Francheteau (1978) for slow spreading ridges with normal faulting and formation of a rift valley occurring within the failure zone. Another feature of this model is that when the axial morphology is predicted for a thickened crust and hotter mantle, as expected close to a hotspot, a ridge axis high is produced by essentially the same mechanism as the fast spreading ridge, i.e. the decoupled region is wider than failure zone due to the relative shallowness of isotherms marking the onset of olivine creep.

To summarise, a slow spreading ridge has a crust of thickness ~5-9 km near the ridge axis which depends upon spreading rate, proximity to a hotspot and the underlying mantle temperature. This thickness is kept constant by extrusion of basalt at the surface and cooling of mantle on the underside. At a distance of about 5-15 km from the axis the lithosphere is strong enough to halt the creation of large normal faults and presumably the oceanic layering observed is also present. This is also dependent upon spreading rate, crustal thickness and temperature of the underlying mantle. At 2 Ma the crust has matured sufficiently for a Moho to become observable seismically.

4.1.4 Previous Work

4.1.4.1 Geophysical Investigations of the Reykjanes Ridge

Searle and Laughton (1981) first described the high resolution tectonic and morphological details of this obliquely spreading ridge primarily through use of the GLORIA sidescan sonographs. They noted the prominent highly backscattering en-echelon axial volcanic ridges (AVRs). These features lie at the ridge axis and strike north-south. The high acoustic backscatter has been interpreted as evidence of the constructive nature of these features which are seen as the primary sites of newly intruded and extruded material. Observations from the EW9008 cruise have shown that

AVRs are a persistent feature along the length of the ridge (Parson et al., 1993). Searle and Laughton (1981) and Strange (1991) confirm the morphological transition from ridge axis high to median valley at 59°N, attributing the cause of this change to an underlying higher temperature field to the north. Spreading of the Reykjanes Ridge is assumed to be steady at a half-rate of 10 mm a^{-1} from observations of magnetic lineaments. Assuming such a steady rate of spreading, Bunch and Kennett (1980), using refraction seismic results, concluded that the crust apparently became thicker with age, reaching ~8.5-10 km for 9 Ma crust at 59°30'N on the Reykjanes Ridge. A crustal thickness of 10 km was cited for 10 Ma crust to the east of the Reykjanes Ridge abutting Iceland (Angenheister et al., 1980). A rapid increase in P-wave velocity in the top 400 m of crust was also observed by Bunch and Kennett (1980) and attributed to the infilling of pore spaces and cracks over time.

4.1.4.2 Three-Dimensional Marine Gravity Work

Kuo and Forsyth (1988) analysed gravity data from a ridge-transform system in the South Atlantic between 31°S and 34°30'S. They observe a circular-shaped mantle Bouguer low, which they propose may represent the existence of a mantle upwelling beneath a ridge segment. They also find that the Fracture Zone (FZ) and median valleys are not fully isostatically compensated, implying that they must be dynamically supported or receive support from an elastic plate. Prince and Forsyth (1988) deal mainly with the Vema FZ and the thinning of the crust in the vicinity of the FZ walls, but they also note that the zone is not fully isostatically supported by the thinned crust. Morris and Detrick (1991), on the Mid-Atlantic Ridge near the Kane FZ, interpret gravity data as indicating thinner crust beneath the FZ and beneath a non-transform offset. Lin et al. (1990) carried out a survey of the Mid-Atlantic ridge-transform system between 27°50'N and 30°40'N. They showed that accretion of magma implied from circular Mantle Bouguer Anomaly (MBA) lows leads to increased crustal thickness (up to 3 km) if crustal thickness is the only cause of the MBA, and that MBA lows occurred at discrete ridge segments along the ridge axis. Blackman and Forsyth (1991) also report thinned crust (2-3 km, if crustal thickness variations are assumed to be the sole cause of the MBA) at 25°S to 27°30'S on the Mid-Atlantic Ridge, and that topographic features whose dominant wavelength is less than 80 km are isostatically uncompensated.

Bell and Buck (1992) working on gravity data from a single line along the Reykjanes Ridge axis north of area C, where the ridge exhibits the morphology of a fast spreading ridge, have concluded that residual anomalies are no greater than 10 mGal and can be explained by density anomalies in the upper crust. They cite the absence of large

bathymetric relief and large mantle Bouguer anomalies as the visible expression of a hot flowing crust. The cause of such a hot crust is the proximity of the Iceland hotspot. They propose that the base of the crust is hot and can spread along axis to accommodate any irregularities in crustal thickness that may appear as a result of a segmented mantle flow or magma supply.

4.1.5 Summary

The Reykjanes Ridge at 58°N exhibits a median valley in contrast to the ridge axis high to the north. Small and Sandwell's (1989) observations implied that ridge morphology was controlled by spreading rate with fast spreading ridges exhibiting a uniform gravity signal whereas slow spreading ridges gave rise to a highly variable gravity signal. Perhaps the Reykjanes Ridge is one of the best examples of this variable nature due to its transition from ridge axis high to median valley. The reason for this variability is probably due to the proximity of the Iceland hotspot. If the Chen and Morgan's (1990b) model for ridge behaviour is correct, the Reykjanes Ridge at 58°N marks a transition in some physical properties which are just as important as spreading rate to ridge dynamics. At 58°N the crust has thinned sufficiently, relative to the Reykjanes Ridge to the north, or the mantle temperature has reduced enough to produce a median valley. These observations of the Reykjanes Ridge at 58°N will be able to provide constraints on future modelling to assess the importance of crustal thickness and mantle temperature on ridge morphology.

In this chapter gravity data acquired in the EW9008 cruise have been used in conjunction with the bathymetry to obtain a Mantle Bouguer Anomaly (MBA) and residual anomaly for the survey area at 58°N (area C, figure 4.1). This was done by subtracting the gravitational effect of a constant thickness crust (computed using a Fourier method proposed by Parker (1972)) and the effect due to a diffusively cooling lithosphere. The results suggest that a non-transform offset (second order discontinuity) exists at 57°50'N on the Reykjanes Ridge.

4.2 Methodology

4.2.1 Outline of the Reduction Method

The object of the reduction method is to remove all of the predictable components of the gravity signal to allow interpretation of the residual field. The gravitational effect of the

crust is modelled by making use of the Parker (1972) method for the rapid calculation of potential anomalies. The gravitational effect of density variations due to the thermal effects of a spreading lithosphere is computed by making use of the solution of the two dimensional thermal equation (Pearson and Lister, 1979; Morgan and Forsyth, 1988). These two components are added and removed from the observed signal to leave an interpretable residual signal which is inverted to provide an estimate of the crust-mantle interface relief.

4.2.2 Theory

4.2.2.1 Introduction

Parker (1972) showed how to calculate the potential field caused by a non-uniform and uneven layer of material using Fourier transforms. The basis and result of this theory is given below.

4.2.2.2 The 'Forward' Computation

Consider an x, y, z or $\mathbf{r}$, z (where $\mathbf{r} = [x, y]$) cartesian coordinate system with z directed downwards. The gravity anomaly, $\Delta g(\mathbf{r})$ produced by a three dimensional perturbing layer of density ρ, is calculated at the surface, $z = 0$. The perturbing layer is defined relative to $z = 0$ and $z = z_0$ as $z = z_0 - h(\mathbf{r})$, where $h(\mathbf{r})$ is measured positively downwards from z to z_0.

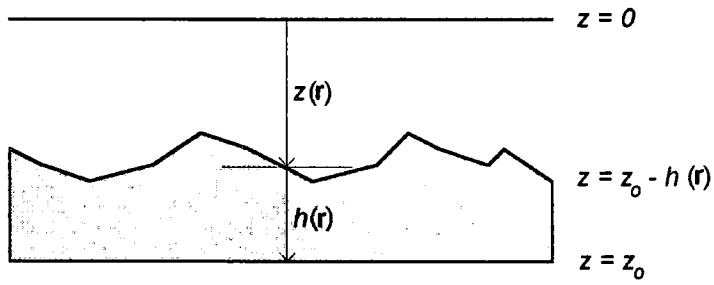

Figure 4.8. An uneven layer is described by $z(\mathbf{r})$ relative to the reference plane $z = 0$. The distance between the uneven layer and another reference plane $z = z_0$ is $h(\mathbf{r})$.

For convergence there are two restrictions: (i) $h(\mathbf{r})$ tends to zero outside some finite area, therefore giving rise to negligible variations in the gravity signal outside this region; and (ii) $z_0 - h(\mathbf{r})$ is always greater than zero, which is true for marine and airborne surveys. Given these conditions and the above geometry, the Fourier transform of $\Delta g(\mathbf{r})$ is given by

$$\mathrm{F}[\Delta g(\mathbb{r})] = 2\pi G\rho \exp(-|\mathbb{k}|z_0) \sum_{n=1}^{\infty} \frac{|\mathbb{k}|^{n-1}}{n!} \mathrm{F}\left[h^n(\mathbb{r})\right] \qquad (4.1)$$

where G is the Universal Gravitational Constant, $\mathbb{k}$ is the wave vector and the definition of the two dimensional Fourier transform is:

$$\mathrm{F}[f(\mathbb{r})] = \iint f(\mathbb{r}) \exp(\mathrm{i}\,\mathbb{k}\cdot\mathbb{r}).\mathrm{d}x\,\mathrm{d}y \qquad (4.2)$$

The reference level z_O is an arbitrary plane, but setting it mid-way between the highest and lowest parts of the interface, z_O - $h(\mathbb{r})$, provides the fastest convergence of the series. In the oceanic reduction method there are usually two interfaces: the water-crust and the crust-mantle. If the additional interface is described by $w(\mathbb{r})$, then the Fourier transform of $\Delta g(\mathbb{r})$ is given by:

$$\mathrm{F}[\Delta g(\mathbb{r})] = 2\pi G \exp(-|\mathbf{k}|z_0) \sum_{n=1}^{\infty} \frac{|\mathbb{k}|^{n-1}}{n!} \mathrm{F}\left[\rho_h h^n(\mathbb{r}) - \rho_w w^n(\mathbb{r})\right] \qquad (4.3)$$

The summation is carried out for a finite number of terms and then the appropriate inverse Fourier transform is made to obtain $\Delta g(\mathrm{r})$.

4.2.2.3 The Inverse Problem

One inverse problem related to the Parker (1972) forward modelling method is computing $h(\mathrm{r})$ if $\Delta g(\mathrm{r})$ is known, i.e. calculating the relief of a density interface at a given depth below the gravity observations.

Oldenberg (1974) rearranged equation 4.1 to obtain

$$F[h(\mathbf{r})] = \frac{F[\Delta g(\mathbf{r})]\exp(|\mathbf{k}|z)}{2\pi G\rho} - \sum_{n=2}^{\infty} \frac{|\mathbf{k}|^{n-1}}{n!} F\left[h^n(\mathbf{r})\right] \qquad (4.4)$$

where z is the depth at which the relief of the interface is computed. The first term of equation 4.4 is essentially the downward continuation of the observed gravity field. The first term is subject to short wavelength instability when downward continuation is performed.

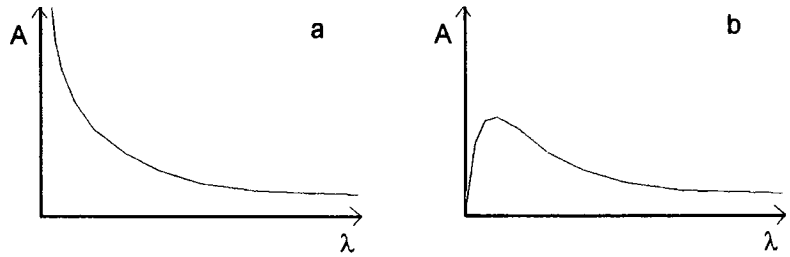

Figure 4.9. Plots of the first term in equation 4.4 (A) as a function of wavelength, a) unfiltered, b) filtered.

Figure 4.9a shows the first term of equation 4.4 as a function of wavelength and graphically illustrates how short wavelengths can be amplified to the extent of obscuring the longer wavelength component of the signal. To suppress these instabilities, a cosine filter is applied to remove the short wavelength components. Figure 4.9b illustrates schematically the effect of filtering in conjunction with downward continuation: the amplification of shorter wavelengths is truncated. The amplification effect is input data-dependent and so the filtering applied varied according to the dataset being studied.

To find $h(\mathbb{r})$ the solution is iterated until the change in $h(\mathbb{r})$ becomes negligible. For the first iteration, setting $h(\mathbb{r})$ equal to zero is sufficient.

4.2.2.4 Lithospheric Thermal Models

The lithospheric model used in this reduction (Pearson and Lister, 1979) has been outlined below, as has another method formulated by Morgan and Forsyth (1988) which was used for comparison.

Pearson and Lister's (1979) model used to predict the temperature distribution of the lithosphere as a function of distance from the spreading axis and depth, solves for the flux of heat using the two dimensional thermal equation. There are two major assumptions. The first assumption is that new lithospheric material is emplaced in a narrow zone at the axis facilitating an approximation to horizontal plate motion only. The second assumption is that ridge axis is infinitely long.

The equation for temperature within a moving material is:

$$\rho c \frac{\partial T}{\partial t} + \rho c u \frac{\partial T}{\partial x} = \kappa \nabla^2 T + H \qquad (4.5)$$

where u is the spreading velocity, κ is the thermal conductivity, H is the rate of internal heat generation, T is the temperature, and c is the specific heat.

The case of interest here is that of steady state and no internal heat generation. Equation 4.5 then reduces to:

$$\rho c u \frac{\partial T}{\partial x} = \kappa \nabla^2 T \tag{4.6}$$

To obtain the temperature distribution the model comprises a lithosphere of constant thickness, l. The boundary conditions are that the base of the lithosphere and the ridge axis are both at the same constant temperature, T_m, and that the top surface (the seafloor) is at 0°C. The solution can then be found by means of a series (McKenzie, 1967) and is given by:

$$T(x,z) = T_m\left\{1 - \frac{z}{l} + \sum_{n=1}^{\infty} A_n \exp\left(\alpha_n \frac{x}{l}\right)\sin\left(n\pi\frac{z}{l}\right)\right\} \tag{4.7}$$

$$\alpha_n = \frac{ul}{2\kappa} - \sqrt{\frac{u^2 l^2}{4\kappa^2} + n^2\pi^2}$$

where

$$A_n = \frac{2(-1)^{n+1}}{n\pi\left(1 - \frac{\alpha_n \kappa}{ul}\right)}$$

Another model which has been used by other workers (e.g. Morris and Detrick, 1991; Lin et al., 1990) is that of Morgan and Forsyth (1988). Their method makes use of a finite element model which is used to produce the thermal effects of passive plate-driven flow in more geometrically complex ridge-transform systems.

4.2.3 Implementation

4.2.3.1 Implementing the 'Forward' Computation.

To make practical use of the Fourier Transform method of Parker (1972), the Fast Fourier Transform algorithm of Cooley and Tukey (1965) is used in a program written by D. Forsyth. This requires the input data to be in a form such that the number of grid nodes in each direction is a factor of 2^n. Bearing this factor in mind, the sub-bottom bathymetry data recorded along the shiptracks shown in figure 4.10 were interpolated onto a 128 x 128 grid (Smith and Wessel, 1990), with internodal spacing of 0.6 km in the east-west and north-south directions, close to the along-track resolution. As the ship track spacing was ~3.6 km, an anti-alias filter was applied to allow shorter nodal spacing without introducing artifacts. Another practical problem encountered when making use of the Fourier transform is the Gibbs phenomena caused by discontinuities in the signal. To overcome this problem the dataset was mirrored in the east and south borders to provide a data surface which was continuous in all directions.

In the model used here, the lower boundary of the crust was constrained so that it was exactly the same shape as the top surface, but set 6 km deeper. It was also necessary to truncate the infinite sum in equation 4.1. It was found that the fifth term contributed less than 0.1 mGal to the predicted signal. Hence summation to five terms was deemed adequate.

The Free Air Anomaly (FAA) was interpolated onto a similar grid as the bathymetry and the crustal gravity effect. The Mantle Bouguer Anomaly (MBA) was obtained by subtracting the crustal effect from the FAA.

4.2.3.2 Implementing the Lithospheric Model

Equation 4.7 was evaluated in a program written by R. Searle. For practical use some assumptions were made. The temperature at the top and bottom boundaries of the lithosphere were 0°C, and 1250°C respectively. The spreading rate was set at 10 mm a^{-1} and the thermal coefficient of expansion was 3.4 x 10^{-5} $°C^{-1}$ .The thickness, *l*, was set at 100 km and the temperature field was calculated out to 100 km from the axis. Multiplying the temperature field by the expansion coefficient results in a density structure which can be forward modelled (in this case, by placing the density contrasts into the GRAV program written by M. H. P. Bott), to provide the gravitational attraction at sea level due to the underlying thermal structure. The top boundary of the model is placed at the sea floor.

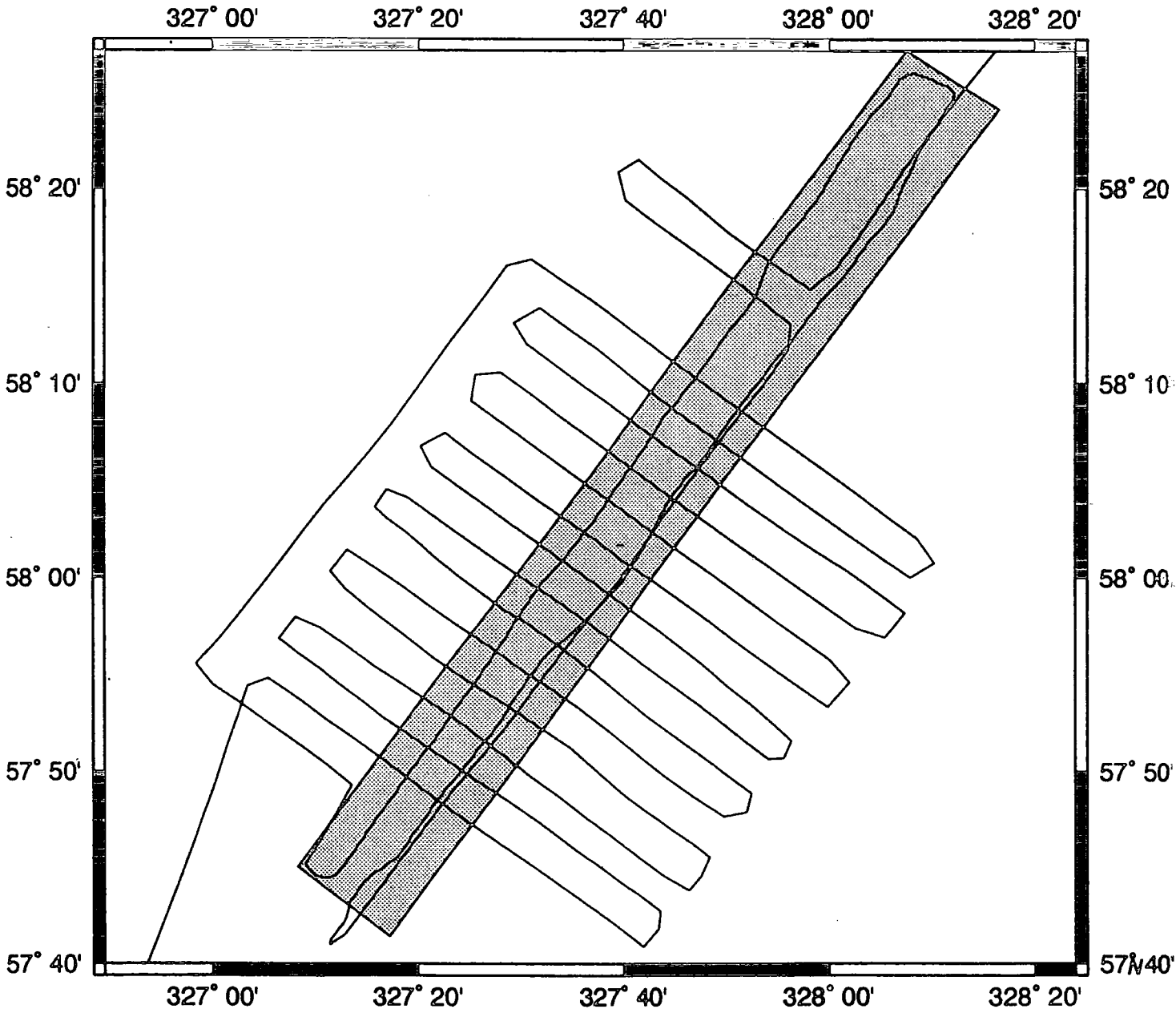

Figure 4.10. Shiptracks for the EW9008 cruise in area C: the subject of this chapter. The stippled box represents the area covered by TOBI observations.

In figure 4.11 the gravitational effect of the cooling lithosphere is depicted. Curve A was the one used for this reduction and curve B denotes the result of using a model formulated by Morgan and Forsyth (1988). It can be seen that the difference between the two different methods is quite small and below the error for the data. It also should be noted that the model does not take into account the compositional difference between the mantle and crust.

The gravitational effect of the spreading lithosphere is then rotated onto a grid the same size as that of the MBA (128 x 128), aligning the spreading axis with the centre of the median valley. The thermal effect is then subtracted from the MBA to produce the residual gravity: the component of the gravity signal that is not predicted by the model.

4.2.3.3 Implementing the Inversion

The residual anomaly was downward continued to the base of the crust (7.5 km below sea level) to aid with interpretation of the signal. As was mentioned earlier, a filter is needed to eradicate any unwanted noise. Several filters were tested to see which produced the best results. If the taper cut-off is at too short a wavelength then the results appear 'ringy' and if the cut off is at too long a wavelength then the final map is devoid of features. To evaluate the performance of the filters the RMS of the inferred crust-mantle relief was plotted against the RMS difference between the residual gravity and the gravity produced by the crust-mantle relief (figure 4.12). The filter which produced the smallest signal in both the gravity and the relief was picked as the best. The filter chosen had the following properties. It tapered to zero those components of the wavefield of less than 20 km. It cosine tapered the signal between 20 - 30 km. It allowed components of wavelength greater than 30 km to pass unaffected.

4.3 Data

4.3.1 Acquisition

The location of the study area is shown in figure 4.1. "Area C" is a 50 x 50 km area at 58°N on the Reykjanes Ridge axis. The R/V Maurice Ewing was equipped with geophysical intrumentation that included a swath-bathymetry multibeam echosounder (Krupp Atlas HYDROSWEEP, Grant and Schreiber, 1990), a Bell BGM-3 gravimeter and a proton magnetometer (the last of whose survey results were interpreted by

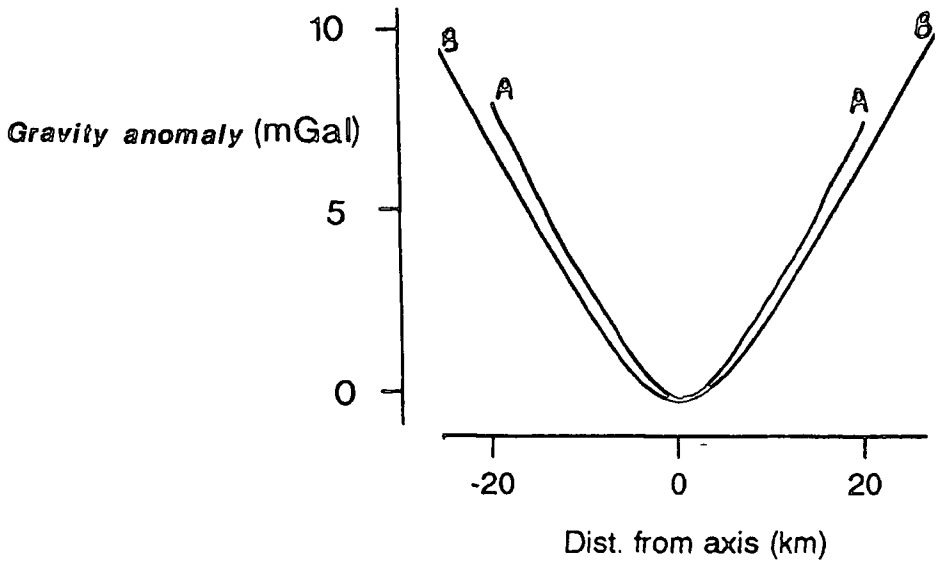

Figure 4.11. A plot showing the ridge normal gravity signature of the lithospheric cooling effect for two slightly different methods of calculation. Curve A represents the effect removed from the Mantle Bouguer Anomaly in this chapter. Curve B represents the same effect but computed using Forsyth's programs.

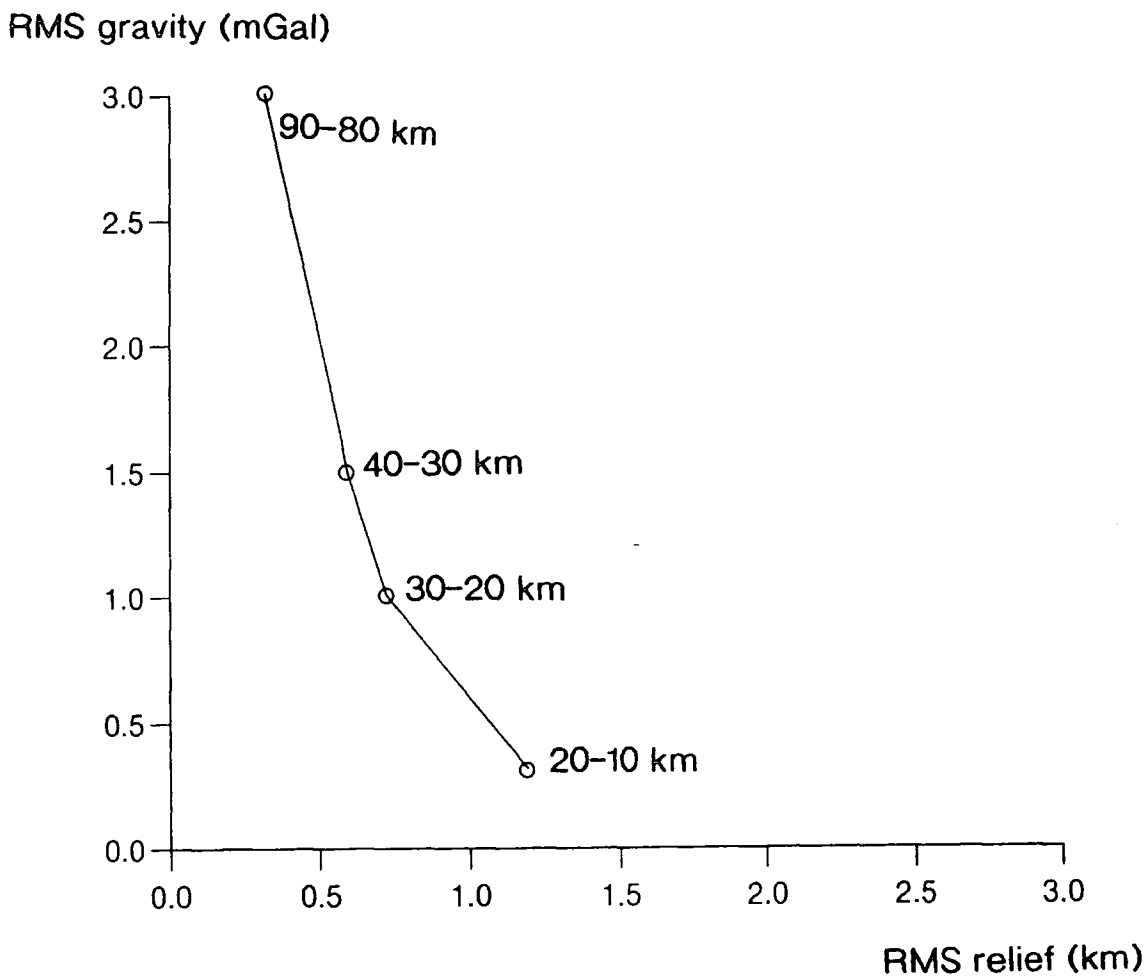

Figure 4.12. A plot depicting the RMS gravity versus RMS crust-mantle relief for different filters. The RMS relief is the RMS signal of the inverted residual gravity converted to crustal variation. The RMS gravity is the RMS signal of the difference between the original residual gravity used for the inversion and the gravity field produced by the computed crust-mantle relief.

Owens, 1991). The multibeam echosounder has a swath width of twice the water depth which meant that with tracks oriented perpendicular to the axis and spaced ~3.6 km apart, almost complete bathymetric coverage of the area was obtained. Figure 4.10 indicates the shiptracks within area C and figure 4.13 is a plot of the bathymetry data. The primary navigation tool was the Global Postioning System (GPS) which reverted to LORAN C when less than two satellites became visible at any time. The ship's position was logged at twenty second time intervals and used to produce a one minute time interval navigation file. Coincident with depth soundings along track are gravity readings made with a BGM-3 gravimeter, at one second intervals with a five point running average and cubic spline smoothing to remove data spikes. These data were merged with the navigation to produce gravity readings at one minute time intervals corresponding to an along track data separation of 300 m (at 10 knots). The stippled area in figure 4.10 represents Towed Ocean Bottom Instrument (TOBI) sidescan coverage of the area. The TOBI vehicle was brought aboard by the Institute of Oceanographic Sciences and carried a 30 kHz side-scan sonar capable of a resolution of 5 m across by 20 m along track.

4.3.2 Shipboard Data Reduction

Reduction of the gravity data was carried out using equation 4.8:

$$g_{FAA} = g_{obs} - g_{\Phi} - g_{E\ddot{o}t} \quad , \tag{4.8}$$

where g_{FAA} is the free air anomaly at sea level obtained by subtracting the theoretical gravity, g_{Φ} , calculated from the Geodetic Reference System 1980 (Torge, 1989) and the Eötvös correction, $g_{E\ddot{o}t}$, from the observed gravity, g_{obs} .The Eötvös correction is only needed for gravity measurements made on a moving platform and takes into account the difference in vertical component of acceleration experienced by the gravimeter due to its motion relative to the Earth. This effect is dependent upon the azimuth of the heading, α, the velocity, v, and the latitude, Ψ, of the platform. Assuming a spherical Earth model of radius 6371 km, the expression of the Eötvös effect is (Torge, 1989),

$$g_{E\ddot{o}t} = 4v \cos \Psi \sin \alpha + 0.0012v^2 \text{ mGal} \tag{4.9}$$

In marine gravity surveys, the Eötvös correction has a large bearing upon the accuracy of the data. With the Global Positioning System (GPS), instantaneous positions are accurate to ± 50 m and velocities to ± 0.1 m s^{-1}, equivalent to about 0.5 mGal (Torge,

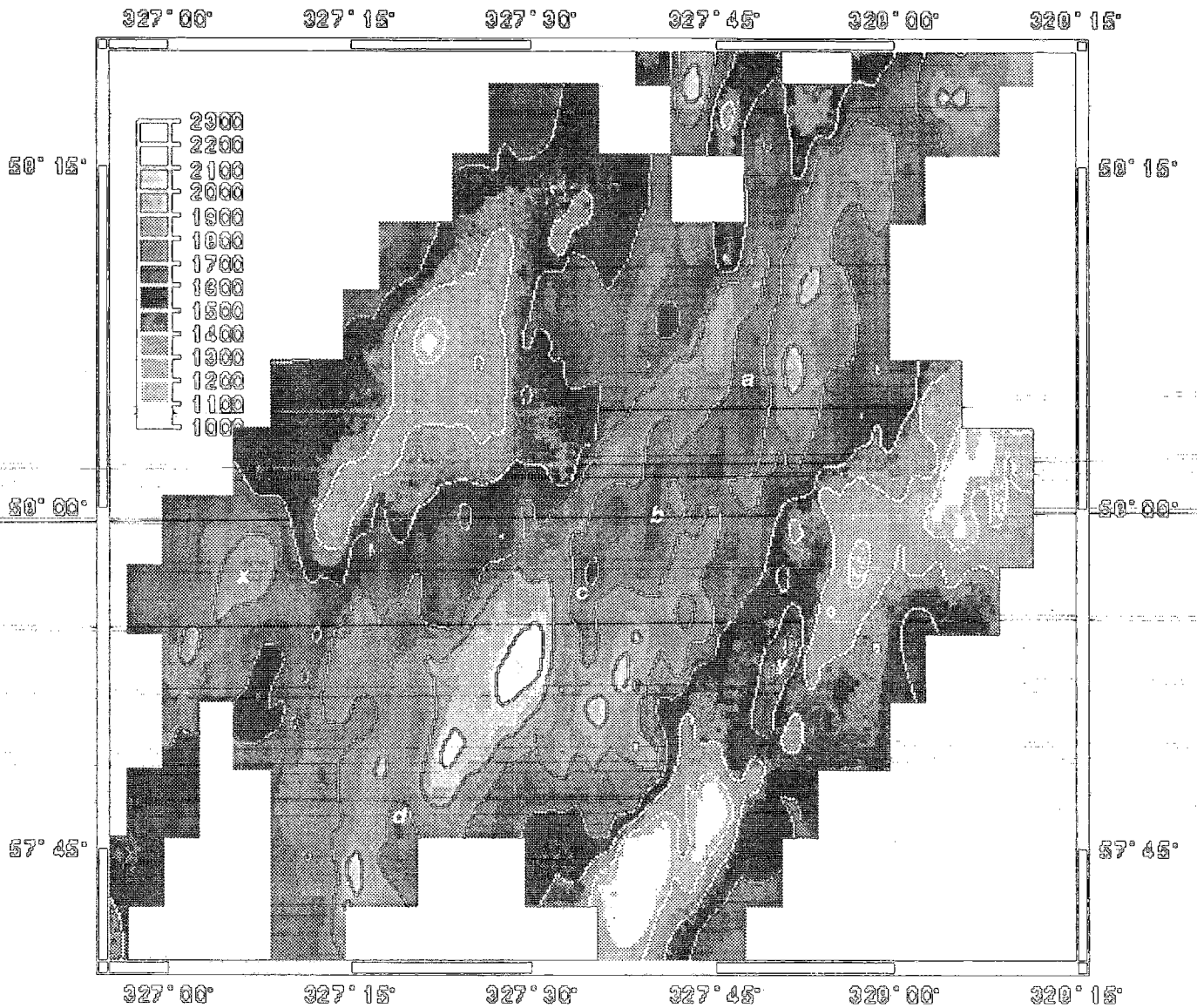

Figure 4.13. Bathymetry plot for area C. The plot was created by gridding the centre-beam of the HYDROSWEEP data onto a 128x128 grid using splines in tension (Smith and Wessel, 1990). The white contour line interval is 200 m. x and y are the 'offset' basins. a, b, c, and d are interpreted as axial volcanic ridges.

1989), allowing accurate surveys to be undertaken. An attempt was made to link the gravity observations with IGSN71. There was no pre-cruise tie at Bergen (the start of the cruise), therefore a tie from August 1990 was used (Bhudypramano, pers. comm.).

4.3.3 Errors in Sea Gravimetry

Bell Aerospace (Buffalo, New York) commercially produce the BGM-3 gravimeter which was aboard the R/V Maurice Ewing. The gravimeter is based on an accelerometer used originally for inertial navigation. Its sensor comprises a small 'proof' mass that sits inside a coil constrained by three springs. The mass is allowed to move vertically between the N poles of two permanent magnets. The electromagnetic force produced by current in the coil holds the mass at a reference position. Any changes in gravity cause the mass to be displaced relative to the coil and the current produced by the displacement of the mass is used to restore it to the reference position. The signal generated by the displacement, which is filtered and output digitally, is proportional to the change in gravity. The whole sensor arrangement is operated on a gyro-stabilised platform to account for rapid motion and to maintain the machine in a vertical position. The BGM-3 gravimeter arrangement also has the advantage of an absence of cross-coupling which would require the additional monitoring of horizontal accelerations (Torge, 1989).

Bell and Watts (1986) showed that the BGM-3 gravimeter was far more accurate than contemporary sea gravimeters such as spring and vertical string gravimeters. They showed that the system recovered in ~3 minutes after sudden changes in the ship's heading. They also executed a test survey to check the accuracy of the BGM-3 in the field. The accuracy was assessed by comparing the sea survey free air anomaly with that produced from a comprehensive network of ocean bottom gravimeters accurate to 0.15 mGal. The method of estimating the accuracy of a ship survey is to calculate the cross-over error (figure 4.14). This is the difference in the interpolated free air anomaly at a position where the ship-track crosses itself. The internal cross-over error (i.e. cross-over error in one leg) was found to have an RMS of 0.38 mGal, whereas the actual RMS difference between the two datasets was 0.58 mGal. Another survey carried out offshore developed a cross-over error of 0.7 mGal.

The causes of the error lie with instrument error, which include un-filtered vertical accelerations, and navigation. In October 1990, the full constellation of GPS satellites was not yet installed and bad weather experienced during the cruise may have added to uncertainties in position and velocity, especially changes in altitude. For example, a ten

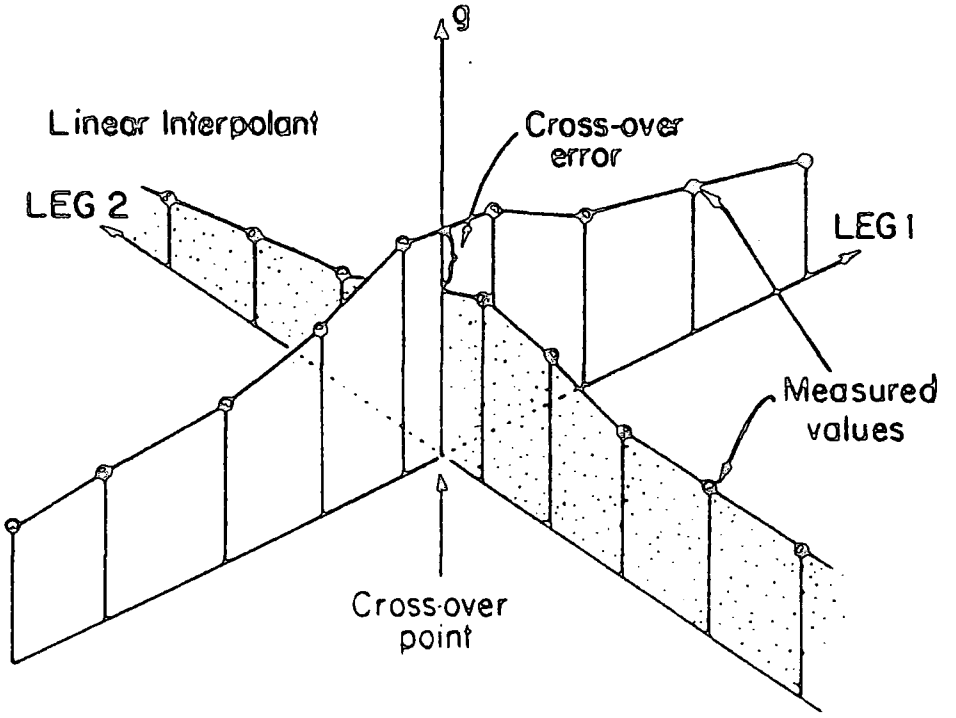

Figure 4.14. A sketch defining the term cross-over error. When two shiptracks cross the cross-over error is the discrepancy between the two reading at the same point. After Wessel and Watts (1988).

metre uncertainty in altitude would lead to a 3 mGal uncertainty. The BGM-3 gravimeter also suffered a drift of approximately 6 mGal per month (Bhudypramano, pers. comm.). The survey of area C was carried out in ~1 day and so the error due to drift is likely to be ~0.2 mGal. The accuracy of the gravity data for the EW9008 survey was quantified by examining points where the shiptracks crossed in area C. For 39 crossings this was done by hand, and it was found that the RMS error was 2.0 mGal which is taken to be the error in the gravity data.

4.4 Modelling the Oceanic Crust

4.4.1 Introduction

Examination of what is known about oceanic crustal structure suggests that to model the crust four points must be addressed:

i) whether to use one layer or many layers for the crustal model;
ii) the density of the crustal layers;
iii) the thickness of the crust; and
iv) the density of the mantle.

4.4.2 One Layer Crust versus Multilayered Crust

Kuo and Forsyth (1988) report that using a single mean density for a single layer as opposed to multiple densities for many layers shows little change in the final outcome of the model. To check this finding different crustal models of layered densities were compared with a crust of uniform density for the data used in this study.

All of the multi-layer models had a 6 km thick crust whose top layer coincided with the seafloor, an average density of 2700 kg m^{-3} and were underlain by a 3300 kg m^{-3} mantle. The composition of these crusts is described in figure 4.15.

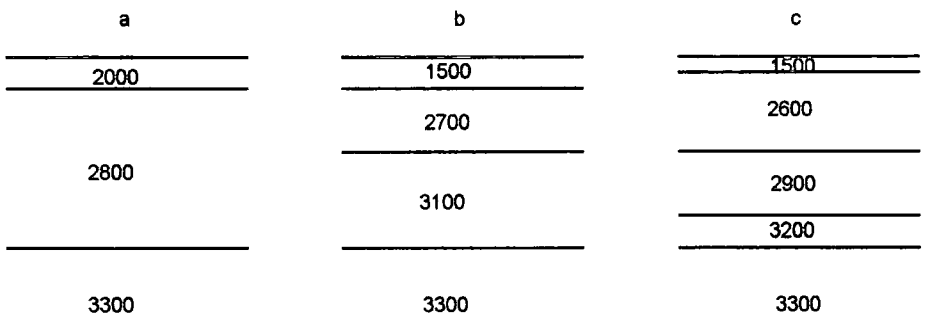

Figure 4.15. Composition of the modelled crusts used to test the gravitational effect of a one layer crust versus a multi-layered crust. (a) top 1km: ρ = 2000 kg m^{-3}; bottom 5 km: ρ = 2800 kg m^{-3}; (b) top 1km: ρ = 1500 kg m^{-3}; next 2 km: ρ = 2700 kg m^{-3}; bottom 3 km: ρ = 3100 kg m^{-3}; (c) top 0.5 km: ρ = 1500 kg m^{-3}; next 2.5 km: ρ = 2600 kg m^{-3}; next 2 km: ρ = 2900 kg m^{-3}; bottom 1 km: ρ = 3200 kg m^{-3}

The gravitational effects of these models were compared with the effect of a single layer crust of thickness 6 km, and density 2700 kg m^{-3} , again underlain by a 3300 kg m^{-3} mantle. The difference between the gravitational effects produced by models a, b, c (figure 4.15) and the one layer model are depicted in figure 4.16a, b and c. The deepest and shallowest points in the bathymetry give rise to the greatest discrepencies (~2 mGal), but overall the difference in amplitude is much smaller (~0.5 mGal) than the cross-over error. Therefore, in view of this result a single-layered model has been adopted.

4.4.3 Crustal Densities

Bunch and Kennet (1980) and Fowler (1976) carried out seismic refraction surveys at 59°30'N and 37°N, respectively, on or near the ridge crest in the North Atlantic. When the P-wave velocities were converted to density using the Ludwig, Nafe and Drake (1970) velocity-density relationship (figure 4.17), they gave densities ranging from 2400 kg m^{-3} at the top to 2900 kg m^{-3} at the base of the crust.

Another method of estimating crustal density is Parasnis' (1962) method, where the equation for the Bouguer anomaly, g_b, is rearranged thus

$$(\rho - \rho_{water})(2\pi Gz) = g_{faa} - g_b \qquad (4.10)$$

So plotting depth, z, against the free air anomaly, g_{faa}, (neglecting terrain correction) gives the gradient as $1/2\pi G\rho$, where the symbols are as above, assuming that g_b is

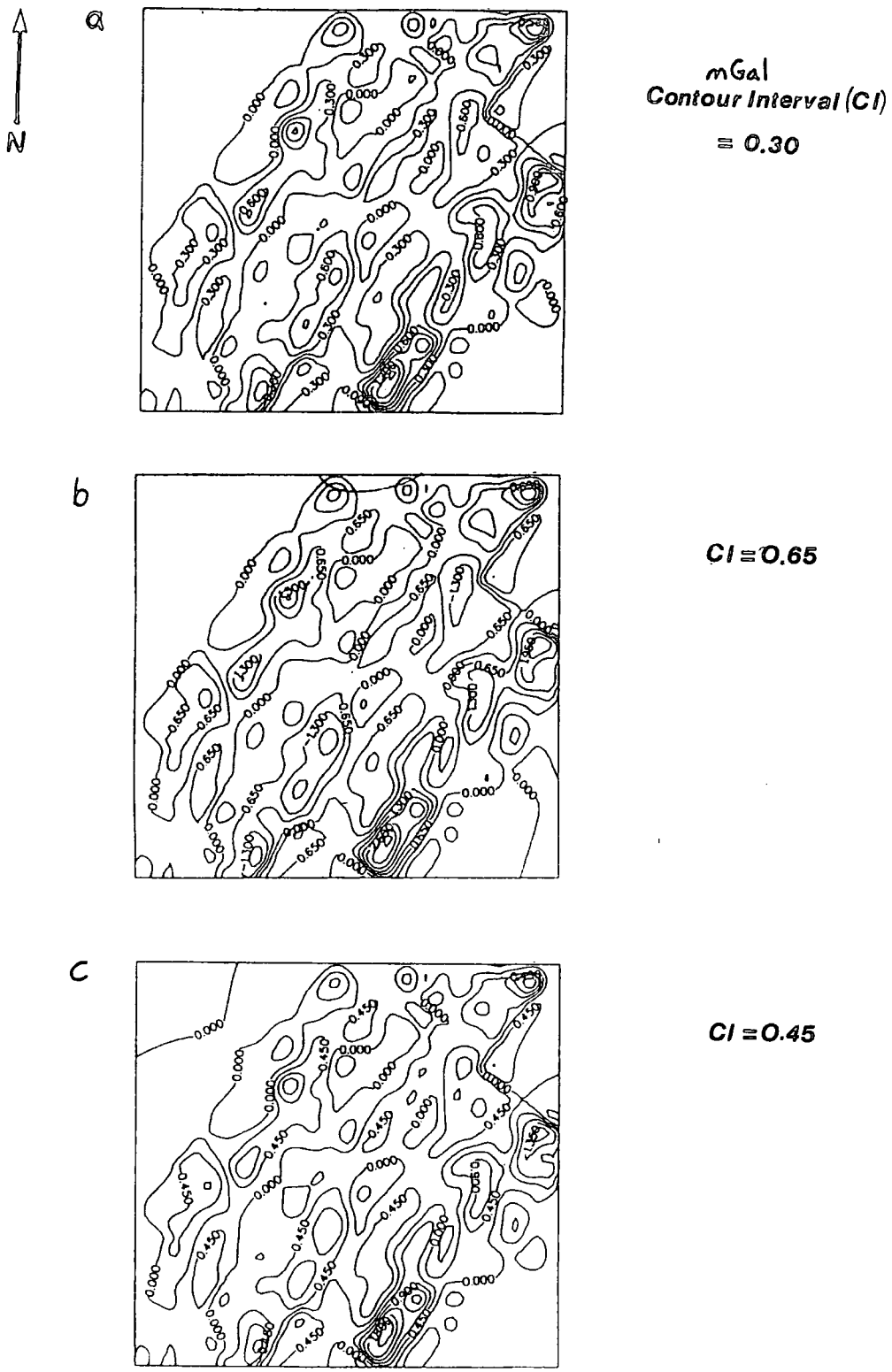

Figure 4.16. Contour plots showing the effect of using multiple density stratifications for the crust when using the Parker (1972) method. a) The difference between a single layer and a two layer crust. b) The difference between a single and a three layer crust. c) The difference between a single and a four layer crust.

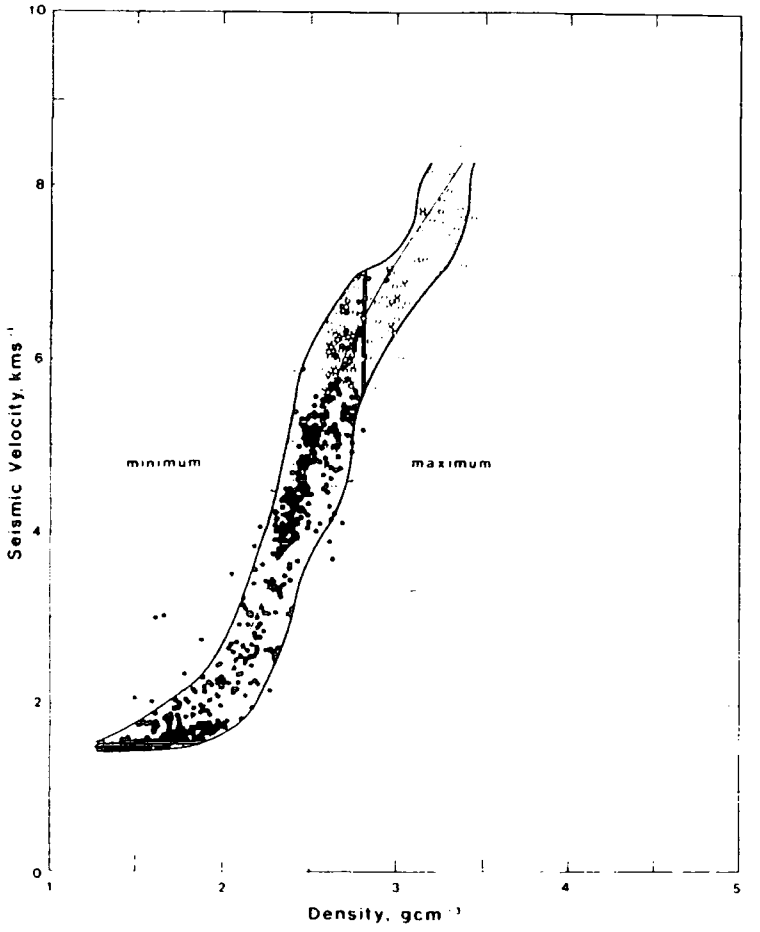

Figure 4.17. A compilation of laboratory measurements of P-wave seismic velocity and density after Ludwig, Nafe and Drake (1970). The thin line in the centre of the scatter is taken as the mean velocity-density relationship. The solid vertical bar represents 2800 kg m^{-3}. Open circles represent metamorphic and igneous rocks while black dots represent sediments. From Barton (1986).

uncorrelated with depth when the correct density is chosen. Hence an estimate of the water-rock density contrast can be obtained for the topmost crust. From figure 4.18, two discrete gradients can be discerned resulting in densities of about 1800 kg m^{-3} above 1500 m depth and about 3100 kg m^{-3} below that. The terrain correction that was omitted would modify the actual values, but it is plain to see that the shallower material that probably forms the mountains is less dense than that in the basal regions. The mountainous regions off-axis are probably equivalent to the AVRs and so as such are formed by extrusion of basalt into sea water at ~0°C. As in Iceland, when basalt erupts into a glacial environment the hyaloclastite rock formed is of low density caused mainly by the high porosity. This could be what is observed here: highly porous volcanic constructional features allowing large scale hydrothermal circulation, and in the basal regions, less porous sheet flows or even a possibility of ultrabasics in fracture zone walls. Alternatively, and probably more likely, the variation in density is seen because the off-axis, shallower regions generally have a higher Bouguer anomaly because of the lithospheric cooling effect. This means that the Bouguer anomaly and depth are correlated and so Parasnis' (1962) method is not valid.

Finally, DSDP hole 409 drilled at 62°37'N 25°17'W on the Reykjanes Ridge has recovered cores to 319 m below the seafloor and 240 m into volcanic rocks. The results of wet density experiments on the cored rock agree with gamma ray attenuation logs giving an average result of 2700 kg m^{-3} (Luyendyke et al., 1978). Therefore in view of the uncertainty attached to the Parasnis method results, the DSDP drill results have been favoured for forward modelling purposes, and hence the single layer model is chosen to have a crustal density of 2700 kg m^{-3}.

4.4.4 The Thickness of the Crust

For the purpose of forward modelling, the shape of the crust is taken to be one that has a crust-mantle interface of exactly the same shape as the water-crust interface, i.e. has a constant thickness of 6 km. However, Bell and Buck (1992), assume a crustal thickness of 9 km for the Reykjanes Ridge north of area C (at ~59°30'N) and seismic results suggest a thickness of this order (Bunch and Kennet, 1980). The gravitational effect of an 8 km thick crust was subtracted from the effect of a 6 km crust to assess the differences that this choice would give rise to. The result is plotted as figure 4.19 and shows that the amplitude of the difference is less than the cross-over error of this survey and so a crustal thickness of 6 km is considered sufficiently accurate.

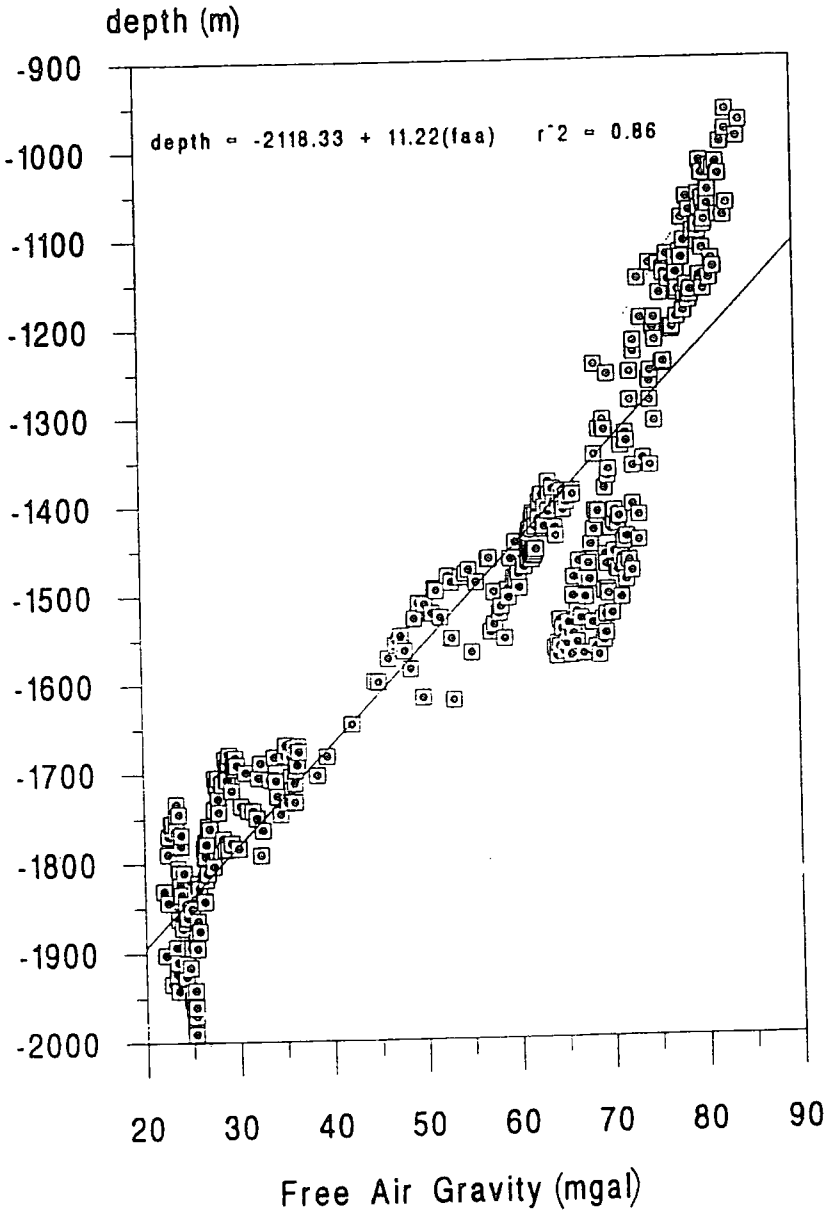

Figure 4.18. A scatter plot of the Free Air Anomaly versus depth for area C. The gradients of the plot are equal to $1/2\pi G\rho$, where ρ is the density contrast between the rock and water.

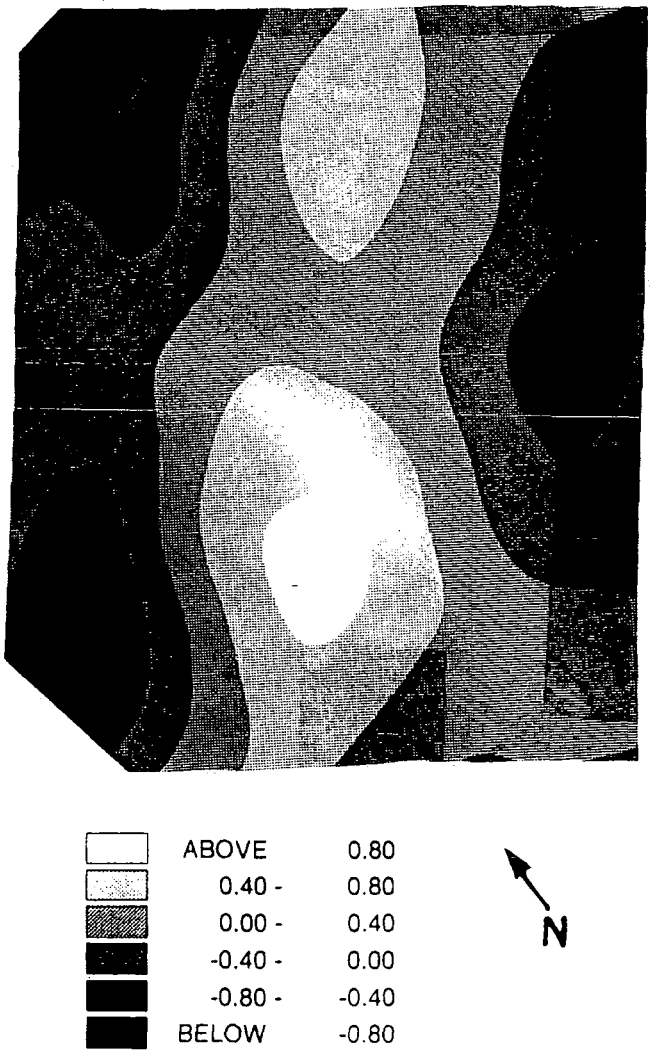

Figure 4.19. A black and white shaded plot showing the difference in the forward modelled gravity field due to crusts (using the Parker[1972] method) of thickness 6 km and 8 km. The contour shade interval is 0.4 mGal. The plot covers the same area as the bathymetry data in figure 4.13.

4.4.5 Density of the Upper Mantle

Bullen (1975) gives a range of mantle densities from 3300 - 3400 kg m^{-3}. Kuo and Forsyth (1988) and others (e.g. Morris and Detrick, 1991) doing similar mantle Bouguer reduction work choose a value of 3330 kg m^{-3}. For this study 3300 kg m^{-3} was chosen, which is equivalent to a mantle velocity of ~8.2 km s^{-1} when converted using the Ludwig, Nafe and Drake (1970) velocity-density relationship. This value is not as important as that for the crust since the gravitational effect of the mantle-crust interface is only ~20% that of the water-crust interface (for the same density contrast). This is because of the ~1/depth relationship experienced by this model (Kuo and Forsyth, 1988).

4.4.6 The Model

The final model chosen had a density of 2700 kg m^{-3} and constant thickness of 6 km causing the crust-mantle interface to be the same shape as the water-crust interface. The mantle in the model is set at a density of 3300 kg m^{-3}.

4.5 Results

4.5.1 Bathymetry

Gridded bathymetry data is displayed in figure 4.13. A modest median valley striking at 034° runs through the centre of the area. The valley has a width of ~15 km and the valley walls have a height of the order of 200 m. In the centre of the valley there are three evenly spaced shallower features, (a, b and c), 200 m above the valley floor, 10 km in length and 2 km wide. These are interpreted as axial volcanic ridges (AVRs) and are dealt with in more depth by Searle et al. (under review). Two AVRs (c and d, figure 4.13) border a large, partially fault-bounded basin (57°53'N), one to the north and one to the south, offset in the ridge normal direction by ~10 km. The basin has a maximum depth in excess of 2400 m, some 500 m below the valley floor, and length and breadth of 20 km and 10 km respectively. East and west of the basin along the flowline are observed lesser basins (x, y) at 10-15 km intervals. These are interpreted as traces of the central basin as it is transported off-axis indicating its stability for at least the past 2 Ma. The seafloor flanking the median valley lies at a depth of 1600 m, but rises to less than 1200 m where there are mountains present, those to the east being ~200 m higher. It is noticeable that some of the flank walls of the mountains have strikes similar to the

AVRs, indicating the partial preservation of AVRs as they become tectonised and carried off axis.

4.5.2 TOBI Observations

A mosaic of TOBI data for the rift valley region of this area (figure 4.20) consists of two swaths running along the axis. Obvious in the central part of the mosaic is an area of relatively low backscatter: this is the main basin. The low acoustic return is thought to be due to the presence of a thin sediment cover. Also present within the basin are large faults giving strong signal return. To the south of the basin is an AVR. Very high backscatter and hummocky texture indicate that this is a constructional volcanic feature echoing the en echelon volcanic zones seen on Iceland (in appearance at least) (Walker, 1992). To the north of the basin many seamounts and highly backscattering terrain can be seen. These areas are again AVRs. Note that only the basin contains visible large scale faulting near the axis.

4.5.3 Tectonics at 58°N

Shaw (1992) uses data from between 28°N and 31°N on the MAR to show that crust near segment centres displays more frequent smaller throw faults relative to larger less frequent faults observed near segment ends, and implies that colder weaker lithosphere at segment ends is responsible for this. He further states that normal fault initiation occurs at the axial valley walls and that most linear topographical relief observed on the MAR is a result of the growth of large normal faults at rift walls rather than by constructional volcanism. Using the bathymetry data obtained for this area, gridded at 100 m intervals, it is possible to look at the gradients of the slopes. By taking the component of the gradient normal to the ridge axis and highlighting the positions where it exceeds a threshold, it becomes possible to observe the spatial occurence of large faults. What must be borne in mind, however, is that the horizontal resolution of 100 m means that as faults become steeper they become much more difficult to observe, and therefore steep faults may be missed. Although this is statistically unsatisfactory the method at least gives a first order estimate of the occurrence of major normal faulting. Figure 4.21 shows the case for gradients (dz/dx) greater than 0.4 for which the borders of the median valley may be quite easily discerned. Spacing of the fault zones are 2-4 km on each side of the median valley.

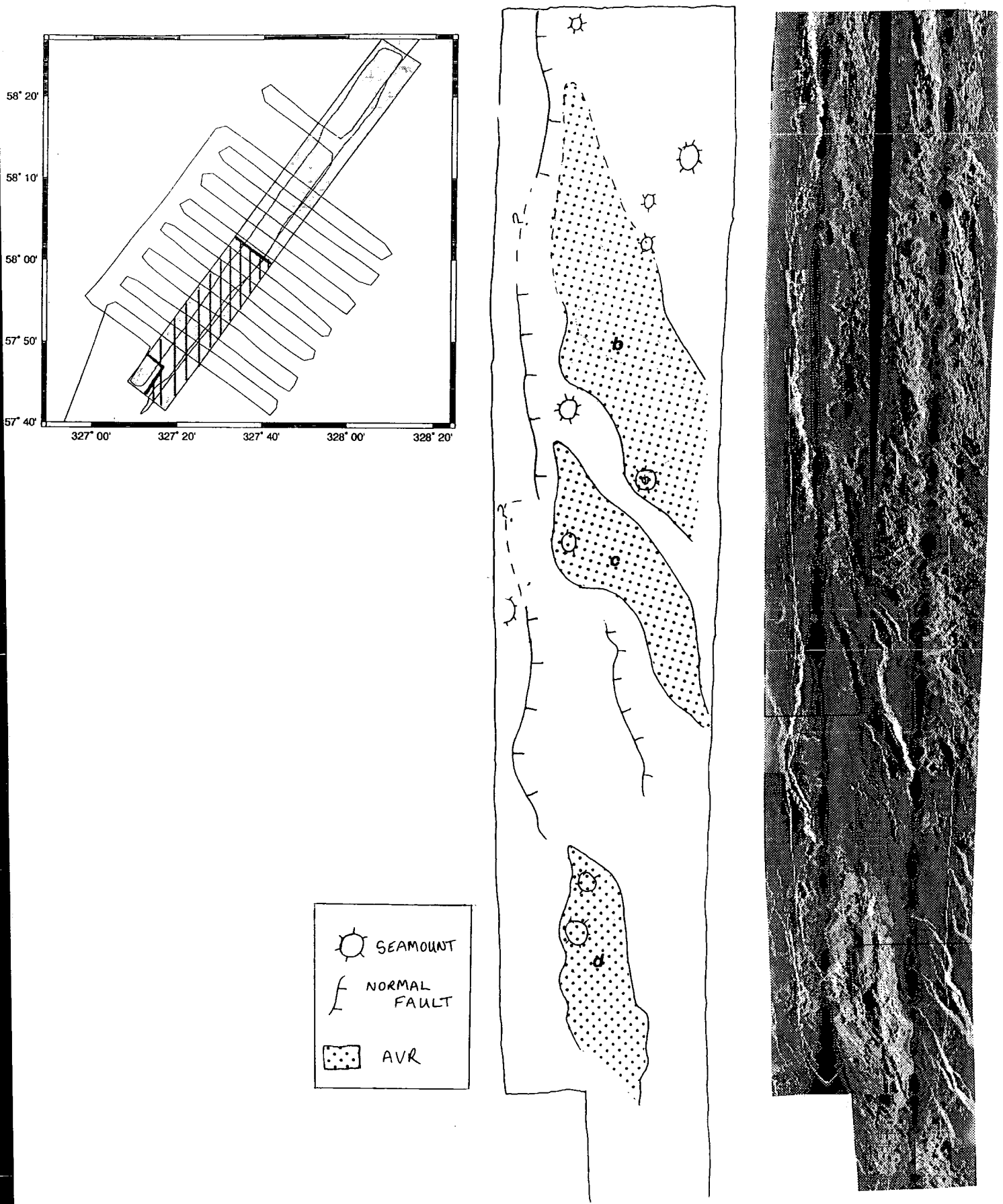

Figure 4.20. TOBI mosaic for the median valley region of area C with a simplified line drawing interpretation. Bright areas represent regions having high backscatter properties and dark areas represent the converse. b, c, and d refer to the axial volcanic ridges indicated in figure 4.13. Hatched region in inset map is the approximate extent of the mosaic.

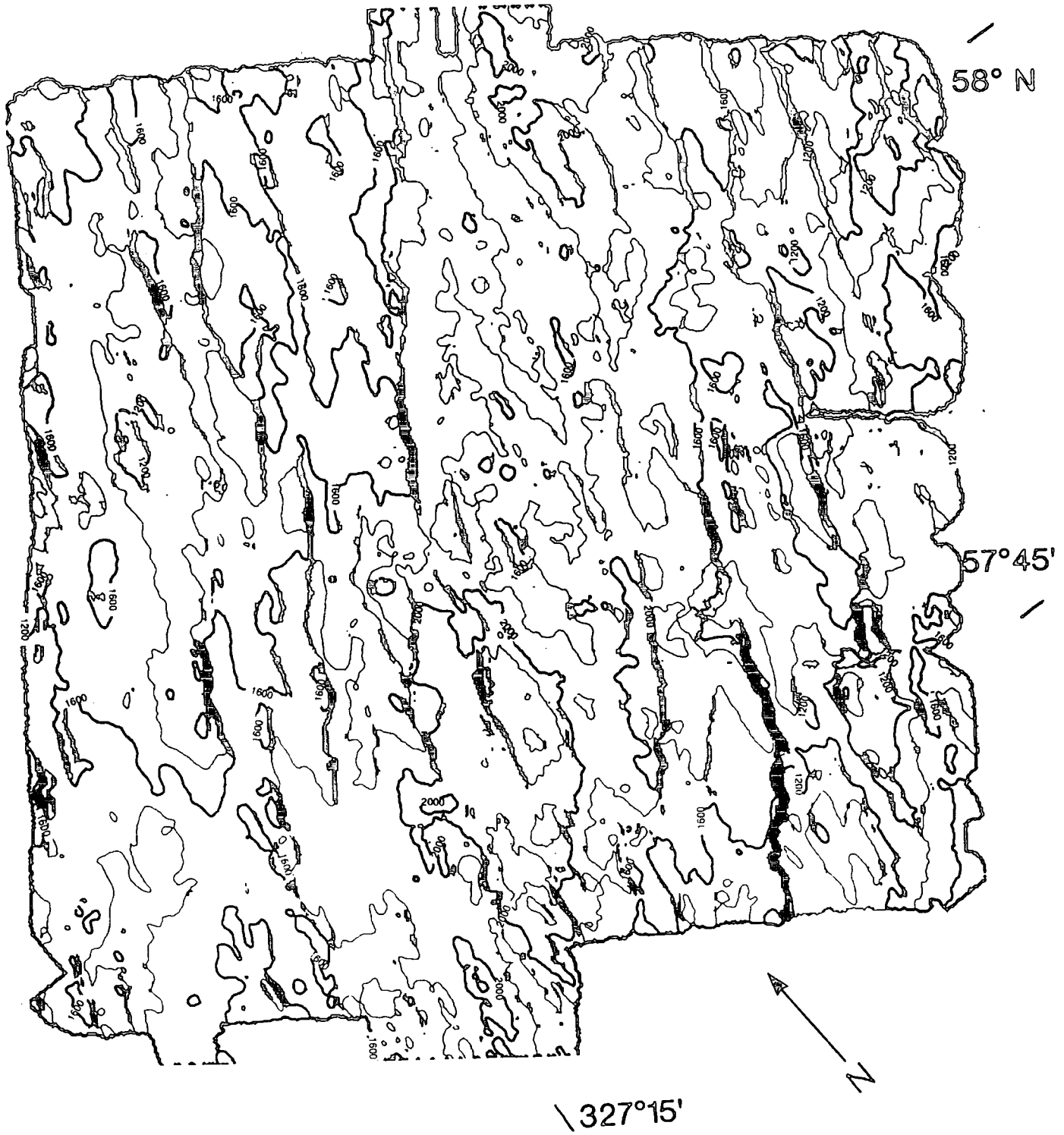

Figure 4.21. Contour map of the bathymetry for area C. Black areas represent a bathymetric gradient in excess of 0.4. The contour interval is 200m annotated every 400 m.

The rift basin is the only site within the rift valley exhibiting major faulting. Existence of large normal faults within the basin may be the mechanism for accommodating plate separation when insufficient new crustal material is available in contrast to the AVR rich environment to the north and south where highly backscattering terrain and volcanoes are seen on TOBI sonographs and bathymetry plots.

4.5.4 Gravity

4.5.4.1 Free Air Anomaly

The free air anomaly has a peak to peak amplitude of 70 mGal, the highest being above the mountains and lowest over the deep basin. The values given in figure 4.22 are not absolute as no satisfactory port ties were made to calibrate the readings into the International Gravity Standardisation Net.

As is commonly known and can be seen in this figure 4.22 the free air anomaly has a strong positive correlation with the bathymetry due to the high density contrast between the water and crust. This property was used earlier to obtain an estimate for the density of the crustal rock.

4.5.4.2 The Mantle Bouguer Anomaly

Removal of the gravitational effect due to a single layer crust described earlier results in the so called Mantle Bouguer Anomaly (figure 4.23). This anomaly represents the effect of subtracting the calculated attraction of a constant thickness crust from the FAA. Thus, MBA highs exist above areas where either the crust is thinned or denser, or the mantle is denser, and lows are found above zones of thicker or lower density crust or lower density mantle, or a combination of the two.

Removal of the crustal layer has resulted in a gravity field with a peak to peak range of 30 mGal. Immediately noticable in this result is the removal of the low observed in the FAA over the basin. Instead this has now become a gravity high (+4 mGal) relative to field north and south of the basin along the axis. This effect can also be seen off axis with higher amplitude effects (~8-10 mGal) over the lesser basins to the east and west. A pattern now readily observable in the MBA is the increase in magnitude of the anomaly away from the axis. This is thought to be mainly due to the effect of the

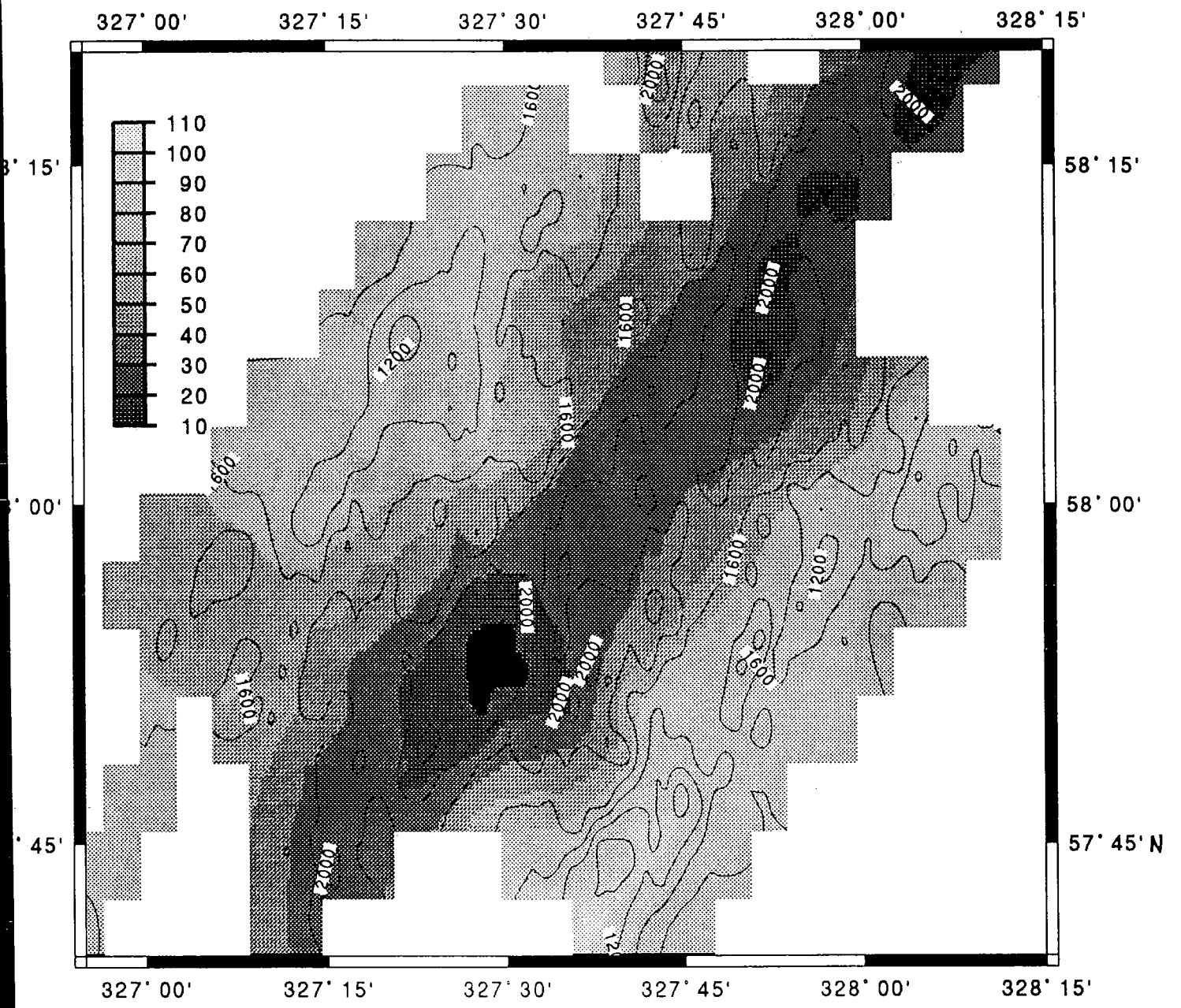

Figure 4.22. Black and white shaded map of the Free Air Anomaly for area C. The shade interval is 10 mGal with black representing low and light grey representing high. The black contour lines represent the bathymetry contoured every 200 m and are annotated at 400 m depth intervals.

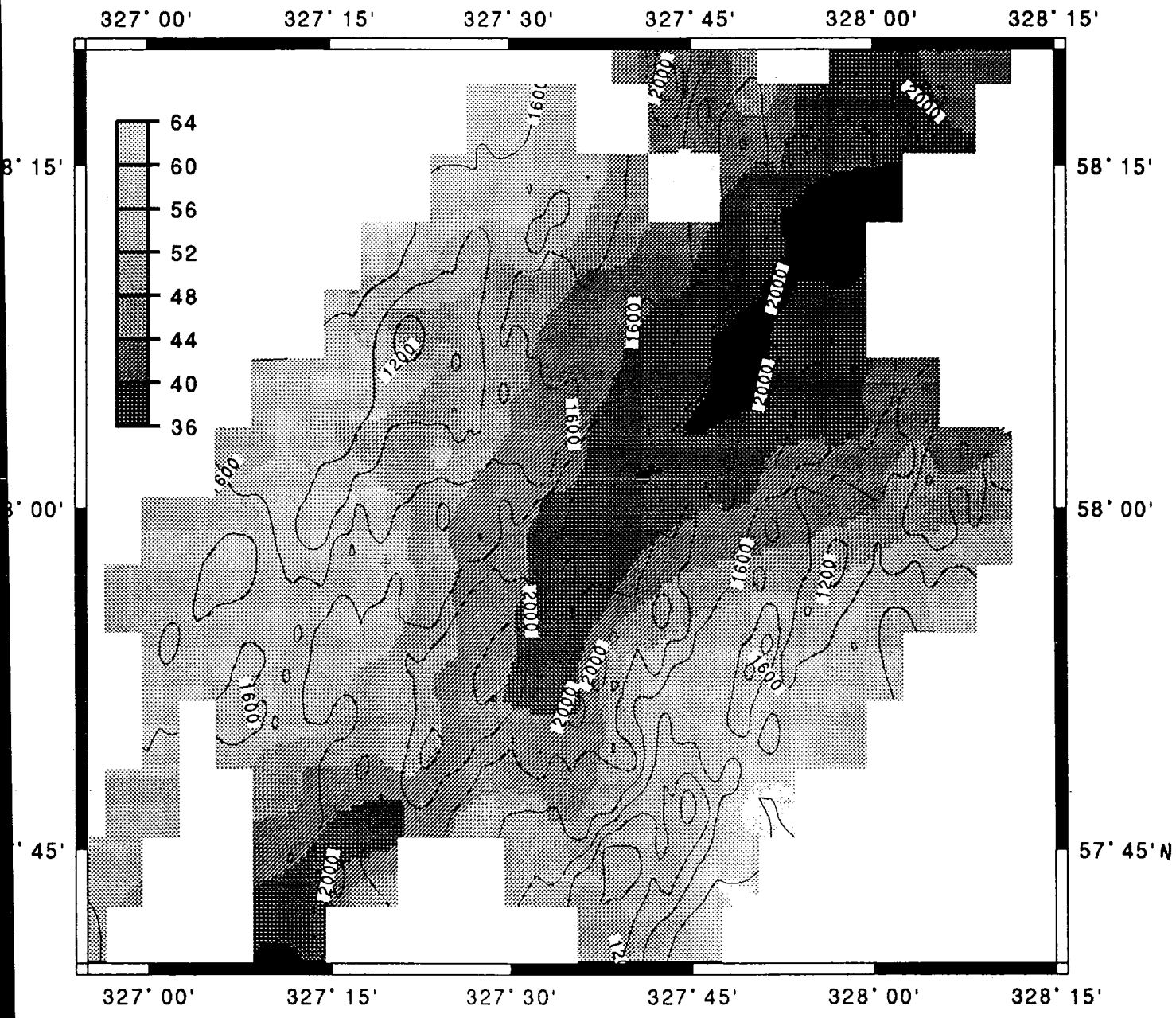

Figure 4.23. Black and white shaded map of the Mantle Bouguer Anomaly for area C. The shade interval is 4 mGal with black representing low and light grey representing high. The black contour lines represent the bathymetry contoured every 200 m and are annotated at 400 m depth intervals.

temperature variations in the underlying lithosphere and its removal is the next and last step in the reduction.

4.5.4.3 Residual Anomaly

The residual anomaly (figure 4.24) shows the result of subtracting the modelled lithospheric thermal effects from the MBA. Any anomalies still visible indicate departures from the assumptions of the model, i.e. a constant thickness and constant density crust and the modelled temperature distribution. The gravity field is now reduced to a range of 20 mGal, some 10 % of the energy in the FAA.

Looking along the axis, the gravity peaks (+6 mGal, relative) over the basin before falling again as the median valley progresses southwards. However, the orientation of the low as it approaches the basin from the north changes from along the strike of the axis to becoming parallel with the strike of the AVRs and coincident with AVR (c) to the east of the basin. Off axis, but along the axial strike, it can be seen that the lesser basins (x, y) also display highs of 6-12 mGal along axis.

The two regions of high gravity relative to the axis correlate with the off axis basins and are observed along the flowline which cuts the major basin in the south of the region. There still seems to be a minimum related with the axis. This may be the result of imperfections in the thermal model used.

4.5.4.4 Inversion

Downward continuation of the residual gravity field to the base of the crust and conversion to basal crust relief results in a map of crustal thickness (assuming all the residual anomaly is due to variations in crustal thickness) having a mean of 6 km. This indicates that total variations in the thickness of the crust of ~800 m (figure 4.25) in the vicinity of the off axis basins relative to the AVR region would account for the observed anomalies. For an 8 km thick crust the magnitude of the total crustal thickness variation is ~1000 m

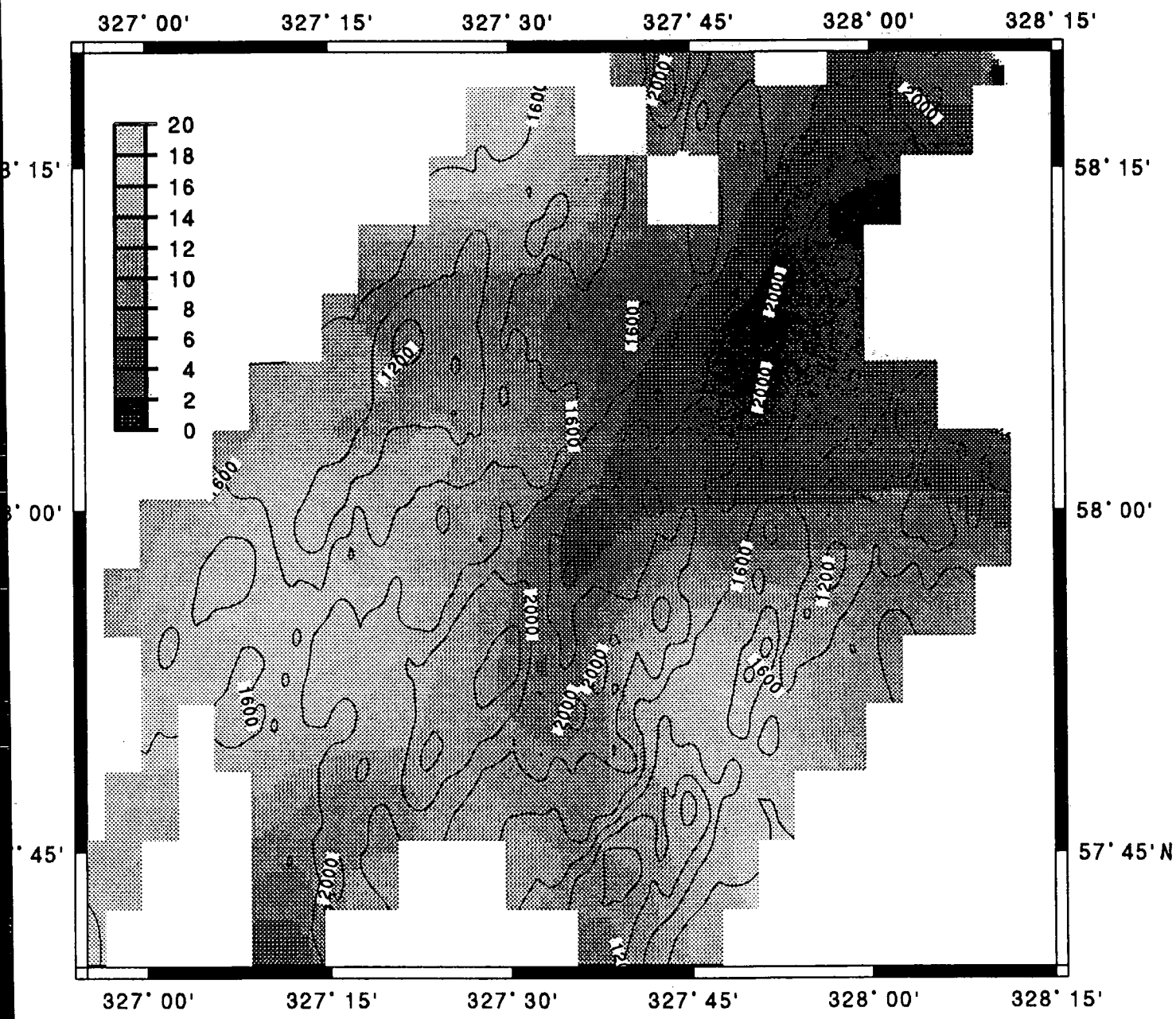

Figure 4.24. Black and white shaded map of the Residual Anomaly for area C. The shade interval is 2 mGal with black representing low and light grey representing high. The black contour lines represent the bathymetry contoured every 200 m and are annotated at 400 m depth intervals.

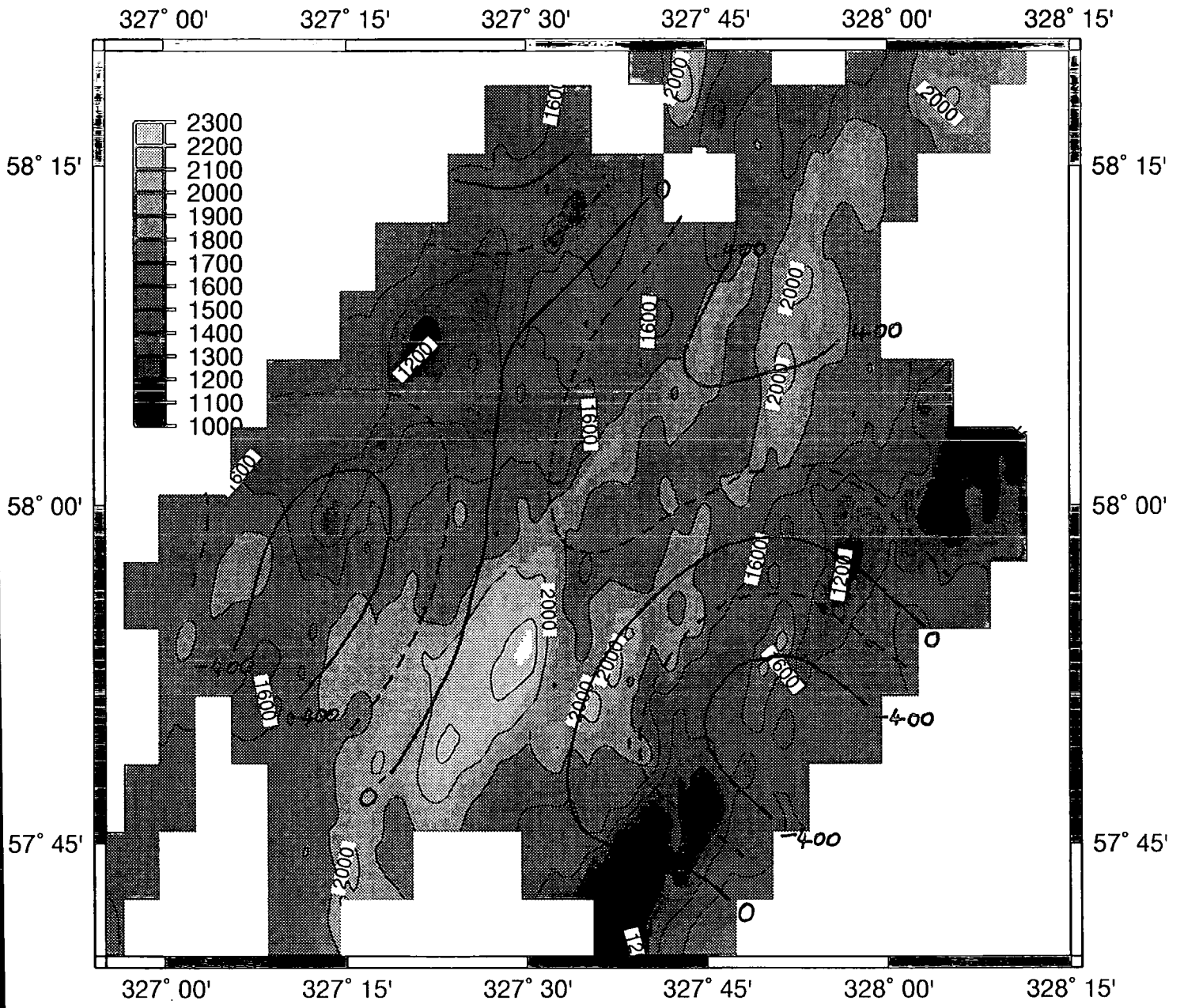

Figure 4.25. Black and white shaded map of the bathymetry for area C with the contours (thick black, and thick black dashed) representing the crust-mantle relief in metres at a depth of 7.5 km.

4.6 Discussion

4.6.1 Causes of the Residual Gravity Anomaly

The residual gravity anomalies are due to differences between reality and the simple crustal and thermal models. Possible explanations for this difference are anomalous thickness of the crust, variations in crustal density, and variations in the density of the mantle. In reality all of these effects probably contribute towards the final anomaly, but each shall be examined in turn.

4.6.2 Crustal Thickness Variations

Figure 4.25 shows that the thinnest crust is under the basins (x, y; figure 4.13). This could be interpreted as being indicative of a poorer magma supply to the basin region at the axis. A reduction in magma supply of 15% (for a 6 km thick crust) in the basin region relative to elsewhere would lead to a 1km difference in the thickness of the crust. The persistence of the off-axis residual gravity highs would imply that less magmatic accretion in the basin region relative to the AVR-rich environment along axis has been stable for at least 2 Ma, creating a ribbon of thinned crust which extends along the flowline from the basin. Along the axis the crust is also seen to thin by 400-500 m over the basin indicating the possibility that variable magma supply is still unevenly distributed. Magnetic results also imply that the magnetic layer 2 is thinned in the basin area or that there is a lower volume magnetisation (Owens, 1991).

The two highs in the residual in the south of the region, as mentioned before, are separated by a relative low at the axis. Since the temperature effects of the lithosphere are thought to have already been removed this could be taken to mean that there is thicker crust at the basin relative to off-axis. A further 10% decrease in crustal accretion relative to the present day accretion at the axis would account for this apparent lack of crust. Alternatively the increased thinning of the crust off-axis could be just due to the addition of the effects of repeated normal faulting off-axis as Shaw (1992) suggests.

4.6.3 Variations in Crustal Density

The gravity low seen in the residual gravity could be said to be correlated to some extent with extrusive features such as AVRs. For example, a cuboid of length 20 km, width 5 km, thickness 300 m, density contrast 600 kg m^{-3} (relative to the surrounding

rock) at a depth of 1500 m, which could be said to be comparable to an AVR, would give rise to an anomaly of 5 mGal, which is similar to the size of anomaly observed within the median valley. This anomaly would diminish with time due to infilling of pore spaces and closing of fractures as the rocks age. Holmes and Johnson (1993) infer increasing density of shallow rocks with age from submersible gravity data from the Juan de Fuca Ridge. The correlation of the residual field with the AVR bordering the north of the basin lends some weight to Bell and Buck's (1992) proposal that the residual anomalies on the Reykjanes Ridge are caused by shallow crustal density contrasts.

One other possibility is that mid-crustal density contrasts are responsible for the residual signal. On the East Pacific Rise mid-crustal low velocity zones are attributed to the presence of partial melt (Toomey et al., 1990). The results show a zone of low velocity ($\sim$ -1 km s^{-1}) extending from ~1 km below the seafloor to ~3 km below the seafloor. If the effect of this anomalous zone is estimated by calculating the gravitational influence of an infinite horizontal cylinder, we find that a radius of 1 km, a density contrast relative to the crustal model of 50 kg m^{-3} and at a depth of 2 km below the sea surface, results in an anomaly of magnitude ~1 mGal - below the observational errors encountered.

4.6.4 Mantle Density Variations

An alternative to a crustal explanation of the observed residual gravity is that of a density anomaly in the upper mantle. Lin et al. (1990) imagine ascending plumes of mantle beneath ridge segment centres giving rise to MBA 'bulls eye' lows (figure 4.26), the density of the mantle being least at the plume's centre and greatest at its extremities, where offsets occur. If the mantle density does contribute to the resultant anomaly then its density must be lower at the ridge axis than predicted by the mantle model and, as Lin et al. (1990) suggest, of greater density beneath the basin region. Sparks et al. (1993) predict that the mantle effect may only amount to a few milli-Gal and so variations within the residual anomaly are probably mostly due to crustal anomalies. In this study no bull's eye was enclosed in the area surveyed and the behaviour of the gravity field to the north is unknown. The absence of a bull's eye could mean that the upwelling plume mechanism does not operate here on the ridge and something more complex may be in its place, although further surveying would be required to take this argument any further.

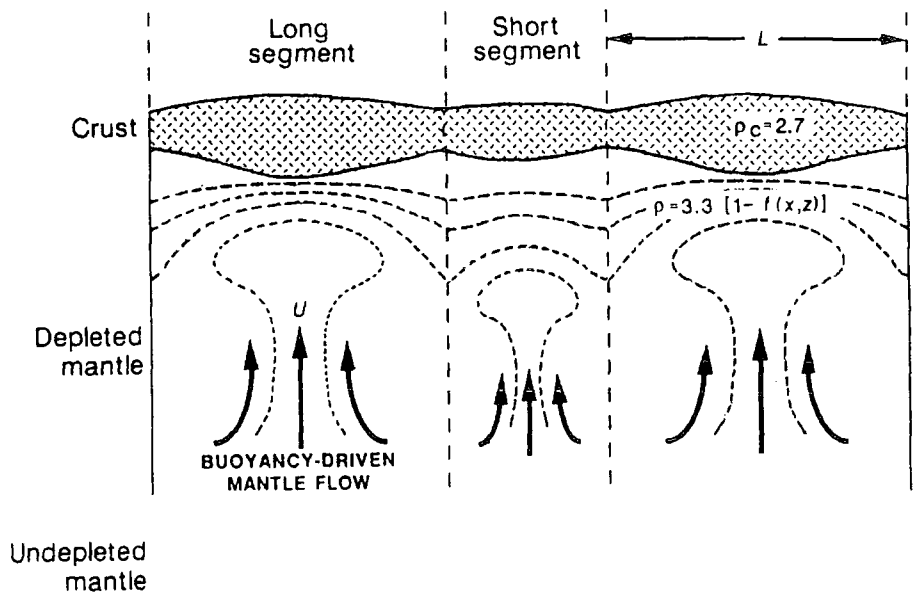

Figure 4.26. The 'mantle diapir model' after Lin et al.(1990). Thick arrows represent mantle flow, The broken lines represent isodensity curves. Diapirs give rise to more decompressional melting under segment centres which gives rise to thicker crust.

4.6.5 Isostasy on the Reykjanes Ridge

Blackman and Forsyth (1991) have performed coherency analysis of gravity and bathymetric data for the Mid-Atlantic Ridge (~26°N) and conclude that bathymetric features shorter in wavelength than 80 km are not compensated isostatically. This conclusion can be tested here. The bathymetry varies by ~600 m between the basin, x, and the mountains at 58°07'N 327°20'. For complete Airy isostatic compensation of this feature a crust-mantle relief of ~1700 m would be required. The crust-mantle relief generated by inverting the residual field results in only ~400 m of total variation between these two points. Although there is some local compensation of the off-axis basins in the form of possibly thinner crust beneath them, it is far from complete. Presumably they are supported by the finite strength of the crust.

4.6.6 Comparison of Other Work with Reykjanes Ridge Residual Gravity Field

The bathymetric, gravitational and magnetic signal for the Reykjanes Ridge at 58°N are interpreted as the basin region at 57°53'N being a non-transform offset.

It is helpful to compare the observations from this study with those from previous work that encountered non-transform offsets. In particular, Morris and Detrick (1991) and Lin et al. (1990) have published results from areas containing an axial basin with associated off-axis traces.

Morris and Detrick (1991) interpret a 'V'-shaped zone of faulting, fissuring and outcropping of serpentinised peridotites just to the south of the Kane Fracture Zone as a non-transform offset. They observe residual gravity highs either side of the median valley at the offset which they interpret as being due to crustal thinning that is persistent for millions of years, although no explanation is offered for the axial thickening of the crust relative to the thinned off-axis areas. Within the same area as Morris and Detrick's (1991) work, Karson (1990) also interpreted the geology of the region. Karson (1990) observed that magmatism was keeping pace with the tectonic extension south of the offset, but at the site of the offset many large fault bounded blocks could be seen, some of which were 400 m high. This observation was interpreted as showing that there was less magmatism at the offset and tectonic extension was accommodated by large normal faulting. Lin et al. (1990) also observe gravity highs which flank the median valley at

non-transform offsets which they attribute to a combination of thinned crust and higher density mantle at the offset.

Comparing the residual anomaly obtained for this part of the Reykjanes Ridge with those from other parts of the MAR produced by the workers mentioned above reveals that all show high gravity flanking the median valley (figure 4.27). The implication is that the Reykjanes Ridge at 58°N in exhibiting a similar gravity signal as other areas on the MAR (in this respect) may also be similar in crustal structure. Alternatively, the thermal model used in all these studies is equally deficient at reproducing the axial behaviour. However, a factor to bear in mind is the magnitude of the anomalies in relation to the depth to the source. The residual anomaly in this study is 20 mGals peak to peak whereas those from the other studies are ~ 30 mGals at twice the water depth.

The work of Sparks et al. (1993) implies that the cause of the residual anomalies is confined to the crust and so enables the residual anomaly to be interpreted as crust-mantle relief variations, crustal density variations or both. Unfortunately, without seismic control on crustal thickness, the contribution of the crust-mantle relief component to the residual field is unknown. The bathymetric analysis described earlier, suggests that magma supply may be reduced to the basal region (relative to the AVRs to the north and presumably the south), with normal faulting, rather than magmatism, accommodating tectonic extension. If Bell and Buck's (1992) 'hot flowing crust' hypothesis is correct, bathymetric variation may be the only manifestation of variations in magma supply along the axis. If this is the case, near surface density variations will be the major contributor towards the residual anomaly. This ascertion is in agreement with Holmes and Johnson (1993) who, on the basis of submersible gravity observations, propose that shallow crustal density increases from 2400 to 2700 kg m^{-3} at 20 km from the axis of the Juan de Fuca Ridge (half spreading rate: 29 mm a^{-1}). An increase in shallow crustal density is also in keeping with increased shallow P-wave velocities with distance from the axis (Bunch and Kennet, 1980). The general increase in residual gravity with distance from the axis can be explained for the case of the evolved AVR-rich region and the evolved basin region. The AVRs are initially composed of low density material but closure of cracks and pore spaces cause the AVR material to increase in density with age. The basin regions are subject to repeated large throw normal faulting which gradually exposes, originally deeper, higher density rock to the surface over time.

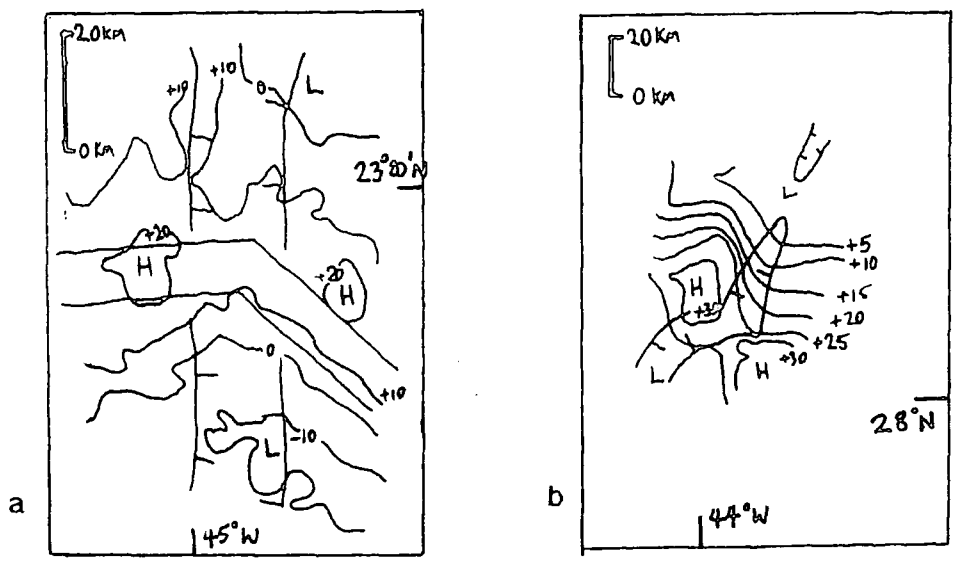

Figure 4.27. Contour maps showing detail of gravity anomalies, H represents a region of high residual gravity. L represents a region of low residual gravity. Lines with ticks represent the median valley wall. a) Contour map showing detail from Morris and Detrick's (1991) residual anomaly for the MARK area. The contour interval is 10 mGal. b) Contour map showing detail of Lin et al.s (1990) residual anomaly for the Mid-Atlantic Ridge (28°50'N).

4.7 The Reykjanes Ridge and the Icelandic Mantle Plume

At 58°N on the Reykjanes Ridge, the onset of second order segmentation is seen as a result of the diminishing effect of the mantle plume beneath Iceland. With increasing distance from the plume the ridge deepens, eventually exhibiting a median valley. An increase in the severity of ridge axis discontinuities is also observed as evidenced by second order segmentation at ~ 58°N, and eventually the first order segmentation of the Bight Fracture Zone (57°N) ~ 900 km away from Iceland. If the anomalously thick crust of the Reykjanes Ridge is assumed to be due to the influx of additional melt along the ridge from the plume (Vogt, 1974; Schilling, 1973), an estimate of the amount of plume melt supplied to the Reykjanes Ridge may be made. The oceanic crust is thought to be ~10 km thick immediately south of Iceland (Angenheister et al., 1980). Assuming that the crustal thickness linearly decreases from 10 km, at Iceland, to a normal oceanic crustal thickness (6 km) somewhere between the Bight Fracture Zone and the Charlie Gibbs Fracture Zone (53°N) (~1200 km southwest of Iceland), the additional crust along the length of the ridge would require between 0.04-0.05 $km^3\ a^{-1}$ (36-45 % of the plume flux estimated in section 3.7) of plume derived melt, for a whole spreading rate of 20 mm a^{-1}.

The Kolbeinsey Ridge to the north of Iceland is not as pronounced as the Reykjanes Ridge. It seems likely that the mantle temperature beneath the Kolbeinsey Ridge would be similar to that beneath the Reykjanes Ridge at the same distance from Iceland. The implication is that the difference between the Kolbeinsey and Reykjanes Ridges may be mainly of a crustal nature. An additional flux of melt from the plume, feeding along pre-existing weaknesses to create anomalously thick crust (the Mid-Atlantic Ridge), may be blocked to the north by the Tjörnes Fracture Zone but be unhindered along the Reykjanes Ridge to the southwest. The Reykjanes Ridge axis high is thus attributed mainly to crustal thickness rather than anomalous mantle temperatures. Thickening of the crust causes the base of the crust to penetrate deeper isotherms, increasing the width of the decoupled zone below the crust until it becomes greater than the width of the failure zone. The result is a ridge axis high.

4.8 Summary

The crustal structure at 58°N is complex with a variety of causes contributing to the final residual gravity field and observed bathymetry:

1. The presence of large throw normal faults within the median valley where constructional features (AVRs) are absent indicates that magmatic accretion is occurring to differing degrees along axis. New crust is filling the gap left by separating tectonic plates within the AVR, magmatically rich region; this is contrasted with normal faulting, rather than new crust, to accommodate plate motion at the magma starved offset basin.

2. The gravity results imply possible relative thinning of the crust of up to 800 m at the offset region and its off-axis trace, indicating that crustal accretion is occurring beneath the AVRs to a greater extent than at the basin. Hence thinned crust is associated with the non-transform offsets and has been for at least the past 2 Ma.

3. There remains a ridge-normal trend of an increase in the gravity signal away from the axis. This implies that either the thermal model used here is inadequate or that there are temporally related density changes, or crustal thickness variations occurring in the upper crust that have not been modelled, such as closure of fractures and pore spaces by hydrothermal action and the exposing of lower crustal rocks at the surface by faulting.

4. The concurrence of bathymetric and magnetic field minima and gravity maxima, along axis, suggest that 57°53'N on the Reykjanes Ridge is the site of a non-transform offset.

Chapter 5
Summary

5.1 Icelandic Plateau

5.1.1 The Mantle

Evidence from different geophysical studies points to the existence of an anomalous mantle beneath Iceland. The anomalous properties of the mantle extend to a depth of several hundred kilometres and include low viscosity, low velocity, presence of partial melt, and low density (see chapter 1). Gravity results from chapter 3 support a low density mantle model and suggest a shallow constraint for the top of the anomalous mantle of no deeper than ~ 40 km. A seismic tomographic image of the plume and geochemical evidence (Schilling, 1973) yielded plume radius estimates of 50 and 200 km, respectively. By crudely assuming that the physical nature of the plume could be approximated by a cylinder, a radius of ~100 km was obtained on the basis that a cylinder having this radius required the least density perturbation (-35 kg m^{-3}) to approximately model the long wavelength Bouguer anomaly. If instead all the long wavelength Bouguer anomaly were attributed to crustal thickening then the crust would be about 7 km thicker than the neighbouring oceanic crust. Assuming that only the Iceland plateau is a consequence of the plume flux (0.8 km^3 a^{-1}) leads to the conclusion that ~14% (0.18 km^3 a^{-1}) of the annual plume flux must melt and be assimilated by the crust. If plume material is 'piped' along the Reykjanes Ridge to create anomalously thickened crust then the plume may be responsible for a further 0.04-0.05 km^3 a^{-1} of melt.

5.1.2 Crustal Accretion

Results from chapter 3 suggest that Iceland may have an average crustal thickness of 17 km if crustal thickening accounts for all of the Bouguer anomaly, much thicker than the 10 km of crust predicted by Palmason's accretionary model. This result is additional evidence in support of an underplating crustal accretion mechanism as proposed by Hermance (1981a,b). Underplating proceeds as partial melt is continually supplied from the plume to a presumably steady state melt accumulation at the base of the crust. To balance the influx of 'new' material to the melt zone, melt which is not incorporated into the crust via dyking/intrusion at (or near) the axis, or extruded at the surface, cools and 'freezes' onto older, colder, adjacent, previously underplated crust. Palmason's model

predicts ~10 km of crust which implies that underplating may be responsible for the extra crust.

5.1.3 Shallow Crustal Heterogeneity

5.1.3.1 Axial Structure

In chapter 2 the upper crust was examined with gravity data in conjunction with results from local earthquake seismic tomography. A comparison of the two datasets was facilitated by forward modelling the seismic results with the program GRAV3D to generate synthetic gravity maps. The Hengill-Grensdalur and Krafla areas are both loci of spreading. At both Hengill-Grensdalur and Krafla, relative positive gravity anomalies are associated with surface eruptions at Husmuli and Leirhnjukur. Below these sites seismic tomography (Husmuli) and the presence of intense seismicity (Leirhnjukur) led to the interpretation of these volumes as containing frozen or cooling magma conduits. This is consistent with the gravity observations which infer the presence of dense sub-surface bodies. At Krafla the caldera ring faults are coincident with underlying high density bodies, possibly 250 kg m^{-3} denser than the caldera infill. The seismic velocities of these bodies suggested that they are dense gabbroic bodies and a positive gravity anomaly supports this conclusion. Similarly, a positive gravity anomaly is situated over the extinct Grensdalur volcano and supports the original seismic tomography based interpretation of a dense basic body. Regions of possible hydrothermal alteration are characterised by relatively low gravity. It is difficult to deduce whether the cause of the relatively low gravity as being due to lowered density through hydrothermal alteration, or the proximity of high density intrusives, or some combination of the two. The gravity fields within the Hengill-Grensdalur and Krafla areas show variations of ~5 mGal, reflecting the heterogeneity present within the shallow crust due to intrusive, extrusive and hydrothermal activity.

5.1.3.2 Regional Structure

On a larger scale, chapter 3 resolved the component of the gravity field that was thought to be produced by crustal heterogeneity. At this scale, with station spacing of ~ 10 km, geological features such as geothermal fields, caldera intrusions and eroded volcanoes seen on a local scale (<10 km) appear to be unresolvable. It was seen that the axial neovolcanic zones correlated quite well with the shallow P-wave velocity and suggest that density variations in the top kilometre of crust are sufficient to explain the axial gravity anomaly. This anomaly is due to a thick low density layer at the axis gradually

thinning with distance. The low density layer corresponds to high porosity extrusives that are eventually eroded or undergo compaction, increasing in density with burial. In support of a shallow crustal source for the Icelandic residual anomaly near the WVZ, Palmason (1971, p.115) reports no obvious seismic structure associated with the WVZ, apart from thickened low velocity layer. Anomalies within the older, western Tertiary zone correlated with depth to the lower crust and may be a result of local isostasy. Relative gravity lows south of Vatnajokull, may be explained by the presence of a thick sedimentary layer. Variations in the gravity field in the east of Iceland are probably due to the frequent shifting of the plate boundary.

5.1.4 Reykjanes Ridge

The concurrence of bathymetric and magnetic minima and gravity maxima, along-axis, suggest that 57°53'N is the site of a non-transform offset. This is the farthest north along the Mid-Atlantic Ridge south of Iceland that this order of segmentation has been documented.

Relative residual gravity highs are associated with the basins of the non-transform offset. This residual gravity field is similar in pattern to, but smaller in amplitude than residual gravity anomalies over other non-transform offsets. The highs are due either to a one or combination of the following: crustal thinning (by up to 800 m); increases in mantle density; mid-crustal or shallow crustal density variations.

The gravity field in this area was shown to have residual variations of ~20 mGal, and an overall increase in gravity correlating with an increase in age. Such a temporally related effect may be associated with an inability of the thermal model to adequately describe the situation at the axis, but another possibility is that of age related density increase. Density increase with age in the upper crust may also occur in Iceland away from the WVZ. Such shallow sources of the oceanic residual anomaly over hotspot affected ridges is in accordance with the 'hot flowing crust' hypothesis of Bell and Buck (1991).

5.2 The Fidelity of Seismic Tomography

Three comparisons between gravity data and seismic tomography results have been considered in this thesis by utilising a linear velocity-density relationship. In all cases, there were shown to be inconsistencies between the two. For example, at Krafla the presence of a significant high density body below one of the caldera ring faults was inferred from the gravity field, but local earthquake seismic tomographic analysis failed

to image such a body. At the Hengill-Grensdalur area, an extensive, shallow low density zone was similarly overlooked by local earthquake tomography, but located from the gravity field. On an Iceland-wide scale, the seismic image of the hypothesised mantle plume did not produce a forward modelled gravity field consistent with the observed gravity field. Possible reasons for these inconsistencies are:

(i) the presence of partial melt, within the region studied, which drastically affects velocity-density relationships.
(ii) the presence of differing velocity-density relationships within the same region.
(iii) an incorrect Bouguer reduction leading to unreal anomalies.
(iv) (most importantly) the presence of artefacts introduced by the tomographic method.

Although solutions to gravity data are non-unique it is still possible to use gravity data to delineate the horizontal extent of any locally occurring density perturbation encompassed by the gravity stations, and to this end it has been used in oil prospecting. Unfortunately, gravity data alone cannot yield definite depth estimates for such bodies. In contrast, seismic tomography, in theory at least, has the ability to spatially locate velocity perturbations in three dimensions. However, unlike more conventional laboratory tomography, such as medical imaging, seismic tomography suffers from the lack of a well controlled experimental setup. This gives rise to a number of problems. The inverse problem of three dimensional local earthquake tomography using a method involving determination of velocity perturbations in discrete cells usually results in a matrix system that is ill-conditioned. This is because of the imperfect source and receiver coverage which means that small data errors may contribute to a large effect in the solution.

Relative seismic P-wave delay times are most commonly used for seismic tomography and if compared to say, medical X-ray tomography, the P-wave time delays are obtained with relatively low precision. For example, geodynamical processes give rise to velocity perturbations which tomography attempts to detect, but the data often have standard errors of the same order of magnitude as the time shifts caused by the velocity perturbation. Furthermore the seismic rays describe curved paths rather than the straight lines of X-rays in medical tomography, thus introducing another unknown. Compounding these problems is the complication that arises through faster rays concealing the arrival of slower rays at a station which leads to a distorted dataset biased towards 'fast' bodies.

The plume almost certainly contains partial melt and extends to a depth of several hundred kilometres, encountering many different solid phases. It seems that the

inconsistencies between the tomographic gravity forward model and the observed gravity field are likely to be due mainly to (iv) and possibly (i) and (ii), for such large scale investigations. With local earthquake seismic tomography (i) is less applicable in the two regions studied. Reason (ii) may be true for hydrothermally altered rock explaining the un-predicted low density zone at Hengill-Grensdalur. Assessment of errors suggest that (iii) is an unlikely cause, but could still provide a partial explanation. In chapter 2 it was suggested that the travel time uncertainty as well as ray geometry and wavelength were important to the fidelity of the final velocity structure. Table 2.3 demonstrated that significant geological features having a thickness of the order of 1 km could be overlooked by local earthquake seismic tomography for the Hengill-Grensdalur and Krafla surveys.

It seems that although a discrepancy between the gravity data and the forward modelled tomography may be due to a body unseen by the seismic rays it could also quite easily be due to the problems inherent in seismic tomography of solving ill-conditioned matrices caused by an incomplete source-receiver coverage which may generate artefacts.

References

Ahern, J. L. and Turcotte, D. L., Magma migration beneath an ocean ridge, Earth Planet. Sci. Lett., 45, 115-122, 1979.

Aki, K., 3-D seismic inhomogeneities in lithosphere and asthenosphere: evidence for decoupling in the lithosphere and flow in the asthenosphere, Rev. Geophys. Space Phys., 20, 161-170, 1981.

Angenheister, G., Gebrande, H., Miller, H., Goldflam, P.,Weigel, W., Jacoby, W., Pálmason, G., Björnsson, S., Einarsson, P., Pavlenkova, .N.I., Zverev, S.M., Litvenenko, I.V., Loncarevic, B., Solomon, S. and Richard, S., Reykjanes Ridge seismic experiment (RRISP 77), J. Geophys., 47, 228-238, 1980.

Armannsson, H., Gudmundsson, A. and Steingrimsson, B.S., Exploration and development of the Krafla geothermal area, Jökull, 37, l3 29, 1987.

Árnason, K., Haraldsson, G. I., Johnsen, G. V., Thorbergsson, G., Hersir, G. P., Sæmundsson, K., Georgsson, L. S., Rognvaldsson, S. T., and Snorrason, S. P., Nesjavellir-Olkelduhals. Yfirbordsrannsoknir 1986. (Nesjavellir-Olkelduhals. Surface research 1986), Nat. Energy Auth., Reykjavik, Iceland, Rep. OS-87018/JHD-02, 112 pp., 1987.

Arnott, S. K., A seismic study of the Krafla volcanic system, Iceland, Ph.D. thesis, Univ. Durham, 260 pp., 1990.

Barton, P. J., The relationship between seismic velocity and density in the continental-crust - a useful constraint?, Geophys. J. R. Astron. Soc., 87, 195-208, 1986.

Båth, M., Crustal structure of Iceland, J. Geophys. Res., 65, 1793-1807, 1960.

Beblo, M. and Björnsson, A., A model of electrical resistivity beneath NE Iceland, correlation with temperature, J. Geophys., 47, 184-190, 1980.

Beblo, M., Björnsson, A., Arnason, K., Stein, B. and Wolfgram, P., Electrical conductivity beneath Iceland-constraints imposed by magnetotelluric results on temperature, partial melt, crust- and mantle structure, J. Geophys., 53, 16-23, 1983.

Becker, K., Sakai, H., Adamson, A. C., Alexandrovich, J., Alt, J. C., Anderson, R. N., Bideau, D., Gable, R., Herzig, P. M., Houghton, S., Ishizuka, H., Kawahata, H., Kinoshita, H., Langseth, M.G., Lovell, M. A., Malpas, J. Masuda, H., Merrill, R. B., Morin, R. H., Mottl, M. J., Pariso, J. E., Pezard, P., Phillips, J., Sparks, J. and Uhlig, S., Drilling deep into young oceanic-crust, hole-504b, Costa-Rica Rift, Rev. Geophys., 27, 79-102, 1989.

Bell, R. E. and Watts, A. B., Evaluation of the BGM-3 sea gravity meter system onboard the R/V Conrad, Geophysics, 51, 1480-1493, 1986.

Bell, R. E. and Buck, W. R., Crustal control of ridge segmentation inferred from observations of the Reykjanes Ridge, Nature, 357, 583-586, 1992.

Bhattacharyya, B. K. and Chan, K. C., Reduction of magnetic and gravity data on an arbitrary surface acquired in a region of high topographic relief, Geophysics, 42, 1411-1430, 1977.

Birch, F., The velocity of compressional waves in rocks to 10 kilobars, 2, J. Geophys.Res., 66, 2199-2224, 1961.

Bjarnason, I., Menke, W., Flóvenz, O. and Caress, D., Tomographic image of the Mid-Atlantic plate boundary in Southwestern Iceland, J. Geophys. Res., 98, 6607-6622, 1993.

Björnsson, A., Dynamics of crustal rifting in N.E. Iceland, J. Geophys. Res., 90, 10151-10162, 1985.

Björnsson, A., Sæmundsson, K., Einarsson, P., Tryggvason, E. and Gronvold, K., Current Rifting episode in North Iceland, Nature, 266, 318-323, 1977.

Björnsson, A., Johnsen, G., Sigurdsson, S., Thorbergsson, G. and Tryggvason, E., Rifting of the plate boundary in North Iceland 1975-1978, J. Geophys. Res., 84, 3029-3038, 1979.

Björnsson, S., Iceland and mid-ocean ridges, Soc. Sci. Islandica, 38, 1967.

Blackman, D. K. and Forsyth, D.W., Isostatic compensation of tectonic features of the Mid-Atlantic Ridge: 25-27 30'S, J. Geophys. Res., 96, 11741-11758, 1991.

Bott, M. H. P., The upper mantle beneath Iceland, Geophys. J. R. Astron. Soc., 9, 275-277, 1965.

Bott, M. H. P., The evolution of the Atlantic north of the Faeroe Islands, in: Implications of Continental Drift to the Earth Sciences, edited by Tarling, D. H. and Runcorn, S. K., Academic Press, London, 1, 175-189, 1973.

Bott, M. H. P., A new look at the causes and consequences of the Icelandic hot-spot, in: Early Tertiary Volcanism and the Opening of the NE Atlantic, edited by Morton, A. C. and Parson, L. M., 15-23, Geological Society Special Publication No 39, 1988.

Bott, M. H. P. and Smith, R. A., The Estimation of the Limiting Depth of Gravitating Bodies, Geophys. Prosp., 6, 1-10, 1958.

Bott, M. H. P. and Gunnarsson, K., Crustal structure of the Iceland-Faeroe Ridge, J. Geophys., 47, 221-227, 1980.

Bullen, K. E., The Earth's density, Chapman and Hall, London, 420 pp., 1975.

Bullen, K. E. and Bolt, B. A., An introduction to the theory of seismology, 4th edition, Camb. Univ. Press., 1985.

Bunch, A. W. H. and Kennet, B. L. N., The crustal structure of the Reykjanes Ridge at 59°30'N, Geophys. J. R. Astron. Soc., 61, 141-166, 1980.

Campbell, I. H. and Griffiths, R. W., Implications of mantle plume structure for the origin of flood basalts, Earth Planet. Sci. Lett., 99, 79-93, 1990.

Chen, Y. S. and Morgan, W. J., Rift-valley no rift-valley transition at mid-ocean ridges, J. Geophys. Res., 95, 17571-17581, 1990a.

Chen, Y. S. and Morgan, W. J., A nonlinear rheology model for mid-ocean ridge axis topography, J. Geophys. Res., 95, 17583-17604, 1990b.

Christensen, N.I. and Salisbury M.H., Structure and constitution of the lower oceanic crust, Rev. Geophys. Space Phys., 13, 57-86, 1975.

Christensen, N.I. and Wilkins R.H., Seismic Properties Density and Composition of the Icelandic Crust near Reydarfjordur, J. Geophys. Res, 87 , 6389-6395, 1982.

Cooley, J. W. and Tukey, J. W., An algorithm for the machine calculation of complex Fourier series, Math. of Comp., 19, 297-301, 1965.

Dampney, C. N. G., The equivalent source technique, Geophysics, 34, 39-53, 1969.

DeMets, C., Gordon, R. G., Argus, D. F. and Stein, S., Current plate motions, Geophys. J. Int., 101, 425-478, 1990.

Eaton, G. P., Christiansen, R. L., Iyer, H. M., Pitt, A. M., Mabey, D. R., Blank Jr, H. R., Ziety, I. and Gettings, M. E., Magma beneath Yellowstone National Park, Science, 188, 787-796, 1975.

Einarsson, P., S-wave shadows in the Krafla caldera in NE-Iceland, evidence for a magma chamber in the crust, Bull. Volcanol., 41-3, 1-9, 1978.

Einarsson, P., Earthquakes and present-day tectonism in Iceland, Tectonophysics, 189, 261-279, 1991.

Einarsson, P. and Björnsson, S., Earthquakes in Iceland, Jökull, 29, 37-43, 1979.

Einarsson, P. and Brandsdottir, B., Seismological evidence for lateral magma intrusion during the July 1978 deflation of the Krafla volcano in NE Iceland. J. Geophys., 47, 160-165, 1980.

Einarsson, T., A survey of gravity in Iceland. Soc. Sci. Islandica, Rit 30, 1954.

Ellsworth, W.L. and Koyanagi R.Y., Three-dimensional crust and mantle structure of Kilauea volcano, Hawaii, J. Geophys. Res., 82, 5379-5394, 1977.

Ervin, P., Theory of the Bouguer anomaly, Geophysics, 47, 1468, 1977.

Evans, J. R. and Sacks, I. S., Lithospheric structure in the North Atlantic from observations of Love and Raleigh waves, J. Geophys. Res., 84, 6859-6866, 1979.

Evoy, J.A., Precision gravity reobservations and simultaneous inversion of gravity and seismic data for subsurface structure of Yellowstone, MS thesis, Univ. Utah, pp. 212, 1978.

Eysteinsson, H. and Hermance, J., Magnetotelluric measurements across the eastern neovolcanic zone in south Iceland, J. Geophys. Res., 90, 10093-10103, 1985.

Ewart, J. A., Voight, B. and Björnsson, A., Elastic deformation models of the Krafla volcano, Iceland, for the decade 1975 through 1985, Bull. Volc., 53, 436-459, 1991.

Flóvenz, O. G., Seismic structure of the Icelandic crust above layer three and the relation between body wave velocity and the alteration of the basaltic crust, J. Geophys., 47, 211-220, 1980.

Flóvenz, O. G., Georgsson, L. and Árnason, K., Resistivity structure of the upper crust in Iceland, J. Geophys. Res., 90, 10136-10150, 1985.

Flóvenz, O. G. and Gunnarsson, K., Seismic crustal structure in Iceland and the surrounding area, Tectonophysics, 189, 1-17, 1991.

Flóvenz, O. G. and Sæmundsson, K., Heat flow and geothermal processes in Iceland, Tectonophysics, 225, 123-138, 1993.

Foulger, G. R., The Hengill triple junction, SW Iceland: 1. Tectonic structure and the spatial and temporal distribution of local earthquakes, J. Geophys. Res., 93, 13493-13506, 1988a.

Foulger, G. R., The Hengill triple junction, SW Iceland: 2. Anomalous earthquake focal mechanisms and implications for process within the geothermal reservoir and at accretionary plate boundaries, J. Geophys. Res., 93, 507-523, 1988b.

Foulger, G.R. and Long R.E., Anomalous focal mechanisms : tensile crack formation on an accreting plate boundary, Nature, 310, 43-45, 1984.

Foulger, G.R. and Toomey, D.R., Structure and evolution of the Hengill-Grensdalur central volcano complex, Iceland: Geology, geophysics and seismic tomography, J. Geophys. Res., 94, 17,511-17,522, 1989.

Foulger, G. R., Jahn, C. -H., Seeber, G., Einarsson, P., Julian, B. R. and Heki, K., Post-rifting stress relaxation at the divergent plate boundary in Northeast Iceland, Nature, 358, 488-490, 1992.

Foulger, G. R. and Arnott, S. K., Local tomography: volcanoes and the accretionary plate boundary in Iceland, in: Seismic Tomography, Theory and Practice, edited by Iyer, H. and Hirahara, K., Chapman and Hall, London, 644-672, 1993.

Fowler, C. M. R., Crustal structure of the Mid-Atlantic Ridge crest at 37 N, Geophys. J. R. Astron. Soc., 47, 459-491, 1976.

Franzson, H., Nesjavellir. Borholujardfrædi. Vatnsgengd i jardhitageymi (Nesjavellir. Borehole geology. Permeability in the geothermal reservoir), Nat. Energy Auth., Reykjavik, Iceland, Rep. OS-88046/JHD-09, 1988.

Gebrande, H., Miller, H. and Einarsson, P., Seismic structure of Iceland along RRISP profile 1, J. Geophys., 47, 239-249, 1980.

Granser, H., Deconvolution of gravity-data due to lateral density distributions, Geoexploration, 23, 537-547, 1985.

Granser, H., Meurers, B. and Steinhauser, P., Apparent density mapping and 3D gravity inversion in the Eastern Alps, Geophys. Pros., 37, 279-292, 1989.

Grant, J. A. and Schreiber, R., Modern swath sounding and sub-bottom profiling technology for research applications: The Atlas Hydrosweep and parasound systems, Mar. Geophys. Res., 12, 9-19, 1990.

Hammer, S., Terrain corrections for gravimeter stations, Geophysics, 4, 184-194, 1939.

Hansen, R. O. and Miyazaki, Y., Continuation of potential fields between arbitrary surfaces, Geophysics, 49, 787-795, 1984.

Haxby, W. F., Karner, G. D., LaBreque, J. L. and Weissel, J. K., Digital images of combined oceanic and continental datasets and their use in tectonic studies, EOS Trans. AGU, 64, 995-1004, 1983.

Helgason, J., Frequent shifts of the volcanic zone in Iceland, Geology, 12, 212-216, 1984.

Helgason, J., Shifts of the plate boundary in Iceland: some aspects of tertiary volcanism, J. Geophys. Res., 90, 10084-10092, 1985.

Henderson, R. G. and Cordell, L., Reduction of unevenly spaced potential field data to a horizontal plane by means of finite harmonic series, Geophysics, 36, 856-866, 1971.

Hermance, J., Gravity compensation in the mantle beneath the neovolcanic zone of Iceland, Earth Planet. Sci. Lett., 54, 157-166, 1981a.

Hermance, J., Crustal genesis in Iceland: geophysical constraints on crustal thickening with age, Geophys. Res. Lett., 8, 203-206, 1981b.

Hersir, G.P., Electric and electromagnetic measurements across the mid-Atlantic ridge in southeast Iceland, with special reference to the high temperature area of Hengill, Specialearbejde, Laboratoriet for Geofysik, Aarhus Universitet, 165 pp. 1980.

Hersir, G.P., Björnsson A. and Pedersen L.B., Magnetotelluric survey across the active spreading zone in southwest Iceland, J. Volcanol. Geotherm. Res., 20, 253-265, 1984.

Hersir. G., Björnsson G. and Björnsson A., Eldstodvar og jardhiti a Hengilssvædi. Jardedlisfraedileg konnun, (Volcanoes and geothermal activity in the Hengill area. Geophysical exploration.), Nat. Energy Auth., Reykjavik, Iceland, Rep. OS-90031/JHD-06, 1990.

Hill, R. I., Mantle plumes and continental tectonics, Lithos, 30, 193-206, 1993.

Holmes, M. L. and Johnson, H. P., Upper crustal densities derived from seafloor gravity measurements - northern Juan de Fuca Ridge, Geophys. Res. Lett., 20, 1871-1874, 1993.

Houtz, R. and Ewing, J., Upper crustal structure as a function of plate age, J. Geophys. Res., 81, 2490-2498, 1976.

Hu, G., Menke, W. and Rognvaldsson, S., A demonstration of the joint use of P-wave polarization and travel-time data in tomographic inversion - crustal velocity

structure near the south Iceland lowland network, Geophys. Res. Lett., 20, 1407-1410, 1993.

Isherwood, W. F., Gravity and magnetic studies of the Geysers-Clear Lake geothermal region, California, U.S.A., in: Proceedings of the Second U.N. Symposium on the Development and Use of Geothermal Resources, vol. 2, Washington, D.C. (U.S. Govt. Printing Office), 1065-1073, 1976.

Ivan, M., On the upward continuation of potential-field data between irregular surfaces, Geophys. Prosp., 34, 735-742, 1986.

Jonsson, G., Kristjansson, L. and Sverrisson, M., Magnetic surveys of Iceland, Tectonophysics, 189, 229-247, 1991.

Karlsdóttir, R., Johnsen, G., Björnsson, A., Sigurdsson, O. and Hauksson, E., The geothermal area of Krafla: general report on geophysical research 1976-1978 (in Icelandic), Nat. Energy Auth., Reykjavik, report OS/JDH-7847, 1978.

Karson, J. A., Seafloor spreading on the Mid-Atlantic Ridge: Implications for the structure of ophiolites and the oceanic lithosphere produced in slow spreading environments, in: Ophiolites: oceanic crustal analogues, edited by Malpas, J., Moores, E., Panaycotou, A. and Xenophontos, C., Cyprus Geological Survey, 547-555, 1990.

Kuo, B.-Y., and Forsyth, D. W., Gravity anomalies of the ridge-transform system in the South Atlantic between 31° and 34.5° S: Upwelling centers and variations in crustal thickness, Mar. Geophys. Res., 10, 205-232, 1988.

Lahmeyer, B., Gravity-field continuation of irregularly spaced data using least-squares collocation, Geophys. J., 95, 123-134, 1988.

Lin, J., Purdy, G.M., Schouten, H., Sempere, J.C. and Zervas, C., Evidence from gravity data for focussed magmatic accretion along the Mid-Atlantic Ridge. Nature, 344, 627-632, 1990.

Locke, C. A., Geophysical investigations of gold-bearing hydrothermally altered rocks in New Zealand, Geophys. J., 92, 540, 1988.

Long, R.E. and Mitchell, M.G., Teleseismic P-wave delay times in Iceland. Geophys. J. R. Astron. Soc., 20, 41-48, 1970.

Longman, I.M., Formulas for computing the tidal acceleration due to the moon and the sun, J. Geophys. Res., 64, 2351-2355, 1959.

Ludwig, J. L., Nafe, J. E. and Drake, C. L., Seismic Refraction, in: The Sea, vol. 4, part 1, New Concepts of Sea Floor Evolution, edited by Maxwell, A. E., John Riley and Sons, New York, 53-84, 1970.

Luyendyke, B., Cann, J. et al., Init. Repts. DSDP, 49, Washington (U.S. Govt. Printing Office), 161-226, 1978.

McConnel Jr, R. K., Isostatic adjustment in a layered Earth, J. Geophys. Res., 70, 5171-5188, 1965.

McKenzie D, P., Some Remarks on Heat Flow and Gravity Anomalies, J. Geophys. Res., 72, 6261-6273, 1967.

Macdonald, K.C., Mid-ocean ridges - fine scale tectonic, volcanic and hydrothermal processes within the plate boundary zone, Ann. Rev. Earth Planet. Sci., 10, 155-190, 1982.

Macdonald, K.C., Fox, P.J., Perram, L.J., Eisen, M.F., Haymon, R.M., Miller, S.P., Carbotte, S.M., Cornier, M.H. and Shor, A.N., A new view of the mid-ocean ridge from the behaviour of ridge-axis discontinuities, Nature, 335, 217-225, 1988.

Mavko, G. M., Velocity and attenuation in partially molten rocks, J. Geophys. Res., 85, 5173-5189, 1980.

Möller, D. and Ritter, B., Geodetic measurements and horizontal crustal movements in the rift zone of NE-Iceland, J. Geophys., 47, 110-119, 1980.

Moores, E. M. and Vine, F. J., The Troodos Massif, Cyprus and other ophiolites as oceanic crust: evaluation and implications, Phil. Trans. R. Soc., A268, 443-466, 1971.

Morgan, J., and Forsyth, D. W., 3-D Flow and temperature perturbations due to a transform offset: Effects on oceanic crustal and upper mantle structure, J. Geophys. Res., 93, 2955-2966, 1988.

Morgan, J. P. and Smith, W. H. F., Flattening of the seafloor depth-age curve as a response to asthenospheric flow, Nature, 359, 524-527, 1992.

Morris, E., and Detrick, R. S., Three dimensional analysis of the gravity anomalies in the MARK area, Mid-Atlantic Ridge 23° N, J. Geophys. Res., 96, 4355-4366, 1991.

Murase, T. and McBirney A.R., Properties of some common igneous rocks and their melts at high temperatures, Geol. Soc. Am. Bull., 84, 3562-3592, 1973.

Nettleton, L. L., Determination of density for reduction of gravity observations, Geophysics, 4, 176-183, 1939.

Oldenburg, D. W., The inversion and interpretation of gravity anomalies, Geophysics, 39, 526-536, 1974.

Oppenheimer, D.H. and Herkenhoff K.E., Velocity-density properties of the lithosphere from three-dimensional modeling at The Geysers-Clear Lake region, California, J. Geophys. Res., 86, 6057-6065, 1981.

Oskarsson, N., Sigvaldason, G. and Steinthorsson, S., A dynamic model of rift zone petrogenesis and the regional petrology of Iceland, J. Petrol., 23, 28-74, 1982.

Owens, R., An inversion of magnetic anomalies from the Reykjanes Ridge 58°N 32°20'W, M.Sc. thesis, Univ. Durham, 54 pp., 1991.

Pálmason, G., Crustal structure of Iceland from explosion seismology, Soc. Sci. Islandica, 40, 187 pp., 1971.

Pálmason, G., Kinematics and heat flow in a volcanic rift zone, with applications to Iceland, Geophys. J. R. Astron. Soc., 33, 451-471, 1973.

Pálmason, G., A continuum model of crustal generation in Iceland: Kinematic aspects, J. Geophys., 47, 7-18, 1980.

Pálmason, G., Crustal rifting and the related thermomechanical processes in the lithosphere beneath Iceland, Geol. Rundsch., 70, 244-260, 1981.

Pálmason, G., Nilsen, T. H. and Thorbergsson, G., Gravity base station network in Iceland 1968-1970, Jöjull, 23, 70-125, 1973.

Pálmason, G. and Sæmundsson, K., Iceland in relation to the Mid-Atlantic Ridge, Ann. Rev. Earth Planet. Sci., 2, 25-50, 1974.

Pálmason, G., Arnórsson, S., Fridleifsson, I., Kristmannsdóttir, H., Sæmundsson, K., Stefánsson, V., Steingrimsson, B., Tómasson, J. and Kristjánsson, L., The Iceland crust: Evidence from drillhole data on structure and processes, in: Deep Drilling Results in the Atlantic Ocean: Ocean crust, Maurice Ewing Ser., vol. 2, edited by Talwani, M., 43-65, AGU, Washington, D. C., 1979.

Parasnis, D.S., Principles of Applied Geophysics, London, Methuen, 402 pp., 1962.

Parker, R. L., The rapid calculation of potential anomalies, Geophys. J. R. Aston. Soc., 31, 447-455, 1972.

Parmentier, E. M., Turcotte, D. L. and Torrance, K. E., Numerical experiments on the structure of mantle plumes, J. Geophy. Res., 80, 4417-4424, 1975.

Parson, L. M., Murton, B. J., Searle, R. C., Booth, D., Evans, J., Field, P., Keeton, J., Laughton, A., McAllister, E., Millard, N., Redbourne, L., Rouse, I., Shor, A., Smith, D., Spencer, S., Summerhayes, C., Walker, C., En-echelon axial volcanic ridges at the Reykjanes Ridge - a life-cycle of volcanism and tectonics, Earth Planet. Sci. Lett., 117, 73-87, 1993.

Pearson, W. C. and Lister, C. R. B., The gravity signatures of isostatic, thermally-expanded ridge crests, Phys. Earth Planet. Int., 19, 73-84, 1979.

Press, W. H., Teukolsky, S. A., Vetterling, W. T. and Flannery, B. P., Numerical recipes in FORTRAN, 2nd ed., Camb. Univ. Press, 963 pp., 1992.

Prince, R. A., and Forsyth, D. W., Horizontal extent of anomalously thin crust near the Vema Fracture Zone from the three dimensional analysis of gravity anomalies, J. Geophys. Res., 93, 8051-8063, 1988.

Raitt, R. W., The crustal rocks, in: The sea, vol. 3, edited by Hill, M. N., Interscience, New York, 85-102, 1963.

RUSKA reservoir engineering instrumentation, Universal Porometer data sheet, 403.1-1, RUSKA Instrument Corp., PO Box 36010, Houston, Texas 77036.

Ryan, M. P., The physical nature of the Icelandic magma transport system, in: Magma Transport and Storage, edited by Ryan, M. P, John Wiley and Sons, New York, 175-224, 1990.

Sæmundsson, K., Vulkanismus und Tektonik des Hengill-Gebietes in Sudwest-Island. (Volcanology and tectonics of the Hengill area in SW Iceland), Acta Natur. Island., 2(7), 109 pp., 1967.

Sæmundsson, K., Evolution of the axial rifting zone in Northern Iceland and the Tjörnes fracture zone, Geol. Soc. Am. Bull., 85, 495-504, 1974.

Sæmundsson, K. Fissure swarms and central volcanoes of the neovolcanic zones of Iceland, Geol. J. Spec. Issue, 10, 415-432, 1978.

Sæmundsson, K., An outline of the geology of Iceland, Jökull, 29, 7-28, 1979.

Sæmundsson, K., Subaerial volcanism in the western North Atlantic, in: The Geology of North America, vol. V, the Western North Atlantic Region, edited by Vogt, P. R., and Tucholke, B. E., 69-86, Geological Society of America, Boulder, Col., 1986.

Sato, Y., Velocity of elastic waves propagated in media with small holes, Bull. Earthquake Res. Inst. Tokyo Univ., 30, 178-190, 1952.

Savino, J.M., Rodi W.L., Goff R.C., Jordan T.H., Alexander J.H. and Lambert D.G., Inversion of combined geophysical data for determination of structure beneath the Imperial Valley geothermal region, Systems, Science and Software Final Technical Report SSS-R-78-3412 to the Dept. Energy, USA, 1977.

Savino, J.M., Rodi W.L., Jordan T.H., Goff R.C. and Lambert D.G., Joint inversion of geophysical data as a geothermal exploration tool: Applications to Yellowstone Park and the Imperial Valley, Geotherm. Res. Council, Trans. 3, 625-628, 1979.

Schilling, J.G., Iceland mantle plume, geochemical evidence along Reykjanes Ridge. Nature, 242, 565-578, 1973.

Schleusener, A., Torge, W. and Drewes, H., The gravity field of Northeastern Iceland, J. Geophys., 42, 27-45, 1976.

Schoenharting, G. and Pálmason, G., A gravity survey in the Reydarfjordur area, eastern Iceland, with interpretation, J. Geophys. Res., 87, 6419-6422, 1982.

Schouten, H., Klitgord, K. D. and Whitehead, J. A., Segmentation of mid-ocean ridges, Nature, 317, 225-229, 1985.

Searle, R. C. and Laughton, A. S., Fine-scale sonar study of tectonics and volcanism on the Reykjanes Ridge, Oceanol. Acta, Proc. 26th Int. Geo. Con., 5-13, 1981.

Searle, R. C., Field, P. R. and Owens, R. B., Segmentation and a non-transform ridge offset on the Reykjanes Ridge near 58°N, J. Geophys. Res., submitted.

Shaw, P., Ridge segmentation, faulting and crustal thickness in the Atlantic Ocean, Nature, 358, 490-493, 1992.

Sigmundsson, F., Postglacial rebound and asthenosphere viscosity in Iceland, Geophys. Res. Lett., 18, 1131-1134, 1991.

Sigmundsson, F. and Einarsson, P., Glacio-isostatic crustal movements caused by historical volume change of the Vatnajökull icecap, Iceland, Geophys. Res. Lett., 19, 2123-2126, 1992.

Sigurdsson, O., Surface deformation of the Krafla fissure swarm in two rifting events. J. Geophys., 47, 154-159, 1980.

Sleep, N. H., Hotspots and mantle plumes - some phenomenology, J. Geophys. Res., 95, 6715-6736, 1990.

Small, C. and Sandwell, D. T., An abrupt change in ridge axis gravity with spreading rate, J. Geophys. Res., 94, 17383-17392, 1989.

Small, C. and Sandwell, D. T., Imaging mid-ocean ridge transitions with satellite gravity, Geology, 22, 123-126, 1994.

Smith, W. H. F. and Wessel, P., Gridding with continuous curvature splines in tension, Geophysics, 55, 293-305, 1990.

Sparks, D. W., Parmentier, E. M., and Morgan, J., Three dimensional convection beneath a segmented spreading centre: Implications for the along axis variations in crustal thickness and gravity, J. Geophys. Res., 98, 21977-21995, 1993.

Spudich, P. and Orcutt, J., Petrology and porosity of an oceanic crustal site: Results from waveform modelling of seismic refraction data, J. Geophys. Res., 85, 1409-1433, 1980.

Stefansson, V., The Krafla Geothermal Field, Northeast Iceland. in: Geothermal Systems : Prtnciples and Case Hitstorites. ed. L. Rybach and L.J.P. Muffler. John Wiley and Sons Ltd, 273-294, 1981.

Stefansson, V., Tomasson J., Gunnlaugsson E., Sigvaldason H., Franzson H. and Sigurdsson O., Nesjavellir, Hola NG-6. Borun, rannsoknir og vinnslueiginleikar (Nesjavellir, Drilling, research and production characteristics), Nat. Energy Auth., Reykjavik, Iceland, Rep. OS-83023/JHD-04, 1983.

Steingrimsson, B., Gudmundsson A., Sigvaldason H., Sigurdsson O., and Kjartansson E., Nesjavellir, hola NG-11, borun, ranns knir, og vinnslueiginleikar (Nesjavellir, well NG-11, drilling, research and production characteristics), Nat. Energy Auth., Reykjavik, Iceland, Rep. OS-886025/JHD-05, 1986.

Steinthorsson, S., Oskarsson, N. and Sigvaldason, G., Origin of alkali basalts in Iceland: A plate tectonic model, J. Geophys. Res., 90, 10027-10042, 1985.

Strange, T. M., The determination and geophysical applications of free air gravity anomalies using satellite altimetry and ship gravity. Ph.D. thesis, Univ. Oxford, 323 pp., 1991.

Taib, S. Hj., Interpretation of the aeromagnetic anomalies of mainland Scotland using pseudogravimetric transformation and other methods, Ph.D. thesis, Univ. Durham, 1990.

Talwani, M., Computer Usage in the Computation of Gravity Anomalies, Methods in Computational Physics, 13, 343-389, 1973.

Talwani, M., Windisch, C. and Langseth, M., Reykjanes Ridge crest: A detailed geophysical study, J Geophys. Res., 76, 473-517, 1971.

Tapponier, P. and Francheteau, J., Necking of the lithosphere and the mechanics of slowly accreting plate boundaries, J. Geophys. Res., 83, 3955-3970, 1978.

Thorarinsson, F., Magnusson, S., Einarsson, P., Kristjansson, L. Pálmason, P. and Björnsson, A., Gravity, aero-magnetism and earthquakes in SW-Iceland, Jökull, 39, 41-55, 1989.

Thorbergsson, G., Magnusson I.T., Gunnarsson A., Johnsen G.V. and Björnsson A., Landmælingar og thyngdarmælingar a Hengilssvædi 1982 og 1983 (Surveying and gravity measurements in the Hengill area 1982 and 1983), Nat. Energy Auth., Reykjavik, report OS-84003/VOD-03 B, 1984.

Thorbergsson, G., Magnusson I.T. and Pálmason G., Thyngdamæligögn og thyngdakort af Islandi (Gravity data and gravity map of Iceland), Nat. Energy Auth., Reykjavik, report OS-90001/JHD-01, 1990.

Thurber, C. H., Earthquake locations and three-dimensional crustal structure in the Coyote Lake area, central California, J. Geophys. Res., 88, 8226-8236, 1983.

Toomey, D.R. and Foulger, G.R., Application of tomographic inversion to local earthquake data from the Hengill-Grensdalur central volcano complex, Iceland. J. Geophys. Res., 94, 17,497-17,510, 1989.

Toomey, D.R., Purdy, G.M., Solomon, S.C. and Wilcock, S.D., The three-dimensional seismic velocity structure of the East Pacific Rise near latitude 9° 30'N. Naturc, 347, 639-645, 1990.

Torfason, H., Hersir G.P., Sæmundsson K., Johnsen G.V., and Gunnlaugsson E., Vestur-Hengill. Yfirbordsrannsokn jardhitasvædisins. (West Hengill. Surface research of the geothermal area), Nat. Energy Auth., Reykjavik, Iceland, Rep. OS-83119/JHD-22, 113 pp., 1983.

Torge, W., Geodesy, Walter de Gruyter, Berlin, 254 pp., 1980.

Torge, W., Gravimetry, Walter de Gruyter, New York, 465 pp., 1989.

Tryggvason, E., Arrival times of P-waves and upper mantle structure, Bull. Seismol. Soc. Am., 54, 727-736, 1964.

Tryggvason, E., Tilt observations in the Krafla-Myvatn area 1976-1977. Nordic Volcanological Institute Report 7802, 1978.

Tryggvason, E., Widening of the Krafla fissure swarm during the 1975-1981 volcanotectonic episode. Bull. Volcanol., 47, 47-69, 1984.

Tryggvason, K., Husebye, E.S. and Stefansson, R., Seismic image of the hypothesised Icelandic hotspot. Tectonophysics, 100, 97-119. 1983.

Turcotte, D. L. and Schubert, G., Geodynamics: Applications of continuum physics to geological problems, John Wiley, New York, 450 pp., 1982.

Vink, G.E., A hotspot model for Iceland and the Vøring plateau. J. Geophys. Res., 89, 9949-9959, 1984.

Vogt, P. R., Evidence for global synchronism in mantle plume convection and possible significance for geology, Nature, 240, 338-342, 1972.

Vogt, P. R., The Iceland phenomenon: imprints of hot spots on the ocean crust, and implications for flow below the plates, Geodynamics of Iceland and the North Atlantic Area, ed. L. Kristjansson, Reidel publishing co., 105-126, 1974.

Walker, C.L., The volcanic history and geochemical evolution of the Hveragerdi region, SW Iceland, Ph.D. thesis, Univ. Durham, 365 pp., 1992.

Ward, P.L. and Björnsson, S., Microearthquakes, swarms and the geothermal areas of Iceland. J. Geophys. Res., 76, 3953-3982, 1971.

Wendt, K., Möller, D. and Ritter, B., Geodetic measurements of surface deformation during the recent rifting episode in NE Iceland, J. Geophys. Res., 90, 163-172, 1985.

Wessel, P. and Watts, A. B., On the accuracy of marine gravity measurements, J. Geophys. Res., 93, 393-413, 1988.

Wessel, P. and Smith, W. H. F., Free software helps map and display data, EOS Trans. AGU, 72, 441, 445-446, 1991.

White, R. S., Atlantic ocean crust: Seismic structure of a slow spreading ridge, in: Ophiolites and oceanic lithosphere, edited by Gass, I. G. et al., Geol. Soc. Lond., 34-44, 1984.

Whitehead, J. A., Dick, H. J. B. and Schouten, H., A mechanism for magmatic accretion under spreading centers, Nature, 312, 146-148, 1984.

Zverev, S.M., Litvinenko, I.V., Pálmason, G., Yarashevskaya, G.A., Osokin, N.N. and Akhmetjev, M.A., A seismic study of the rift zone in northern Iceland, J. Geophys., 47,191-201, 1980.

Appendix

The programs contained in this appendix were written by the author and were used in this thesis. There are three FORTRAN programs: GRAV3D, EQSM, and INVRHO. The program EQSM calls two subroutines: ludcmp.f and lubksb.f which can both be found in 'Numerical Recipes in FORTRAN, 2nd edition' (Press et al., 1992). The program INVRHO calls a fast fourier transform subroutine called fourt.f. A copy of this subroutine is provided with the GMTsystem (Wessel and Smith, 1991).

GRAV3D

```
      program GRAV3D

c   Enter all data in SI units ie m, kg/m3
c
c   The program calculates the gravitational effect due to an assembly
c   of parallelepipeds(boxes) of like dimensions (but different densities)
c   using the equation of M. Talwani: Computer Usage in the Computation
c   of Gravity Anomalies; Methods in Computational Physics,  p357 eq25.
c
c-----------------------------------------------------------------
c   Input data:  (file=grav.in)
c       dx dy dz sw
c       x(i) y(i) z(i) rho(i)          repeat for i=1,number of bodies
c
c       dx is the xsize of the box
c       dy        ysize
c       dz        zsize
c       sw:  0=all stations at sea level;  1=stations have z coord
c
c
c    Station data:  (file=station)
c       xx(j) yy(j)                    if sw=0
c       xx(j) yy(j) ht(j)              if sw=1
c  put   -1    -1    -1                to terminate
c
c    Output data:   (file=grav.out)
c       xx(j) yy(j) ht(j) g(j)
c
c-----------------------------------------------------------------
c
c    This is how the program uses the data:
c
c       x(i),y(i),z(i) .... see diagram
c
c       x1 is xx-x(i) , y1 is yy-y(i) , z1 is ht+z(i)
c
c ########################################################################## c
c                                                                          c
c   gravitational effect at O (stn posn) of a parallelepiped               c
c                                                                          c
c                O      -----> xy plane          |                        c
c                 \                              |                        c
c                  \                             |                        c
c              _____\  x1,y1,z1                  V z +ve downwards        c
c             /     /|                                                     c
c      |     ------- |                                                     c
c   dz v     |  rho  ||    / dy                                           c
c            |       |/   v                                               c
c  x2,y2,z2  -------                                                      c
c               <-                                                       c
c                dx                                                      c
c                                                                          c
c ########################################################################## c

      parameter(np=163000)
      parameter(GE=6.67e-11)

      integer i,k,sw
      real dx,dy,dz,x(np),y(np),z(np),rho(np),xx,yy,ht,g,dg
      double precision t1,t2,t3,t4,t5,t6,t7,t8,l1,l2,l3,l4
      double precision x1,x2,y1,y2,z1,z2
      double precision r111,r112,r121,r211,r122,r212,r221,r222
      double precision a1,b1,a2,b2,a3,b3,a4,b4,a5,a6,a7,a8

      open(unit=1,file='grav.in')
      open(unit=2,file='grav.out')
      open(unit=3,file='station')

      read(1,*)dx,dy,dz,sw
      k=0
      do 3 i=1,999999
      k=k+1
3     read(1,*,end=4)x(k),y(k),z(k),rho(k)
```

```
 4      k=k-1
        print*,'data read in'

c Read in position of station
        do 60 l=1,999999
        if(sw) 10,10,11
10      read(3,*)xx,yy
        ht=0
        goto 12
11      read(3,*)xx,yy,ht
12      if(xx.eq.-1.)then
          goto 999
        endif

c  Work out the box postion relative to the station
        do 50 i=1,k
        x1=xx-x(i)
        y1=yy-y(i)
        if(x1.eq.0.)x1=.0001
        if(y1.eq.0.)y1=.0001

c  when z(i) is above sealevel i.e. 0 then put heights in as -ve
c  so when z(i)=ht then z1=0
        z1=ht+z(i)
        if(z1.eq.0.)z1=.0001
c  put .0001 instead of 0 to avoid floating point errors

c+++++++++++++++++++++++++++++++++++++++++++++++++++++++++++++++++++++++++++++
c  Do calculation for effect of box at station position


        x2=x1+dx
        y2=y1+dy
        z2=z1+dz
        r111=(x1*x1+y1*y1+z1*z1)**.5
        r112=(x1*x1+y1*y1+z2*z2)**.5
        r121=(x1*x1+y2*y2+z1*z1)**.5
        r211=(x2*x2+y1*y1+z1*z1)**.5
        r221=(x2*x2+y2*y2+z1*z1)**.5
        r212=(x2*x2+y1*y1+z2*z2)**.5
        r122=(x1*x1+y2*y2+z2*z2)**.5
        r222=(x2*x2+y2*y2+z2*z2)**.5
        a1=(x1*y1)/(z1*r111)
        a2=(x2*y1)/(z1*r211)
        a3=(x1*y2)/(z1*r121)
        a4=(x2*y2)/(z1*r221)
        a5=(x1*y1)/(z2*r112)
        a6=(x2*y1)/(z2*r212)
        a7=(x1*y2)/(z2*r122)
        a8=(x2*y2)/(z2*r222)
        t1=(atan(a1))
        t2=(atan(a2))
        t3=(atan(a3))
        t4=(atan(a4))
        t5=(atan(a5))
        t6=(atan(a6))
        t7=(atan(a7))
        t8=(atan(a8))
        b1=((r111+y1)*(r122+y2))/((r112+y1)*(r121+y2))
        b2=((r212+y1)*(r221+y2))/((r211+y1)*(r222+y2))
        b3=((r111+x1)*(r212+x2))/((r112+x1)*(r211+x2))
        b4=((r122+x1)*(r221+x2))/((r121+x1)*(r222+x2))
        l1=x1*log(b1)
        l2=x2*log(b2)
        l3=y1*log(b3)
        l4=y2*log(b4)

20      dg=GE*rho(i)*(z1*(-t1+t2+t3-t4)+z2*(t5-t6-t7+t8)+l1+l2+l3+l4)
        g=g+dg

c+++++++++++++++++++++++++++++++++++++++++++++++++++++++++++++++++++++++++++++
50      continue

c  output is in m and mgal
c        g=g*1e5
        write(2,*)xx,yy,ht,g
        g=0
60      continue

999     close(1)
        close(2)
        close(3)

        stop
        end
```

EQSM

```
      program EQSM
c-------------------------------------------------------------
c
c   This program takes irregularly spaced gravity data in x,y,z space
c   and produces a regularly spaced grid of gravity values on a horizontal
c   plane. It does this using an equivalent source method. Briefly, the obs
c   grav field is inverted to find the masses of point sources on a fixed
c   plane below the obs. These 'equiv sources' are then used to calculate
c   the gravity field on a horizontal plane at a given altitude.
c   See Dampney (1969) for details.
c
c
c    x    x    x    x    x    x    x    reg spaced continued data
c                                   /\
c
c       o         o          o     alt          original
c     o    o    o     o      o             positions of grav stns
c  o        o          o              \/
c  ++++++++++++sealevel+++++++++++++++ /\
c                                     depth
c  s  s s  ss   s s   s s     ss       \/     equivalent sources
c
c
c
c   input file: x(1), y(1), z(1), grav(1)
c                .      .     .      .
c                .      .     .      .
c              x(np),y(np),z(np),grav(np)
c
c   np is the number of points (alter in prog). z is +ve upwards.
c   Doesnt really matter about the units used but km and mGal are
c   probably best to avoid rounding errors if numbers get too big
c   or small.
c
c   Also need to edit the parameter statements for:
c   (i)  the required final grid size e.g. nx=128, ny=128.
c        where nx and ny are the number of grid nodes (can be anything).
c  (ii)  the number of real data points  np
c (iii)  the node spacing in the final grid  dx dy
c  (iv)  the grid registration of node (1,1) - bottom left hand corner of grid.
c        xinit and yinit; top right corner is then:
c           (xinit+(nx-1)*dx),(yinit+(ny-1)*dy)
c   (v)  the depth to the equivalent source layer   depth (+ve down)
c  (vi)  the altitude of the of the continuation plane  alt (+ve up)
c
c  input/output filenames are also hardwired into prog
c
c  This program calls two subroutines from 'Numerical Recipes in Fortran'
c  Press et al. (19##). They are lubksb.f and ludcmp.f
c
c
c-------------------------------------------------------------------------

        parameter(nx=128,ny=128,np=896)
        parameter(dx=4.1471,dy=2.961, xinit=0.,yinit=0.)
        parameter(depth=16.0, alt=1.0)

        real aa(np,np),x(np),y(np),z(np),g(np),newg,indx(np)
        real depth,alt,dx,dy,xinit,yinit,xgrid,ygrid,z2,r2
        character*32 ifile,ofile

c-------------input and output files-----------------------------------------
        ifile='s26.1'
        ofile='s26o.1'

c--------------read in data-------------------------------------------------

        open(unit=1,file=ifile)
        do 10 i=1,np
        read(1,*)x(i),y(i),z(i),g(i)
        close(1)

c-----------------create matrix A-----------------------------------------

       do 50 i=1,np
          do 50 a=1,np
          z2=(z(a)+depth)**2
          r2=(x(a)-x(i))**2+(y(a)-y(i))**2
          aa(a,i)=sqrt(z2)/((r2+z2)**1.5)
50      continue

        call ludcmp(aa,np,np,indx,d)
        call lubksb(aa,np,np,indx,g)

c-----------work out grav vals at new alt on reg grid-----------------------

        open(unit=2,file=ofile)
        do 60 j=1,ny
          do 60 i=1,nx
            xgrid=xinit+dx*(i-1)
            ygrid=yinit+dy*(j-1)
            z2=(alt+depth)**2
            newg=0.
            do 65 l=1,np
              r2=(x(l)-xgrid)**2+(y(l)-ygrid)**2
              newg=newg+(g(l)*sqrt(z2)/((z2+r2)**1.5))
```

```
65          continue
            write(2,*)newq
60      continue

        close(2)

        stop
        end
```

INVRHO

```
      program INVRHO
c-----------------------------------------------------------------------
c    Deconvolution of gravity data due to lateral densitydistributions
c    Granser, H., Geoexploration, 23, 537-547, 1985.
c-----------------------------------------------------------------------

c  input file: regularly spaced gravity field in mGal and km.
c
c              dx dy nx ny
c              grav(1,1)
c                .   .
c                .   .
c              grav(nx,ny)
c
c  dx and dy are the node spacings in km. nx and ny are the number
c  of nodes.
c
c  prompted inputs:  input/ouput filenames
c                    distance to top of slab in km (z down is postive)
c                    thickness of slab in km.
c                    low pass filter parameters in km.
c                        the filter tapers high frequencies between a
c                        large and small wavelength and cuts off below
c                        the small wavelength.
c
c
c  output file: regularly spaced density values in kg m-3 at the same
c               grid points as the input file
c
c
c-----------------------------------------------------------------------

c  change parameter statements for size of grid, need power of 2.
c-----------------------------------------------------------------------
       parameter (nxi=128,nyi=128,nxi2=nxi*2,nyi2=nyi*2)
c      parameter (nxi=64,nyi=64,nxi2=nxi*2,nyi2=nyi*2)
c-----------------------------------------------------------------------

      character*80 input_file,output_file, titl, rms_file
      character*3 ans
      dimension nn(2), tapl(4)
      dimension u0(nxi2,nyi2)
      complex u(nxi2,nyi2),ul(nxi2,nyi2)
      complex density(nxi2,nyi2),dl(nxi2,nyi2)
      real kwnl(nxi2,nyi2)
      real kintl, kint2, kx2, ky2, kcutl, kcut2
      real wl,w2,val,thick,arg,argl,expp,expt
      logical*4 bindat

      data bindat/.true./

      pi=3.141592654
      twopi=2.*pi

      print *,' input gravity file (mgal) = ?'
      read(*,*)input_file
      print *,' output crustal density (kg m-3) file = ?'
      read(*,*)output_file
      print *,'distance (km) to top of slab = ?'
      read(*,*)z
      print *,'thickness of slab = ?'
      read(*,*)thick

      print*,*,'give range of the cosine taper'
      print *,'from large to small wavelength (km) :'
      read(*,*)wlarge,wsmall

      do 5 j=1,nyi
      do 5 i=1,nxi
5     u(i,j)=cmplx(0.,0.)

c--------------------read in grav data---------------------------------

      call rgrid(u0,nxi2,nyi2,dx,dy,input_file,1.0)
      call mnmxa(nxi,nyi,nxi,nyi,u0,zmin,zmax)
      umed = zmin + (zmax - zmin)/2
      print *,'min,max gravity (mgal) =',zmin,zmax
      print *,'median gravity (mgal) =',umed
      nx=nxi
      ny=nyi

c-----------------------------------------------------------------------
c            ifold=1 : fold in x and y direction.
c            ifold=2 : no fold.
c-----------------------------------------------------------------------

             ifold=1

c--------------set up dimensions based on fold choice---------------

      if(ifold.eq.1)then
      nxt=nx*2
      nyt=ny*2
      mfx=nx+1
```

```
      mfy=ny+1
      else
      nxt=nx
      nyt=ny
      mfx=nx/2+1
      mfy=ny/2+1
      end if

      mfx2=mfx*2
      mfy2=mfy*2

      if(ifold.eq.1)then
          call mirrorx(u0,nxi2,nxt,nyt,nx,ny)
      end if

c----------change everything to SI units-----------------------

      do 50 j=1,nyt
      do 50 i=1,nxt
          uval = 0.00001*(u0(i,j) - umed)
      u1(i,j)=cmplx(uval,0.)
50    continue

      dx=dx*1000.
      dy=dy*1000.
      z=  z*1000.
      thick=thick*1000.

c---------------------------------------------------------------
c       prod=correction for product of x and y dimensions
c       G=6.673*10**-11
c       topo1 is used to convert "gravity" to "topography"
c       grav1 is used to convert "topography" to "gravity"
c---------------------------------------------------------------

      prod=1./(nxt*nyt)
      const=twopi*6.673*10.**(-11)
      topo1=1./const
      grav1=   const

      kint1=twopi/(nxt*dx)
      kint2=twopi/(nyt*dy)
      kx2=kint1*kint1
      ky2=kint2*kint2

      nn(1)=nxt
      nn(2)=nyt

c---------------calculate the wavenumbers. k=0 at (1,1)----------

      do 110 j=1,nyt
        yj=j
        if(j .gt. mfy) yj=mfy2-j
        yyk=(yj-1.)*(yj-1.)*ky2

      do 100 i=1,nxt
        xi=i
        if(i .gt. mfx) xi=mfx2-i
        xxk=(xi-1.)*(xi-1.)*kx2
        kwn1(i,j) = sqrt(xxk + yyk)

  100 continue
  110 continue

      call fourt (u1,nn,2,-1,0,0)

c---------------------------------------------------------------
c   wavenumber between kcut1 & kcut2 will be tapered; wavenumber
c   > kcut2 will be truncated.   kcut1 < kcut2
c---------------------------------------------------------------

      wlarge=wlarge*1000.
      wsmall=wsmall*1000.
      kcut1=twopi/wlarge
      kcut2=twopi/wsmall
      dkcut=kcut2-kcut1

c--------modify fft coeffs and deconv the density structure--------

      do 300 j=1,nyt
      do 300 i=1,nxt
      arg=kwn1(i,j)*z
      arg1=kwn1(i,j)*thick*-1
      expp=exp(arg)
      expt=exp(arg1)
      weight=1.
      if(kwn1(i,j).gt.kcut2)then
        weight=0.
      else if(kwn1(i,j).gt.kcut1)then
        t=(kwn1(i,j)-kcut1)/dkcut*pi
        weight=(cos(t)+1)/2.
      end if
                if(kwn1(i,j).eq.0.)then
                u(i,j)=cmplx(0.,0.)
                else
           u(i,j)=(u1(i,j)*kwn1(i,j)*expp*weight)/(1-expt)
                endif
  300 continue

c----------------do inv transform to get densities---------------
```

```
      print *,'inverse fft'
      call fourt (u,nn,2,1,1,0)
      t = 0.
      do 310 j=1,nyt
      do 310 i=1,nxt
      u(i,j) = u(i,j)*prod
      density(i,j) =(u(i,j))/const
310   continue

c---------------------write out density--------------------------

      open(unit=10,file=output_file)
      do 1500 j=1,nyt/2
        do 1500 i=1,nxt/2
1500     write(10,*) real(density(i,j))
      close (10)
      print*,' done writing ', output_file

      stop
      end

c=======================================================================
c subroutine mirror
c program to do two reflections of raw topographic data
c need array that is double the size of raw topographic data
c in each direction. raw data must be written 1 to nx
c and 1 to ny. data first reflected across nx then across
c ny.
      subroutine mirrorx(sdata,nxi2,nx2,ny2,nx,ny)
      dimension sdata(nxi2,ny2)

      do 10 i=1,nx
      k=nx2+1-i
      do 10 j=1,ny
   10 sdata(k,j)=sdata(i,j)

      do 20 j=1,ny
      l=ny2+1-j
      do 20 i=1,nx2
   20 sdata(i,l)=sdata(i,j)
      print*,'done mirror'
      return
      end
c=======================================================================

      subroutine rgrid(dat,m,n,dx,dy,fin,conv)
      real dat(m,n), conv, tmp(128)
      character*80 fin, titl

      open(unit=10,file=fin)
      read(10,*) dx,dy,nx,ny
       do 1000 j=1,ny
         do 1000 i=1,nx
           read(10,*)dat(i,j)
1000  continue

      close(10)
      return
      end

c=======================================================================
      SUBROUTINE MNMXA(nxi,nyi,nx,ny,dat,zmin,zmax)
      dimension dat(nyi,nxi)
      print*,'mnmxa'

      zmax = -1.0e10
      zmin =  1.0e10
      do 1200 i=1,ny
      do 1200 j=1,nx
        if(dat(i,j).lt.zmin) zmin = dat(i,j)
        if(dat(i,j).gt.zmax) zmax = dat(i,j)
1200  continue

      return
      end
```

Acknowledgements

Thanks are due to: Gill Foulger for obtaining the Icelandic gravity datasets used in this project which were supplied by the National Energy Authority of Iceland (Orkustofnun); Lyndsay Parson, Roger Searle (P.I.s), the scientists and crew of the R/V Maurice Ewing on which the marine gravity data in this thesis was acquired; Stuart Arnott, Gill Foulger and D. Toomey for copies of their tomography results; D. Forsyth, B. Kuo, and Roger Searle for programs; Cherry Walker for some rocks; and Bernard McEleavey for density and porosity measurements.

I acknowledge N.E.R.C. for the funding they provided for this project.

I would like to thank my supervisors, Roger Searle and Gill Foulger, for advice and suggestions. Thanks to Roger for inviting me on the EW9008 research cruise and Gill for organising fieldwork in Iceland. Thanks also to Geoff Brown and Hazel Rymer for their time at Krafla.

Ellis Leazes was my latest abode and i thank the 'clique' for some great parties. I'd also like to thank my house mates for sharing the bills, the hassles and the cooking: Cherry (10 months), Salim (12 months), Sue (20 months), and Berty (6 months).

In the department, I'd like to thank Dave Stevenson for whisky and parties (and for computer related 'things' too). Thanks too to Dave Asbury, Carol, and Lynne for favours and help.

Thanks Mom and Dad for always being willing to collect my stuff, have me home to stay, and making sure you've always got my new address. Thanks Julie for making sure that I still got the odd holiday now and again.

Oh, almost forgot. Thanks Jane for sticking some pictures down (well quite a few really) and both Jane and Sue for reading and checking parts of the text.

The text of chapter 2 of this thesis draws substantially on that of a manuscript jointly authored with my supervisor, Dr G. Foulger, whose contribution I hereby acknowledge.